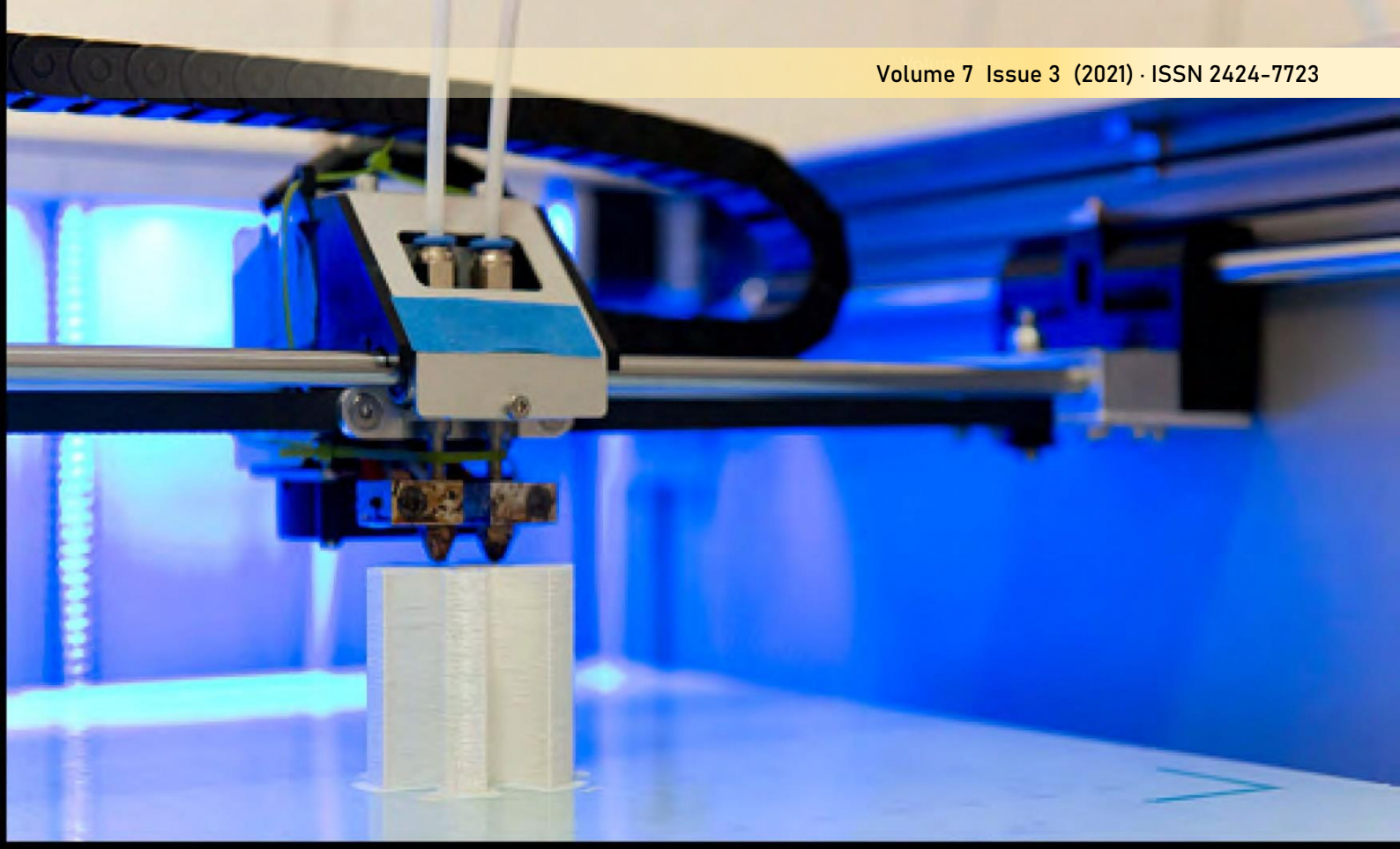
Volume 7 Issue 3 (2021) · ISSN 2424-7723



INTERNATIONAL JOURNAL OF BIOPRINTING

WHIOCE PUBLISHING PTE. LTD.
PROVIDING
FIRST-CLASS SCIENTIFIC INFORMATION
FOR TOP SCHOLARS

Volume 7 Issue 3 • 2021
ISSN 2424-7723 (print) ISSN 2424-8002 (online)

INTERNATIONAL JOURNAL OF BIOPRINTING

Editor-in-Chief

Chee Kai Chua

Singapore University of Technology and Design, Singapore

WHIOCE PUBLISHING PTE. LTD.

Volume 7 | Issue 3 | 2021 | Page 1 – 162 |

International Journal of Bioprinting

https://ijb.whioce.com/index.php/int-j-bioprinting

CONTENTS

Special Section: Bioprinting of 3D Functional Tissue Constructs

1 **Bioprinting of 3D Functional Tissue Constructs** *EDITORIAL*
Jiankang He, Mao Mao, Xiao Li, Chee Kai Chua

3 **Bio-assembling and Bioprinting for Engineering Microvessels from the Bottom Up** *REVIEW ARTICLE*
Xiaoming Liu, Tao Yue, Masaru Kojima, Qiang Huang, Tatsuo Arai

18 **Developments and Opportunities for 3D Bioprinted Organoids** *REVIEW ARTICLE*
Ya Ren, Xue Yang, Zhengjiang Ma, Xin Sun, Yuxin Zhang, Wentao Li, Han Yang, Lei Qiang, Zezheng Yang, Yihao Liu, Changxu Deng, Liang Zhou, Tianchang Wang, Jingsheng Lin, Tao Li, Tao Wu, Jinwu Wang

37 **3D Bioprinting Photo-Crosslinkable Hydrogels for Bone and Cartilage Repair** *REVIEW ARTICLE*
Quanjing Mei, Jingdong Rao, Ho Pan Bei, Yaxiong Liu, Xin Zhao

54 **Fabrication and Biomedical Applications of Heart-on-a-chip** *REVIEW ARTICLE*
Qingzhen Yang, Zhanfeng Xiao, Xuemeng Lv, Tingting Zhang, Han Liu

71 **3D Printing of Layered Gradient Pore Structure of Brain-like Tissue** *RESEARCH ARTICLE*
Na Pei, Zhiyan Hao, Sen Wang, Binglei Pan, Ao Fang, Jianfeng Kang, Dichen Li, Jiankang He, Ling Wang

86 **Coaxial Electrohydrodynamic Bioprinting of Pre-vascularized Cell-laden Constructs for Tissue Engineering** *RESEARCH ARTICLE*
Mao Mao, Hongtao Liang, Jiankang He, Ayiguli Kasimu, Yanning Zhang, Ling Wang, Xiao Li, Dichen Li

97 **Elastic and Stretchable Double Network Hydrogel as Printable Ink for High-Resolution Fabrication of Ionic Skin** *RESEARCH ARTICLE*
Kaiwen Chen, Qiwei Ying, Xingxing Hao, Kai Sun, Huanan Wang

108 **A Systematic Thermal Analysis for Accurately Predicting the Extrusion Printability of Alginate–Gelatin-Based Hydrogel Bioinks** *RESEARCH ARTICLE*
Qi Li, Bin Zhang, Qian Xue, Chunxiao Zhao, Yichen Luo, Hongzhao Zhou, Liang Ma, Huayong Yang, Dapeng Bai

Regular Section

124 **Graphene Oxide-Embedded Extracellular Matrix-Derived Hydrogel as a Multiresponsive Platform for 3D Bioprinting Applications** *RESEARCH ARTICLE*
Laura Rueda-Gensini, Julian A. Serna, Javier Cifuentes, Juan C. Cruz, Carolina Muñoz-Camargo

140 **A Dual-sensitive Hydrogel Based on Poly(Lactide-co-Glycolide)-Polyethylene Glycol-Poly(Lactide-co-Glycolide) Block Copolymers for 3D Printing** *RESEARCH ARTICLE*
Yang Zhou, Yuecheng Cui, Li-Qun Wang

153 **3D Topology Optimization and Mesh Dependency for Redesigning Locking Compression Plates Aiming to Reduce Stress Shielding** *RESEARCH ARTICLE*
A. A. Al-Tamimi

EDITORIAL

Bioprinting of 3D Functional Tissue Constructs

Jiankang He[1,2]*, Mao Mao[1,2], Xiao Li[1,2], Chee Kai Chua[3]

[1]State Key Laboratory for Manufacturing Systems Engineering, Xi'an Jiaotong University, Xi'an 710049, China
[2]NMPA Key Laboratory for Research and Evaluation of Additive Manufacturing Medical Devices, Xi'an Jiaotong University, Xi'an 710049, China
[3]Engineering Product Development Pillar, Singapore University of Technology and Design, Singapore 487372, Singapore

*Correspondence to: Jiankang He, State Key Laboratory for Manufacturing Systems Engineering, Xi'an Jiaotong University, Xi'an 710049, China; jiankanghe@mail.xjtu.edu.cn

Citation: He, J,Mao M, Li X, *et al.*, 2021, Bioprinting of 3D Functional Tissue Constructs. *Int J Bioprint.* 7(3):395. http://doi.org/10.18063/ijb.v7i3.395

In recent years, bioprinting has attracted growing research interest due to its unique capability in fabricating complex tissue-specific architectures and precisely positioning living cells in a controllable and reproducible manner. Bioprinting involves multiple disciplines such as biomaterials, mechanical engineering, life science, and medicine. It has become a powerful tool to generate 3D living tissue constructs that replicate the physiological environments, sustain long-term culture, and function as native tissues. Extensive research efforts have been made to print large and functional tissue constructs with biomimetic vascular networks and micro/nanoscale architectures similar to native organs. This special issue is dedicated to summarizing the most recent advances, strategies, and applications of bioprinting techniques ranging from the development of bioinks to engineering of 3D tissue constructs. Four original research articles and four review articles are included in this special issue.

A key aspect of bioprinting is bioinks, which should have optimal rheological and biological properties for successful printing as well as maintaining cell viability and growth capability. In this special issue, Li *et al.* proposed a quantitative thermal model to predict the printability and printing accuracy of alginate–gelatin composite bioinks[1]. Photo-crosslinkable bioinks, which can respond to light and induce structural or morphological transition, were considered as a promising bioink candidate for bioprinting, due to their high biocompatibility, ease of fabrication, as well as controllable mechanical, and degradation properties. A review article by Mei *et al.* summarized the commonly used photo-crosslinkable hydrogels and discusses their potential applications for printing bone and cartilage constructs[2]. In addition, Chen *et al.* developed an elastic and stretchable bioink by combining a polyacrylamide covalent network with a gelatin colloidal network, which was successfully used for high-precision fabrication of ionic skins[3].

Vascular-like networks can be bioprinted to support the growth of 3D tissue constructs. Mao *et al.* presented a novel coaxial electrohydrodynamic bioprinting strategy to generate perfusable core-sheath hydrogel filaments, which can be assembled into 3D constructs with a thickness of more than 3 mm[4]. Their success in printing the thick 3D pre-vascularized cardiac constructs shows great potential to engineer living tissues with complex vascular structures. In a review article, Liu *et al.* compared bioprinting and bioassembling methods for engineering microvessels from the perspectives of fabrication efficiency, the sizes of the engineered microvessels, and the ability to construct complex 3D microvascular networks[5].

Bioprinting can be applied to generate various *in vitro* biological models with complex structural features and tissue-specific functions. With respect to organoids as emerging biological models, Ren *et al.* examined existing bioprinting methods and bioinks and envisioned possible directions for future organoid bioprinting[6]. Similarly, Yang *et al.* reviewed recent advances regarding the fabrication methods and applications of heart-on-a-chip, where various bioprinting techniques underpin the construction of cardiac microtissues[7]. In an original research article, Pei *et al.* reported an integrated bioprinter that enabled the fabrication of layered gradient pore structures of brain-like tissues while maintained a high cell viability[8].

© 2021 He, *et al*. This is an Open Access article distributed under the terms of the Creative Commons Attribution License (https://creativecommons. org/licenses/by/4.0/), permitting distribution and reproduction in any medium, provided the original work is cited.

Conflict of interest

No conflict of interest was reported by the authors.

References

1. Li Q, Zhang B, Xue Q, *et al*., 2021, A Systematic Thermal Analysis for Accurately Predicting the Extrusion Printability of Alginate-Gelatin-Based Hydrogel Bioinks. *Int J Bioprint*, 7:394.
   http://doi.org/10.18063/ijb.v7i3.394
2. Mei Q, Rao J, Bei HP, *et al*., 2021, 3D Bioprinting Photo-crosslinkable Hydrogels for Bone and Cartilage. *Int J Bioprint*, 7:367.
   http://doi.org/10.18063/ijb.v7i3.367
3. Chen K, Ying Q, Hao X, *et al*., 2021, Elastic and Stretchable Double Network Hydrogel as Printable Ink for High-resolution Fabrication of Ionic Skin. *Int J Bioprint*, 7:377.
   http://doi.org/10.18063/ijb.v7i3.377
4. Mao M, Liang H, He J, *et al*., 2021, Coaxial Electrohydrodynamic Bioprinting of Pre-vascularized Cell-laden Constructs for Tissue Engineering. *Int J Bioprint*, 7:362.
   http://doi.org/10.18063/ijb.v7i3.362
5. Liu X, Yue T, Kojima M, *et al*., 2021, Bioassembling and Bioprinting for Engineering Microvessels from the Bottom Up. *Int J Bioprint*, 7:366.
   http://doi.org/10.18063/ijb.v7i3.366
6. Ren Y, Yang X, Ma Z, *et al*., 2021, Developments and Opportunities for 3D Bioprinted Organoids. *Int J Bioprint*, 7:364.
   http://doi.org/10.18063/ijb.v7i3.364
7. Yang Q, Xiao Z, Lv X, *et al*., 2021, Fabrication and Biomedical Applications of Heart-on-a-chip. *Int J Bioprint*, 7:370.
   http://doi.org/10.18063/ijb.v7i3.370
8. Pei N, Hao Z, Wang S, *et al*., 2021, 3D Printing of Layered Gradient Pore Structure of Brain-like Tissue. *Int J Bioprint*, 7:359.
   http:/doi.org/10.18063/ijb.v7i3. 359

REVIEW ARTICLE

Bio-assembling and Bioprinting for Engineering Microvessels from the Bottom Up

Xiaoming Liu[1]*, Tao Yue[2,3], Masaru Kojima[4], Qiang Huang[1]*, Tatsuo Arai[1,5]

[1]Key Laboratory of Biomimetic Robots and Systems, Ministry of Education, State Key Laboratory of Intelligent Control and Decision of Complex System, Beijing Advanced Innovation Center for Intelligent Robots and Systems, and School of Mechatronical Engineering, Beijing Institute of Technology, Beijing 100081, China
[2]School of Mechatronic Engineering and Automation, Shanghai University, Shanghai 200444, China
[3]Shanghai Institute of Intelligent Science and Technology, Tongji University, Shanghai 200092, China
[4]Department of Materials Engineering Science, Osaka University, Osaka 5608531, Japan
[5]Center for Neuroscience and Biomedical Engineering, the University of Electro-Communications, Tokyo 1828585, Japan.

Abstract: Blood vessels are essential in transporting nutrients, oxygen, metabolic wastes, and maintaining the homeostasis of the whole human body. Mass of engineered microvessels is required to deliver nutrients to the cells included in the constructed large three-dimensional (3D) functional tissues by diffusion. It is a formidable challenge to regenerate microvessels and build a microvascular network, mimicking the cellular viabilities and activities in the engineered organs with traditional or existing manufacturing techniques. Modular tissue engineering adopting the "bottom-up" approach builds one-dimensional (1D) or two-dimensional (2D) modular tissues in micro scale first and then uses these modules as building blocks to generate large tissues and organs with complex but indispensable microstructural features. Building the microvascular network utilizing this approach could be appropriate and adequate. In this review, we introduced existing methods using the "bottom-up" concept developed to fabricate microvessels including bio-assembling powered by different micromanipulation techniques and bioprinting utilizing varied solidification mechanisms. We compared and discussed the features of the artificial microvessels engineered by these two strategies from multiple aspects. Regarding the future development of engineering the microvessels from the bottom up, potential directions were also concluded.

Keywords: Microvessels; Bio-assembling; Bioprinting; Bottom-up; Tissue engineering

*Correspondence to: Xiaoming Liu, School of Mechatronical Engineering, Beijing Institute of Technology, Beijing 100081, China; liuxiaoming555@bit.edu.cn; Qinag Huang, School of Mechatronical Engineering, Beijing Institute of Technology, Beijing 100081;qhuang@bit.edu.cn

Received: April 7, 2021; **Accepted:** May 7, 2021; **Published Online:** June 11, 2021

(This article belongs to the *Special Section*: *Bioprinting of 3D Functional Tissue Constructs*)

Citation*:* Liu, X, Yue, T, Kojima, M, *et al*., 2021, Bioassembling and Bioprinting for Engineering Microvessels from the Bottom Up. *Int J Bioprint.* 7(3):366. http://doi.org/10.18063/ijb.v7i3.366

1. Introduction

Tissues such as bone and skin have the ability to repair slight injuries by themselves[1-3]. However, many serious tissue injuries and multiple organ failures can hardly be effectively cured by conventional interventional, pharmacological, and surgical therapies, except organ transplantation[4-6]. Unfortunately, organ transplantation in the clinic is greatly limited by the shortage of donors[7,8]. Tissue engineering was introduced by Langer 30 years before targeting to build artificial functional tissue substitutes through combining specific cell lines, molecules, and organic materials[4]. In the past two decades, significant advances have been achieved in tissue engineering. Many different kinds of tissues have been fabricated, but most of these engineered tissues feature thin slices and simple architectures[9,10]. The main reason is the challenges in including the microvascular networks in the large functional regenerated tissues[11].

Blood vessels are essential in transporting nutrients, oxygen, metabolic wastes, and maintaining the homeostasis of the whole human body. Mass of engineered microvessels is required to deliver nutrients to the cells

© 2021 Liu, *et al*. This is an Open Access article distributed under the terms of the Creative Commons Attribution License (https://creativecommons. org/licenses/by/4.0/), permitting distribution and reproduction in any medium, provided the original work is cited.

included in the constructed large three-dimensional (3D) functional tissues by diffusion which is limited within an area of smaller than 200 μm[12-15]. Traditional tissue engineering strategies adopt the "top-down" approach, in which cells are seeded on a biodegradable scaffold. The seeded cells then populate on the scaffold and generate the appropriate extracellular matrix[16-20]. However, this approach can only fabricate vessels larger than 6 mm, which are mainly used to replace the damaged vessels of patients with cardiovascular diseases[21]. It is a formidable challenge to regenerate microvessels and build a microvascular network, mimicking the cellular viabilities and activities in the engineered organs, such as the liver, the heart, and the kidney, with traditional, or existing manufacturing techniques[9-11,21].

Modular tissue engineering adopting the "bottom-up" approach builds one-dimensional (1D) or two-dimensional (2D) modular tissues in micro scale first and then uses these modules as building blocks to generate large tissues and organs[22-32]. It allows recreating complex but indispensable microstructural features of the engineered tissues. Building the microvascular network using this approach could be appropriate and adequate. However, fabricating the basic modular tissues and building the microvessels with these modules in micro scale face tough challenges in precision, efficiency, and configuration complexity. Existing methods using the "bottom-up" concept developed to fabricate microvessels can be divided into bio-assembling powered by developing micromanipulation techniques and bioprinting utilizing varied solidification mechanisms. Some researchers tend to treat bioprinting as a particular assembly approach in modular tissue engineering. The main difference of bioprinting from the common bio-assembling is its ability to create modular tissues and build 3D structures simultaneously[33].

In this review, we describe the bio-assembling and bioprinting strategies for engineering the microvessels. First, we introduce the 1D or 2D modular tissues with different geometries for assembling the microvessels and the bioinks used in bioprinting. Then, assembly methods applying different micromanipulation techniques and bioprinting devices adopting different mechanisms are reviewed. Finally, we compare and discuss the features of the artificial microvessels constructed by these two strategies from the aspects of the fabrication efficiency, the sizes of the engineered microvessels, and the ability to construct the complex 3D microvascular networks.

2. Engineering microvessels from the bottom up

At present, there are two construction strategies in tissue engineering, which are "top-down" and "bottom-up" approaches. In most "top-down" approaches, a scaffold is fabricated first, and cells are then seeded on the scaffold. In the following culture process, cells populate on the scaffold and generate the appropriate extracellular matrix with the external chemical and mechanical stimulations. While developing the "top-down" approaches, researchers focus on improving the fabrication of scaffold or testing various combinations of the cell sources and stimulation ways during culture[16-21]. Nowadays, the main challenge in applying "top-down" approaches to the construction of the independent vascular networks or tissues including the microvascular architectures is that "top-down" approach is by nature a 2D construction strategy. The cells are seeded on the surface of the scaffold which is a 2D space. Along with increasing the complexity of the scaffold architectures, it becomes difficult for seeding the cells on the scaffold and giving the necessary support or stimulations to the seeded cells. Moreover, "top-down" approach features extremely low flexibilities in constructing tissues with varied sizes and architectures.

Different from the "top-down" approaches, "bottom-up" approaches start from constructing fabricating the micro modular tissues with cells and biocompatible materials[22-32]. As shown in **Figure 1**, 1D or 2D modules such as spheroids, rings especially for engineering microvessels, fibers, plates with arbitrary shapes, and cell sheets can be fabricated through cell aggregation and microfabrication techniques with mass production. Then, these micromodules as the basic blocks can be used to build the large tissues with desired micro architectures including the microvascular networks. The existing "bottom-up" approaches for engineering microvessels can be divided into bio-assembling and bioprinting. Some researchers also classify the bioprinting into a particular bio-assembling way. In engineering microvessel by bioassembling, the key is the geometry design of the micro modules, which governs the selection of the micromanipulation methods in the assembling procedure. The geometry of the micromodules and the micromanipulation utilized in the assembling determines the fabrication efficiency, complexity, and size of the constructed microvessels. In engineering microvessel by bioprinting, the bioink compositions and solidification mechanisms are the two major factors as they influence the mechanical property, curing time, curing degree, printing speed, and printing resolution. In the following sections, we will introduce existing bio-assembling approaches utilizing various micro modular tissues and bioprinting approaches based on different printing mechanisms.

3. Modules and bioinks

According to the morphology, we divide modules for assembling microvessels into five categories: fiber,

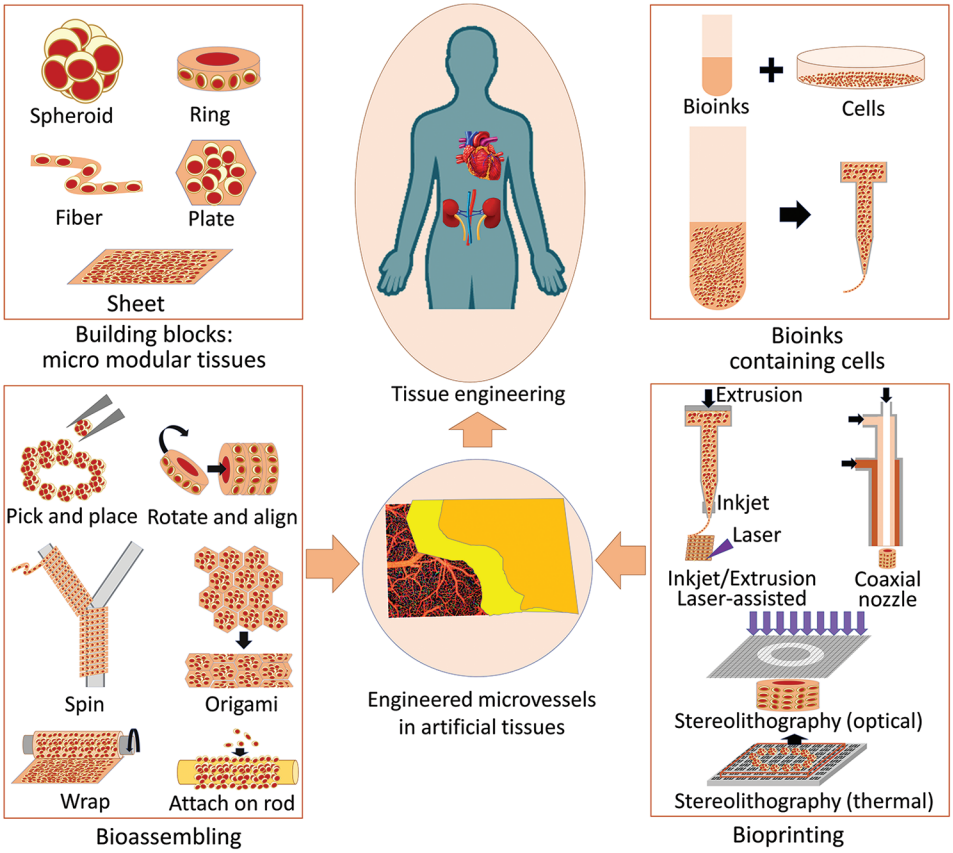


Figure 1. Artificial microvessels by modular tissue engineering: bio-assembling and bioprinting microvessels from the bottom up.

sheet, plates, rings, and spheroid. The bioinks can be divided into the pure polymer and composite polymer. In this section, we focus on introducing the existing fabrication method of the micro modular tissues for assembling microvessels, and bioinks that can be utilized in bioprinting the microvessels.

3.1. Cell spheroids

Cell spheroids usually refer to cell clusters composed of multiple cells that do not adhere to any culture substrate. In the cell spheroids, cells are typically surrounded by the extracellular matrix, which is a substance that affects cell growth and proliferation[34-36]. In most biological research, cells adhere to cell culture-compatible polystyrene and proliferate in a 2D monolayer. However, this *in vitro* environment is thought significantly different from the natural cellular environment. Nowadays, with novel microfabrication techniques, cells can be cultured as spherical aggregates or be embedded in spherical structures made by biocompatible materials. With these cell culturing methods, cells stay in the extracellular matrix interacting with each other just like in their natural environment. The biological research conducted with these cell culturing methods is considered more convincing. Moreover, these cell spheroids are also considered as ideal basic building blocks in "bottom-up" tissue engineering since they offer a stable natural cellular microenvironment in the assembling process. The fabrication of cell spheroid is closely related to cell 3D culture, as shown in **Figure 2A**. The traditional cell spheroid fabrication methods are hanging drop and cell suspension. These methods achieve aggregation by avoiding cell contact with the substrate, but the size of cell spheroids cannot be well controlled. Microwell hanging drop technique was developed to address this issue because it has pores that can be used to filter the size. It ensured that the collected cell spheroids are small enough with a similar outer diameter. Besides, using photolithography or customized channels to make and collect cell spheroids can also yield products with an unfirm size because cells can gather into clusters in a chamber with a fixed size. However, the fabrication efficiency of the latter two methods is low, and the cost is high.

3.2. Cell-embedded fibers

Fiber is popular in "bottom-up" tissue engineering as the basic module. The advantage of using the fibers as the basic modules to construct large 2D and 3D structures (mainly clothes) can be traced back thousands of

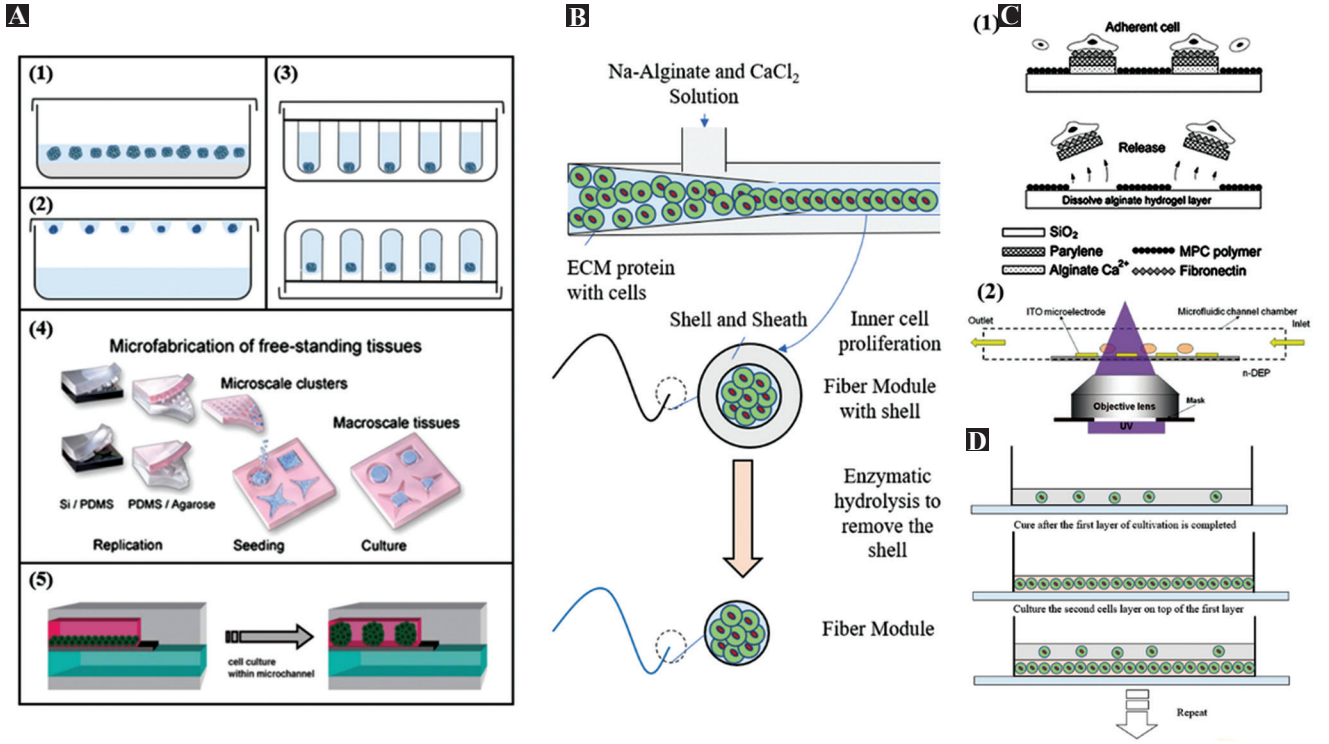


Figure 2. The fabrication process of several kinds of modules. (A) Six fabrication methods of cell spheroids modules[34], including (A1) suspension cell culture, (A2) hanging drop, (A3) microwell, (A4) microwell array from micropatterned agarose wells (Republished with permission from Rivron NC, Vrij EJ, Rouwkema J, *et al*., *Proc Natl Acad Sci,* 2012, 109:6886–91.[35]), and finally, (A5) microchannel forming (Reproduced from ref. 36 with permission from The Royal Society of Chemistry). (B) Fabrication process of fiber module by microchannels[30]. (C) Fabrication process of microplates and rings by **(C1)** photolithography (Republished with permission from Teshima T, Onoe H, Kuribayashiashiashias K, *et al*., Small, © 2013 WILEY-VCH Verlag GmbH & Co. KGaA, Weinheim[38]). and (C2) dielectrophoresis (from ref.[39] licensed under Creative Commons Creative Commons Attribution License). (D) Layer-by-layer fabrication process of cell sheets[44].

years ago. Furthermore, inspired by the ancient fiber production methods and being assisted by the recent microfabrication techniques, researchers have developed many methods to fabricate cell-embedded fiber modules. Nearly all these methods follow the same way, which is to make biocompatible materials (together with some other materials) pass through narrow channels or pipes, and finally fabricate the fibers close to the outlet by solidification. The microfluidic manufacturing method is recognized as an efficient solution, as shown in **Figure 2B** derived from the paper by Onoe *et al*.[30], which depicts an advanced fiber manufacturing process. The extracellular matrix protein with cells in the pre-gel state is covered by stiff Ca-alginate hydrogel formed by the chemical reaction between the Na-alginate solution and the $CaCl_2$ solution. Since the alginate in the outer layer forms a shell to avoid the diffusion of the inner extracellular matrix protein gel, the cells inside can proliferate and form the cell-embedded fibers under suitable conditions. Finally, the outer alginate shell is removed with enzymes, and the fibers as the building blocks in "bottom-up" tissue engineering can be obtained. In addition to the method of microfluidic spinning introduced in the above, electrospinning, wet spinning, biospinning, and melt spinning are all feasible methods for fabricating microfibers[37]. Using these fabrication methods, encapsulation of cells, fabrication efficiency, damages to cells during the fabrication, size control, and mechanical property of the fabricated fibers should be well considered.

3.3. Cell-laden 2D modules

Compared with the 1D cell spheroids and fibers embedded cells, 2D modules with designed geometry could accelerate the following assembling process. For example, assembling the ring-shaped 2D modules to microvascular structures could be more efficient than assembling the spheroids. Nowadays, photolithography and soft lithography are commonly utilized in the fabrication of 2D modules with arbitrary shapes. **Figure 2C** shows the fabrication of cell-laden microplates using photolithography[38,39]. The expected microplate is composed of the cell-adhesion layer, the core layer, and the sacrificial layer. During the manufacturing process, first, the core layer with a metal plate is covered to ensure

that the required part can be left. Second, MPC polymer, the hard-to-attach layer, is covered first. The metal part is washed off then. Thus, the adhesion layer can stay on the surface of the core layer to allow the cells to attach. Finally, to make the microplate fall off from the substrate, the sacrificial layer is washed away, and the standardized cell-attached microplates can be obtained. Different from the cells that adhere to the surfaces of the microplates, cells can also be maintained inside 2D structures. As shown in **Figure 2C**, mixing cells with photo-cross-linkable resin (PEGDA, polyethylene glycol diacrylate), and ring-shaped (arbitrary shape is available) cellular modules can be fabricated by exposing the resin inside a thin microchannel to the patterned Ultraviolet light[40]. Here, dielectrophoresis is employed to array the cells in the resin to ensure the uniform distribution of cells in the fabricated 2D modules. Moreover, in the fabrication of the 2D modules utilizing soft lithography, the template patterns are first fabricated. Then, by molding the templates, poly(dimethylsiloxane) (PDMS) microwell arrays are obtained. The PDMS microwell array also serves as the template for shaping the curable solutions. After solidification of the solution, the 2D modules with arbitrary shapes can be fabricated[41,42].

3.4. Cell sheets

Researchers have a wide variety of choices available in the fabrication of the cell sheets which can also act as the modular tissues in the "bottom-up" tissue engineering. The typical methods include the layer-by-layer covering method and the textile method. The layer-by-layer covering method is one of the simplest approaches to fabricate the sheet modules. In the research of Yokoyama *et al*., they used elastin to wrap smooth muscle cells arranged in a multilayer spiral[43]. In the fabrication process, Yokoyama *et al*. used the layer-by-layer method, as shown in **Figure 2D**, which cultivates a layer of smooth muscle cells in the elastin. When the cells are proliferated to the required number, they are gelled, and then the second layer of cells is cultivated on it, and so on. Hinds *et al*. used a similar method to fabricate a cell sheet and then used it to build a vascular structure[44]. Although the fabrication was conducted on a cylinder mold, all the contents are uploaded layer-by-layer through a syringe. Electrospun uses the electric field to gel the woven elastin fiber. After weaving the fiber gels, the final output is the sheet module.

3.5. Bioinks: pure polymers

In "bottom-up" tissue engineering by bioprinting, the bioinks are important. The concept of bioinks comes with the development of bioprinting technology. Many studies on bioinks in recent years have discovered or developed various materials suitable for bioprinting. In general, bioinks need to have the following characteristics: bioinks should protect cells from extrusion, inappropriate environments, and other damages in the fabricating processes[45]; they should have suitable mechanical properties, such as high mechanical integrity, viscoelasticity, and stability; they should consider the biocompatibility, such as non-toxicity, and non-immunogenicity, and also cell adhesion promotion properties; and they should also own other necessary characteristics including printability, insolubility in the culture medium, commercial feasibility, and manufacturing efficiency.

Researchers such as Saito *et al*., Jia *et al*., and Mobaraki *et al*. have made a summary of the materials suitable to be used as bioinks[20,46,47]. Here, we only introduce the inductive nature of various materials. Almost all bioinks used currently are composed of polymer components, most of which are used in the form of hydrogels. Pure polymers can be used in bioprinting, but some composite polymers are also used to improve the mechanical properties of materials or expand the other physical properties. Some popular pure polymers are as follows. Collagen is a triple helix biocompatible protein of natural origin, which has the smallest immune response[48]. Collagen can also promote cell culture and enhance cell adhesion and attachment to the culture medium[49]. Collagen stays in a liquid state at a low temperature and will gel when the temperature rises, but the solidification speed is slow; it takes 30 min at 37°C to gel totally, which is a barrier to 3D bioprinting[46]. Fibrin is a kind of bioink with considerable mechanical properties (especially elasticity) and short gelation time. It is also biocompatible and able to promote cell growth and is thus a choice to fabricate microvessels. However, the price of fibrin is also high. Silk is one of the most common biological protein materials, derived from biological activities such as spider silk or silkworm cocoons. Silk has ideal mechanical properties while being smooth, non-toxic, and not easy to be contaminated by bacteria. However, it usually needs to be mixed with other substances to optimize some other important printing properties, such as transparency and fluidity. Alginate is one of the most popular natural hydrogels. It is a natural polysaccharide with special characteristics such as high biocompatibility, low price, different crosslinking options, and high compatibility with various printing methods[46]. Low cell adhesion and average mechanical properties are its two main shortcomings. Chitosan, similar to cellulose, is also a natural polymer polysaccharide, which is generally used to make tissues or organs with high mechanical strength (resistance to tension and compression). Its price is also very low, and it is often used in the medical field as well. Gelatin[50] is mainly derived from the hydrolysis of collagen. Therefore, it can be directly extracted from animal connective tissue and other materials. It has low immunogenicity, no cytotoxicity, and low cost, but

its mechanical strength is average. Hyaluronic acid is well known to many people as a material in the fields of medicine, hygiene, and beauty. However, it also can make flexible hydrogels. When subjected to force, it is prone to deformation.

3.6. Bioinks: composite polymers

Compared with pure polymers, composite polymers are utilized to improve the mechanical properties, modify other physical properties of the printed construes, and retain the excellent biocompatibility of pure polymers. According to the operation mode, composite materials can be divided into five types: multimaterial, stimuli-responsive, biomolecular, self-assembling, and materials based on nanotechnology. Many pure bioinks, as described before, have insufficient deformability during use, or their nature is not conducive to 3D printing operations. Therefore, they can be doped with some other substances. For example, calcium ions can add to alginate to improve the mechanical strength and crosslinking performance[51]; chitosan hydrogel and hydroxyapatite can mix as artificial cartilage material[52]. Biomolecular material is a vital branch of the bioinks for our research, which is widely used in the fabrication of engineered vessels. This material includes cytoplasmic matrix, decellularized extracellular matrix, or DNA and other living tissues elements as a bioink, which can simulate the life state and mechanical properties of cells to the greatest extent[47]. Essentially, these materials are also a mixture of polysaccharides, lipids, and proteins. In addition to simple doping methods, controllable combinations of multiple materials also play an important role in enhancing the mechanical properties of materials and expanding other physical properties (such as magnetism), where nanotechnology is required, including nanofabrication and nanoparticle reinforced polymer composites. Self-assembling materials are a kind of hydrogel materials with better mechanical properties by catalyzing the automatic combination of proteins or peptides in a specific way or shape[53]. Besides, current popular bioprinting targets are not only limited to satisfy sufficient mechanical properties and biocompatibility but also to provide obvious features so that external field forces can manipulate these structures. Researchers gave bioinks additional characteristics such as magnetism. Using the magnetic force can expand the methods of printing and further operations, achieve higher precision, and manufacture more stable artificial blood vessels. Nanotechnology is urgently needed among the above two materials. It is still very important to explore and develop new excellent bioinks in the future.

4. Bio-assembling powered by micromanipulations

Micromanipulation has been widely used to construct artificial tissues[54]. Adopting the "bottom-up" approach, bio-assembling powered by micromanipulation techniques provides a robust and highly scalable method to build 3D engineered tissue through assembling micro modular tissues[20,28,55]. This section lists the typical bio-assembling methods depending on the morphology of the fabricated micromodules.

4.1. Pick-and-place of spheroids

The concept of "cell as a material" proposed by Kasza *et al*. implies that micro-spherical modular tissues can be considered as the basic building blocks of blood vessels, which is a more intuitive and feasible way to realize the construction of artificial microvascular networks or any other engineered tissues with complex architectures[56]. Using this method, the diameter of the microvessels can be controlled under 1 mm. In the process of assembling the micro spheroids into microvessels, the most commonly adopted method is using a high-precision and high-speed motorized micromanipulator that can pick and place the spherical modules to the planned locations. This primitive manipulation has high flexibility in the construction of microvessels with varied sizes and branches. However, assembling a huge number of spherical modules can hardly allow efficient construction. **Figure 3A** shows an a schematic diagram of building microvascular structures by assembling spherical micro modular tissues[33]. In the relevant research, picking progress was avoided to improve the fabrication efficiency. Arai *et al*. designed a high-speed piezo-driven two-finger microhand system, which can realize extremely high-speed automated assembly of the spherical structures with the assistance of computer vision technique[57,58]. Although the pick-and-place operations in micro scale become faster and faster, the fabrication efficiency is still the main challenge in building microvessels through assembling spherical modules.

4.2. Wrapping sheets

Due to the tubular structure of the blood vessels, directly assembling the planar 2D cell sheet into microvascular structures features high fabrication efficiency. Heureux *et al*. first achieved cell-sheet-based tissue-engineered vascular structures in 1998 without the use of any synthetic or exogenous biomaterials[59]. Based on this approach, many more efficient methods have been explored to fabricate engineered vessels with smaller diameters. Bourget *et al*. developed a decellularized matrix scaffold generated from dermal fibroblasts or saphenous vein fibroblasts to implant smooth muscle cells and produce tissue-engineered vascular media to shorten the time required for their generation[60]. This approach reduced the total production time from 6 weeks to 4 weeks (**Figure 3B**). Moreover, assisted by micromanipulation tools, it allows the fabrication of sub-millimeter vascular structures directly with the smooth

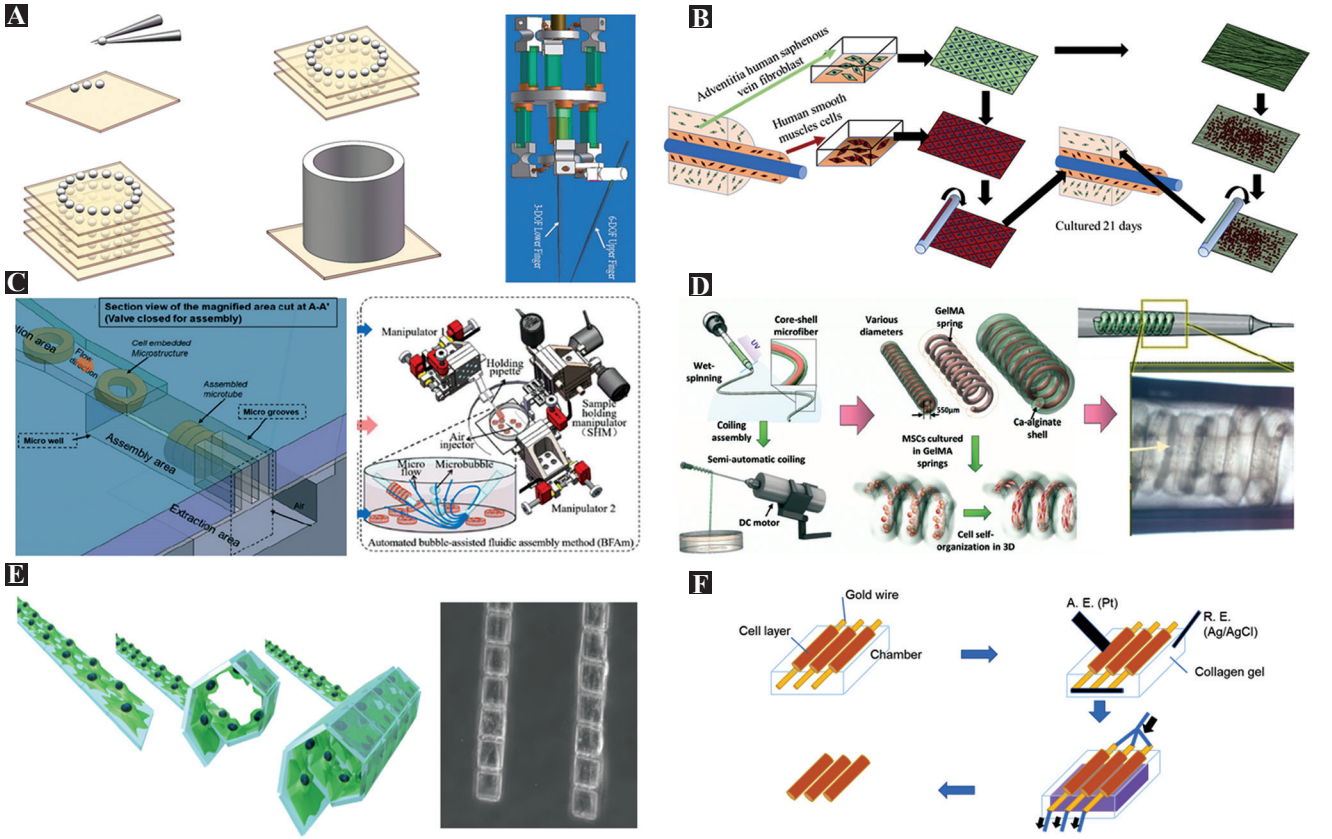


Figure 3. Bio-assembling powered by micromanipulations. (A) Building microvessels by pick-and-place of the cell spheroids and the piezo-driven two-finger microhand for high speed pick-and-place assembly (Republished with permission from Ramadan AA, Takubo T, Mae Y, *et al., IEEE Trans Ind Electron, 56:1121–35*.[58]). (B) Construction of the microvessels by wrapping a cell sheet[60]. (C) A 4-layer PDMS microfluidic device for microfluidic self-assembly of ring-shaped modules (left, reproduced from ref 63 with permission from The Royal Society of Chemistry), and automated assembly of microvascular structures using a multimicromanipulator system (Republished with permission, from Liu X, Shi Q, Wang H, *et al. IEEE/ASME Trans Mechatron, 2018, 23:667–78*[65]). (D) Semi-automatic fabrication of microvascular structures by spinning fibers containing cells (Reproduced from ref. 66 with permission from the Royal Society of Chemistry). (E) Construction of microvessels using cell origami based on the self-folding driven by cell traction force (from ref.[39] licensed under Creative Commons Creative Commons Attribution License). (F) The cells are electrically assembled to a microvascular structure on the capillary surface by applying an electrical potential and extracting the rods from the collagen gel[22,76].

muscle cells, regardless of their ability to synthesize extracellular matrix.

4.3. Rotation and alignment of rings

Cell-embedded 2D ring-shaped units are important building blocks for engineering the microvessels from the bottom up. Du *et al*. first realized the efficient assembly of the ring-shaped micromodules utilizing the surface tension force to drive rotation and alignment of the modules during the interaction between each other[61]. The interaction was initialed by manually swiping a needle to generate physical forces and fluidic shear. Wang *et al*. developed a dual-micromanipulator system to achieve the automated rotation and alignment of the ring-shaped modules[62]. The modules were rotated and picked up using the micropipette fixed on one micromanipulator to press the modules and then pushed up along the micropipette utilizing the micropipette fixed on another micromanipulator. Depending on the specific shape, the assembly process can also be carried out in the microchannels using microfluidic forces. On-chip assembly driven by fluidic force is a promising efficient method for fabricating artificial microvessels with ring-shaped modules[22,63,64]. **Figure 3C** shows the assembly of ring-shaped micromodules conducted in the 4-layer PDMS microfluidic device. The microfluidic device provides a closed environment for biological applications while allowing integration with other functional components for multiple tasks, including the rotation area, aligning area, and collection area. However, the whole assembly process is not as flexible as the robotic assembly using based on the micromanipulator. It can only assemble the ring-shaped modules with fixed sizes. Liu *et al*. integrated robotic assembly and fluidic assembly in the bubble-

based fluidic assembly method[65]. The method allows the assembly of ring-shaped modules in an open environment using microbubble-excited microflow and automates the assembly process by a multi-micromanipulator system with the assistance of computer vision techniques. This non-contact assembly method does not involve any picking and releasing operations, thus minimizing the time spent in precise micromanipulation. The operations in the open environment and the robotic system also allow the flexible assembly of the microvessels with varied sizes. The outer diameter of the assemble microvessels ranged 150-500 μm. The reported longest microvessels adopting this method were longer than 3 mm. This research suggests that the combination of fluidic assembly and robotic assembly can be a potential solution for micro-assembly where high throughput and flexibility are required.

4.4. Spinning fibers

In the fabrication of artificial microvessels, spinning the cell-laden microfibers into tubular structures is also an important assembly approach. As shown in **Figure 3D**, Sun *et al*. successfully constructed a spring-like microstructure for promoting the formation of the microvascular structures in a 3D environment[66]. By including magnetic materials inside the microfibers, Sun *et al*. set a magnetic tweezer system to operate and assemble these magnetic microfibers by direct mechanical contact. The magnetic microfibers can be guided to move around a rod to form microvascular structures directly[67-69]. This method required high-precision manipulation, and the efficiency was extremely low. In another research work, magnetic alginate microfibers were used to fabricate the ring-shaped microstructures by spinning first. Then, ring-shaped modules were picked by the magnetic tweezers in a non-contact way and subsequently stacked along the micropillars[70,71]. This method has higher operational efficiency than the direct fiber spinning by the magnetic tweezer and no damage caused by mechanical contact. The diameter of the microvessels assembled by microfibers can be controlled to smaller than 1 mm.

4.5. Self-folding origami of microplates

The traditional art of origami has always been popular because it allows the production of various 3D sculptures by folding only 2D pages. In recent years, engineers inspired by have applied the art of origami in a variety of ways, including the spatial deployment of solar panels for manufacturing, flexible medical scaffolds, microrobots, and DNA objects[29,72,73]. Kuribayashi-Shigetomi *et al*. introduced a technique called cellular origami using living cells as the driving force for self-folding to create a variety of different 3D cellular microstructures, including microvascular structures[39]. They mentioned that cells could naturally generate cellular traction as a contractile force, which is generated by actin-globin interactions and actin polymerization, pulling toward the center of the cell body. Thus, various 3D microstructures can be generated by changing the geometric design of the 2D template. **Figure 3E** shows a schematic diagram of the microvascular structure generation based on such a principle. It is a highly biocompatible, simple, and efficient technique for encapsulating cells into microstructures with just one step. It is particularly suitable for the efficient production of simple microvessels. The outer diameter of the microvessels fabricated by this method can be as small as 50 μm.

4.6. Attaching on rod

Based on the research on the electrochemical detachment and patterning of the self-assembled cellular monolayers[74,75], Seto *et al*. proposed a microvessel fabrication method combining the self-assembly of the cells based on chemical bond and electrochemical detachment (**Figure 3F**)[22,76]. Human umbilical vein endothelial cells are attached to the gold surface by an oligopeptide. In this research, the oligopeptide CCRRGDWLC chemically adhered to the gold surface of the rod driven by the gold–thiolate bond. Then, the cells were automatically assembled on the rod and formed a tubular cellular monolayer. Finally, to separate the microvascular structure from the rod, the cells are detached by applying a negative potential to the rod for reductively splitting the gold–thiolate bond. This technique can detach more than 90% of the attached cells within minutes of applying a negative potential.

5. Devices for direct bioprinting

5.1. Inkjet, extrusion, and laser-assisted bioprinting

The inkjet, extrusion, and laser-assisted bioprinting all adopt a point-by-point printing approach, featuring excellent flexibility in constructing large high-resolution tissues with complex microarchitectures. **Figure 4A** shows the general concept of using these bioprinting methods for fabricating microvascular structures[77]. The inkjet bioprinting is developed by modifying the conventional 2D inkjet printer[78-81]. The common ink is replaced by the bioink, and a Z motorized stage is employed to expand the 2D printing to 3D. Due to the well-developed 2D inkjet printing devices, inkjet bioprinting costs the least among the existing bioprinting methods. It is capable of printing microvessels with outer diameter smaller than 300 μm[80,81]. According to the working mechanism of the inkjet, the inkjet bioprinting can be divided into two types categorized by the use of either the piezoelectric actuator or the thermal actuator. With multiple inkjets and varied inks containing different cell sources, inkjet bioprinting is capable of composite

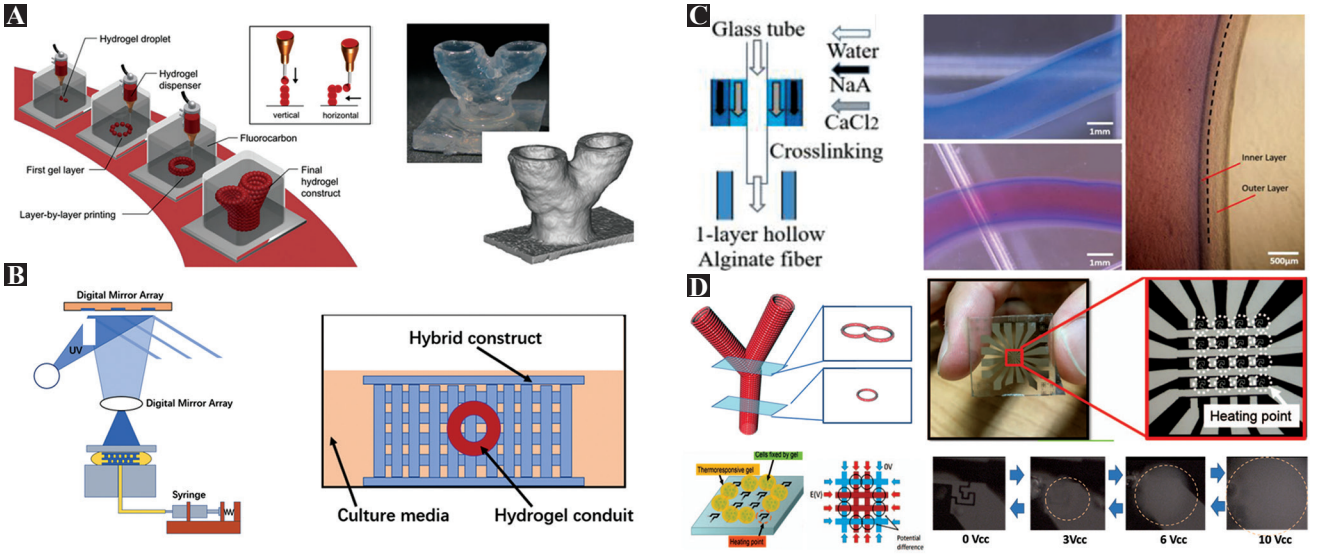


Figure 4. Devices developed for bioprinting microvessels. (A) Microvascular structures could be built by bioprinting based on inkjet, extraction, and direct laser writing (from ref.[77] licensed under Creative Commons Attribution License. Copyright © Mary Ann Liebert). (B) Direct bioprinting of microvascular structures based on the coaxial nozzle, and microscopic view of L929 mouse fibroblasts encapsulated by tubular alginate (Republished with permission from reference[88]). (C) Experimental setup and fabrication of engineered tissues containing microvascular structures using optical stereolithography[93]. (D) Microscopic photograph of a microheater array used to perform thermal stereolithography (Republished with permission, from Kojima M, Horade M, Takata S, *et al*., IEEE International Conference on Cyborg and Bionic Systems, IEEE, 2018.[97]).

bioprinting. However, its disadvantages are low cell density and low mechanical properties of the printed structures.

Targeting to printing the materials with better mechanical properties, researchers developed extrusion bioprinting to deposit viscous materials[82]. The extrusion is commonly actuated by air pump screw plunger. Similar to inkjet bioprinting, extrusion bioprinting is also capable of composite bioprinting with multiple bioinks. It also allows high cell density. However, the relatively low cell viability limited its application, since the large pressure is harmful to the living cells[83-85].

Laser-assisted bioprinting is based on laser direct writing and laser-induced transfer techniques[86,87]. The laser-assisted bioprinting devices' core is a three-layer laser-responsive plate. The plate contains a top energy-absorbing layer, a middle donor layer, and a bottom bioink layer. When the focused laser is at a small local area of the energy-absorbing layer, a small part of the donor layer under the laser exposure will be vaporized to form a high-pressure microbubble. The bubble will impel the bioinks, and the formed small droplet of bioink will fall onto the substrate. In laser-assisted bioprinting, cells are protected from the damages of the high pressure, thereby achieving high cell viability. However, the system is complex and expensive. Its unable to print multiple materials.

5.2. Coaxial nozzle

Considering the special structure of microvessels, it is possible to prepare hydrogel 3D structures with built-in microchannels by controlling the crosslinking time sequence and using the fusion of adjacent hollow filaments. As shown in **Figure 4B**, a novel 3D bioprinting method was proposed for fabricating cell-loaded built-in hollow hydrogel structures in the study by Arai *et al*. and Gao *et al*.[88,89]. The inner diameter of the fabricated microvessels could be smaller than 200 μm and longer than 10 cm. Coaxial nozzles are used to fabricate hollow alginate fibers that are able to move in the XY direction, with a Z-shaped platform, and raw materials such as calcium chloride solution to precisely control the XY direction to determine the coaxial nozzle position for planar feature printing. In contrast to other bioprinting methods used to fabricate built-in microchannel structures, this method allows for simultaneous printing of scaffolds and microchannels[88-90].

5.3. Optical stereolithography

Bioprinting based on stereolithography technique belongs to layer-by-layer printing featuring high efficiency. Stereolithography is a technique applying the selective solidification of curable bioinks[91,92]. As shown in **Figure 4C**, the digital mirror device (DMD) is most commonly utilized in optical stereolithography to pattern the 2D parallel light. The printing resolution can be as high as 1 μm. Compared with the extrusion-based bioprinting using high pressure, optical stereolithography can achieve relatively higher cell viability. In the process of engineering the microvessels using this method,

researchers commonly printed the microvascular structures together with other microarchitectures simultaneously. However, stereolithography originally does not allow the printing of multiple materials. Shanjani and Yan developed special devices to print more than one kind of material[93,94]. The printed artificial tissue including microvascular structure is shown in **Figure 4C**. However, patterned light utilized in bioprinting based on optical stereolithography requires the bioink to be transparent, and the system is extremely complex and expensive.

5.4. Thermal stereolithography

Thermally responsive gels have the potential to build large artificial tissues with complex architectures in the presence of precise local heating[95-97]. As shown in **Figure 4D**, to realize layer-by-layer curing and printing of microvessels, a microheater array is fabricated to shape the thermally responsive gel in 2D plane. Specifically, a microheater with a 2D arrangement structure is used as a DMD that allows area-selective heating at any position[79]. Since the temperature distribution on the glass substrate can be digitally processed, when combined with a thermally responsive polymer, its temperature variation can be controlled, and high-speed graphing can be achieved. This system allows reversible pasting and liquefaction at arbitrary locations. The relatively simpler system and low cost make it an extremely promising solution for building microvascular structures.

6. Discussion and prospects

Emerging microfabrication techniques have significantly advanced the bio-assembling for engineering microvessels[28,29,33,39,54-76]. Since the smaller and more precise fabricated micro modular tissues are now available, we can build larger artificial tissues without sacrificing the necessary microarchitectural feature[30,34-44]. The newly developed micromanipulation methods are necessary for the building of microvessels by modules with varied geometries. Fully automated assembly utilizing the robotic micromanipulation, self-assembly, and on-chip assembly by microfluidic devices significantly improve the efficiency of fabricating the microvessels by bio-assembling approaches[61-71].

Engineering microvessels by bioprinting highly relies on the overall development of bioprinting[77-100]. With the advanced bioinks featuring short curing time and better mechanical property, and efficient respective bioprinting devices, we can now achieve fabrication of the microvessels with high throughput[98,99]. Conventional inkjet-based bioprinting holds advantages for printing microvessels together with the other tissues simultaneously with composite bioprinting techniques while the 3D stereolithography can only deal with one bioink containing the same cell source[77-81,91-94,100]. However, 3D stereolithography has incomparable efficiency. Moreover, bioprinting devices specifically designed for printing microvessels are expected to achieve more attractive efficiency[88-90]. The extrusion-based bioprinting has relatively low printing speed and poor cell viability[82-85]. Except the extrusion-based bioprinting, engineering microvessels using bioprinting can achieve satisfied cell viability[98,99]. When the high mechanical property is required, the extrusion-based bioprinting strategies are recommended. A disadvantage of using the inkjet-based bioprinting to engineer microvessels is the weak mechanical property of the fabricated artificial microvessels. The optical stereolithography can guarantee the resolution of printing the microvessels to as low as 1 μm, but the system setup is much more complex than the bioprinting based on inkjet and extrusion. Laser-assisted bioprinting also needs a complex system setup.

Although bio-assembling and bioprinting techniques for engineering microvessels are all based on the "bottom-up" concept[21-32,98,99,101], they still have significant differences in the following aspects: resolution, fabrication efficiency, mechanical property, and complexity of fabricated microvessels. Limited by the speed of integrating the most recent advanced microfabrication techniques into the bioprinting devices, the bio-assembled microvessels still hold a higher resolution than the bioprinted structure, but the gap will be bridged by the effort in developing the bioprinting devices over time[30,34-44,77-97,100]. At present, bioprinting has much higher fabrication efficiency in engineering the microvessels from the bottom up; however, it is not absolute. Recent advances in micromanipulation keep improving the efficiency of the bio-assembling[61-71]. The self-assembly and on-chip assembly achieved satisfied fabrication efficiency but inevitably sacrificed the complexity of the engineered microvessels. Fully automated robotic microassembly provides a solution to the problem caused by the conflict of the fabrication efficiency and the complexity of the engineered microvessels. Although the fabricated micromodules have excellent mechanical properties, the overall mechanical property highly relies on the secondary crosslinking quantity. Moreover, smaller gaps between the assembled micromodules achieved by the precise assembly contribute to better mechanical property[61-67]. The mechanical property of the printed microvessels depends on the utilized bioinks and the respective solidification mechanisms[51-53,98,99]. Sometimes, researchers are in a dilemma of either choosing higher efficiency to reduce the curing time or opting for better mechanical property in the products at the expense of longer curing time. Both bio-assembling and bioprinting hold the potential in constructing complex 3D microvascular networks. Bio-assembling can construct complex microvessels by fabricating the complex 2D

modules at the beginning and through further dexterous micromanipulations, while bioprinting realizes this through composite bioprinting techniques.

Recent review articles related with the fabrication of artificial blood vessels mainly focus on artificial vascular grafts required in coronary angioplasty and coronary artery bypass grafting for treating coronary artery disease[20,21,22,98,99,101]. These artificial blood vessels with diameter larger than 2 mm are used for blood circulation instead of delivering nutrients and oxygen at single cell level. Fabricating mass of microvessels required in transporting nutrients, oxygen, and metabolic wastes in the constructed large 3D functional tissues requires the use of more advanced microfabrication techniques. Building the microvascular network using "bottom-up" approach could be appropriate and adequate. Existing methods using the "bottom-up" concept developed to fabricate microvessels can be divided into bio-assembling powered by different micromanipulation techniques and bioprinting utilizing different solidification mechanisms. Existing reviews mainly revolve around the use of bioprinting methods in the fabrication of microvessels, while many research works on bio-assembling for engineering microvessels have not been summarized in any reviews. Our review has summarized all the important bio-assembling methods and bioprinting methods for engineering microvessels and compared them in different aspects.

With regard to the future development of microvessel engineering through bioprinting and bio-assembling methods from the bottom up, we conclude with the future directions as follows: (i) fabricating microvessels across the micro to macro with higher efficiency; (ii) fabricating multilayer structure with stem cells and other cell sources; (iii) using noncytotoxic biodegradable materials with the strong mechanical property; (iv) building microvascular networks and other tissues simultaneously; (v) achieving 3D structure design and optimization of the microvascular network; and (vi) attempting in creating clinically relevant engineered microvessels for implantation and the treatment of disease on a small scale.

Acknowledgments

This work was supported by the National Natural Science Foundation of China under Grants (61903039, 61873037, 61803250), China Postdoctoral Science Foundation (BX20190035, 2020M680015), the Grant-in-Aid for Scientific Research (JP19H02093, JP19H02097) from the Ministry of Education, Culture, Sports, Science and Technology of Japan, and Shanghai Science and Technology Committee Rising-Star Program (19QA1403700).

Conflict of interest

The authors declare no conflicts of interest.

Author contributions

X.L. conceived the ideas and drafted the manuscript. Q.H. and T.A. advised the organization of the main contents. M.K. and T.Y. collected the detailed research results.

References

1. Hillsley MV, Frangos JA, 1994, Bone Tissue Engineering: The Role of Interstitial Fluid Flow. *Biotechnol Bioeng*, 43:573–81. http://doi.org/10.1002/bit.260430706
2. Martin P, 1997, Wound Healing--Aiming for Perfect Skin Regeneration. *Science*, 276:75–81. http://doi.org/10.1126/science.276.5309.75
3. Bello YM, Falabella AF, Eaglstein WH, 2001, Tissue-Engineered Skin. Current Status in Wound Healing. *Am J Clin Dermatol*, 2:305–13. http://doi.org/10.2165/00128071-200102050-00005
4. Langer R, Vacanti JP, 1993, Tissue Engineering. *Science*, 260:920–6. http://doi.org/10.1126/science.8493529
5. Stock UA, Vacanti JP, 2001, Tissue Engineering: Current State and Prospects. *Annu Rev Med*, 52:443–51. http://doi.org/10.1146/annurev.med.52.1.443
6. Vacanti CA, 2006, The History of Tissue Engineering. *J Cell Mol Med*, 10:569–76. http://doi.org/10.1111/j.1582-4934.2006.tb00421.x
7. Aikawa E, Nahrendorf M, Sosnovik D, *et al*., 2007, Multimodality Molecular Imaging Identifies Proteolytic and Osteogenic Activities in Early Aortic Valve Disease. *Circulation*, 115:377–86. http://doi.org/10.1161/circulationaha.106.654913
8. Walther G, Gekas J, Bertrand OF, 2009, Amniotic Stem Cells for Cellular Cardiomyoplasty: Promises and Premises. *Catheter Cardiovasc Interv*, 73:917–24. http://doi.org/10.1002/ccd.22016
9. Wang X, Yan, Y, Zhang R, 2010, Gelatin-Based Hydrogels for Controlled Cell Assembly. New York: Springer.
10. Wang X, 2012, Intelligent Freeform Manufacturing of Complex Organs. *Artif Organs*, 36:951–61. http://doi.org/10.1111/j.1525-1594.2012.01499.x
11. Orive G, Hernández RM, Rodríguez Gascón A, *et al*., 2004, History, Challenges and Perspectives of Cell Microencapsulation. *Trends Biotechnol*, 22:87–92. http://doi.org/10.1016/j.tibtech.2003.11.004
12. Khademhosseini A, Langer R, Borenstein J, *et al*., 2006, Microscale Technologies for Tissue Engineering and Biology. *Proc Natl Acad Sci U S A*, 103:2480–7.

http://doi.org/10.1073/pnas.0507681102

13. Chung BG, Kang L, Khademhosseini A, 2007, Micro-and Nanoscale Technologies for Tissue Engineering and Drug Discovery Applications. *Expert Opin Drug Discov*, 2:1653–68. http://doi.org/10.1517/17460441.2.12.1653
14. Miller JS, Stevens KR, Yang MT, *et al*., 2012, Rapid Casting of Patterned Vascular Networks for Perfusable Engineered Three-dimensional Tissues. *Nat Mater*, 11:768–74. http://doi.org/10.1038/nmat3357
15. Yue T, Zhao D, Phan DT, *et al*., 2021, A Modular Microfluidic System Based on a Multilayered Configuration to Generate Large-Scale Perfusable Microvascular Networks. *Microsyst Nanoeng*, 7:4. http://doi.org/10.1038/s41378-020-00229-8
16. Niklason LE, Gao J, Abbott WM, *et al*., 1999, Functional Arteries Grown *In Vitro*. *Science*, 284:489–93. http://doi.org/10.1126/science.284.5413.489
17. Gooch KJ, Blunk T, Courter DL, *et al*., 2002, Bone Morphogenetic Proteins-2, -12, and -13 Modulate *In Vitro* Development of Engineered Cartilage. *Tissue Eng*, 8:591–601. http://doi.org/10.1089/107632702760240517
18. Tranquillo RT, 2002, The Tissue-engineered Small-diameter Artery. *Ann N Y Acad Sci*, 961:251–4. http://doi.org/10.1111/j.1749-6632.2002.tb03094.x
19. Boublik J, Park H, Radisic M, *et al*., 2005, Mechanical Properties and Remodeling of Hybrid Cardiac Constructs Made From Heart Cells, Fibrin, and Biodegradable, Elastomeric Knitted Fabric. *Tissue Eng*, 11:1122–32. http://doi.org/10.1089/ten.2005.11.1122
20. Saito J, Kaneko M, Ishikawa Y, *et al*., 2021, Challenges and Possibilities of Cell-Based Tissue-Engineered Vascular Grafts. *Cyborg Bionic Syst*, 2021:1532103. http://doi.org/10.34133/2021/1532103
21. Ng HY, Lee KA, Kuo CN, *et al*., 2018, Bioprinting of Artificial Blood Vessels. *Int J Bioprint*, 4:140. http://doi.org/10.18063/IJB.v4i2.140
22. Arai T, Arai F, Yamato M, 2015, Hyper Bio Assembler for 3D Cellular Systems. Japan: Springer. https://doi.org/10.1007/978-4-431-55297-0
23. Yang J, Yamato M, Sekine H, *et al*., 2009, Tissue Engineering Using Laminar Cellular Assemblies. *Adv Mater*, 21:3404–9. http://doi.org/10.1002/adma.200801990
24. Kinstlinger IS, Saxton SH, Calderon GA, *et al*., 2020, Generation of Model Tissues with Dendritic Vascular Networks via Sacrificial Laser-sintered Carbohydrate Templates. *Nat Biomed Eng*, 2020:1–17. https://doi.org/10.1038/s41551-020-0566-1
25. Bertassoni LE, Cecconi M, Manoharan V, *et al*., 2014, Hydrogel Bioprinted Microchannel Networks for Vascularization of Tissue Engineering Constructs. *Lab A Chip*, 14:2202–11. https://doi.org/10.1039/c4lc00030g
26. Matsunaga YT, Morimoto Y, Takeuchi S, 2011, Molding Cell Beads for Rapid Construction of Macroscopic 3D Tissue Architecture. *Adv Mater*, 23:H90–4. http://doi.org/10.1002/adma.201004375
27. Tan A, Fujisawa K, Yukawa Y, *et al*., 2016, Bottom-up Fabrication of Artery-Mimicking Tubular Co-cultures in Collagen-based Microchannel Scaffolds. *Biomater Sci*, 4:1503–14. http://doi.org/10.1039/c6bm00340k
28. Nichol JW, Khademhosseini A, 2009, Modular Tissue Engineering: Engineering Biological Tissues from the Bottom Up. *Soft Matter*, 5:1312–9. http://doi.org/10.1039/b814285h
29. Gurkan UA, Tasoglu S, Kavaz D, *et al*., 2012, Emerging Technologies for Assembly of Microscale Hydrogels. *Adv Healthc Mater*, 1:149–58. https://doi.org/10.1002/adhm.201200011
30. Onoe H, Okitsu T, Itou A, *et al*., 2013, Metre-long Cell-laden Microfibres Exhibit Tissue Morphologies and Functions. *Nat Mater*, 12:584–90. https://doi.org/10.1038/nmat3606
31. Connon CJ, 2015, Approaches to Corneal Tissue Engineering: Top-down or Bottom-up? *Proc Eng*, 110:15–20. https://doi.org/10.1016/j.proeng.2015.07.004
32. Bova L, Billi F, Cimetta E, 2020, Mini-review: Advances in 3D Bioprinting of Vascularized Constructs. *Biol Direct*, 15:22. http://doi.org/10.1186/s13062-020-00273-4
33. Mironov V, Visconti RP, Kasyanov V, *et al*., 2009, Organ Printing: Tissue Spheroids as Building Blocks. *Biomaterials*, 30:2164–74. http://doi.org/10.1016/j.biomaterials.2008.12.084
34. Fennema E, Rivron N, Rouwkema J, *et al*., 2013, Spheroid Culture as a Tool for Creating 3D Complex Tissues. *Trends Biotechnol*, 31:108–15. https://doi.org/10.1016/j.tibtech.2012.12.003
35. Rivron NC, Vrij EJ, Rouwkema J, *et al*., 2012, Tissue Deformation Spatially Modulates VEGF Signaling and Angiogenesis. *Proc Natl Acad Sci*, 109:6886–91. https://doi.org/10.1073/pnas.1201626109
36. Torisawa YS, Chueh BH, Huh D, *et al*., 2007. Efficient Formation of Uniform-sized Embryoid Bodies Using a

Compartmentalized Microchannel Device. *Lab Chip*, 7:770–6. https://doi.org/10.1039/B618439A.

37. Tamayol A, Akbari M, Annabi N, *et al*., 2013, Fiber-based Tissue Engineering: Progress, Challenges, and Opportunities. *Biotechnol Adv*, 31:669–87. https://doi.org/10.1016/j.biotechadv.2012.11.007
38. Teshima T, Onoe H, Kuribayashiashiashias K, *et al*., 2014, Parylene Mobile Microplates Integrated with an Enzymatic Release for Handling of Single Adherent Cells. *Small*, 10:912–21. https://doi.org/10.1002/smll.201301993
39. Kuribayashi-Shigetomi K, Onoe H, Takeuchi S, 2012, Cell Origami: Self-Folding of Three-Dimensional Cell-Laden Microstructures Driven by Cell Traction Force. *PLoS One*, 7:e51085. https://doi.org/10.1371/journal.pone.0051085
40. Yue, T, Nakajima M, Tajima H, *et al*., 2013. Fabrication of Microstructures Embedding Controllable Particles inside Dielectrophoretic Microfluidic Devices. *Int J Adv Robot Syst*, 10:132–40. https://doi.org/10.5772/55598
41. Gach PC, Wang Y, Phillips C, *et al*., 2011, Isolation and Manipulation of Living Adherent Cells by Micromolded Magnetic Rafts. *Biomicrofluidics*, 5:32002–12. https://doi.org/10.1063/1.3608133
42. Liu Z, Takeuchi M, Nakajima M, *et al*., 2016, Batch Fabrication of Microscale Gear-Like Tissue by Alginate-Poly-L-lysine (PLL) Microcapsules System. *IEEE Robot Autom Lett*, 1:206–12. https://doi.org/10.1109/lra.2016.2514500
43. Yokoyama U, Tonooka Y, Koretake R, *et al*., 2017, Arterial Graft with Elastic Layer Structure Grown From Cells. *Sci Rep*, 7:140–55. https://doi.org/10.1038/s41598-017-00237-1
44. Hinds MT, Rowe RC, Ren Z, *et al*., 2006, Development of a Reinforced Porcine Elastin Composite Vascular Scaffold. *J Biomed Mater Res Part A*, 77A:458–69. https://doi.org/10.1002/jbm.a.30571
45. Rutz AL, Lewis PL, Shah RN, 2017, Toward Next-generation Bioinks: Tuning Material Properties Pre-and Post-printing to Optimize Cell Viability. *MRS Bull*, 42:563–70. https://doi.org/10.1557/mrs.2017.162
46. Mobaraki M, Ghaffari M, Yazdanpanah A, *et al*., 2020, Bioinks and Bioprinting: A Focused Review. *Bioprinting*, 18:e00080–95. https://doi.org/10.1016/j.bprint.2020.e00080
47. Jia J, Richards DJ, Pollard S, *et al*., 2014, Engineering Alginate as Bioink for Bioprinting. *Acta Biomater*, 10:4323–31. https://doi.org/10.1016/j.actbio.2014.06.034
48. Guvendiren M, Molde J, Soares RM, *et al*., 2016, Designing Biomaterials for 3D Printing. *ACS Biomater Sci Eng*, 2:1679–93. https://doi.org/10.1021/acsbiomaterials.6b00121
49. Hospodiuk M, Dey M, Sosnoski D, *et al*., 2017, The Bioink: A Comprehensive Review on Bioprintable Materials. *Biotechnol Adv*, 35:217–39. https://doi.org/10.1016/j.biotechadv.2016.12.006
50. Gomez-Guillen MC, Turnay J, Fernandez-Dıaz MD, *et al*., 2002, Structural and Physical Properties of Gelatin Extracted from Different Marine Species: A Comparative Study. *Food Hydrocoll*, 16:25–34. https://doi.org/10.1016/S0268-005X(01)00035-2
51. Rowley JA, Madlambayan G, Mooney DJ, 1999, Alginate Hydrogels as Synthetic Extracellular Matrix Materials. *Biomaterials*, 20:45–53. https://doi.org/10.1016/S0142-9612(98)00107-0
52. Demirtas TT, Irmak G, Gümüs M, *et al*., 2017, A Bioprintable form of Chitosan Hydrogel for Bone Tissue Engineering. *Biofabrication*, 9:35003. https://doi.org/10.1088/1758-5090/aa7b1d
53. Loo Y, Hauser CA, 2015, Bioprinting Synthetic Self-assembling Peptide Hydrogels for Biomedical Applications. *Biomed Mater*, 11:14103. https://doi.org/10.1088/1748-6041/11/1/014103
54. Du Y, Lo E, Ali S, *et al*., 2008, Directed Assembly of Cell-laden Microgels for Fabrication of 3D Tissue Constructs. *Proc Natl Acad Sci*, 105:9522–7. https://doi.org/10.1073/pnas.0801866105
55. Elbert DL, 2011, Bottom-up Tissue Engineering. *Curr Opin Biotechnol*, 22:674–80. https://doi.org/10.1016/j.copbio.2011.04.001
56. Kasza KE, Rowat AC, Liu J, *et al*., 2007, The Cell as a Material. *Curr Opin Cell Biol*, 19:101–7. https://doi.org/10.1016/j.ceb.2006.12.002
57. Avci E, Ohara K, Nguyen CN, *et al*., 2015, High-Speed Automated Manipulation of Microobjects Using a Two-Fingered Microhand. *IEEE Trans Ind Electron*, 62:1070–9. https://doi.org/10.1109/TIE.2014.2347004
58. Ramadan AA, Takubo T, Mae Y, *et al*., 2009, Developmental Process of a Chopstick-Like Hybrid-Structure Two-Fingered Micromanipulator Hand for 3-D Manipulation of Microscopic Objects. *IEEE Trans Ind Electron*, 56:1121–35. https://doi.org/10.1109/TIE.2008.2008753
59. L'Heureux N, Quet SP, Labbe R, *et al*., 1998, A Completely

Biological Tissue-Engineered Human Blood Vessel. *FASEB J*, 12:47–56.
https://doi.org/10.1096/fasebj.12.1.47

60. Bourget JM, Gauvin R, Larouche D, *et al*., 2012, Human Fibroblast-derived ECM as a Scaffold for Vascular Tissue Engineering. *Biomaterials*, 33:9205–13.
https://doi.org/10.1016/j.biomaterials.2012.09.015
61. Du Y, Ghodousi M, Qi H, *et al*., 2011, Sequential Assembly of Cell-laden Hydrogel Constructs to Engineer Vascular-like Microchannels. *Biotechnol Bioeng*, 108:1693–703.
https://doi.org/10.1002/bit.23102
62. Wang H, Huang Q, Shi Q, *et al*., 2015, Automated Assembly of Vascular-like Microtube with Repetitive Single-step Contact Manipulation. *IEEE Trans Biomed Eng*, 62:2620–8.
https://doi.org/10.1109/TBME.2015.2437952
63. Yue T, Nakajima M, Takeuchi M, *et al*., 2014, On-chip Self-assembly of Cell Embedded Microstructures to Vascular-like Microtubes. *Lab Chip*, 14:1151.
https://doi.org/10.1039/c3lc51134k
64. Yue T, Liu N, Liu Y, *et al*., 2019, On-Chip Construction of Multilayered Hydrogel Microtubes for Engineered Vascular-Like Microstructures. *Micromachines*, 10:840.
https://doi.org/10.3390/mi10120840
65. Liu X, Shi Q, Wang H, *et al*., 2018, Automated Fluidic Assembly of Microvessel-Like Structures Using a Multimicromanipulator System. *IEEE/ASME Trans Mechatron*, 23:667–78.
https://doi.org/10.1109/TMECH.2018.2796182
66. Sun T, Shi Q, Liang Q, *et al*., 2020, Fabrication of Vascular Smooth Muscle-like Tissues Based on Self-organization of Circumferentially Aligned Cells in Microengineered Hydrogels. *Lab Chip*, 20:3120–31.
https://doi.org/10.1039/D0LC00544D
67. Sun T, Wang H, Shi Q, *et al*., 2016, Micromanipulation for Coiling Microfluidic Spun Alginate Microfibers by Magnetically Guided System. *IEEE Robot Autom Lett*, 1:808–13.
https://doi.org/10.1109/LRA.2016.2524991
68. Sun T, Shi Q, Huang Q, *et al*., 2017, Magnetic Alginate Microfibers as Scaffolding Elements for the Fabrication of Microvascular-like Structures. *Acta Biomater*, 66:272–81.
https://doi.org/10.1016/j.actbio.2017.11.038
69. Sun T, Huang Q, Shi Q, *et al*., 2015, Magnetic Assembly of Microfluidic Spun Alginate Microfibers for Fabricating Three-dimensional Cell-laden Hydrogel Constructs. *Microfluid Nanofluid*, 19:1169–80.
https://doi.org/10.1007/s10404-015-1633-x
70. Sun T, Shi Q, Yao Y, *et al*., 2019, Engineered Tissue Micro-rings Fabricated from Aggregated Fibroblasts and Microfibres for a Bottom-up Tissue Engineering Approach. *Biofabrication*, 11:035029.
https://doi.org/10.1088/1758-5090/ab1ee5
71. Sun T, Yao Y, Shi Q, *et al*., 2020, Template-based Fabrication of Spatially Organized 3D Bioactive Constructs Using Magnetic Low-concentration Gelation Methacrylate (GelMA) Microfibers. *Soft Matter*, 16:3902–13.
https://doi.org/10.1039/C9SM01945F
72. Onoe H, Takeuchi S, 2008, Microfabricated Mobile Microplates for Handling Single Adherent Cells. *J Micromech Microeng*, 18:095003.
https://doi.org/10.1088/0960-1317/18/9/095003
73. Yoshida S, Sato K, Takeuchi S, 2014, Three-Dimensional Microassembly of Cell-Laden Microplates by *In Situ* Gluing with Photocurable Hydrogels. *Int J Automation Technol*, 8(1):95–101.
https://doi.org/10.20965/ijat.2014.p0095
74. Jiang X, Ferrigno R, Mrksich M, *et al*., 2016, Electrochemical Desorption of Self-Assembled Monolayers Noninvasively Releases Patterned Cells from Geometrical Confinements. *J Am Chem Soc*, 125:2366–7.
https://doi.org/10.1021/ja029485c
75. Inaba R, Khademhosseini A, Suzuki H, *et al*., 2009, Electrochemical Desorption of Self-assembled Monolayers for Engineering Cellular Tissues. *Biomaterials*, 30:3573–9.
https://doi.org/10.1016/j.biomaterials.2009.03.045
76. Seto Y, Inaba R, Okuyama T, *et al*., 2010, Engineering of Capillary-like Structures in Tissue Constructs by Electrochemical Detachment of Cells. *Biomaterials*, 31:2209–15.
https://doi.org/10.1016/j.biomaterials.2009.11.104
77. Blaeser A, Campos DF, Weber M, *et al*., 2013, Biofabrication Under Fluorocarbon: A Novel Freeform Fabrication Technique to Generate High Aspect Ratio Tissue-Engineered Constructs. *Biores Open Access*, 2:374–84.
https://doi.org/10.1089/biores.2013.0031
78. Saunders RE, Derby B, 2014, Inkjet Printing Biomaterials for Tissue Engineering: Bioprinting. *Int Mater Rev*, 59:430–48.
https://doi.org/10.1179/1743280414Y.0000000040
79. Ramiah P, du Toit LC, Choonara YE, *et al*., 2020, Hydrogel-Based Bioinks for 3D Bioprinting in Tissue Regeneration. *Front Mater*, 7:76.
https://doi.org/10.3389/fmats.2020.00076
80. Liu X, Wang X, Zhang L, *et al*., 2021, A Novel Method for Generating 3D Constructs with Branched Vascular Networks

Using Multi-materials Bioprinting and Direct Surgical Anastomosis. *bioRxiv*, 3:436268.
https://doi.org/10.1101/2021.03.21.436268

81. Kolesky DB, Truby RL, Gladman AS, *et al*., 2014, Bioprinting: 3D Bioprinting of Vascularized, Heterogeneous Cell-Laden Tissue Constructs. *Adv Mater*, 26:3124–30. https://doi.org/10.1002/adma.201470124
82. Iwan Z, Dietmar WH, *et al*., 2002, Fused Deposition Modeling of Novel Scaffold Architectures for Tissue Engineering Applications. *Biomaterials*, 23:1169–85. https://doi.org/10.1016/S0142-9612(01)00232-0
83. Ibrahim TO, Monika H, 2016, Current Advances and Future Perspectives in Extrusion-based Bioprinting. *Biomaterials*, 76:321–43. https://doi.org/10.1016/j.biomaterials.2015.10.076
84. Fielding GA, Bandyopadhyay A, Bose S, 2012, Effects of Silica and Zinc Oxide Doping on Mechanical and Biological Properties of 3D Printed Tricalcium Phosphate Tissue Engineering Scaffolds. *Dent Mater*, 28:113–22. https://doi.org/10.1016/j.dental.2011.09.010
85. Wang Y, Huang X, Shen Y, *et al*., 2019, Direct Writing Alginate Bioink Inside Pre-polymers of Hydrogels to Create Patterned Vascular Networks. *J Mater Sci*, 54:883–7892. https://doi.org/10.1007/s10853-019-03447-2
86. Bohandy J, Kim BF, Adrian FJ, 1986, Metal Deposition from a Supported Metal Film Using an Excimer Laser. *J Appl Phys*, 60:1538–9. https://doi.org/10.1063/1.337287
87. Duocastella M, Colina M, Fernández-Pradas JM, *et al*., 2007, Study of the Laser-induced Forward Transfer of Liquids for Laser Bioprinting. *Appl Surf Sci*, 253:7855–9. https://doi.org/10.1016/j.apsusc.2007.02.097
88. Kihara T, Kojima M, Horade M, *et al*., 2016, A Channel Device Generating Multilayer Tubular Structure *In Situ* Delivering Nutrients. In: The Proceedings of JSME annual Conference on Robotics and Mechatronics (Robomec). p2A2-19b5. https://doi.org/10.1299/jsmermd.2016.2A2-19b5
89. Gao Q, He Y, Fu J, *et al*., 2015, Coaxial Nozzle-assisted 3D Bioprinting with Built-in Microchannels for Nutrients Delivery. *Biomaterials*, 61:203–15. https://doi.org/10.1016/j.biomaterials.2015.05.031
90. Li S, Wang K, Jiang X, *et al*., 2020, Rapid Fabrication of Ready-to-Use Gelatin Scaffolds with Prevascular Networks using Alginate Hollow Fibers as Sacrificial Templates. *ACS Biomater Sci Eng*, 6:2297–311. https://doi.org/10.1021/acsbiomaterials.9b01834
91. Gauvin R, Chen YC, Lee JW, *et al*., 2012, Microfabrication of Complex Porous Tissue Engineering Scaffolds using 3D Projection Stereolithography. *Biomaterials*, 33:3824–34. https://doi.org/10.1016/j.biomaterials.2012.01.048.
92. Raman R, Bhaduri B, Mir M, *et al*., 2016, High-Resolution Projection Microstereolithography for Patterning of Neovasculature. *Adv Healthc Mater*, 5:610–9. https://doi.org/10.1002/adhm.201500721
93. Shanjani Y, Pan CC, Elomaa L, *et al*., 2015, A Novel Bioprinting Method and System for Forming Hybrid Tissue Engineering Constructs. *Biofabrication*, 7:045008. https://doi.org/10.1088/1758-5090/7/4/045008
94. Yan J, Huang Y, Chrisey DB, 2012, Laser-assisted Printing of Alginate Long Tubes and Annular Constructs. *Biofabrication*, 5:015002. https://doi.org/10.1088/1758-5082/5/1/015002
95. Tsuda Y, Yamato M, Kikuchi A, *et al*., 2007, Thermoresponsive Microtextured Culture Surfaces Facilitate Fabrication of Capillary Networks. *Adv Mater*, 19:3633–6. https://doi.org/10.1002/adma.200700988
96. Horade M, Kojima M, Kamiyama K, *et al*., 2014, Development of Micro-heater Array Device with Regional Selective Heating for Biochemical Applications. International Conference.
97. Kojima M, Horade M, Takata S, *et al*., 2018, Development of Micro Heater Array System for Cell Manipulation. IEEE International Conference on Cyborg and Bionic Systems, IEEE.
98. Heinrich MA, Liu W, Jimenez A, *et al*., 2019, 3D Bioprinting: From Benches to Translational Applications. *Small*, 15:1805510. http://dx.doi.org/10.1002/smll.201805510
99. Mandrycky C, Wang Z, Kim K, *et al*., 2016, 3D Bioprinting for Engineering Complex Tissues. *Biotechnol Adv*, 34:422–34. https://doi.org/10.1016/j.biotechadv.2015.12.011
100. Grigoryan B, Paulsen SJ, Corbett DC, *et al*., 2019, Multivascular Networks and Functional Intravascular Topologies Within Biocompatible Hydrogels. *Science*, 364:458–64. http://dx.doi.org/10.1126/science.aav9750
101. Liu LB, Wang XH, 2015, Creation of a Vascular System for Organ Manufacturing. *Int J Bioprint*, 1:77-86. http://dx.doi.org/10.18063/IJB.2015.01.009.

REVIEW ARTICLE

Developments and Opportunities for 3D Bioprinted Organoids

Ya Ren[1,2†], Xue Yang[1,2†], Zhengjiang Ma[1†], Xin Sun[1], Yuxin Zhang[3], Wentao Li[1], Han Yang[4], Lei Qiang[5], Zezheng Yang[6], Yihao Liu[1], Changxu Deng[1], Liang Zhou[7], Tianchang Wang[1], Jingsheng Lin[8], Tao Li[9]*, Tao Wu[10]*, Jinwu Wang[1,4]*

[1]Shanghai Key Laboratory of Orthopaedic Implant, Department of Orthopaedic Surgery, Shanghai Ninth People's Hospital Affiliated Shanghai Jiao Tong University School of Medicine, 639 Zhizaoju Rd, Shanghai 200011, China
[2]Southwest JiaoTong University College of Medicine, No. 111 North 1st Section of Second Ring Road, Chengdu 610036, China
[3]Department of Rehabilitation Medicine, Shanghai Ninth People's Hospital Affiliated to Shanghai Jiao Tong University School of Medicine, Huangpu District, Shanghai 200011, China
[4]Med-X Research Institute, School of Biomedical Engineering, Shanghai Jiao Tong University, 1954 Huashan Rd, Shanghai 200030, China
[5]Key Laboratory of Advanced Technology of Materials, Ministry of Education, School of Materials Science and Engineering, Southwest Jiaotong University, Chengdu 610036, China
[6]Department of Orthopedics, The Fifth People's Hospital of Shanghai, Fudan University, Minhang District, Shanghai 200240, P. R. China
[7]Center for Medicine Intelligent and Development, China Hospital Development Institute, Shanghai Jiao Tong University, Shanghai 200020, China
[8]Department of Information Technology, Ruijin Hospital Shanghai Jiao Tong University School of Medicine, Shanghai 200025, China
[9]Department of Orthopaedics, Xinhua Hospital affiliated to Shanghai Jiaotong University School of Medicine, Shanghai 200092, P. R. China
[10]Shanghai University of Medicine and Health Sciences, Shanghai 200120, China
[†]*These authors contributed equally to this work.*

Abstract: Organoids developed from pluripotent stem cells or adult stem cells are three-dimensional cell cultures possessing certain key characteristics of their organ counterparts, and they can mimic certain biological developmental processes of organs *in vitro*. Therefore, they have promising applications in drug screening, disease modeling, and regenerative repair of tissues and organs. However, the construction of organoids currently faces numerous challenges, such as breakthroughs in scale size, vascularization, better reproducibility, and precise architecture in time and space. Recently, the application of bioprinting has accelerated the process of organoid construction. In this review, we present current bioprinting techniques and the application of bioinks and summarize examples of successful organoid bioprinting. In the future, a multidisciplinary combination of developmental biology, disease pathology, cell biology, and materials science will aid in overcoming the obstacles pertaining to the bioprinting of organoids. The combination of bioprinting and organoids with a focus on structure and function can facilitate further development of real organs.

Keywords: Bioprinting; Organoid; Tissue engineering; Organ development

*Correspondence to: Tao Li, Department of Orthopaedics, Xinhua Hospital affiliated to Shanghai Jiaotong University School of Medicine, Shanghai 200092, P. R. China; litaoxyeyy@sina.com; Tao Wu, Shanghai University of Medicine and Health Sciences, Shanghai 200120, China; wutao0324@shsmu.edu.cn; Jinwu Wang, Shanghai Key Laboratory of Orthopaedic Implant, Department of Orthopaedic Surgery, Shanghai Ninth People's Hospital Affiliated Shanghai Jiao Tong University School of Medicine, 639 Zhizaoju Rd, Shanghai 200011, China; wangjw-team@shsmu.edu.cn

Received: April 3, 2021; **Accepted:** May 8, 2021; **Published online:** June 28, 2021

(This article belongs to the *Special Section: Bioprinting of 3D Functional Tissue Constructs*)
Citation: Ren Y, Yang X, Ma Z, *et al*., 2021, Developments and Opportunities for 3D Bioprinted Organoids. *Int J Bioprint*, 7(3):364. http://doi.org/10.18063/ijb.v7i3.364

© 2021 Ren, *et al*. This is an Open Access article distributed under the terms of the Creative Commons Attribution License (https://creativecommons.org/licenses/by/4.0/), permitting distribution and reproduction in any medium, provided the original work is cited.

1. Introduction

An organoid is a three-dimensional (3D) model, similar to the source tissue or organ *in vivo*, of an *in vitro* cell culture system.[1]. In addition, an organoid is a collection of organ-specific cells that are developed from pluripotent stem cells (PSCs) or adult stem cells (AdSCs). They can self-form in a similar manner to the body through cell sorting and spatially restricted lineage differentiation[2-4] (**Figure 1**). At present, animal models are typically used for experiments, such as drug screening, disease modeling, and tissue regeneration and repair; however, such models do not accurately reflect the physiological characteristics of the human body[5]. The new *in vitro* model organoid bridges the gap between animal models and humans by replicating the cellular composition and behavior of a normal organism meticulously to recreate the physiological structure of human organs. The construction of organoids offers the advantages of individualization, short modeling times, high-throughput genetic or drug screening, and the possibility of gene editing[6]. The organoid compensates for the shortcomings of simple cellular models and complex animal models, and provides an important experimental basis for studying key functions of living organisms. Organoids have become a current research hotspot with great theoretical significance and broad development prospects in basic biology research, drug testing, and molecular medicine[6]. However, the construction of organoids poses certain limitations, such as the inability to fully simulate the *in vivo* microenvironment, inadequate vascularization, the slightly different size of the self-organization of organoids from that of normal organs and lack of precise spatial ordering, and unestablished co-culture system with other types of cells. Recent bioprinting techniques have been used to overcome some of these shortcomings.

Bioprinting is an additive manufacturing technology that can design and selectively distribute cells, bioactive materials, and cytokines to construct 3D living organs and tissues[7]. Bioprinting defines two types of fabricated structural properties or smart surface properties of cell-free constructs characterized by layering, which guides cellular activity and cell-filled biological constructs[7]. Before the rise of biomanufacturing technologies, the fusion of developmental biology and cellular self-organization has emerged as a new paradigm for advancing tissue engineering. The formation of self-organizing multicellular modules is a key step in this technology; however, the ability to assemble intermediate modules into larger tissue units in a controlled manner is a major challenge[8]. Thus, the synergistic development of bioprinting and cellular self-organization technologies, working in tandem, can significantly facilitate the functionalization of organ tissues. Bioprinting can apply a specific spatial architecture design similar to actual organs for PSCs or AdSCs so that the specific structure of organoids can be quickly printed with high-precision and high-throughput. Accordingly, they can self-organize better and faster to form organoids. In addition, stem cell suspensions can self-organize into millimeter-scale structures, which contain only moderate complexity, and can be further printed into more complex tissues and organs, with the use of the resulting geometry to guide organoid formation.

Here, we review existing bioprinting methods and bioinks, highlight the recent success stories in the field of organ bioprinting, and summarize strategies and possible directions for future organoid bioprinting.

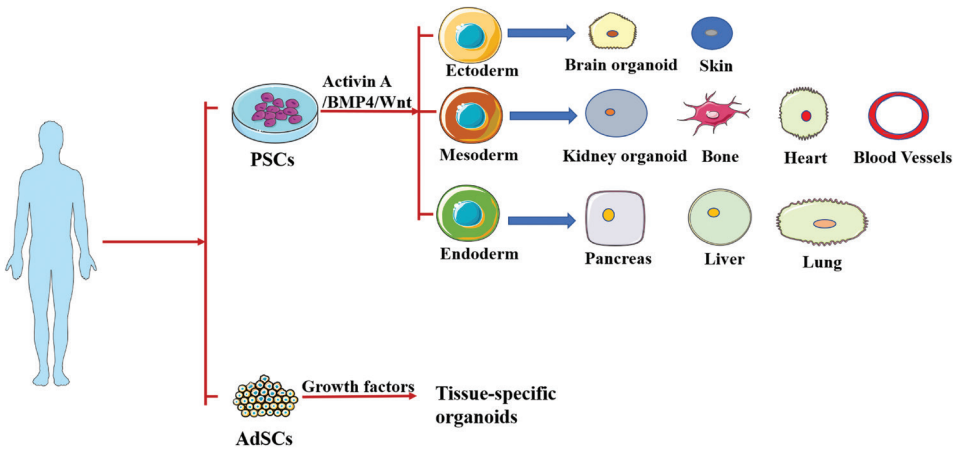


Figure 1. Organoids can be identified based on PSCs or AdSCs that are created autotrophically. PSC-derived organoids need to pass through the endoderm, mesoderm, or ectoderm, and then be induced and matured by applying certain growth signals and then differentiate into the phenotype required for a particular organ. A few PSC-derived organoids may be determined from numerous distinctive germ layers of cells. AdSC-derived organoids require segregation of tissue-specific stem cell populations, which are at that point implanted in extracellular matrix (ECM) and engendered in combination with particular tissue development components.

Organoid construction and bioprinting have become research hotspots in the scientific community, and they can facilitate the development of truly artificial organs in the future, signifying a substantial step forward in the field of regenerative medicine.

2. Technologies of organoid bioprinting

3D printing is also known as a layer-by-layer stacking, additive manufacturing method, and the printing technology associated with cell printing is known as 3D bioprinting. According to different molding principles and printing materials, existing bioprinting methods can be classified into extrusion bioprinting (pneumatic, piston, and spiral), inkjet bioprinting (temperature control and piezoelectric), laser-assisted bioprinting, and photo-curing bioprinting. Biological 3D printing techniques use biomaterials, cells, and/or cytokines as bio-inks to build human tissues and organs. However, to date, no biological printing technology can produce synthetic tissues of all sizes and complexities. The aforementioned four primary biological printing techniques pose certain advantages, disadvantages, and limitations **(Table 1).**

2.1. Inkjet-based bioprinting

The inkjet-based bioprinting method was the first bioprinting method used to print cells[9]. It is a contactless printing process based on traditional inkjet printing technology, which uses piezoelectric or thermal driving nozzles to form a series of liquid droplets according to a predetermined 3D structure of biological ink (a mixture of hydrogels and cells). Inkjet-based bioprinting has the advantages of high cell activity, fast printing speed, higher resolution, and low cost[10,11]. In addition, inkjet-based bioprinting can use multiple nozzles simultaneously, enabling the simultaneous printing of different bioactive materials, cells, or cytokines. Using inkjet-based bioprinting technology, scientists have made significant progress in drawing the patterns of molecules, cells, and organs. Researchers have reported the use of inkjet-based bioprinting and fibroblasts to design curved, vascular-like suspension structures without scaffolds[12]. A method of applying high-throughput inkjet printing to control cell attachment and proliferation through precise, automated deposition of collagen was also reported[13]. However, due to the low driving pressure, inkjet biological printing cannot print high-viscosity materials or high-concentrations of cells. Therefore, it is often difficult to fabricate complex biomimetic tissues or organoids with high cell density using the inkjet bioprinting method. Low-viscosity biomaterials can reduce the mechanical properties of bioprinted structures but fail to provide a normal or similar physiological environment for cells to the extent that subsequent *in vitro* and *in vivo* cultures are less effective. In addition, the nozzles are prone to wear and clogging during inkjet bioprinting, and cells may also suffer thermal or mechanical damage, limiting the widespread use of inkjet-based bioprinting technologies.

2.2. Laser-assisted bioprinting

Laser-assisted bioprinting utilizes laser direct-write and laser-induced transfer technologies[14]. A focused laser pulse is used to generate high-pressure bubbles on the ribbon absorption layer, and the suspended bioink is pushed onto the receiving substrate and then cross-linked. Compared with other printing techniques, non-nozzle printing methods, such as laser-assisted bioprinting, can avoid direct contact between the inkjet and bioink, thereby preventing the cell/biomaterial from clogging the nozzle and mechanical damage to the cell[15]. Thus, laser-assisted bioprinting allows the printing of highly viscous biomaterials as well as printing with a high cell density. The constructed organoids exhibit high cellular activity, high cell density, and improved functionality. The use of laser-based bioprinting to prepare 3D patterns for spinal cord repair with axon-like extensions and high cellular activity has been reported[16]. Moreover, laser-assisted bioprinting has been used to deposit human umbilical vein endothelial cells (HUVECs) onto the surface of biopaper using a simple crossover technique; these cells were differentiated and stretched into a network of vascularized tissues[17]. However, laser-assisted bioprinting pose several shortcomings. First, laser-assisted bioprinting devices are difficult to commercialize because the cost is relatively high, the control of the laser printing system is complex, and there are limited hydrogel materials suitable for laser-assisted bioprinting. Second, the printing efficiency is low, and each layer of ink is coated repeatedly. In addition, uniformity cannot be guaranteed, and the process is time-consuming and laborious. This makes it difficult to apply to complex structure printing. Moreover, the side effects of laser exposure on cells are not fully understood, which limits the use of this technology.

2.3. Extrusion-based bioprinting

Extrusion bioprinting is currently the most widely used bioprinting strategy that uses air pressure or mechanical stress to control the extrusion of bioink through a nozzle. It can print high-viscosity biomaterials and high-density cell suspensions[18]. Its greatest advantage is that it features a wide range of printable biocompatible materials, covering biomaterials with viscosities extending from 30 to 6×10^7 mPa/s, particularly hydrogels with shear diminishing, and fast cross-linking properties. In contrast to the aforementioned two techniques, the biomaterial or cell suspension is squeezed by continuous squeezing pressure to form uninterrupted deposits of

Table 1. Performance comparison between inkjet-based bioprinting, laser-based assisted bioprinting, extrusion-based bioprinting, and photo-curing bioprinting.

	Inkjet-based bioprinting	**Laser-assisted bioprinting**	**Extrusion-based bioprinting**	**Photo-curing bioprinting**
Cost	Low	High	Medium	Low
Speed	Fast	Medium	Slow	Fast
Resolution	75 μm	10-100 μm	200-500 μm	50 μm
Cell density	10^6-10^7 cells/ml	>10^8 cells/ml	10^8-10^9cells/ml	>10^7 cells/ml
Cell Viability	High	High (>95%)	Low	High
Nozzle	Exist	No	Exist	No
Features	• Piezoelectric or thermodynamic driven nozzles • Can be equipped with multiple nozzles • Requires the printed biomaterial to be in liquid form	• No clogging of the cell/biomaterial nozzle • Does not cause mechanical damage to cells, thus increasing cell survival rates (typically above 95%) • Multiple biomaterials can be used to print high-viscosity bioinks	• Printable high-viscosity biomaterials • Wide range of printable biocompatible materials • Most commonly used	• Selective cross-linking of bioink using light and layer-by-layer solidification to form a 3D structure • High efficiency • Simpler device • Easy to control
Limitations	• Low drive pressure • Cannot print high-viscosity materials or high concentration of cells • May cause mechanical or thermal damage to cells during printing • Print head is also prone to wear and clogging	• Complex control of laser printing systems • Few hydrogel materials suitable for laser bioprinting • Low printing efficiency • Side effects of laser irradiation on cells are not fully understood	• High mechanical pressure and shear stress • Relatively low cell viability	• Ultraviolet light and its initiator can damage cells

fibrillated filaments, rather than just individual droplets, resulting in greater mechanical pressure, and shear stress on biomaterials and cells. Therefore, using this technique can reduce the survival rate of printed cells, which is more obvious when printing bioinks with high cell density. Extrusion bioprinting is currently a common method used to construct organoids, and new bioprinting methods have emerged based on traditional extrusion bioprinting methods. Researchers have built an extrusion bioprinter equipped with two nozzles and a motorized X-Z robot. Using hepatocyte- and fibroblast-loaded GelMA hydrogels, the feasibility of the technique was demonstrated for bioprinting organoids or cellular aggregates that maintained a certain level of cellular activity over time[19]. In addition, a prominent study has recently proposed a printing method referred to as bioprinting-assisted tissue emergence (BATE) that combines an extrusion printing system and a microscope system to build a printing system with its own microscope image for real-time observation and precise control of tissue development temporally and spatially[20].

2.4. Photo-curing bioprinting

Photo-curing bioprinting is a biological 3D printing method based on surface projection, which is now often subdivided into stereolithography (SLA) and digital light processing (DLP). Both methods use light-induced photopolymer molding. SLA applies this molding to light-cure using laser light from point to line and line to surface, while DLP uses a projector to irradiate the photopolymer and light-cure it layer-by-layer[21]. The photo-curing printing device uses a digital light projector to solidify the entire surface of the bioink with high efficiency. Regardless of the complexity of the single-layer structure, the printing time is the same, and the printing accuracy is high[22]. The printer requires only a vertically moving platform. Compared with other methods, the device is relatively simple and easy to control, and the printing mode without nozzles does not cause problems, such as nozzle blockage and shear force affecting cell activity[23]. Photo-curing bioprinting is a promising printing method for cell assemblies and organoid construction because of its ability to guide cell self-organization and relatively controlled differentiation. Creff *et al*. used SLA technology and a photosensitive polymer hydrogel (polyethylene glycol diacrylate/acrylic acid polymer) that supports the growth of intestinal cell lines to construct intestinal epithelial structures, demonstrating that these structures support small intestinal epithelial cell proliferation and differentiation for 3 weeks[24]. However, the disadvantage is that ultraviolet light and its initiator can damage the cells. Photo-curing bioprinting is a progressively imperative part of cell printing strategies, and it is anticipated to supplant extrusion bioprinting as the foremost standard biological 3D printing in the future.

3. Bioinks for bioprinting organoids

Bioinks are crucial for bioprinting. The ideal bioink should meet certain printability requirements, demonstrate suitable mechanical properties; and possess sufficient levels of biodegradability, biocompatibility, and cytocompatibility. For bioprinting organoids, the bioink is selected based on the printability of the ink and its effect on cell behavior. Printability implies that during bioprinting, bioinks are required to exhibit proper flowability and the capability to quickly mold into a shape after printing and cross-linking (photo cross-linking, chemical cross-linking, and physical cross-linking). Increasing the hydrogel concentration can accelerate the curing time and improve the hydrogel strength, which is conducive for better forming. However, it reduces the gel water content and narrows the micro-pore size inside the gel, which is not conducive for cell survival and deposition of the extracellular matrix (ECM). In addition, different types of bioinks produce cells with different microenvironments, affecting cell proliferation, differentiation, migration, and self-organization. Therefore, bioinks have a suitable printing window for printing complex geometric organ shapes.

Both natural and synthetic polymeric materials can be used as raw materials for bioprinting. The commonly used bioinks are agarose-based, alginate-based, collagen-based, hyaluronic acid-based, fibrin-based, cellulose-based, silk protein-based, and ECM bioinks. Each bioink possess its own advantages and disadvantages **(Table 2)**. Agarose, a marine polysaccharide extracted from seaweed, exhibits suitable mechanical properties. However, its ability to support cell growth is limited, which is not conducive to organoid construction. Therefore, its use often requires mixing with other biomaterials to improve its biocompatibility. The earliest reported strategy for bioprinting blood vessels by Norotte *et al*. was the use of 300–500 μm diameter blood vessels and supporting cell spheres. These spheres were then allowed to deposit on each other on molds printed with agarose to form a single blood vessel[25]. Alginate is a negatively charged polysaccharide that can be transiently cross-linked with divalent cations to form hydrogels. However, it lacks cell adhesion sites[26], and different polymers, such as PCL and gelatin, are often mixed with alginate to form different structures for 3D printed tissues. Zhang *et al*. used alginate and nano-hydroxyapatite to promote osteochondral repair[27]. Collagen is the primary component of the ECM, which exhibits appropriate biocompatibility. It can be cross-linked by changing the temperature or pH. Using a mixture of collagen and alginate bioink produces a stronger effect than using

Table 2. Performance comparison of different bioinks for organoids

Bioink types	Cell types	Printing methods	Gelation method	Properties	References
Collagen-based	Human stem cell–derived cardiomyocytes	Extrusion	pH	Better biocompatibility Slow gelation rate Low mechanical properties	[33]
ECM-based	Human induced pluripotent stem cells (hiPSCs)	Extrusion	Light	Better biocompatibility Better functionality	[36]
Alginate-based	HepaRG	Extrusion	Temperature/ ion	Easy to prepare Fast gelation Better cytocompatibility	[52]
Hyaluronic acid-based	Primary cell liver	Extrusion	Chemical crosslinking	Better biocompatibility Slower gelation lower Mechanical properties	[28]
Agarose-based	Human umbilical vein smooth muscle cells (HUVSMCs) Human skin fibroblasts (HSFs)	Extrusion	Chemical crosslinking	Good gel forming ability Good mechanical properties and biological tolerance Limited ability to support cell growth	[25]
Fibrin-based	Human adipose-derived stem cells (ASCs) Endothelial colony-forming cells (ECFCs)	Laser-assisted	Thrombin	Better biocompatibility, biodegradability Poor mechanical properties	[30]
Cellulose-based	Human nasoseptal chondrocytes cells (hNCs)	Inkjet	Temperature	Environmentally sensitive Easy to gel	[29]
Gelatin-based	HepG2 cells	Extrusion	Light	Better biodegradability and remodeling	[31]

alginate ink alone. The application of bioink with two or even three biomaterials will improve the stability of polymer systems, tissues, and organoid constructs and will be more beneficial for cell proliferation, differentiation, and self-organization. Hyaluronic acid (HA) is a natural ECM. HA gels slowly, have low mechanical properties after gel formation, and are usually double cross-linked or chemically modified to improve its mechanical properties. Skardal *et al*. developed a versatile HA and gelatin-based hydrogel system to print primary liver spheroids[28]. Carboxymethylcellulose (CMC) is a semi-flexible polysaccharide derived from cellulose. CMC can be converted into environmentally sensitive hydrogels by changing its concentrations and molecular weights, as appropriate. Markstedt *et al*. combined nanofibrillated cellulose–alginate complexes and chondrocytes to prepare ear-shaped and curved-moon scaffolds[29]. Fibrin is a pro-coagulant protein. It is enzymatically thrombinized to prepare hydrogels with adequate biocompatibility and biodegradability. Gruene *et al*.[30] used laser-assisted bioprinting to produce stable vascular networks using natural hydrogels composed of fibrin precursors and HA as cell carriers and environmental materials. Gelatin is a protein obtained by the partial hydrolysis of collagen and is homologous with collagen.

Its strength depends on the concentration of the solution. Gelatin exhibits sufficient degradability and remodeling. ECM bioink, formed by crushing the removed cellular tissue, dissolving it in buffer, and adding other easy-to-form gels, is the most suitable bioink for cell survival. Matrigel™, an ECM secreted from murine Engelbreth–Holm–Swarm tumors, is the most commonly used ECM for bioprinting. Salvador *et al*. used hydrogels composed of alginate, gelatin, and matrix gel-controlled fractions for bioprinting tumor models to maintain and prolong patient-derived tumor spheres in culture without disrupting tumor sphere formation[31].

4. Bioprinting organoids applications

Organoids and bioprinting are two of the most popular areas of tissue engineering. Although the use of bio-3D printers to print organoids is nascent, the combination of bioprinting and organoids has demonstrated successful examples, indicating their promising future. Here, we present the current state of research on bioprinting of organoids.

4.1. Heart

The heart is one of the most important organs in the human body, providing power to support the flow of blood, supplying various nutrients and oxygen to other organs and tissues, and eliminating the waste products of metabolism so that the body can function properly. A mature heart contains 9 billion cells, including fibroblasts, cardiomyocytes, smooth muscle cells, connective tissue cells, and immune cells[32,33]. Furthermore, unlike other parts of the body, the heart tissue cannot heal itself from damage. The current challenge faced in bioprinting cardiac organs is that the biomaterials used in bioprinting cardiac organs are primarily the soft materials that possess low mechanical strength and weak support, making it difficult to print and shape layer by layer. Another challenge is the fact that current cardiac organ constructs are either lacking in cells[34,35] or have no evidence of electromechanical function and lack functionality[36].

Certain studies have been conducted for heart organoid construction. Ishino Fumitoshi's team from Tokyo Medical and Dental University developed a 3D heart organoid, similar to the developing heart, using mouse embryonic stem cells in the presence of FGF4 and LN/ET complexes[37]. Zweigerdt *et al*. of the Hannover Medical School, Germany, encapsulated free-suspended human PSCs in a matrix gel (Matrigel) in suspension culture in response to the classical Wnt signaling pathway, thereby effectively differentiating them into highly purified cardiomyocytes and establishing a 3D heart-like structure of a certain size with different cell layer patterns and a foreground endoderm structure[38]. However, the organoid thus constructed successfully replicates some aspects of heart tissue, including stromal cells, endothelial cell network, and epicardial layer, and even resembles to early heart developmental morphology, but the macroscopic structure of the organoid moderately differs from that of the real organ. The incorporation of bioprinting has shown satisfactory results. In April 2019, scientists in Israel successfully 3D printed an "artificial heart," which is the first successfully designed and printed heart comprising cells, blood vessels, ventricles, and atria (**Figure 2A, B and C**). Although the cells in this heart appear to contract, they cannot beat and pump blood like a normal heart[36]. Recently, Professor Adam Feinberg's team at Carnegie Mellon University used collagen as a freely embeddable suspension hydrogel (FRESH) to bioprint heart organoids, combining MRI images of coronary arteries and 3D images of the heart to achieve fine structures at different structural scales from capillaries to the entire heart organ, as well as high-resolution printing of heart organoids with systolic function.[34] (**Figure 2D, E, and F**). Previously constructed organoids are almost always millimeter-sized. However,

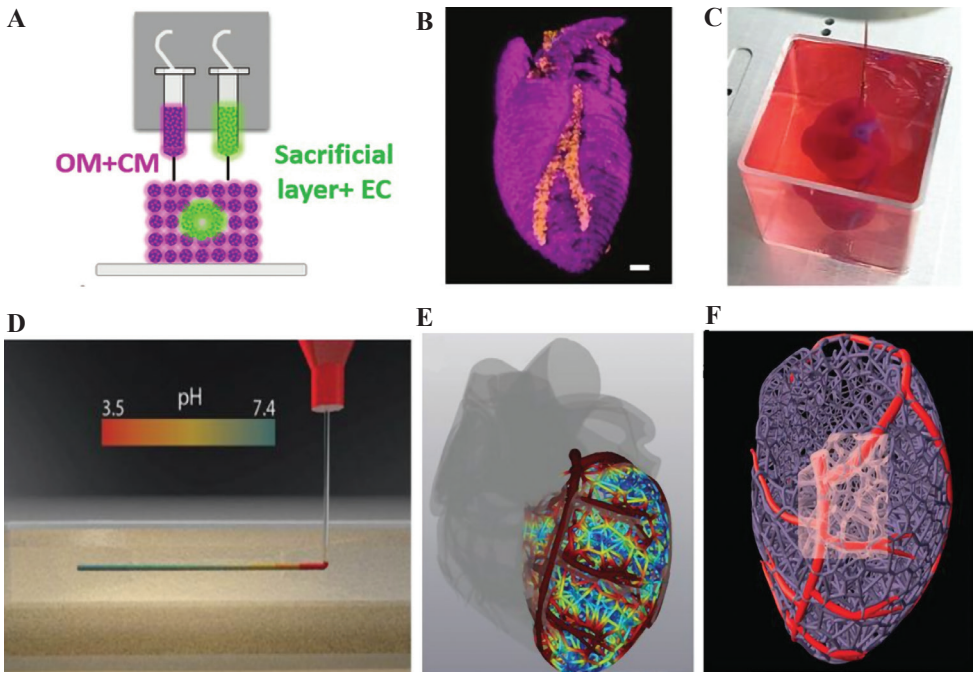


Figure 2. (A) Side view of the bioprinting concept and the unique cellular bioink. (B) 3D confocal image of a bioprinted heart (CM in pink, EC in orange), scale bar =1 mm. (C) Bioprinted heart in a support bath. (D) A schematic diagram of fast cross-linking by squeezing the collagen solution in a support bath with a pH of 7.4. (E and F) Magnetic resonance imaging (MRI) post-processed images of the heart model, showing it has a coronary vascular network. (Adapted with permission from Lee *et al*, Science, 2019, 482–487 (2019)[34]) and (from ref.[36] licensed under Creative Commons Attribution 4.0 license).

researchers at the University of Minnesota in the U.S. have recently 3D printed the first ever centimeter-sized heart organoids. They optimized a specialized bioink, made from ECM proteins and human stem cells, to print into ventricular structures. The corresponding stem cells were first expanded to high cell density on the ventricular structures. Then, the cells were differentiated into cardiomyocytes, with critical cell density and the ability to make the cells beat like a heart[39]. This is a major advance in organoid studies of the heart to bioprint stem cells in a tissue synergistic manner and to be able to direct their differentiation into cardiomyocytes in similar situations with *in vivo* stem cells adjacent to each other. While their printed cardiac muscle models demonstrated encouraging results in small kinetic models, this is insufficient in large animal models with thicker myocardial walls and more demanding vascularization; therefore, further exploration is required.

4.2. Kidney

Kidney organoids primarily comprise metanephros (MM) cells, which have been successfully used for nephron-related disease modeling and drug screening. Significant barriers in using the current systemic approach persist, such as in experimental modeling and kidney transplantation. scRNA-seq and transcriptomic studies have identified renal organoids as a very premature renal system. Cultured kidney organoids do not produce all kidney cells, specifically a wide variety of mesenchymal cells, and do not allow the formation of advanced renal structures with a vascular system[40]. Kidney organoids cannot grow above the millimeter level because they become necrotic internally as they develop and have difficulty developing a higher form of the dermal medulla. In addition, the main limitation of kidney organoids is the lack of a functional vascular system.

To construct kidney organoids, based on the finding that Metanephric Mesenchyme (MM) Ureteric Bud (UB) have distinctive roots, Taguchi *et al*. established a method to extract MM from mouse ESCs and human iPSCs cultured into 3D spheres and promoted the development of mesoderm with Wnt agonists, retinoic acid, etc., thereby producing pedunculated, Bowman's capsule cells, and tubular epithelial cells[41]. Takasato *et al*. used human embryonic stem cells in 3D spheroids to develop kidney cells[42]. They first performed induced culture in a 2D plane and then subjected the stem cells to aggregated culture at a 3D level to produce human iPSC-derived kidney organs containing renal progenitor cell-derived podocytes, Bowman's capsule, and tubules, as well as UB-like cells, stromal cells, and endothelial cells. However, kidney organoids constructed using these methods often suffer from poor reproducibility and high inter-group variability. This is true even in the case of a single iPSC using a single protocol. Kidney unit patterns and cell ratios may also fluctuate between experiments. In the field of bioprinting, the construction of kidney organoids likely yields satisfactory results. Jennifer *et al*. used bioprinting to construct a functional 3D kidney structure containing living human epithelial cells that form the surface of the renal tubules[43] (**Figure 3A, B and C**). Organovo recently developed a proximal tubule-like tissue that was bioprinted as a layered structure in a well membrane by mixing fibroblasts and HUVECs with a proprietary heat-responsive hydrogel. After 3 days of culture, renal PTECs were inoculated onto the bioimprinted layer. On maturation, the kidney cells exhibited a microvascular network with tight junctions and cell polarization (**Figure 3D, E, and F**). In nephrotoxicity tests of mature tissues, the metabolism of renal cells and cellular activity produced greater adverse effects with increasing concentrations of cisplatin[44]. Bioprinting facilitates the precise control of cell deposition in a 3D space in terms of the speed and scale, which could lead to a significant reduction in variability between batches of constructed kidney organoids and even a breakthrough in scale from millimeters to centimeters. Recently, Melissa H. Little's team at the University of Melbourne, Australia, reported the application of extrusion-based bioprinting technology to rapidly prepare a large number of kidney organoids. Extrusion bioprinting was used to prepare human pluripotent stem cells (hPSCs) derived from renal progenitor cells in 6-well and 96-well plates and they developed into initial cellular microclusters of kidney organoids, which were then cultured for 20 days to obtain kidney organoids with morphology, cell type, and gene expression levels comparable to those previously reported for kidney organoids in artificial culture. This study provides high-quality control of cell number, tissue diameter, and cell viability through bioprinting[45]. Extrusion-based automated bioprinting has shown the ability to produce kidney organoids with improved throughput, controlled quality, and scale-up, signaling the potential of this technique in the fabrication of kidney organoids at the scale of actual kidney organs in future.

4.3. Liver

The liver is the largest gland in the body and contains hepatocytes (HCs), hepatic stellate cells (HSCs), hepatic sinusoidal cells (LSECs), Kupffer cells (KCs), and biliary epithelial cells (BECs), which are densely and orderly arranged in the hexagonal hepatic lobules[46]. Although the liver has an innate ability to regenerate, the hepatocytes survive only 2-3 days once they are removed from the body and rapidly lose their characteristic self-replicating proliferative function. With the rapid development of the field of cellular biology, the 3D culture system significantly promotes the maturation of hepatocytes

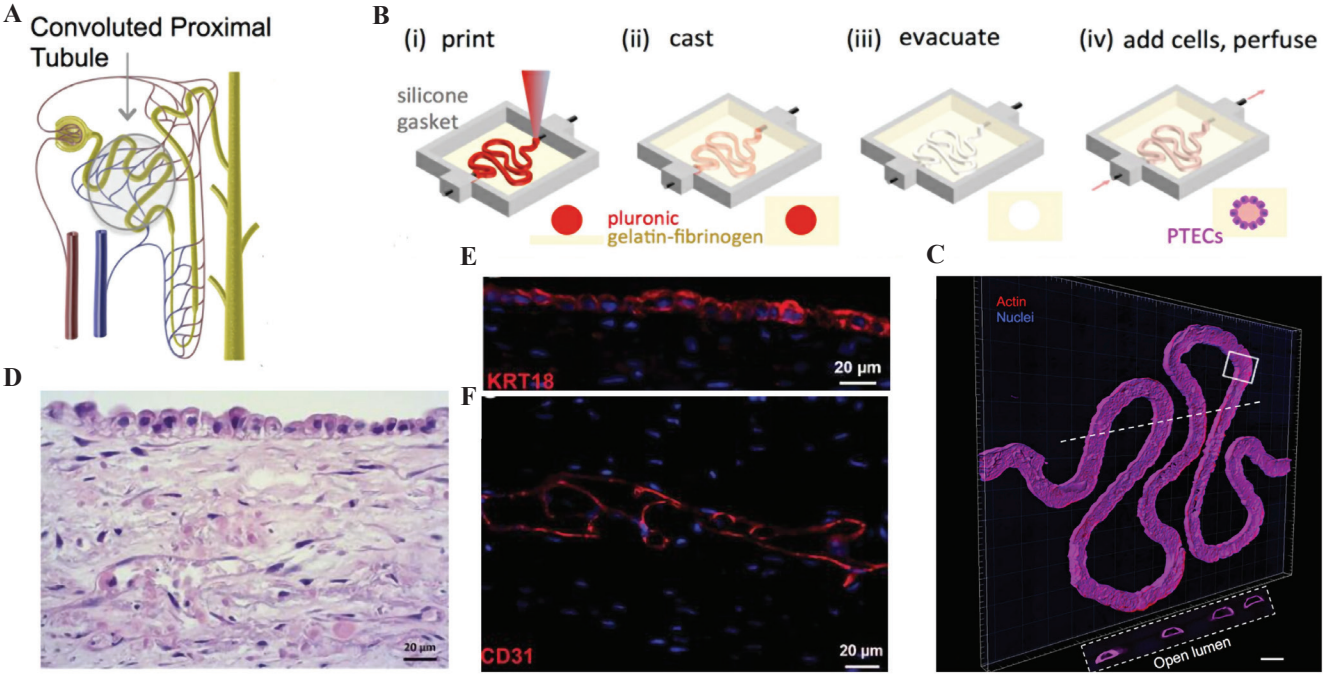


Figure 3. (A) Schematic diagram of the proximal renal tubule. (B) Corresponding schematic diagrams of the different steps for making 3D convoluted perfusable proximal tubules. (C) 3D rendering of a confocal image of the proximal tubule, with actin colored red and the nucleus colored blue, scale bar = 200 µm (D) Hematoxylin and eosin (HE) staining showed complete cellular organization as well as organization of the mesenchymal and epithelial layers. (E) RPTECs form a monolayer and express cytokeratin 18 (red). (F) The interstitial layer exhibits an extensive network of endothelial cell linings (red, CD31), scale bar = 20 µm. (from ref.[43] licensed under Creative Commons Attribution 4.0 license) and (from[44] Creative Commons Attribution license).

in vitro. This implies that the spatial location, pressure signals, and matrix adhesion information provided to the cells in a 3D culture environment play an important role in the survival and function of hepatocytes[47,48]. The use of bioprinted liver tissue can better simulate the *in vivo* static microenvironment and dynamic microenvironment of the liver, which overcomes the limitations of 2D cultures and can better simulate the complexity of the *in vivo* microenvironment.

Over the past decade, researchers have demonstrated that hepatocytes exhibit a high activity and functional capacity when grown and differentiated in assembled spheres[49]. Skardal *et al*. used a multifunctional HA and gelatin-based hydrogel system to print specific primary liver spheroids to create *in vitro* liver constructs with high cell viability and measurable functional albumin and urea output[28]. Conventionally, the most commonly used liver organoids in 3D culture are spheroids. However, spheroids are limited in size due to diffusion barriers in their dense structure, limiting the supply of nutrients, and oxygen. Recently, researchers have attempted to prepare liver organoids using SLA. Grix *et al*. combined HepaRG and human stellate cells using stereolithography to produce bioprinted liver organoids which exhibited the basic properties of liver[50]. The highly vascularized complex liver tissue is divided into lobes, lobules, hepatocytes, and hepatic sinusoids, covering both microscopic and macroscopic scales. To fabricate multiscale heterogeneous tissues, Song *et al*. used a pre-defined extrusion bioprinting technique (**Figure 4A**) to create arrays of liver lobules that could simultaneously create heterogeneous, multicellular, and multi-material structures[51] (**Figure 4B**). Liver vascularization is an important aspect, which should be considered when bioprinting liver models. Recently, Mao *et al*. used a mixture of hepatocyte suspension and 4% sodium alginate solution as bioink (cell density: 1×10^6/ml), then printed and coated in a culture dish, collected the printed structures, and prepared liver tissue layer-by-layer to build liver organoids. Three-dimensionally printed liver organoids formed clusters and exhibited the ability to accumulate hepatic glycogen and transport indole green and acetylated LDL. Remarkably, the mouse liver spontaneously developed a vascular network system 14 days after transplantation[52]. The study of 3D bioprinting liver organoids holds great promise and significance. If 3D printed liver organoids can be mass-produced and survive in large quantities *in vitro*, expensive biologics, such as albumin and clotting factors, can be left to them to produce.

4.4. Intestinal tract

Intestinal organoids are derived from intestinal tissue stem cells or PSCs and possess a 3D structure. Organoids

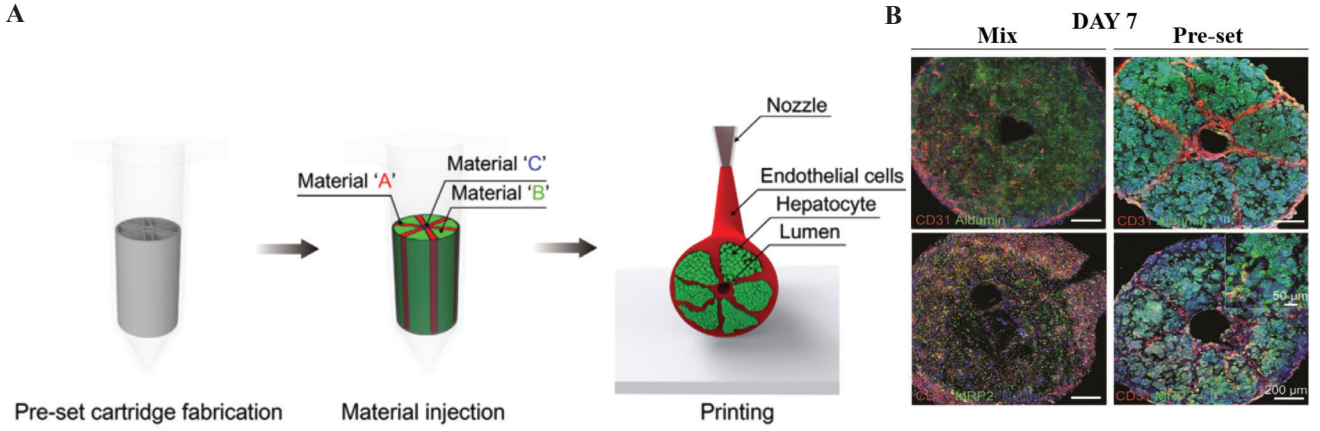


Figure 4. (A) Schematic diagram of the pre-set extrusion 3D bioprinting technique for liver lobule printing. (B) MIX and preset structures were compared to assess liver function, and immunostaining for CD31 (red), albumin (green), MRP2 (green), and DAPI cell nuclei (blue) was performed; scale bar = 200 μm. (Adapted with permission from Kang *et al*, Small, Copyright 2020 Wiley-VCH Verlag[51]).

of the intestine are widely used in scientific research and drug development because of their stable culture system and relatively well-defined developmental processes. At present, intestinal organs, particularly small intestinal organs, are widely studied models, and the establishment of intestinal organs provides a basis for the establishment of other organs. By adding growth factors for the growth and development of different organs based on the intestinal organ culture system, other organs derived from the digestive tract epithelium, such as the liver[47] and pancreas[53], have been established, in addition to other epithelial organs from non-digestive tract sources, such as the prostate[54] and breast[55]. Intestinal organs can simulate the relationship between cells *in vivo* and can be used to study the characteristics of stem cells; they are also widely used in studying ulcerative colitis (UC)[56] and other intestinal diseases.

Deng *et al*. constructed a new intestinal organ culture system that can simulate the regeneration process of proliferative crypts after intestinal epithelial injury and revealed the key role and mechanism of two epigenetic regulators (VPA and EPZ6438) in regulating regeneration after intestinal injury (**Figure 5A and B**)[57]. Meanwhile, a novel engineered plant-based nanocellulose hydrogel was recently reported as a culture medium for small intestine organoids, which has the advantages of clear composition and low cost compared with the currently used organoid culture medium, Matrigel[58] (**Figure 5C**). However, many questions remain unanswered. For example, there are multiple phenotypes (symmetrical, budding, mixed, etc.) that can occur during the culture of human intestinal organoids, and varying phenotypes make experiments less reproducible[59]. The introduction of bioprinting has improved the function and structure of intestinal organoids and reproducibility of experiments. The intestinal surface possesses a microvilli structure that provides a large surface area for efficient digestion and absorption. Using collagen and cell-loaded bioink from the submucosa of the small intestine, microscale villi structures with better permeability coefficients and glucose uptake were prepared through a vertically moving bioprinting method[60]. To overcome the limitations of current 3D culture systems, researchers have attempted to use bioprinting technology to prepare 3D intestinal tissues composed of human primary small intestinal epithelial cells and myofibroblasts. These tissues possess physiological barrier function and damage response to toxicity and inflammation[61]. In the past decade, researchers have cultured intestinal organoids that often assemble hepatocytes into micrometer to millimeter spheres. In a recent study, however, researchers prepared centimeter-sized intestinal organoids using bioprinting technology. Jonathan *et al*. developed a unique 3D bioprinting technique referred to as BATE, which is a combination of a microscope and an extrusion printing system[20]. Using microscopy for continuous monitoring of the process, the researchers combined organoid technology to deposit intestinal stem cells approximately a few centimeters long into the gel to obtain centimeter-scale gastrointestinal tissues with self-organizing features (e.g. lumen, branching blood vessels, and crypt and villi structures of the tubular intestinal epithelium). This study provides new tools for drug discovery, disease diagnosis, and regenerative medicine research.

4.5. Tumor model

Stem cells used in tumor organoid model cultures can be derived from tissue stem cells and PSCs[62], as well as from tumor stem cells. The tumor organoid model provides a new approach for personalized cancer treatment. It not only simulates tumor characteristics [63] and tumor cell heterogeneity[62] but also better reflects human changes compared with traditional animal tumor models. Bioprinting has been applied to alter

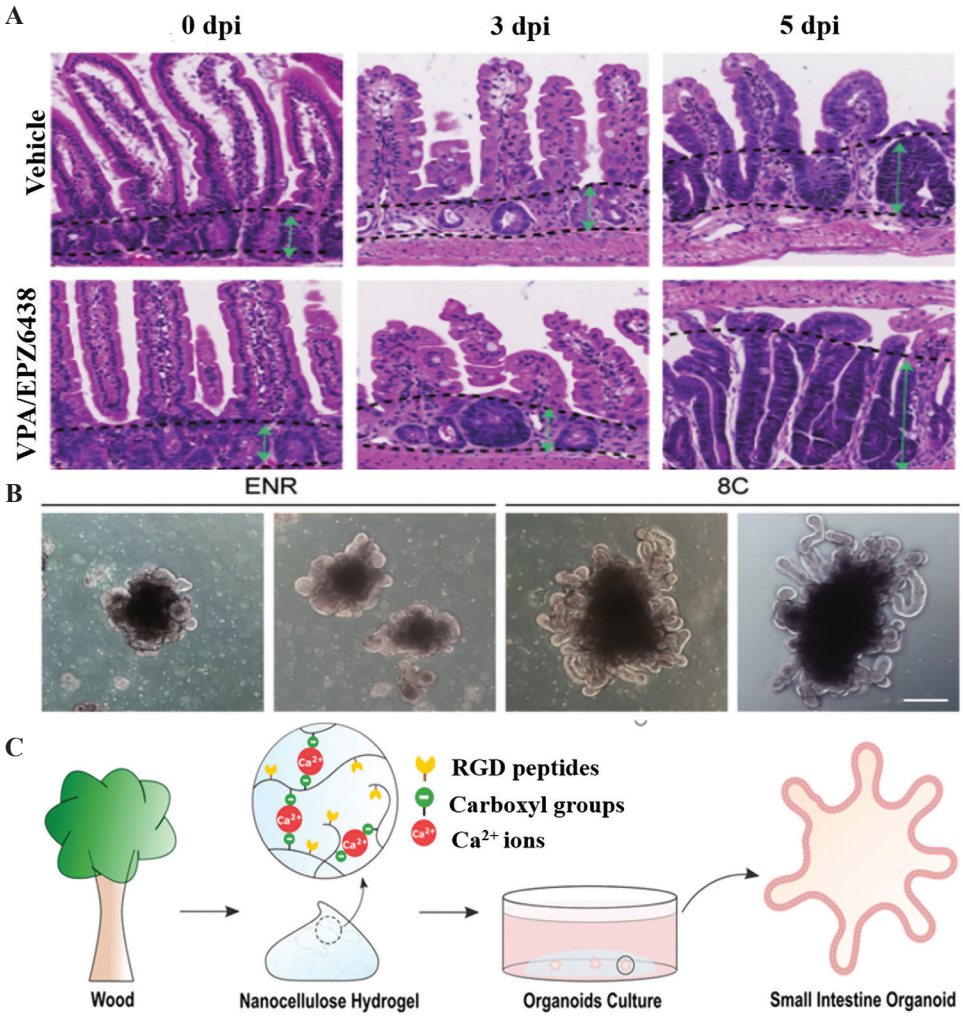


Figure 5. (A) HE staining of the small intestinal crypt was performed on days 3 and 5 (dpi) after irradiation. The green arrow between the two dashed lines indicates the length of the crypt. (B) Typical morphology of intestinal organoids cultured under the indicated conditions. (C) Schematic diagram of small intestine organoid culture in plant-based nanocellulose hydrogel. (from ref.[57] licensed under Creative Commons Attribution 4.0 license) and (from ref.[58] licensed under Creative Commons Attribution 4.0 license).

the tumor microenvironments by precisely controlling the combination of tumor-associated cells and ECM components and organizing them into well-defined spatial distributions. As the field of precision medicine and the development of organoid culture techniques continue to advance, tumor organoid models are being studied at an increasingly rapid pace.[64]

Recently, various tumor organoid models have been successfully established. Clevers *et al*. described a strategy for producing 3D prostate organoid cultures from healthy mice and human prostate cells (single lumen and basal cells sorted in bulk or FACS), metastatic prostate cancer lesions, and circulating tumor cells[65]. This strategy allows for the growth of intraluminal and basal prostate epithelial cell lines, as well as that of advanced prostate cancer. Fujii *et al*. established a model library containing 55 colorectal tumor organoids (including different tumor subtypes) that can help in the understanding of the genesis and pathogenesis of colorectal tumors, and provide insights for promoting patient-centered treatment[66]. However, the currently established tumor models do not accurately simulate the natural ECM components and interactions between tissue, cell, and matrix molecules. The introduction of bioprinting has slightly enhanced the structure of blood vessels and lymphatic vessels in tumor models, as well as the lesion characteristics. Zhao *et al*. used bioprinting to construct the first *in vitro* 3D tumor model of HeLa cells (a type of cervical cancer cell)[67]. The tumor model better reflected the growth and development of the tumor *in vivo* and approximated the lesion characteristics of the cancer cells *in vivo* (**Figure 6A, B, C and D**). To accurately simulate the complex microenvironment of a tumor, Zhang *et al*.

designed a coaxial bioprinting technique to construct a tumor organ model with perfusable hollow blood and lymphatic vessels closed at one end and integrated a gelatin hydrogel gel containing breast cancer cells to form a pair of tumor organs containing both blood vessels and lymphatic vessels (**Figure 6E and F**)[68]. To better simulate the tumor microenvironment, tumor models must be constructed by focusing on the establishment of gradients of physical and chemical properties. Researchers printed tumor cells, vascular endothelial cells, and porcine-derived brain tissue ECM into concentric cancer-stromal rings to form a regionalized structure of vascular matrix surrounding tumor tissue and an oxygen gradient within the tumor tissue[69]. The use of bioprinting technology to construct 3D tumor microenvironments has shown some advantages in reconstructing cellular functions, signaling pathways, and drug screening.

4.6. Brain organoids

Brain organoids are microscopic organs of embryonic stem cells (ESCs) or PSCs that are artificially cultured and have a functional structure similar to that of brain tissue. Brain tissue is composed of tightly packed glial and neuronal cells, and the ability of cells to self-organize depends mostly on the influence of component gradients and intercellular interactions[70,71]. Brain organoids can be used to study neurophysiology and neurodevelopment and can mimic various neurological diseases.

The development of human PSCs into brain organoids encompasses the formation of embryoid bodies, neural induction, neuroepithelial expansion, and maturation of the organoid. In a new study, Trevino *et al*. constructed human forebrain organoids for the first time using PSCs in a 3D culture and increased their lifespan for up to 300 days[72] (**Figure 7A**). However, the challenge with current 3D organoid and spheroid models grown in culture dishes is the insufficient control over cellular localization and diversity. Accordingly, Jodat *et al*. recently designed a photocrosslinkable bioink and a thermotherapeutic support bath using embedded 3D bioprinting to distribute heterogeneous neural populations with neurospheres and glial cell specificity while supporting the formation of self-organizing spheroids in 3D network structures[73]. Bioprinted brain organoids can be used for drug target screening in neurological diseases. Moreover, researchers described how bioprinting could provide a high-throughput and reproducible preparation of neural tissue, as an alternative to expensive animal

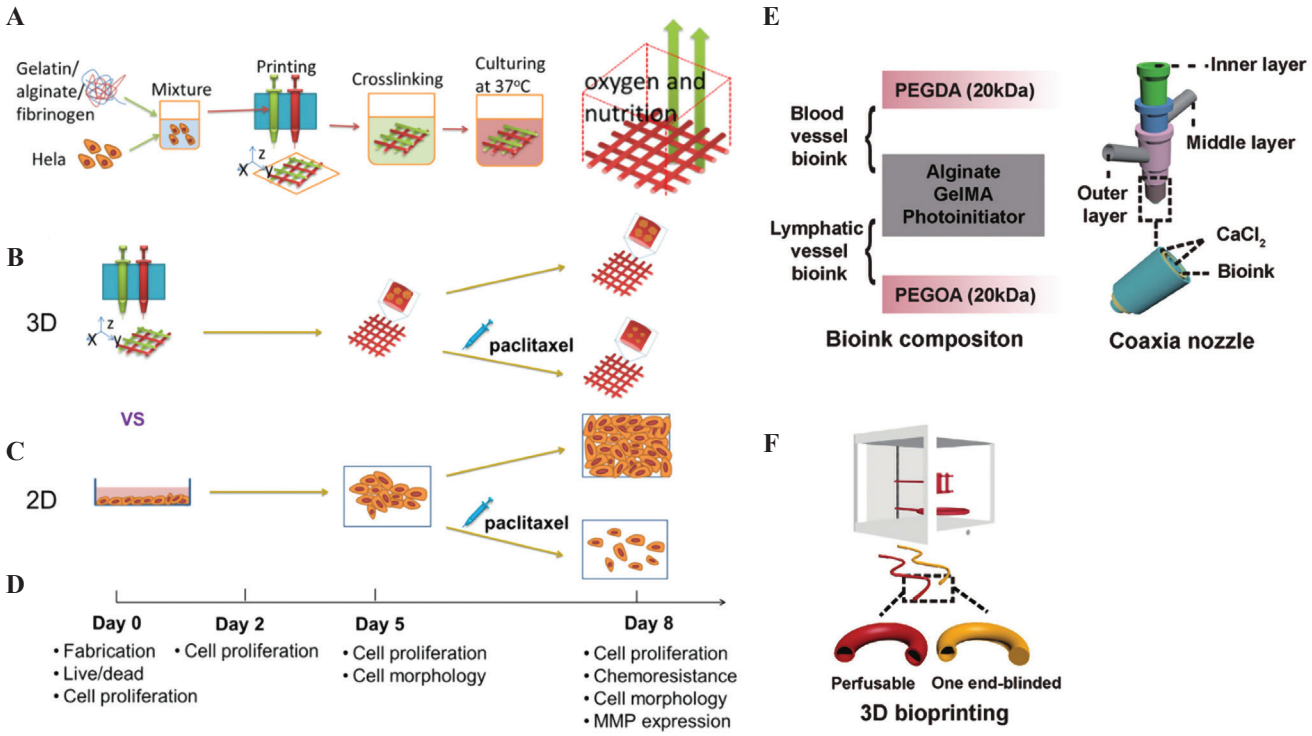


Figure 6. (A) Schematic diagram of the method of 3D bioprinting tumor models with HeLa cells. (B) The plan of the 3D HeLa/hydrogel builds. (C) Both 3D HeLa/hydrogel constructs and 2D planar samples were incubated for 5 and 3 days with/without paclitaxel. The final results were compared. (D) Composition of bioink for bioprinting of blood vessels and lymphatic vessels. (E) Multi-layer coaxial nozzle design for bioink printing as well as cross-linking. (F) Two different hollow tubes were bioprinted using a perfusable hollow tube that mimics a blood vessel and an end-blind hollow tube that mimics a lymphatic vessel. (Adapted with permission from Yu Zhao *et al*, Biofabrication, 2014, 6 035001[67]) and (Adapted with permission from Cao X, Ashfaq R, Cheng F, *et al*., Adv Funct Mater, ©2019 WILEY-VCH Verlag GmbH & Co. KGaA, Weinheim[68]).

experiments, to screen potential drug targets for treating Alzheimer's disease[74]. In the past, the act of culturing brain-like organs often produced only one cell type of interest when transcription factors were overexpressed, rather than the multiple cell type structures found in natural tissues. Therefore, Mark *et al*. used a multi-material bioprinting technique in which they differentiated on-demand orthologous regions composed of neural stem cells, endothelium, and neurons from a mixed class of embryos overexpressing transcription factors and wild-type human induced stem cells (hiPSCs)[75]. When conducting drug screening, a protocol that is simple to operate and highly reproducible is required. Recently, researchers printed PCL scaffolds to culture brain-like organs and designed them into structures with favorable diffusion conditions for engineered flat brain organoids (efBOs) (**Figure 7B**). The efBOs were fabricated in a highly simplified manner. In addition, this was the first study to report the preparation of an *in vitro* model of neural tissue with an intrinsic gyrus[7].

4.7. Other organoids

The cornea possesses a complex structure. It is divided into five layers from anterior to posterior: the epithelial cell layer, preelastic layer, stromal layer, posterior elastic layer, and endothelial cell layer. Therefore, culturing corneal organoids poses certain challenges. Considering the complex spatial structure, bioprinting may have some advantages. Isaacson *et al*. designed corneas with the structure of natural human corneal stroma by obtaining stem cells from the corneas of healthy donors and mixing them with gel (**Figure 8A**)[77]. The pancreas is a relatively small organ, but its functional and structural complexity have always made it difficult to make mechanistic breakthroughs. Kim *et al*. attempted to develop pancreatic tissue constructs enriched with 3D islets for use as a source to enhance key functions of pancreatic tissue[78]. The formation of lung organoids begins with the differentiation of hPSC into a stereotyped endoderm, followed by differentiation into a foregut endoderm, and finally into lung organoids. Recently, Han *et al*. constructed the first lung organoids for the study of COVID-19 and screened therapeutic agents[79]. In a previous report, Grigoryan *et al*. used stereolithography as a 3D bioprinting technique to create a small 3D printed lung model with a multivessel network and "breathing" function (**Figure 8B**)[80]. Conventional breast organoid 3D culture involves mixing dispersed mammary epithelial cells in an ECM matrix before gelling and subsequent self-organization into organoid structures[81,82]. However, there is a large variation between batches of such fabricated mammary organoids. To address this issue, John *et al*. reported the bioprinting of mammary organoids in collagen with minimal variation from batch to batch (**Figure 8C and D**)[83]. More recently, more bionic assemblies have been proposed based on the concept of organoids. Professor Kunyoo Shin's team at Pohang University of Science and Technology in South Korea

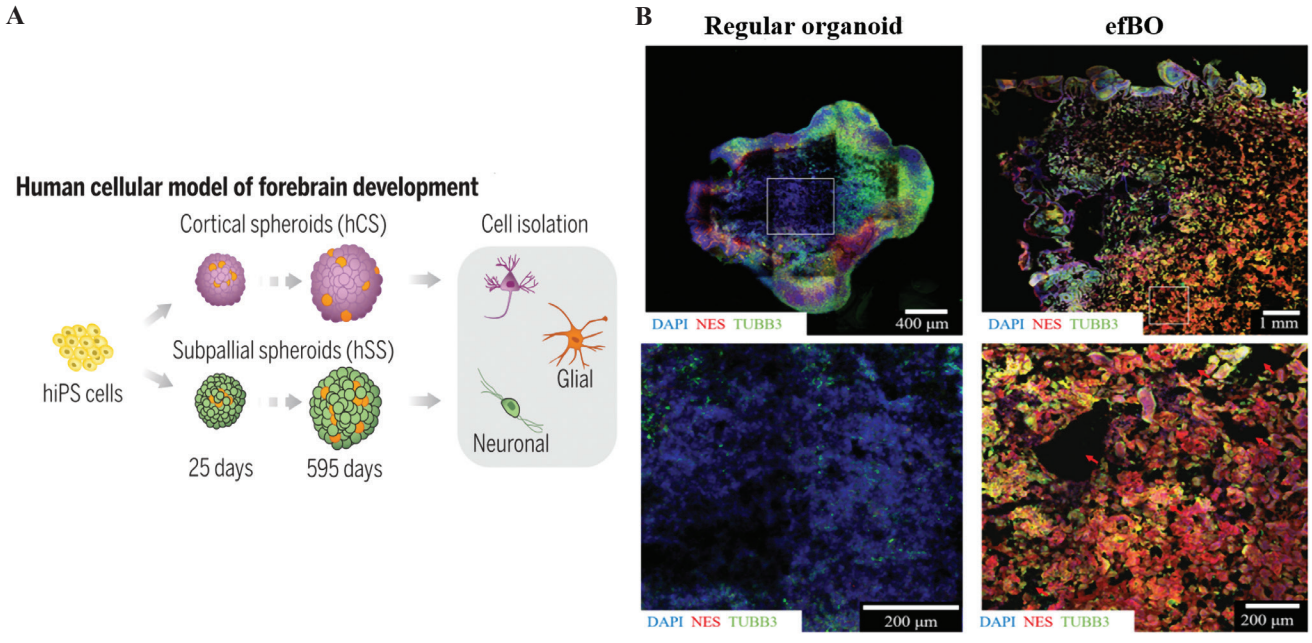


Figure 7. (A) Schematic representation of the flow of human induced PSCs developing into forebrain cells. (B) Comparison of tissue core between regular brain organoids and efBOs. Immunohistochemical staining of NES and TUBB3 was performed to visualize cells. DAPI was used as counterstain. (Adapted with permission from Trevino AE, *et al*., Science, 367: eaay1645, Copyright 2020, The American Association for the Advancement of Science[72]) and (Adapted with permission from Theresa S P Rothenbücher *et al*., Biofabrication, 2021,13 011001, IOP Publishing Ltd[76]).

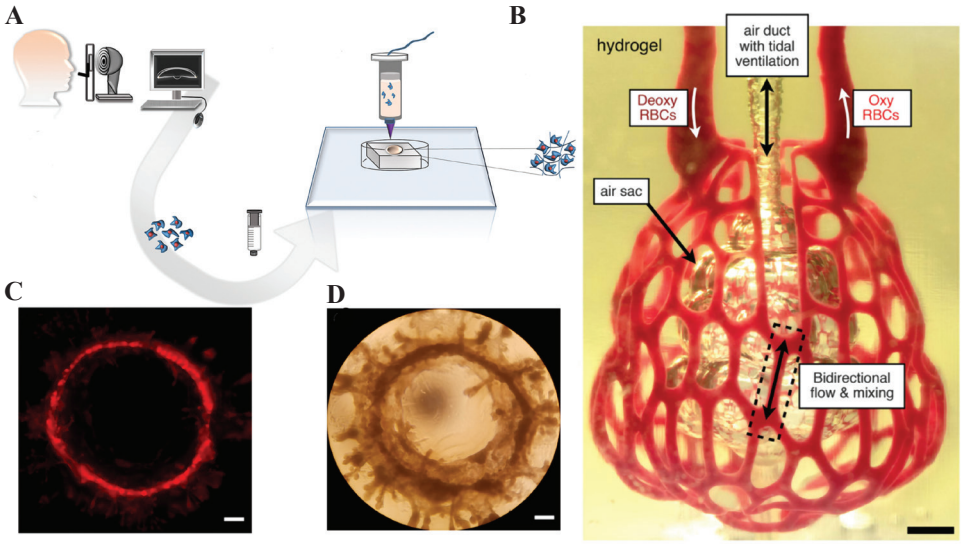


Figure 8. (A) Schematic diagram of the bioprinted cornea process. (B) Photographs of printed hydrogels containing distal lung subunits during red blood cell perfusion when the balloon is ventilated with oxygen, scale bar = 1 mm. (C) Images of red fluorescent protein-positive (RFP+) MCF12A cells forming a large mammary circular organoid at 14 days after printing. (D) Example of a large mammary round-like organ with a diameter of approximately 4 mm at 24 days after printing, scale bar = 500 μm. (from ref.[77] licensed under Creative Commons Attribution 4.0 license), (Adapted with permission from Grigoryan B, *et al*., 2019, Science, 364:458–64, Copyright 2019, The American Association for the Advancement of Science[80]) and (from ref.[83] licensed under Creative Commons Attribution 4.0 license).

used bio-3D printing technology to reconstruct bladder assemblies and develop patient-specific bladder tumor assemblies that accurately mimicked the pathological features of tumors *in vivo*[84].

5. Future outlook for bioprinting organoids

Bioprinting is a developing technology that has the potential for tissue and organ development because of its capacity to accurately control the spatial dissemination of cells and encompassing microenvironment. Organoids are 3D cellular self-organization cultures exhibiting some key characteristics of the corresponding organs and are uniquely similar to actual human organs[85-88]. Since the first successful cell bioprinting experiment in 2003[89], organoid construction and bioprinting have brought hopes, although significant efforts are required before bioprinting of organs actually is put into practical use.

There are numerous problems with the current construction of organoids. Organoids are millimeter-scale 3D culture systems formed by intercellular self-organization. However, certain structural features of organs range from a few hundred microns to a few centimeters. In addition, a large gap remains in the scale of actual organs. Vascularization is crucial for organoid construction. Oxygen and nutrients may successfully sustain organoid development in the early stages of 3D organoid culture. However, in the later stages, a single vasculature may fail to keep up with the organoid's requirements by supplying sufficient nutrients and oxygen[90]. Therefore, a complex vascular system is required. Traditional organoid construction also suffers from variation between culture batches and is less reproducible. The yield of the corresponding organoids is then limited. Bioprinting addresses these problems to some extent. As a breakthrough in addressing the traditional 3D culture-scale limitations, bioprinting has been reported for producing centimeter-level intestinal organoids[20,34]. Bioprinting can also build complex vascular systems for organoids[91-94], and increase the yield of organoids by a factor of nine, while reducing the size variability of organoids, that is, only 1–4%[45,95].

There are a series of difficulties in bioprinting organoids. For example, although bioprinting technology can effectively control the deposition process of cells in 3D space, it is impossible to construct macroscopic tissues through cellular self-organization. To address the current issues pertaining to the scale size of organoids, future studies will focus on how to print small functional units of organoids and then how to deposit and assemble these functional units into larger structures. Therefore, we should find a balance between the architecture of space, vascular network, and self-organization of organoid cells in the bioprinting process. In the precise arrangement of cells, sufficient resolution is also required. However, a considerably high resolution indicates an increase in the density of cells, and an extremely high shear force will aggravate cell damage. In the future, with breakthroughs in bioprinting technology, biomaterials, and a better

understanding of the molecular mechanisms of organ development, more bioprinting strategies for organoid development will emerge. We believe that the future of bioprinting research will revolve around the studies on early developmental stages of organs and tissues. Bioprinting organoid technology will potentially play an extraordinary role in developmental biology, disease pathology, cell biology, regenerative mechanisms, precision medicine, and drug screening.

6. Conclusion

Both bioprinting and organoids are intriguing research topics in the field of regenerative medicine. Bioprinting emphasizes on the reconstrution of tissue structures, while organoids fouces on the rebiulding of biological functions. When these two technologies are combined, bioprinted organs with both physiological function and structure may come into reality in the near future. Although organoid bioprinting is still in its infancy phase, this technique has brought us one step closer to truly 3D printing personalized organs.

Acknowledgments

This research was supported by the Key R and D Program of the Ministry of Science and Technology of China (No. 2018YFB1105600/2020YFC2008700/2018YFB1107000), National Natural Science Foundation of China (No. 92048205/81902195/82072228), the Project of Shanghai Science and Technology Commission (No. 19XD1434200), and Shanghai Municipal Commission of Economy and Information (No. 202001007).

Conflict of interest

The authors declare that they have no conflicts of interest.

References

1. Fatehullah A, Tan SH, Barker N, 2016, Organoids as an *in Vitro* Model of Human Development and Disease. *Nat Cell Biol*, 18:246–54. https://doi.org/10.1038/ncb3312
2. Matano M, Date S, Shimokawa M, *et al.*, 2015, Modeling Colorectal Cancer Using CRISPR-Cas9-Mediated Engineering of Human Intestinal Organoids. *Nat Med*, 21:256–62. https://doi.org/10.1038/nm.3802
3. Ballard DH, Boyer CJ, Alexander JS, 2019, Organoids-Preclinical Models of Human Disease. *N Engl J Med*, 380:1981–2.
4. Huch M, Koo BK, 2015, Modeling Mouse and Human Development using Organoid Cultures. *Development*, 142:3113–25. https://doi.org/10.1242/dev.118570
5. Lui JH, Hansen DV, Kriegstein AR, 2011, Development and Evolution of the Human Neocortex. *Cell*, 146:18–36. https://doi.org/10.1016/j.cell.2011.06.030
6. Kim J, Koo BK, Knoblich JA, 2020, Human Organoids: Model Systems for Human Biology and Medicine. *Nat Rev Mol Cell Biol*, 21:571–84. https://doi.org/10.1038/s41580-020-0259-3
7. Groll J, Boland T, Blunk T, *et al.*, 2016, Biofabrication: Reappraising the Definition of an Evolving Field. *Biofabrication*, 8:5. https://doi.org/10.1088/1758-5090/8/1/013001
8. Heinrich MA, Liu WJ, Jimenez A, *et al.*, 2019, 3D Bioprinting: From Benches to Translational Applications. *Small*, 15:47.
9. Tuan RS, Boland G, Tuli R, 2003, Adult Mesenchymal Stem Cells and Cell-Based Tissue Engineering. *Arthritis Res Ther*, 5:32–45.
10. Xu T, Gregory CA, Molnar P, *et al.*, 2006, Viability and Electrophysiology of Neural Cell Structures Generated by the Inkjet Printing Method. *Biomaterials*, 27:3580–8. https://doi.org/10.1016/j.biomaterials.2006.01.048
11. Li X, Liu B, Pei B, *et al.*, 2020, Inkjet Bioprinting of Biomaterials. *Chem Rev*, 120:10793–833.
12. Xu C, Chai W, Yong H, *et al.*, 2015, Scaffold-Free Inkjet Printing of Three-Dimensional Zigzag Cellular Tubes. *Biotechnol Bioeng*, 109:3152–60. https://doi.org/10.1002/bit.24591
13. Lee YB, Polio S, Lee W, *et al.*, 2010, Bio-Printing of Collagen and VEGF-Releasing Fibrin Gel Scaffolds for Neural Stem Cell Culture. *Exp Neurol*, 223:645–52. https://doi.org/10.1016/j.expneurol.2010.02.014
14. Mandrycky C, Wang Z, Kim K, *et al.*, 2016, 3D Bioprinting for Engineering Complex Tissues. *Biotechnol Adv*, 34:422–34. https://doi.org/10.1016/j.biotechadv.2015.12.011
15. Vijayavenkataraman S, Wei-Cheng Y, Lu WF, *et al.*, 2018, 3D Bioprinting of Tissues and Organs for Regenerative Medicine. *Adv Drug Deliv Rev*, 132:296–332. https://doi.org/10.1016/j.addr.2018.07.004
16. Othon CM, Wu X, Anders JJ, *et al.*, 2008, Single-Cell Printing to form Three-Dimensional Lines of Olfactory Ensheathing Cells. *Biomed Mater*, 3:034101. https://doi.org/10.1088/1748-6041/3/3/034101
17. Pirlo RK, Wu P, Liu J, *et al.*, 2011, PLGA/Hydrogel Biopapers as a Stackable Substrate for Printing HUVEC Networks Via BioLP. *Biotechnol Bioeng*, 109:262–73.

https://doi.org/10.1002/bit.23295

18. Li J, Chen M, Fan X, *et al.*, 2016, Recent Advances in Bioprinting Techniques: Approaches, Applications and Future Prospects. *J Transl Med*, 14:271. https://doi.org/10.1186/s12967-016-1028-0
19. Bertassoni LE, Cardoso JC, Manoharan V, *et al.*, 2014, Direct-Write Bioprinting of Cell-Laden Methacrylated Gelatin Hydrogels. *Biofabrication*, 6:024105. https://doi.org/10.1088/1758-5082/6/2/024105
20. Brassard JA, Nikolaev M, Hübscher T, *et al.*, 2020, Recapitulating Macro-Scale Tissue Self-Organization Through Organoid Bioprinting. *Nat Mater*, 20:22–9. https://doi.org/10.1038/s41563-020-00803-5
21. Daly AC, Prendergast ME, Hughes AJ, *et al.*, 2021, Bioprinting for the Biologist. *Cell*, 184:18–32. https://doi.org/10.1016/j.cell.2020.12.002
22. Cui H, Nowicki M, Fisher JP, *et al.*, 2016, 3D Bioprinting for Organ Regeneration. *Adv Healthc Mater*, 6:1601118. https://doi.org/10.1002/adhm.201601118
23. Quan H, Zhang T, Xu H, *et al.*, 2020, Photo-Curing 3D Printing Technique and Its Challenges. *Bioact Mater*, 5:110–5.
24. Creff J, Courson R, Mangeat T, *et al.*, 2019. Fabrication of 3D Scaffolds Reproducing Intestinal Epithelium Topography by High-Resolution 3D Stereolithography, In: 45th International Conference on Micro and Nano Engineering (MNE 2019). https://doi.org/10.1016/j.biomaterials.2019.119404
25. Norotte C, Marga FS, Niklason LE, *et al.*, 2009, Scaffold-free vascular tissue engineering using bioprinting. *Biomaterials*, 30:5910–7. https://doi.org/10.1016/j.biomaterials.2009.06.034
26. Nair LS, Laurencin CT, 2007, Biodegradable Polymers as Biomaterials. *Prog Polym Sci*, 32:762–98.
27. Zhang H, Huang H, Hao G, *et al.*, 2021, 3D Printing Hydrogel Scaffolds with Nanohydroxyapatite Gradient to Effectively Repair Osteochondral Defects in Rats. *Adv Funct Mater*, 31:2006697. https://doi.org/10.1002/adfm.202006697
28. Skardal A, Devarasetty M, Kang HW, *et al.*, 2016, Bioprinting Cellularized Constructs Using a Tissue-specific Hydrogel Bioink. *J Vis Exp*, 2016:e53606. https://doi.org/10.3791/53606
29. Markstedt K, Mantas A, Tournier I, *et al.*, 2015, 3D Bioprinting Human Chondrocytes with Nanocellulose-Alginate Bioink for Cartilage Tissue Engineering Applications. *Biomacromolecules*, 16:1489–96. https://doi.org/10.1021/acs.biomac.5b00188
30. Gruene M, Pflaum M, Hess C, *et al.*, Laser Printing of Three-Dimensional Multicellular Arrays for Studies of Cell-Cell and Cell-Environment Interactions. *Tissue Eng Part C Methods*, 17:973–82. https://doi.org/10.1089/ten.tec.2011.0185
31. Flores-Torres S, Peza-Chavez O, Kuasne H, *et al.*, 2021, Alginate-gelatin-Matrigel hydrogels enable the development and multigenerational passaging of patient-derived 3D bioprinted cancer spheroid models. *Biofabrication*, 13:025001 https://doi.org/10.1088/1758-5090/abdb87
32. Tirziu D, Giordano FJ, Simons M, 2010, Cell Communications in the Heart. *Circulation*, 122:928–37. https://doi.org/10.1161/circulationaha.108.847731
33. Bergmann O, Zdunek S, Felker A, *et al.*, 2015, Dynamics of Cell Generation and Turnover in the Human Heart. *Cell*, 161:1566–75.
34. Lee A, Hudson AR, Shiwarski DJ, *et al.*, 2019, 3D Bioprinting of Collagen to Rebuild Components of the Human Heart. *Science*, 365:482–7.
35. Hinton TJ, Jallerat Q, Palchesko RN, *et al.*, 2015, Three-Dimensional Printing of Complex Biological Structures by Freeform Reversible Embedding of Suspended Hydrogels. *Sci Adv*, 1:e1500758. https://doi.org/10.1126/sciadv.1500758
36. Noor N, Shapira A, Edri R, *et al.*, 2019, 3D Printing of Personalized Thick and Perfusable Cardiac Patches and Hearts. *Adv Sci*, 6:1900344. https://doi.org/10.1002/advs.201900344
37. Lee J, Sutani A, Kaneko R, *et al.*, 2020, *In Vitro* Generation of Functional Murine Heart Organoids via FGF4 and Extracellular Matrix. *Nat Commun*, 11:4283. https://doi.org/10.1038/s41467-020-18031-5
38. Drakhlis, L., Biswanath, S., Farr, CM. *et al*. Human heart-forming organoids recapitulate early heart and foregut development. *Nat Biotechnol* 39:737–746 (2021).
39. Kupfer ME, Lin WH, Ravikumar V, *et al.*, 2020, *In Situ* Expansion, Differentiation, and Electromechanical Coupling of Human Cardiac Muscle in a 3D Bioprinted, Chambered Organoid. *Circ Res*, 127:207–24. https://doi.org/10.1161/circresaha.119.316155
40. Nishinakamura R, 2019, Human Kidney Organoids: Progress and Remaining Challenges. *Nat Rev Nephrol*, 15:613–24. https://doi.org/10.1038/s41581-019-0176-x
41. Taguchi A, Kaku Y, Ohmori T, *et al.*, 2014, Redefining the *In Vivo* Origin of Metanephric Nephron Progenitors Enables Generation of Complex Kidney Structures from Pluripotent Stem Cells. *Cell Stem Cell*, 14:53–67. https://doi.org/10.1016/j.stem.2013.11.010

42. Takasato M, Er PX, Chiu HS, *et al.*, 2016, Kidney Organoids from Human iPS Cells Contain Multiple Lineages and Model Human Nephrogenesis. *Nature*, 536:238. https://doi.org/10.1038/nature17982
43. Homan KA, Kolesky DB, Skylar-Scott MA, *et al.*, 2016, Bioprinting of 3D Convoluted Renal Proximal Tubules on Perfusable Chips. *Scic Rep*, 6:34845. https://doi.org/10.1038/srep34845
44. King SM, Higgins JW, Nino CR, *et al.*, 2017, 3D Proximal Tubule Tissues Recapitulate Key Aspects of Renal Physiology to Enable Nephrotoxicity Testing. *Front Physiol*, 8:18. https://doi.org/10.3389/fphys.2017.00123
45. Lawlor KT, Vanslambrouck JM, Higgins JW, *et al.*, Cellular Extrusion Bioprinting Improves Kidney Organoid Reproducibility and Conformation. *Nat Mater*, 20:260–71. https://doi.org/10.3390/mi10100676
46. Deng J, Wei WB, Chen ZZ, *et al.*, 2019, Engineered Liver-On-A-Chip Platform to Mimic Liver Functions and Its Biomedical Applications: A Review. *Micromachines*, 10:26.
47. Huch M, Dorrell C, Boj SF, *et al.*, 2013, *In Vitro* Expansion of Single Lgr5(+) Liver Stem Cells Induced by Wnt-Driven Regeneration. *Nature*, 494:247–50. https://doi.org/10.1038/nature11826
48. Takebe T, Sekine K, Enomura M, *et al.*, 2013, Vascularized and Functional Human Liver from an iPSC-Derived Organ Bud Transplant. *Nature*, 499:481–4. https://doi.org/10.1038/nature12271
49. Tostões RM, Leite SB, Serra M, *et al.*, 2012, Human Liver Cell Spheroids in Extended Perfusion Bioreactor Culture for Repeated-Dose Drug Testing. *Hepatology*, 55:1227–36. https://doi.org/10.1002/hep.24760
50. Tobias G, Alicia R, Alexander T, *et al.*, 2018, Bioprinting Perfusion-Enabled Liver Equivalents for Advanced Organ-On-A-Chip Applications. *Genes*, 9:176.
51. Kang D, Hong G, An S, *et al.*, 2020, Bioprinting of Multiscaled Hepatic Lobules within a Highly Vascularized Construct. *Small*, 16:1905505. https://doi.org/10.1002/smll.201905505
52. Kaur S, Tripathi DM, Ghosh S, 2020, Three-Dimensional Bioprinted Hepatorganoids in Liver Failure. *Gut*, 70:998–9. https://doi.org/10.1136/gutjnl-2020-322317
53. Boj SF, Hwang CI, Baker LA, *et al*., 2015, Organoid Models of Human and Mouse Ductal Pancreatic Cancer. *Cell*, 160:324–38.
54. Chua CW, Shibata M, Lei M, *et al.*, 2014, Single Luminal Epithelial Progenitors Can Generate Prostate Organoids in Culture. *Nat Cell Biol*, 16:951. https://doi.org/10.1038/ncb3047
55. Linnemann JR, Miura H, Meixner LK, *et al.*, 2015, Quantification of Regenerative Potential in Primary Human Mammary Epithelial Cells. *Development*, 142:3239–51.
56. Sarvestani SK, Signs S, Hu B, *et al.*, 2021, Induced Organoids Derived from Patients with Ulcerative Colitis Recapitulate Colitic Reactivity. *Nat Commun*, 12:262. https://doi.org/10.1038/s41467-020-20351-5
57. Qu ML, Xiong L, Lyu YL, *et al.*, Establishment of Intestinal Organoid Cultures Modeling Injury-Associated Epithelial Regeneration. *Cell Res*, 31:259–71. https://doi.org/10.1038/s41422-020-00453-x
58. Curvello R, Kerr G, Micati DJ, *et al.*, 2021, Engineered Plant-Based Nanocellulose Hydrogel for Small Intestinal Organoid Growth. *Adv Sci*, 8:2002135. https://doi.org/10.1002/advs.202002135
59. Lukonin I, Serra D, Meylan LC, *et al.*, 2020, Phenotypic Landscape of Intestinal Organoid Regeneration. *Nature*, 586:275–80.
60. Kim WJ, Kim GH, 2020, An Intestinal Model with a Finger-Like Villus Structure Fabricated Using a Bioprinting Process and Collagen/SIS-Based Cell-Laden Bioink. *Theranostics*, 10:2495–508. https://doi.org/10.7150/thno.41225
61. Madden LR, Nguyen TV, Garcia-Mojica S, *et al.*, 2018, Bioprinted 3D Primary Human Intestinal Tissues Model Aspects of Native Physiology and ADME/Tox Functions. *Iscience*, 2:156–67. https://doi.org/10.1016/j.isci.2018.03.015
62. Huang L, Holtzinger A, Jagan I, *et al.*, 2015, Ductal Pancreatic Cancer Modeling and Drug Screening Using Human Pluripotent Stem Cell-and Patient-Derived Tumor Organoids. *Nat Med*, 21:1364–71. https://doi.org/10.1158/1538-7445.panca16-b45
63. Dominijanni A, Mazzocchi A, Shelkey E, *et al.*, 2020, Bioengineered Tumor Organoids. *Curr Opin Biomed Eng*, 13:168–73.
64. Ma L, Li Y, Wu Y, et al., 2020, The Construction of In Vitro Tumor Models Based on 3D Bioprinting. Biodes Manuf, 3:227–36.
65. Drost J, Karthaus W R, Gao D, *et al.*, Organoid Culture Systems for Prostate Epithelial and Cancer Tissue. *Nat Protoc*, 11:347–58. https://doi.org/10.1038/nprot.2016.006
66. Fujii M, Shimokawa M, Date S, *et al.*, 2016, A Colorectal Tumor Organoid Library Demonstrates Progressive Loss of Niche Factor Requirements during Tumorigenesis. *Cell Stem Cell*, 18:827–38.

https://doi.org/10.1016/j.stem.2016.04.003

67. Zhao Y, Yao R, Ouyang L, *et al.*, 2014, Three-Dimensional Printing of Hela Cells for Cervical Tumor Model *In Vitro*. *Biofabrication*, 6:035001. https://doi.org/10.1088/1758-5082/6/3/035001
68. Cao X, Ashfaq R, Cheng F, *et al.*, 2019, A Tumor-On-A-Chip System with Bioprinted Blood and Lymphatic Vessel Pair. *Adv Funct Mater*, 29:1807173. https://doi.org/10.1002/adfm.201807173
69. Yi HG, Jeong YH, Kim Y, *et al.*, A Bioprinted Human-Glioblastoma-On-A-Chip for the Identification of Patient-Specific Responses to Chemoradiotherapy. *Nat Biomed Eng*, 3:509–19. https://doi.org/10.1038/s41551-019-0363-x
70. Bonneh-Barkay D, Wiley CA, 2009, Brain Extracellular Matrix in Neurodegeneration. *Brain Pathol*, 19:573–85. https://doi.org/10.1111/j.1750-3639.2008.00195.x
71. Stiles J, Jernigan TL, 2010, The Basics of Brain Development. *Neuropsychol Rev*, 20:327–48.
72. Trevino AE, Sinnott-Armstrong N, Andersen J, *et al.*, 2020, Chromatin Accessibility Dynamics in a Model of Human Forebrain Development. *Science*, 367:eaay1645. https://doi.org/10.1126/science.aay1645
73. Li YC, Jodat YA, Samanipour R, et al., 2021, Toward a Neurospheroid Niche Model: Optimizing Embedded 3D Bioprinting for Fabrication of Neurospheroid Brain-Like Co-Culture Constructs. Biofabrication, 13:015014. https://doi.org/10.1088/1758-5090/abc1be
74. Willerth SM, 2018, Bioprinting Neural Tissues using Stem Cells as a Tool for Screening Drug Targets for Alzheimer's Disease. *J 3D Print Med*, 2:1–4.
75. Skylar-Scott M, Huang J, Lu A, *et al.*, 2020, An Orthogonal Differentiation Platform for Genomically Programming Stem Cells, Organoids, and Bioprinted Tissues, bioRxiv. https://doi.org/10.1101/2020.07.11.198671
76. Rothenbücher T, Gürbüz H, Emnéus J, *et al.*, 2021, Next Generation Human Brain Models: Engineered Flat Brain Organoids Featuring Gyrification. *Biofabrication*, 13:011001. https://doi.org/10.1088/1758-5090/abc95e
77. Abigail I, Stephen S, Connon CJ, 2018, 3D Bioprinting of a Corneal Stroma Equivalent. *Exp Eye Res*, 173:188–93. https://doi.org/10.1016/j.exer.2018.05.010
78. Kim J, Shim IK, Hwang DG, *et al.*, 2019, 3D Cell Printing of Islet-Laden Pancreatic Tissue-Derived Extracellular Matrix Bioink Constructs for Enhancing Pancreatic Functions. *J Mater Chem B*. 7:4592. https://doi.org/10.1039/c9tb90097g
79. Han Y, Yang L, Duan X, *et al.*, 2020, Identification of Candidate COVID-19 Therapeutics using hPSC-Derived Lung Organoids, bioRxiv.
80. Grigoryan B, Paulsen SJ, Corbett DC, *et al.*, 2019, Biomedicine Multivascular Networks and Functional Intravascular Topologies within Biocompatible Hydrogels. *Science*, 364:458–64.
81. Vichas A, Zallen JA, 2011, Translating Cell Polarity into Tissue Elongation. *Semin Cell Dev Biol*, 22:858–64. https://doi.org/10.1016/j.semcdb.2011.09.013
82. Davis GE, Cleaver OB, 2014, Outside in: Inversion of Cell Polarity Controls Epithelial Lumen Formation. *Dev Cell*, 31:140–2. https://doi.org/10.1016/j.devcel.2014.10.011
83. Reid JA, Mollica PM, Bruno RD, *et al.*, 2018, Consistent and Reproducible Cultures of Large-Scale 3D Mammary Epithelial Structures using an Accessible Bioprinting Platform. *Breast Cancer Res*, 20:122. https://doi.org/10.1186/s13058-018-1045-4
84. Kim E, Choi S, Kang B, *et al.*, 2020, Creation of Bladder Assembloids Mimicking Tissue Regeneration and Cancer. *Nature*, 588:664–9. https://doi.org/10.1038/s41586-020-3034-x
85. Fujii M, Matano M, Toshimitsu K, *et al.*, 2018, Human Intestinal Organoids Maintain Self-Renewal Capacity and Cellular Diversity in Niche-Inspired Culture Condition. *Cell Stem Cell*, 23:787–93. https://doi.org/10.1016/j.stem.2018.11.016
86. Hu H, Gehart H, Artegiani B, *et al.*, 2018, Long-Term Expansion of Functional Mouse and Human Hepatocytes as 3D Organoids. *Cell*, 175:1591–606.e19. https://doi.org/10.1016/j.cell.2018.11.013
87. Sato T, Vries RG, Snippert HJ, *et al.*, 2009, Single Lgr5 Stem Cells Build Crypt-Villus Structures *In Vitro* Without a Mesenchymal Niche. *Nature*, 459:262–5. https://doi.org/10.1038/nature07935
88. Sato T, Stange DE, Ferrante M, *et al.*, 2011, Long-Term Expansion of Epithelial Organoids From Human Colon, Adenoma, Adenocarcinoma, and Barrett's Epithelium. *Gastroenterology*, 141:1762–72. https://doi.org/10.1053/j.gastro.2011.07.050
89. Wilson WC, Boland T, 2003, Cell and Organ Printing 1: Protein and Cell Printers. *Anat Rec A Discov Mol Cell Evol Biol*, 272A:491–6. https://doi.org/10.1002/ar.a.10057
90. Rawal P, Tripathi DM, Ramakrishna S, et al., Prospects for 3D Bioprinting of Organoids. Biodes Manuf, 4:627–40.

https://doi.org/10.1007/s42242-020-00124-1

91. Yap KK, Gerrand YW, Dingle AM, *et al.*, 2020, Liver Sinusoidal Endothelial Cells Promote the Differentiation and Survival of Mouse Vascularised Hepatobiliary Organoids. *Biomaterials*, 251:120091. https://doi.org/10.1016/j.biomaterials.2020.120091
92. Silvestri V L, Henriet E, Linville R M*, et al.*, 2020, A Tissue-Engineered 3D Microvessel Model Reveals the Dynamics of Mosaic Vessel Formation in Breast Cancer. *Cancer Res*, 80:4288–301. https://doi.org/10.1158/0008-5472.can-19-1564
93. Markou M, Kouroupis D, Badounas F, *et al.*, 2020, Tissue Engineering Using Vascular Organoids From Human Pluripotent Stem Cell Derived Mural Cell Phenotypes. *Front Bioeng Biotechnol*, 8:278. https://doi.org/10.3389/fbioe.2020.00278
94. Song KH, Highley CB, Rouff A, *et al.*, 2018, Complex 3D-Printed Microchannels within Cell-Degradable Hydrogels. *Adv Funct Mater*, 28:1801331. https://doi.org/10.1002/adfm.201801331
95. Humphreys BD, 2021, Bioprinting Better Kidney Organoids. *Nat Mater*, 20:128–30.

REVIEW ARTICLE

3D Bioprinting Photo-Crosslinkable Hydrogels for Bone and Cartilage Repair

Quanjing Mei[1,†], Jingdong Rao[1,†], Ho Pan Bei[1], Yaxiong Liu[2], Xin Zhao[1*]

[1]Department of Biomedical Engineering, The Hong Kong Polytechnic University, Hung Hom, Hong Kong, China
[2]Jihua Laboratory, Foshan, Guangdong, China
[†]*These authors contributed equally to this work*

Abstract: Three-dimensional (3D) bioprinting has become a promising strategy for bone manufacturing, with excellent control over geometry and microarchitectures of the scaffolds. The bioprinting ink for bone and cartilage engineering has thus become the key to developing 3D constructs for bone and cartilage defect repair. Maintaining the balance of cellular viability, drugs or cytokines' function, and mechanical integrity is critical for constructing 3D bone and/or cartilage scaffolds. Photo-crosslinkable hydrogel is one of the most promising materials in tissue engineering; it can respond to light and induce structural or morphological transition. The biocompatibility, easy fabrication, as well as controllable mechanical and degradation properties of photo-crosslinkable hydrogel can meet various requirements of the bone and cartilage scaffolds, which enable it to serve as an effective bio-ink for 3D bioprinting. Here, in this review, we first introduce commonly used photo-crosslinkable hydrogel materials and additives (such as nanomaterials, functional cells, and drugs/cytokine), and then discuss the applications of the 3D bioprinted photo-crosslinkable hydrogel scaffolds for bone and cartilage engineering. Finally, we conclude the review with future perspectives about the development of 3D bioprinting photo-crosslinkable hydrogels in bone and cartilage engineering.

Keywords: Bone and cartilage engineering; Hydrogel; Photo-crosslinking; Three-dimensional printing

*Correpondence to: Xin Zhao, Department of Biomedical Engineering, The Hong Kong Polytechnic University, Hung Hom, Hong Kong, China; xin.zhao@polyu.edu.hk

Received: April 1, 2021; **Accepted:** May 31, 2021; **Published Online:** June 24, 2021

(This Article Belongs To The *Special Section: Bioprinting of 3D Functional Tissue Constructs*)

Citation: Mei Q, Rao J, Bei HP, Liu X, Zhao X, *et al.*, 2021, 3D Bioprinting Photo-crosslinkable Hydrogels for Bone and Cartilage Repair. *Int J Bioprint*, 7(3):367. http://doi.org/10.18063/ijb.v7i3.367

1. Introduction

The incidence of skeletal disorders involving both bone and cartilage caused by trauma, injuries, and dysfunction has significantly increased in recent decades, creating a demand for more effective treatment[1]. Despite decades of study, the treatments for large bone and cartilage defects remain a significant clinical problem[2]. Although traditional methods such as autografts, allografts and xenografts have been developed for repairing these defects, they all suffer corresponding restrictions, including limited supply, insufficient function, and immune response[3]. Hence, synthetic biomaterials are developed as alternatives; however, they often fail to be properly integrated into the recipient sites due to the lack of native tissue-mimicking structure and the inability to establish a three-dimensional (3D) niche for different cell types (osteoblasts, osteoclasts, and endothelial cells [EC])[4]. Bone and cartilage are highly complex anisotropic tissues with distinctive structures, various compositions, and excellent mechanical properties. The repair of bone and cartilage involves cell migration, extracellular matrix (ECM) remodeling, and tissue regeneration, of which both functional details and structures should be carefully considered when developing bone and cartilage constructs[5].

3D bioprinting, which not only provides adjustable 3D organizational structures but also encapsulates cells and growth factors, brings forth a new strategy to design biomimetic scaffolds for bone and

© 2021 Mei, *et al*. This is an Open Access article distributed under the terms of the Creative Commons Attribution License (https://creativecommons. org/licenses/by/4.0/), permitting distribution and reproduction in any medium, provided the original work is cited.

cartilage repair[6]. 3D bioprinting can be considered an additive manufacturing technique where biomaterials, cells and growth factors, often referred to as "bio-ink," are printed to create tissue-like structures that imitate natural tissues[7]. It has been applied in bone and cartilage tissue engineering as it can precisely fabricate the 3D scaffolds by controlling the pore size, porosity, and interconnectivity[8,9]. To date, there are four leading 3D printing technologies: Inkjet-based bioprinting, extrusion-based bioprinting, laser-assisted bioprinting, and stereolithography (SLA) bioprinting. In extrusion-based bioprinting, bio-inks are extruded as filaments and undergo fast crosslinking to maintain the desired shape and structure. Laser-assisted bioprinters use a laser pulse to produce a cell suspended bio-ink and deposit it into the substrate in an orderly manner. In inkjet-based bioprinting, a certain volume of bio-inks was injected onto a substrate to form a precise pattern with either thermal or piezoelectric energy. In SLA bioprinting, a digital projector is used to selectively crosslink bio-ink plane-by-plane into desired shapes. The four primary bioprinting techniques each have specific strengths, weaknesses, and limitations. Although no single bioprinting technology can achieve the complete replication of complexities of various tissues, extrusion and SLA bioprinting are commonly used for preparing bone and cartilage scaffolds due to their good biocompatibility and easy combination of multiple crosslinking mechanisms[4,10].

One of the key elements for 3D bioprinting is the bio-ink. Unlike conventional 3D printing process in which inks can be printed in melt form at high temperature (ceramics and alloys) or as a polymer solution dissolved in organic solvents, elevated temperature or organic solvents are unfortunately not cytocompatible with depositing living cells and growth factors in a 3D bioprinting process. Hydrogels, which can provide nutritious environments suitable for cell survival, proliferation, and differentiation, have unique advantages in 3D printing living cells and/or growth factors. In general, click chemistry, enzymatic reactions, Schiff's base reaction, and photo-polymerization can be used to crosslink hydrogels. In this review, we would like to focus on photo-crosslinking due to its rapid *in situ* gelling, good cytocompatibility and low toxicity[11,12]. Besides, the crosslinking density and physicochemical properties of photo-crosslinkable hydrogel could be precisely controlled through adjusting the intensity of light and exposure time to promote cell proliferation and differentiation[12,13]. For example, by controlling crosslinking density of the photo-crosslinkable hydrogel, Li *et al*. regulated the morphology of chondrocytes in 3D gelatin methacrylate (GelMA) environment. Cells exhibited round shape in hard hydrogel with stiffness at ~30 kPa; elongated shape in soft hydrogel (~4 kPa) and chondrogenic phenotype in hydrogels with medium stiffness (~17 kPa)[14]. Cell proliferation could also be influenced by cross-linking density. In one study, Bryant *et al*. found that the increase in crosslinking density of poly(ethylene glycol) diacrylate (PEGDA) hydrogel resulted in a decrease of chondrocytes proliferation and protein expression; in another study, Marklein *et al*. discovered that human mesenchymal stem cells (hMSCs) exhibited increased cell proliferation on a stiff hyaluronic acid methacrylate (HAMA) hydrogel compared to a softer one in 2D condition[15,16]. In terms of cell differentiation, Bian *et al*. investigated the effect of crosslinking density of photo-crosslinkable hydrogels on encapsulated mesenchymal stem cells (MSCs)[17]. They found that the degree of photo-crosslinking can regulate the differentiation of MSCs: Enhanced chondrogenesis in a soft environment and osteogenesis in a stiff environment, which provides important clues for the design of photo-crosslinking hydrogels for cartilage and bone repair. Due to these unique features, photo-crosslinkable hydrogels have shown a wide range of applications in biomedical fields including organ printing, tissue engineering, disease modeling, and high-throughput drug screening[18].

In this review, we summarize the classification, crosslinking mechanism and application of photo-crosslinkable hydrogels for 3D bone and cartilage bioprinting (**Figure 1**). The cell types and additives encapsulated in hydrogels to promote bone and cartilage reconstruction are additionally discussed. Finally, the future prospects of bone and cartilage 3D bioprinting are outlined.

2. Photo-crosslinkable hydrogel bio-ink systems

In this section, we focus on photo-crosslinkable hydrogels, and introduce additives (such as nanomaterials, functional cells, and drugs or cytokines) which can improve the physical and biological properties of hydrogels.

2.1. Photo-crosslinkable hydrogels

For photo-crosslinkable materials, when they are exposed to a suitable light, the liquid state solution can be solidified. In general, photo-polymerization includes free-radical initiated chain polymerization and bio-orthogonal click reaction. In free radical photo-polymerization, the functionalization of hydrogel prepolymers with active groups (such as methacrylates, vinyl esters, and acrylates) is an essential step. Under light irradiation, the absorbed photons of photoinitiator promote its cleavage, thereby encouraging the generation of free-radical molecules. Then, these molecules will react with the vinyl bonds, leading to the formation of chemical crosslinks between prepolymers[19]. In photo-click reaction, the thiol-ene

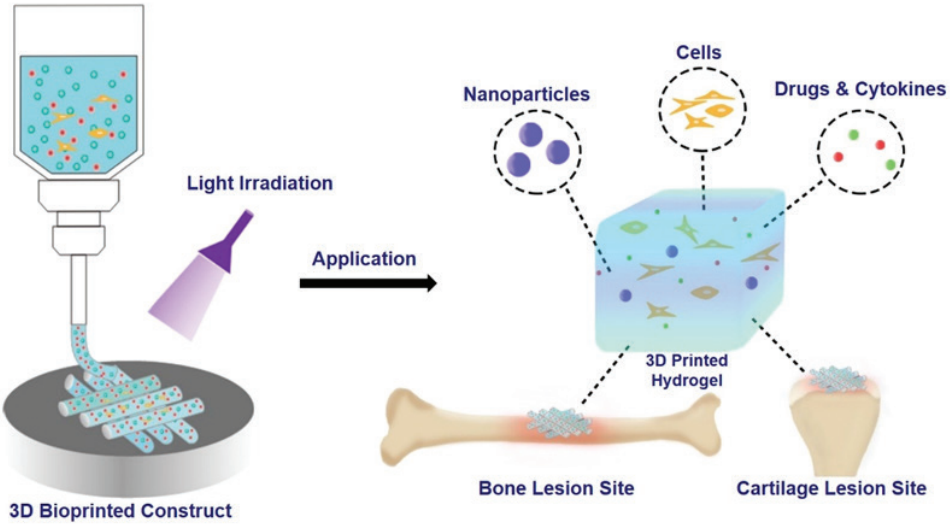


Figure 1. Schematic illustration of photo-crosslinkable hydrogels for bioprinting bone and cartilage tissues.

reaction is widely used in hydrogel fabrication, where the addition of thiols to carbon-carbon double bonds contributes to polymerization[20]. Derived from natural or synthetic polymers, several hydrogel materials undergoing photo-polymerization have been explored. These materials contain various functional groups, which enable different functionalization strategies for photo-crosslinking.

Hyaluronic acid (HA) is a linear glycosaminoglycan[21]. As one of the main components of ECM and important glycosaminoglycan in connective tissues, HA plays a key role in rheological and structural function[22]. Furthermore, due to the interactions between certain cell receptors, HA can regulate cell proliferation, migration and differentiation[23]. Due to many abundant functional groups in its chemical structure such as N-acetyl group, carboxylic acid, and primary/secondary hydroxyl groups, photo-polymerizable groups such as methacrylates and norbornenes can be modified on HA[24,25]. The most popular chemical modification for HA is using methacrylic anhydride (MA), which can be introduced into carboxy or hydroxy groups of HA in mild conditions (referred to as HAMA). The properties of HAMA can be regulated by tuning the polysaccharide derivatization degree and the concentration of pre-polymer or illumination time[26]. For example, the elastic modulus of HAMA hydrogel can be enhanced when increasing the polymer concentration. Furthermore, varying the polymer concentration can also regulate the degradation rate of HAMA hydrogel, where the high degradability is essential for cell remodeling in 3D tissue applications[27].

Gelatin is an FDA-approved food processing material comprising a mixture of peptide sequences (arginine-glycine-aspartic acid) that enhance cell attachment[28]. As one of the popular substrates of hydrogels, gelatin has strong biocompatibility and low antigenicity[29]. Meanwhile, it can be easily obtained by denaturing collagen through acid or base treatment[21]. However, gelatin is a thermo-responsive and water-soluble material which can undergo a reversible sol-gel transition below body temperature[30]. To prevent the degradation of gelatin, forming chemical crosslinks by photo-polymerization is an effective method, which is usually achieved through modifying primary amines with ethylenic/thiol groups or methacrylate groups. The norbornene/thiol-functionalized gelatin can form crosslinked hydrogels through photo-click reaction, and by controlling the concentration of thiol/ene substitution, crosslinking degree of hydrogels can be tuned[31]. Meanwhile, functionalization with MA is also an ideal way to counteract its fast degradation and poor mechanical property[32]. Similar to HAMA hydrogel, by controlling the amount of MA and degrees of methylation, the hydrogels (referred to as GelMA) will possess different mechanical properties. Besides, increasing the degrees of methacrylation can enhance the matrix density, thereby increasing the compressive modulus and reducing the degradation rate of GelMA[6,33]. Furthermore, the elastic modulus and adhesive strength of GelMA can be controlled by regulating the polymer concentration[12,34,35].

Chitosan (CS) is derived from chitin, which can be obtained from the exoskeleton of insects and crustaceans as well as the cell walls of fungi[36]. As a natural material, CS has good biodegradability, and it can stop bleeding and promote tissue regeneration, thus having wide usage in wound healing and scar prevention[37]. Due to active amino and hydroxyl groups in CS, there are many opportunities to introduce photoactive groups into CS through the chemical reactions between -NH_2/-OH and

substituting groups, such as azido-functionalized CS, vinylated CS, and MA-CS[38]. However, this mechanical strength of azido or vinylated-functionalized hydrogel is relatively low, and the insufficient biocompatibility limits further applications. At present, the most common method for preparing photo-crosslinkable CS is by grafting MA groups to provide good mechanical properties as well as suitable biocompatibility[39].

Polyethylene glycol (PEG) has high hydrophilicity with abundant functional groups for chemical modification and adjustable properties, which is widely used in various biomedical applications. PEG hydrogel formed by photo-click reaction is one of the common methods to achieve photo-polymerization. The biophysical or biochemical properties in the thiol-ene PEG hydrogel can be tuned with the degree of substitution[40]. Meanwhile, PEGDA, PEG dimethacrylate (PEGDMA), and ethylene linkage multi-arm PEG (n-PEG) are the most commonly used macromolecules in photo-polymerization and of which, PEGDA is very popular in terms of bioprinting. Under ultraviolet (UV) or visible light exposure, the double-bond acrylate groups in PEGDA can initiate rapid photo-polymerization to form a 3D polymer network and in the presence of a photoinitiator[41], and the mechanical strength can be controlled by changing the molecular weight or the concentration of the hydrogel[42].

2.2. Control of photo-crosslinkable structures with various parameters

The integrity of photo-crosslinkable scaffolds is determined by both the strength of the individual polymer chain as well as the density of crosslinking networks within the hydrogel matrix. Naturally, high molecular weight hydrogels possess higher matrix stiffness due to the larger proportion of less bendable polymer backbones compared with the more flexible connective ends between polymer chains. The increase in polymer concentration naturally enhances matrix strength as the density of inter-linkage between polymer chains increase. Yet increase in hydrogel concentration in aqueous solutions often exhibits high viscosity, which impedes the extrusion process due to the shear stress. Alternatively, the density of crosslinks can be chemically modified through the degree of substitution, which is the ratio of substituent group to unmodified group in a photopolymer. A high degree of substitution greatly increases the chance of successful crosslinks throughout the hydrogel matrix without actual addition of polymer chains, and contributes toward increased complexity of the polymer network as well as improved stiffness and lowered porosity of printed structures[43].

By modulating the light intensity and exposure time, photo-polymerization controls the formation process of the hydrogel and its properties, including the crosslinking density and matrix stiffness[12]. This can be attributed to energy-dependent regulation of photoinitiator activation and crosslinker reactivity[44]. While the presence of photoinitiators can greatly lower the energy barrier for initiating the often-simple click-reactions of crosslinking groups such as acrylates, under appropriate photo-crosslinking conditions, sufficient photonic energy is required to complete the photo-crosslinking process, whereas by intentionally limiting light exposure intensity and duration, partially crosslinked matrixes are formed with reduced stiffness and strength to mimic softer tissues. This creates a two-way array to regulate the mechanical features of photo-crosslinkable hydrogels entirely from tuning the light source alone. To achieve complete crosslinking, light intensity and exposure time are interdependent as the amount to the total energy supplied to the reaction between polymer chains and crosslinkers. Herein, a high intensity enables low exposure time, and vice versa. This creates an interesting dynamic between these two parameters when applied in photo-bioprinting as vigorous limitations exist in terms of biocompatibility in additive manufacturing[45]. In addition, cells are highly sensitive to external changes in the microenvironment including shear, heat, and radiation. As radioactive damage and heat generated by light sources such as lasers are unavoidable when crosslinking cell-embedded hydrogels, a balance of intensity and exposure is required to preserve cell viability of printed structures. For example, alginate/GelMA bio-inks can be crosslinked at as low as 4 mW cm^{-2} with UV light source to ensure 80% survival of cells in printed scaffolds, spanning over 20 – 60 kPa modulus under various UV exposure[46]. Yet the same approach faces difficulties in SLA, where light intensity decays as it goes through the medium in which it is absorbed in accordance with the Beer–Lambert equation. This creates dilemma where light intensity cannot be maintained in deeper areas of the hydrogel matrix to surmount the energy barrier required to achieve photo-crosslinking. In addition, a decrease in intensity impedes resolution as it increases diffraction of light, which greatly limits the fidelity of printed structures in reservoir-based printing. Hence, to elucidate the effects on light intensity, exposure time, and cell density, the previous studies have created GelMA-printed model phase diagram between 7 – 16 mW/cm^2 and 15 – 45 s, where areas for underexposure and overexposure were plotted[47]. With the advancement in neural network technology, machine learning has also been used to predict cell viability in SLA bioprinting, with exceptional accuracies in predictions at as low as 10% of total data supplied[48]. The learning algorithm concluded that exposure time had the greatest effect on cell viability, followed by layer thickness, GelMA concentration, and light intensity. Thus, the adjustment of light source alone in terms of intensity and exposure time

has high controllability as well as predictability in tuning mechanical properties and maintaining cell viability.

2.3. Additives in photo-crosslinkable hydrogel systems

To fabricate functional hydrogel platforms, many additives such as nanomaterials, functional cells, drugs, and/or cytokine are introduced into the hydrogel systems, bestowing on those hydrogels improved physical and biological properties.

(1) Nanomaterials

The majority of human bone tissues range from cancellous to cortical structures. It is difficult to design an ideal scaffold by a single pure hydrogel material due to the diversity in geometric mechanics and mechanical strength of bone tissues. Herein, nanomaterials can be integrated into hydrogels with multiple gradients and good mechanical properties, which may help solve this challenge. Nanomaterials can control the micro- and nano-scale structures of hydrogel as well as regulate hydrogels' mechanical properties without hindering the exchange of nutrients with the surrounding environment[49]. Meanwhile, the nanomaterial itself can also work as a drug delivery system.

For example, Zuo *et al*. combined GelMA with hydroxyapatite (Hap) for osteon biofabrication[50]. As the main inorganic composite material of bone matrix, Hap can guide and induce bone formation. Furthermore, the introduction of Hap into GelMA network could enhance the mechanical rigidity. The results demonstrated that compared to the pure hydrogel, this composite hydrogel showed a lower swelling behavior, higher mechanical modulus, and better biocompatibility, which had a prospective application for bone reconstruction. In another example, Zhang *et al*. prepared a self-assembled metallic-ion nanocomposite hydrogel[49]. This hydrogel consisted of bisphosphonate-grafted HA (HABP) and magnesium chloride ($MgCl_2$). The coordination between BP and magnesium ions (Mg^{2+}) contributed to the formation of acrylated-BP-Mg-nanoparticles (Ac-BP-Mg NPs), which would stabilize the hydrogel network as multi-valent crosslinker, increasing the mechanical properties and contributing to the injectability as well as self-healing characteristics. The acrylate groups could be crosslinked under UV irradiation, and allowed for better control over stiffness. This nanocomposite hydrogel allowed for encapsulation of stem cells, which could be used for bone engineering. In a study of Shi *et al*., the authors fabricated a rapidly photo-crosslinkable hydrogel with Kartogenin (KGN)-loaded nanoparticles to prepare cartilage[51]. The small molecule KGN (which could induce bone marrow-derived MSCs [BMSCs]) into chondrocytes) was encapsulated into poly (lactic-co-glycolic acid) (PLGA) nanoparticles. Then, the KGN-PLGA were incorporated into photo-crosslinkable acrylated HA (m-HA), and this system could form a hydrogel scaffold *in situ* under UV light treatment. *In vivo* experiments demonstrated that the regenerated tissue was close to the natural hyaline cartilage.

(2) Cells

For bone engineering, BMSCs are the most widely used cells since it possesses the ability to differentiate into functional bone cells[52]. Meanwhile, articular cartilage-resident chondroprogenitor cells (ACPCs) represent an opportunity for cartilage regeneration[53]. In addition, some bone cells such as osteoblasts and chondrocytes have also been introduced into hydrogels[54], while other cells associated with bone growth such as human umbilical vein EC (HUVECs) provide abundant opportunities for bone tissue repair[55]. Vascularization is also essential for bone regeneration process especially for large bone defects. ECs are the main cells with angiogenic ability. Three types of ECs, HUVECs, human dermal microvascular EC (HDMVECs), and endothelial progenitor cells (EPC), have been reported to create vessel-like structures in *in vitro* culture[56]. Incorporating ECs in the hydrogel scaffolds could induce the regeneration of new blood vessels by creating capillary networks. These prevascularized constructs could provide nutrients to surrounding cells and reduce the time to anastomose with host vasculature, which would promote angiogenesis and osteogenesis for bone regeneration[57]. To fabricate a suitable microenvironment, photo-polymerized hydrogels can be used for cell transplantation, where the hydrogel materials provide a cell-favorable environment which allows for diffusion of nutrients, oxygen, and metabolic products.

For example, in a study of Zhai *et al*., the authors developed a biodegradable two-channel 3D bioprinting ink consisting of both PEGDA and Laponite nanoclay in channel A, and rat osteoblasts (ROBs)-laden HA in channel B[58]. The bio-ink A, composed of a PEG-clay nanocomposite crosslinked hydrogel, was used to prepare 3D-bioprinting and effectively deliver oxygen and nutrients to cells. Meanwhile, it could promote osteogenesis due to the released silicon ions (Si^{4+}) and Mg^{2+}, while the bio-ink B, ROBs-ladened HA, was adopted to improve distribution uniformity, deposition efficiency and cell viability. The two inks were alternately extruded through a two-channel 3D-bioprinting machine to construct osteoblast-laden nanocomposite hydrogel for bone regeneration. The printed scaffolds showed excellent osteogenic potential in *in vivo* experiments. In another study, Annika *et al.* co-encapsulated EC (HDMVECs) and osteogenic cells (human adipose-derived stem cells) in GelMA hydrogel for engineering vascularized bone. Results showed that this co-culture system could promote

the formation of vascular networks and enhance bone regeneration[59].

(3) Drugs and cytokines

Some drugs or cytokines play a key role in promoting bone cell growth, modulating cell proliferation, and differentiation as well as regulating the formation of ECM. Statins[55], osteoprotegerin[60], αvβ3 integrin antagonists[61], cathepsin K inhibitors[62], parathyroid hormone[63], transforming growth factor-β, and bone morphogenetic protein (BMP)[64] have all been considered for stimulation of bone growth. Apart from drugs and cytokines for bone formation, angiogenic growth factors, vascular endothelial growth factors (VEGF), fibroblast growth factor, hepatocyte growth factor, and platelet-derived growth factor have been used for the modulation of vessel formation[65,66]. For delivering drugs or therapeutic agents to bone sites, various approaches have been investigated, such as nanoparticles, nanofibers, and films. Among them, hydrogel attracts much attention owing to its compatibility and hydrophilicity, and it can regulate release performance by controlling swelling or degradation[67]. Photo-polymerized hydrogels have also been used for localized drug delivery depots due to the *in situ* formation of hydrogels and the direct adhesion to the targeted tissue. As a bulk reservoir, hydrogels allow for encapsulation of cells, drugs or nanoparticles, and provide physical support at bone lesion site.

In a report by Kim *et al*., they fabricated PEGDA/chondroitin sulfate-based hydrogels and studied them as biomineralizing 3D scaffolds[68]. Chondroitin sulfate has negative charge on its sulfate group, so it binds with charged ions such as calcium and phosphate to form an osteogenically favorable microenvironment, which will induce the biomineralization and osteogenic differentiation of stem cells. The results proved that the ion binding and distribution in hydrogel were related to the concentration of chondroitin sulfate, and PEGDA/chondroitin sulfate-based hydrogels induced osteogenic differentiation of stem cells *in vitro*. After transplanting this hydrogel into a critically sized cranial defect model, 10% chondroitin sulfate hydrogel induced effective bone regeneration with the highest bone density.

In another study, Xin *et al*. prepared recombinant human BMP-2 (rhBMP-2)-laden GelMA hydrogel to accelerate bone repair[69]. rhBMP-2 can localize BMSCs to the site of bone injury, promoting proliferation, and osteogenic differentiation. Mesoporous bioglass nanoparticles (MBGNs) were used to load rhBMP-2 by grafting, and then it would photo-crosslink with GelMA hydrogel (GelMA/MBGNs-rhBMP-2), where rhBMP-2 could be controllably released at an early stage of bone regeneration, and calcium/silicon ions in MBGNs would be released to keep promoting osteogenesis in a long term. Incorporation of MBGNs-rhBMP-2 in GelMA hydrogel could better control the release rate as well as local concentration of rhBMP-2, while the MBGNs could be fixed at the lesion site without clearance by body fluids. This hydrogel showed strong ability in osteogenesis and bone tissue regeneration *in vivo*.

In summary, photo-crosslinkable hydrogels have incorporated nanomaterial components, cells, drugs, and/or cytokines to produce viable bone tissue scaffolds. With the improved physical and biological properties, it is of great significance to apply them in 3D printing technology to broaden its application.

4. Applications of 3D bioprinted photo-crosslinkable hydrogels for bone and cartilage regeneration

Over the last decade, there has been immense progress in 3D bioprinting skeletal systems using photo-crosslinkable hydrogels. In this part, we review the applications of 3D bioprinted photo-crosslinkable hydrogels for bone and cartilage tissue engineering.

4.1. Bioprinted hydrogels in bone tissue engineering

Bone has a highly specialized structure with a mineral matrix, multiple cells, and vascular networks. Reconstruction of large-scale bone defects remains challenging due to the lack of biomimetic architectural, bioactive factors, and functional vasculature. With the advance of 3D bioprinting, more complicated bionic 3D constructs could be bioprinted, with different cell types and growth factors with hydrogel for better bone regeneration to imitate the hierarchical structure and function of natural bone. Cui *et al*. developed a mimetic bone structure, with a hard mineral matrix, a soft organic matrix and vascularized networks (**Figure 2A**)[70]. The structure was constructed through a dual 3D bioprinter including a Fused Deposition Modeling (FDM) and SLA 3D bioprinter, by alternately depositing cell-loaded GelMA hydrogel (hMSCs and HUVECs), and biodegradable polylactide (PLA) (**Figure 2Ai**). This capillary structure allows cells to evolve and expand uniformly in the 3D space during culture period (**Figure 2Aii**). Moreover, bioactive growth factors such as BMP-2 and VEGF peptides were added into the scaffold designs to further facilitate osteogenesis and angiogenesis. Results indicated that the 3D printed biomimetic bone constructs could integrate with surrounding native bone tissue, showing an excellent bone regeneration and significant angiogenesis ability. This study also provides a feasible strategy for the construction of a hierarchical structure with multiple functions, thereby meeting the current challenges for large bone repair.

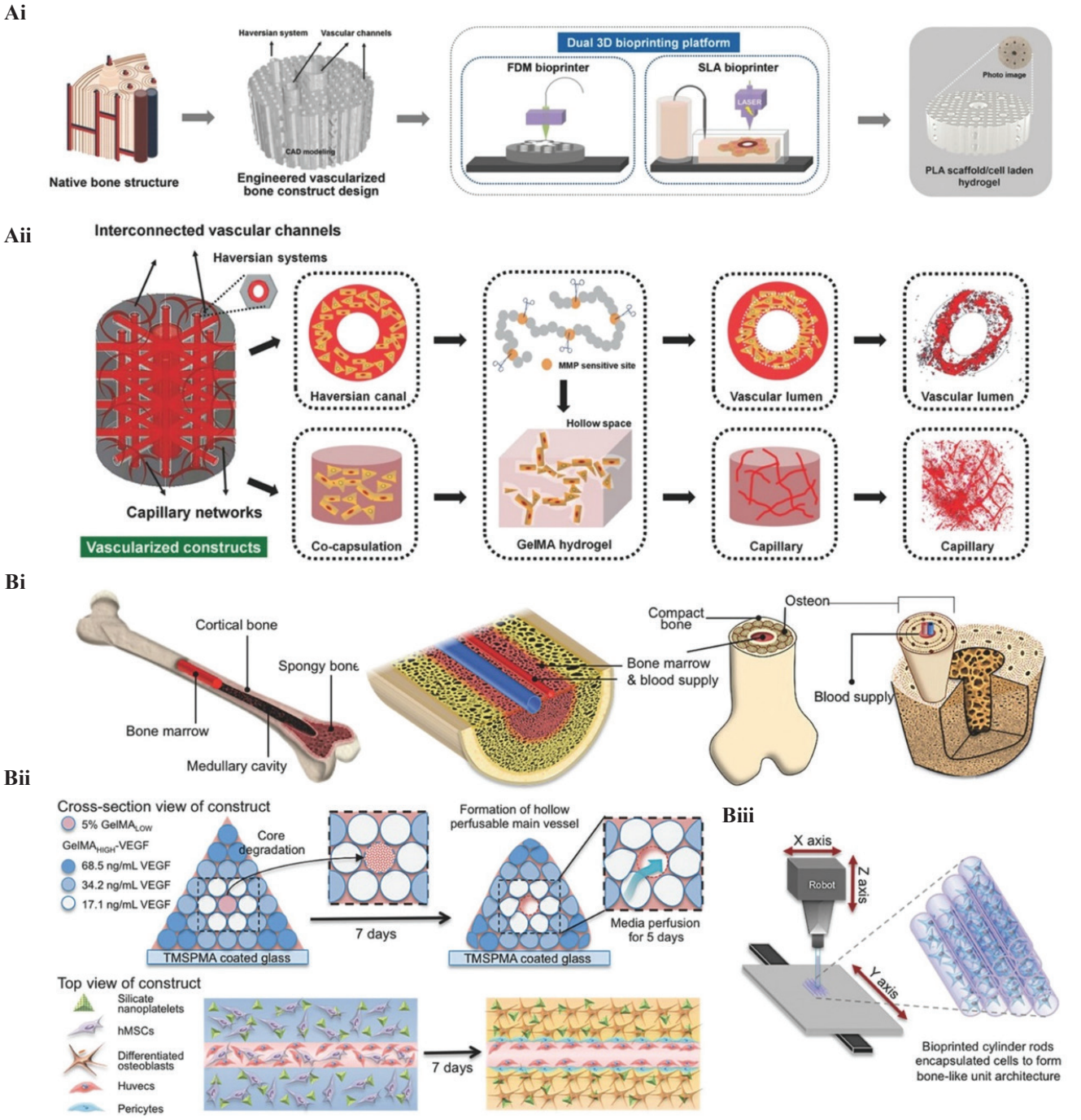


Figure 2. Construction of 3D mimetic bone tissue by 3D bioprinting. (Ai) Schematic diagram of the structure of a native bone; design and fabrication of the engineered vascularized bone structure. (Aii) Schematic diagram of the microstructure of vascularized construct based on matrix metalloproteinase (MMP)-sensitive GelMA hydrogel, the formation of vascular lumen, and capillary network in different regions[70]. (Reproduced from H. Cui, W. Zhu, M. Nowicki, *et al.,* Hierarchical Fabrication of Engineered Vascularized Bone Biphasic Constructs Via Dual 3D Bioprinting: Integrating Regional Bioactive Factors Into Architectural Design, Wiley. © 2016 WILEY-VCH Verlag GmbH Co. KgaA Weinheim). (Bi) Schematic diagram of a complex bone structure. (Bii) Schematic diagram of the fabrication process of complex bone construct through 3D bioprinting strategy. (Biii) Illustration of bioprinted cell-laden hydrogel cylinders through an SLA bioprinter[6]. (Reproduced from B. Byambaa, N. Annabi, K. Yue, *et al.,* Bioprinted Osteogenic and Vasculogenic Patterns for Engineering 3D Bone Tissue Wiley. © 2017 WILEY-VCH Verlag GmbH Co. KGaA, Weinheim).

To address the challenges of large-scale bone tissue with a 3D vascularization network, Khademhosseini *et al*. fabricated a biomimetic bone tissue construct comprised of a perfusable vascular lumen through an extrusion-

based bioprinting strategy (**Figure 2B**)[6]. First, they used bioprinting technology to imitate the overall structure of native bone tissue (**Figure 2 Bi**). Then, the GelMA hydrogel cylinders were individually printed (**Figure 2Bii**). After piling up these cylinders, pyramidal constructs were formed (**Figure 2Biii**). They also encapsulate angiogenic cells, and osteogenic cells and silicate nanoplatelets into the GelMA hydrogel simultaneously to promote bone regeneration ability. Through optimization of bioprinting conditions, they could print a well-defined, multicellular bone tissue construct in a large scale. Results indicated that the biomimetic bone construct has high structural stability and promotes cell proliferation during *in vitro* culture. Immunostaining and reverse transcription quantitative polymerase chain reaction (RT-qPCR) proved the formation of new bone tissue in the HUVEC/hMSC group after *in vitro* culture. Demonstrably, this study provides a superior strategy for the construction of large biomimetic bone-like structures with vasculature meeting the clinical demands of large-scale bone defects.

4.2. Bioprinted hydrogels in cartilage tissue engineering

Natural cartilage is a smooth and elastic tissue with poor self-repair ability. Usually, super-physiological shock load and osteoarthritis result in cartilage defects. The regeneration of cartilage is limited by its low number of cells[71]. The difficulties of fabricating artificial cartilaginous tissue can be solved by bioprinting because this printing technique allows for encapsulation of implanting cells. Meanwhile, the hydrogel has a striking similarity to the ECM of natural cartilage[72]. Thus, 3D bioprinted hydrogels become a potential alternative therapy for cartilage repair. Duchi *et al*. developed a hand-held extrusion-based bioprinter for 3D bioprinting cartilage (**Figure 3A**). They printed a core-shell structure with a cell-free but photo-crosslinkable hydrogel shell and a cell-loaded core hydrogel[73]. The printed structure was cross-linked by UV light for 10 s for photo-polymerization and the viability of cell remained above 90% after 7 days of printing. This study served as a proof-of-concept for the *in situ* cartilage bioprinting and cartilage regeneration. In another study, Burdick *et al*. proposed an *in situ* crosslinking method for 3D bioprinting photo-crosslinkable hydrogel (**Figure 3Bi**)[74]. They further used a norbornene-modified HA (NorHA) as a representative bio-ink for cartilage regeneration. By adjusting the printing parameters (i.e. light intensity, exposure time, and printing speed), they obtained an optimal curing condition. The whole bioprinting process was cytocompatible. Post-printed MSCs distributed homogenously in the printed construct with high cell viability. After 56 days of culture *in vitro*, the bioprinted cartilage constructs showed an

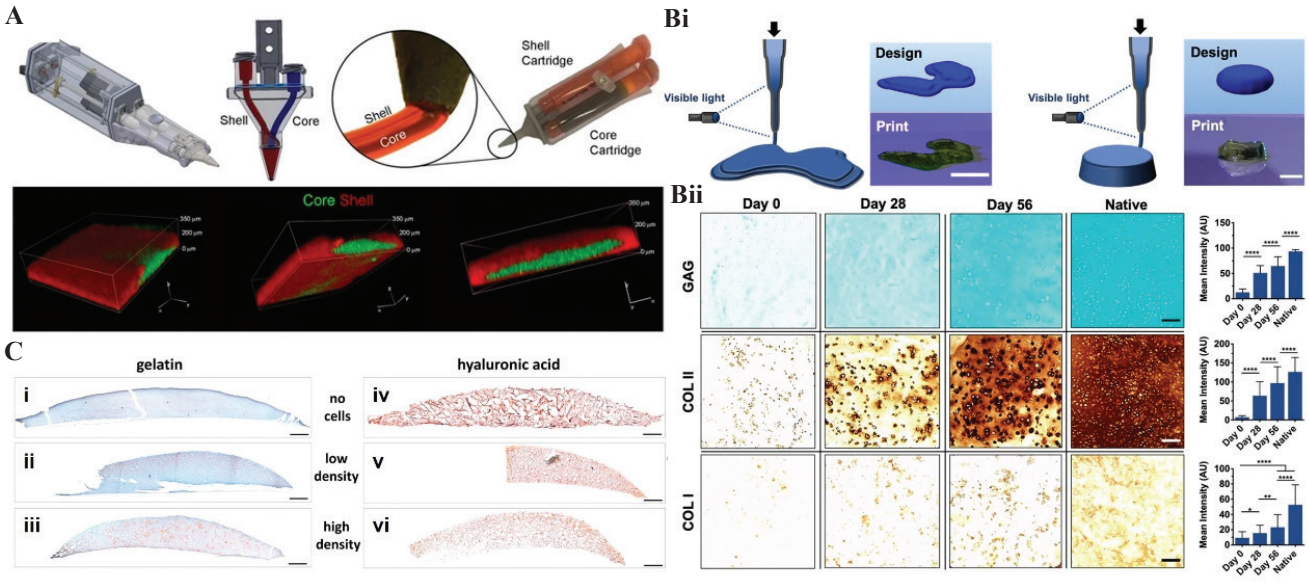


Figure 3. Construction of 3D mimetic cartilage tissue by 3D bioprinting. (A) Schematic representation of a core/shell 3D printing by co-axial extrusion printer and confocal images of 3D printed core/shell structure[73] (from ref.[73] licensed under Creative Commons Attribution 4.0 license with permission). (Bi) Representative images of 3D constructs printed through an *in situ* crosslinking method. (Bii) Histological staining of printed cartilage constructs; left image shows the representative staining images and right image shows quantification analysis in different culture time. Scale bar = 100 μm[74] (from ref.[74] licensed under Creative Commons Attribution 4.0 license). (C) Detection of proteoglycans in printed constructs after 14 days of incubation (red: proteoglycans; green to blue: nuclei and other ECM/bio-ink). Porcine chondrocytes were embedded in gelatin (i, ii, iii) and hyaluronic acid (iv, v, vi) bio-inks. Scale bar = 500 μm[75] (from ref.[75] licensed under Creative Commons Attribution-Non Commercial 4.0).

increase in moduli, biochemical expression, and cartilage regeneration (**Figure 3Bii**).

In a 3D bioprinting process, the interaction between cell patterning and hydrogel matrix has a great effect on the performance of printed cells. For instance, Lutz Klok *et al*. fabricated different 3D cartilage tissue constructs with different cell concentrations (**Figure 3C**)[75]. The bio-inks were prepared by homogeneously mixing cell suspensions with GelMA or HAMA hydrogel separately and then printed in a layer by layer process through SLA-based bioprinting. Histological staining indicated that cells distributed homogeneously in both GelMA (**Figure 3Ci-iii**) and HAMA constructs (**Figure 3Civ-vi**). A noticeable difference in cell number can be observed between low and high cell density constructs. Results indicated that both GelMA scaffolds and HAMA scaffolds supported the recovery of chondrocyte phenotype and formation of cartilage ECM with uniform cellular distribution. Meanwhile, the increase in cartilage-specific genes expression, type II collagen, and aggrecan, in cell loaded hydrogels proved successful cartilage formation. Compared with HAMA, GelMA showed more chondrocyte phenotypes as confirmed by the higher expression of cartilage genes. Another element that affects cartilage formation is the cell density; a high cell density (2.5×10^7 cells/mL) showed better cartilage regeneration ability compared with a low cell density (5×10^6 cells/mL).

4.3. Bioprinted hydrogels in osteochondral tissue engineering

Osteochondral defect involving both the cartilage and subchondral layer is difficult to repair due to their difference in physiological structures and bioactive properties. The cartilage tissues do not have vasculature and nervous systems but the subchondral bone tissues are rich in blood and nerves. In addition, the structure and function of cartilage and subchondral bone are also different[76]. Thus, how to promote cartilage and subchondral bone regeneration simultaneously has become quite the challenge for osteochondral repair. The rise of 3D bioprinting, allowing for the fabrication of complicated 3D scaffolds with precise control of intricate geometry composition and functions, is a promising treatment for osteochondral repair. Meanwhile, photo-crosslinking hydrogels are promising bio-inks for osteochondral regeneration as we discussed in the previous chapters[77].

In an earlier study, Cui *et al*. bioprinted a photo-crosslinkable 3D osteochondral tissue using PEGDMA and human chondrocytes. Simultaneous photo-polymerization maintained the precise positions of deposited cells and reduced photo toxicity[78]. This bioprinted cell-laden hydrogel constructs integrated excellently with the native tissue and promote osteochondral repair. In another study by the same group, Cui *et al*. further printed mechanically strong and tissue differentiated bone and cartilage constructs using photo-crosslinkable PEG-GelMA hydrogel with hMSCs[55]. The printed constructs provided strong mechanical support and showed an excellent osteogenic and chondrogenic regeneration capacity, suggesting their desirable potential in osteochondral repair. Recently, Gao *et al*. developed a biohybrid gradient construct for osteochondral regeneration by 3D bioprinting (**Figure 4A**)[79]. By incorporating cleavable poly (nacryloyl 2-glycine) (PACG) into GelMA, the mechanical properties of hydrogels had been significantly improved with a tensile strength of up to 1.1 MPa and a compressive strength up to 12.4 MPa (**Figure 4B**). Results demonstrated that the photo-crosslinkable gradient hydrogel scaffold could not only facilitate the regeneration of cartilage (**Figure 3Ci-ii**) but also promote the regeneration of subchondral bone (**Figure 4Ciii-iv**).

4.4. Bioprinted hydrogels in bone disease model

Apart from the above discussed applications, 3D bioprinted hydrogels can also be used to create bone disease models and drug screening research. At present, most bone disease models are still 2D, which fails to reconstruct the complex of the *in vivo* environment[80]. Conversely, 3D bioprinting has the promising potential to create 3D mimic bone models as discussed in the previous sections, allowing for cell-cell or cell-matrix interactions and integration of a vascular system[81]. Hence, these bioprinted models could be better used for bone disease study and drug screening purposes[82].

For example, 3D-printed tissue models mimicking the native bone tissues can be applied in drug screening to test the efficacy and toxicity of new drugs, and promoting the translation of new therapeutic molecules in clinic[83]. Recently, Amir K *et al*. designed and bioprinted a musculoskeletal junction model mimicking the musculoskeletal interface by an SLA-based bioprinting platform (**Figure 5Ai**)[84]. Photo-crosslinkable GelMA was selected as a bio-ink due to its high biocompatibility for cell spreading and functionality. The musculoskeletal interface is loaded with three different cell types, MSCs, fibroblasts, and osteoblasts (**Figure 5Aii**). As shown in **Figure 5Aiii-iv**, the printed 3D pattern has a well-defined construct showing a close similarity with the designed one (**Figure 5Aii**). The proposed musculoskeletal junctions provide a multi-material microstructure on demand for multi-applications in skeletal related tissue engineering and regenerative medicine, thus facilitating new drug discovery and clinical use.

In addition, 3D-printed tissue models could also be applied in creating cancer models for cancer metastasis

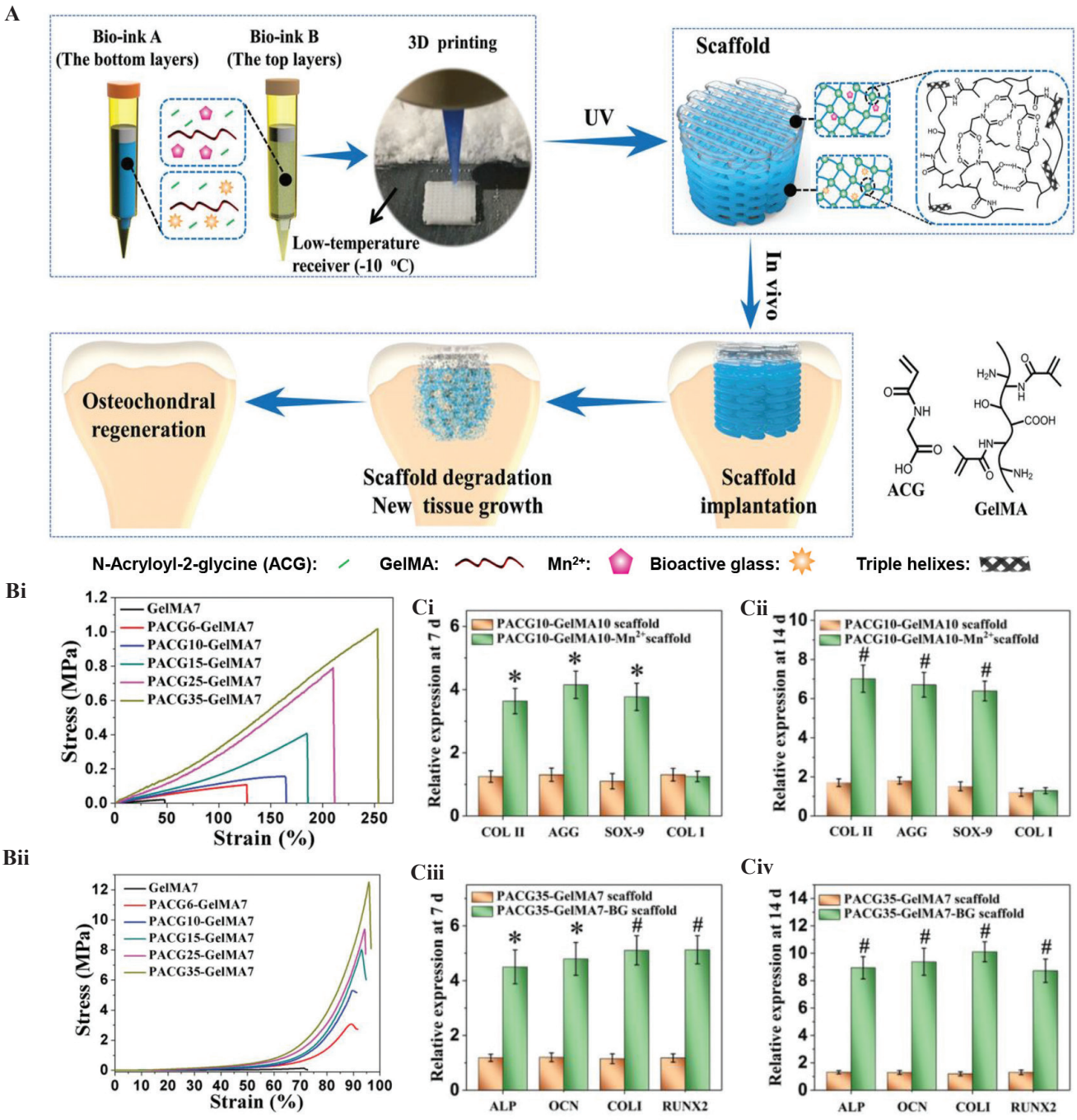


Figure 4. Construction of 3D mimetic osteochondral tissue by 3D bioprinting. (A) Schematic diagram of the biohybrid gradient scaffolds for osteochondral regeneration. (B) Mechanical properties of poly (nacryloyl 2-glycine) -GelMA hydrogels: (i) tensile strength and (ii) compressive strength. **(C)** Genetic analysis for osteochondral differentiation: (i and ii) Expression of cartilage-related genes (*COL II*, *aggrecan*, *SOX-9*, and *COL I*) and (iii-iv) expression of osteogenesis-related genes (*ALP*, *OCN*, *COL I*, and *RUNX2*) after 7 and 14 days of culture, respectively[79] (from ref.[79] licensed under Creative Commons Attribution 4.0 license).

research. One of the primary transfer sites for breast carcinoma is bone; however, the fundamental mechanisms are still unknown because of the lack of 3D biomimetic models for cancer research. Therefore, Zhu *et al*. created a series of 3D bionic bone models for breast cancer bone metastasis study through 3D bioprinting[85]. In their early study, the authors printed the 3D bone matrix using a nano-bioink consisting of Hap and PEGDA (Mn 700) hydrogel with 0.5% photo-initiator (**Figure 5B**). Results indicated that the cocultivation of tumor cells and BMSCs

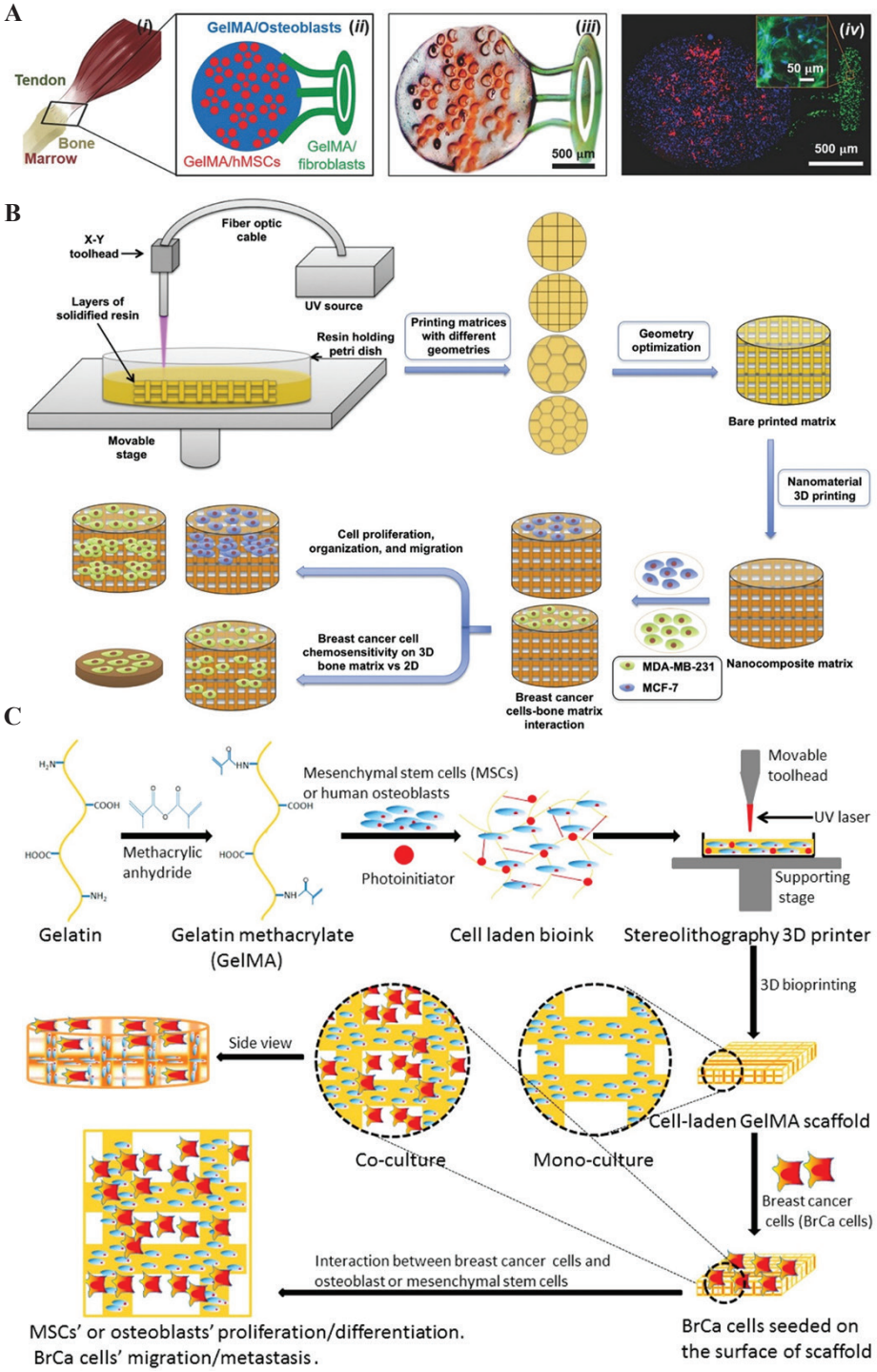


Figure 5. Construction of 3D bioprinted hydrogels in bone disease model. (A) Fabrication of a musculoskeletal interface model: (i) Schematic diagram of a native insertion site; (ii) illustration of the printing model; (iii) a representative image showing the bioprinted structure; (iv) fluorescent image of the bioprinted structure; blue: osteoblasts, red: MSCs, and green: Fibroblasts[84]. (Reproduced from A. K. Miri, D. Nieto, L. Iglesias, *et al.,* Microfluidics-Enabled Multimaterial Maskless Stereolithographic Bioprinting from Wiley. © 2018 WILEY-VCH Verlag GmbH Co. KgaA Weinheim). (B) Illustration of 3D bioprinted PEGDA bone matrix model for breast cancer cell invasion research[85]. (Reprinted from *Nanomed-Nanotechnol*,12(1), W. Zhu, B. Holmes, R. I. Glazer, *et al.,* 3D Printed Nanocomposite Matrix for The Study of Breast Cancer Bone Metastasis, 69 – 79, Copyright (2016), with permission from Elsevier). (C) Schematic diagram of 3D bioprinted GelMA bone matrix model for breast cancer metastasis study[86]. (Reprinted with permission from X. Zhou, W. Zhu, M. Nowicki, *et al.*, Acs Appl Mater Inter, 2016, 8(44): 30017 – 30026, Copyright (2016) American Chemical Society).

increased the formation of spheroid clusters. Zhu *et al*. further investigated the interplay between the cancer cells and bone stromal cells (fetal osteoblasts and MSCs) on a GelMA-based bionic bone matrix fabricated by 3D bioprinting (**Figure 5C**)[86]. These 3D bionic bone models also exhibited better drug fastness of breast cancer cells compared with 2D culture, suggesting its potential for assessing drug sensitivity. Results demonstrated that the 3D bionic bone models, with breast cancer cells and bone stromal cells, offer a suitable 3D model for the research of the interaction between cells and a bionic bone microenvironment, and thus, might serve as a desirable model for the studying the progression of metastatic breast cancer and drug screening in bone.

5. Conclusion and future perspectives

Since 3D printing can control the structure of tissue scaffolds with high resolution, accuracy and reproducibility, it has become a key fabrication process for bone and cartilage engineering[87]. Although there are numerous advantages of 3D printing in biomedical field, the involvement of cells and sensitive biomolecules leads to rigorous requirements for ink selection. Hydrogels are gold standard materials for bioprinting because of its elastic and hydrated properties as well as the ECM-mimetic crosslinked network structure, which enable cell survival and retention of their functions. Among various crosslinking methods, photo-polymerization has been widely used due to low toxicity, high crosslinking efficiency and *in situ* gelling capability. Through modification by computer-aided design/manufacturing or medical imaging systems, photo-crosslinkable hydrogels can be personalized at different bone length scale by 3D printing. With the application of UV light, the photo-crosslinking hydrogels undergo rapid formation immediately after printing[88]. By changing the UV intensity and exposure time, the performance of hydrogels including crosslinking density and matrix stiffness can be exceptionally controlled. In addition, the concentration, degree of substitution or molecular weight of chemical modified precursors, as well as introduction of nanomaterials can further regulate the mechanical properties and swelling behavior of photo-crosslinkable hydrogels to meet different therapeutic needs. Moreover, cells, drugs and biochemical entities (e.g., growth factors) can also be added into photo-crosslinkable bio-inks, thereby endowing the bone scaffold with excellent biological functions and promoting bone repairing as well as regeneration. Up to now, this strategy has been explored in various bone tissues (such as hard bone, osteochondral, and cartilage tissue), and it can reconstruct bone disease models to investigate disease mechanisms and drug screening.

Looking forward, the development of 3D bioprinting bone tissues needs further investigation of the physical properties of bio-ink and combination with other technologies to fabricate functional and optimized bone scaffolds. For example, bioelectrical effect in natural bone has been proven to play a significant role in bone development and fracture healing. The endogenous electric field of living bone contributes to the regulation of cell metabolism, such as proliferation, differentiation, and migration[89]. Consequently, conductive photo-crosslinkable hydrogel can be developed for the construction of a biomimetic electro-microenvironment for bone tissue engineering. In general, conductive hydrogels can be constructed by adding nano-conductive fillers such as metal/carbon/graphene nanoparticles into a hydrogel matrix or by crosslinking with conductive polymers including polyaniline, polypyrrole, and polythiophene[90]. In addition, self-healing enables hydrogels to withstand repeated damage. Self-healing mechanism such as host-guest interactions, Schiff's base reaction, ionic bonding, and hydrogen bonding can be incorporated into photo-crosslinking hydrogel for bone and cartilage tissue engineering to prevent the potential risks of repeated rupture and to restore its original properties after being damaged. In one study, Wei *et al*. introduced the host-guest non-covalent interaction into photo-crosslinked HA hydrogel to develop a double network dynamic hydrogel with excellent self-healing ability, enhanced toughness, and greater collagen deposition to support chondrogenesis and cartilage regeneration[91]. Moreover, to improve the toughness of photo-crosslinking hydrogel, composite hydrogels have been fabricated with enhanced mechanical performance by addition of organic or inorganic additives (e.g., clay, Hap, grapheme, and carbon nanotubes) for bone and cartilage engineering. Another barrier for the application of hydrogel to bone and cartilage repair is the adhesion and integration with surrounding tissues. The surrounding of most tissues, such as cartilage, is slippery and hard to bond with hydrogels; therefore, the integration with surrounding tissue is crucial for hydrogel retention and new tissue development. To address this challenge, adhesive hydrogel, for example, by modifying HAMA hydrogel with 3,4-dihydroxyphenylalanine groups[92], can be developed to improve the mechanical integrity between the hydrogels and the tissues. Meanwhile, the adhesive hydrogel provides sites for cell adhesion, proliferation and thus promotes tissue regeneration *in vivo*. Moreover, piezoelectricity can modulate cellular functions which assist the repair and regeneration of bone tissue[93]. Hence, introducing piezoelectric biomaterials (such as zinc oxide[93], lithium sodium potassium niobate[94], and barium titanate[95]) into 3D bioprinting hydrogels can blaze a new pathway for bone engineering.

When 3D printing is combined with microfluidics, vascularized bone scaffolds can be fabricated for organ-

on-a-chip devices. The microfluidics technique can manipulate and regulate fluid at a small scale, and it can combine the geometry of channels (controlled by 3D printing) and cell confinement with fluid flow to reconstruct a physiological environment[96], which will reconstruct a structure similar to that of a natural bone and investigate the biological responses of cells in specific microenvironment. Moreover, as a new emerging concept, 4D bioprinting has attracted significant attention for constructing a smart and multi-functional bone scaffold. With "time" as a fourth dimension, this bone scaffold will respond and adjust its structure and function to the disease development process as well as mimic the dynamics of the native tissues[97]. To achieve 4D bioprinting, both bio-inks and related technologies should be further explored. Bio-inks should be sensitive to physical, chemical, or biological changes in microenvironment, necessitating the design of smart or stimuli-responsive materials. Meanwhile, advanced scanning system, updated model processing software, and improved printing technologies (such as lithography, femtosecond *et al*.) can simplify the operation process and optimize printed bone tissues. By investigating bio-inks combined with other advanced technologies and transitioning to 4D printing, scientists could construct scaffolds more similar to natural tissues for bone engineering.

In conclusion, 3D bioprinting is a rapidly advancing research field for bone engineering. With the advance of new technologies and biomaterials, we believe that this technique may be the key to giving patients with bone or cartilage defects a chance to improve their quality of life.

Acknowledgments

This work was supported by the grant from the Guangdong Basic and Applied Basic Research Foundation (2020B1515130002).

Conflict of interest

The authors declare that they have no conflict of interest.

Author contributions

X.Z. supervised the entire writing process of the review. Q.M., J.R., and H.P.B. wrote the manuscript. Y.L. edited the manuscript. All the authors approved the review for publication.

References

1. Midha S, Dalela M, Sybil D, *et al.*, 2019, Advances in Three-dimensional Bioprinting of Bone: Progress and Challenges. *J Tissue Eng Regen Med*, 13:925–45. https://doi.org/10.1002/term.2847
2. Liu Y, Luo D, Wang T, 2016, Hierarchical Structures of Bone and Bioinspired Bone Tissue Engineering. *Small*, 12:4611–32. https://doi.org/10.1002/smll.201600626
3. Bai X, Gao M, Syed S, *et al.*, 2018, Bioactive Hydrogels For Bone Regeneration. *Bioact Mater*, 3:401–17.
4. Mandrycky C, Wang Z, Kim K, *et al.*, 2016, 3D Bioprinting for Engineering Complex Tissues. *Biotechnol Adv*, 34:422–34. https://doi.org/10.1016/j.biotechadv.2015.12.011
5. Allen MR, Burr DB, 2014, Bone Modeling and Remodeling. In: Basic and Applied Bone Biology. Amsterdam, Netherlands: Elsevier. p75-90. https://doi.org/10.1016/b978-0-12-416015-6.00004-6
6. Byambaa B, Annabi N, Yue K, *et al.*, 2017, Bioprinted Osteogenic and Vasculogenic Patterns for Engineering 3D Bone Tissue. *Adv Healthc Mater*, 6:1700015. https://doi.org/10.1002/adhm.201700015
7. Groll J, Boland T, Blunk T, *et al.*, 2016, Biofabrication: Reappraising the Definition of an Evolving Field. *Biofabrication*, 8:013001. https://doi.org/10.1088/1758-5090/8/1/013001
8. Ashammakhi N, Hasan A, Kaarela O, *et al.*, 2019, Advancing Frontiers in Bone Bioprinting. *Adv Healthc Mater*, 8:1801048. https://doi.org/10.1002/adhm.201801048
9. Keriquel V, Oliveira H, Rémy M, *et al.*, 2017, *In Situ* Printing of Mesenchymal Stromal Cells, by Laser-assisted Bioprinting, for *In Vivo* Bone Regeneration Applications. *Sci Rep*, 7:1–10. https://doi.org/10.1038/s41598-017-01914-x
10. Yang Y, Zhang Q, Xu T, *et al.*, 2020, Photocrosslinkable Nanocomposite Ink for Printing Strong, Biodegradable and Bioactive Bone Graft. *Biomaterials*, 263:120378. https://doi.org/10.1016/j.biomaterials.2020.120378
11. Nguyen QV, Park JH, Lee DS, 2015, Injectable Polymeric Hydrogels for the Delivery of Therapeutic Agents: A Review. *Eur Polym J*, 72:602–619. https://doi.org/10.1016/j.eurpolymj.2015.03.016
12. Yue K, Trujillo-de Santiago G, Alvarez MM, *et al.*, 2015, Synthesis, Properties, and Biomedical Applications of Gelatin Methacryloyl (GelMA) Hydrogels. *Biomaterials*, 73:254–271. https://doi.org/10.1016/j.biomaterials.2015.08.045
13. Vijayavenkataraman S, Yan WC, Lu WF, *et al.*, 2018, 3D Bioprinting of Tissues and Organs for Regenerative Medicine. *Adv Drug Deliv Rev*, 132:296–332. https://doi.org/10.1016/j.addr.2018.07.004
14. Li X, Chen S, Li J, *et al.*, 2016, 3D Culture of Chondrocytes in Gelatin Hydrogels with Different Stiffness. *Polymers* (*Basel*), 8:269.

https://doi.org/10.3390/polym8080269

15. Bryant SJ, Chowdhury TT, Lee DA, *et al.*, 2004, Crosslinking Density Influences Chondrocyte Metabolism in Dynamically Loaded Photocrosslinked Poly (Ethylene Glycol) Hydrogels. *Ann Biomed Eng*, 32:407–17. https://doi.org/10.1023/b: abme.0000017535.00602.ca
16. Marklein RA, Burdick JA, 2010, Spatially Controlled Hydrogel Mechanics to Modulate Stem Cell Interactions. *Soft Matter*, 6:136–43. https://doi.org/10.1039/b916933d
17. Bian L, Hou C, Tous E, *et al.*, 2013, The Influence of Hyaluronic Acid Hydrogel Crosslinking Density and Macromolecular Diffusivity on Human MSC Chondrogenesis and Hypertrophy. *Biomaterials*, 34:413–21. https://doi.org/10.1016/j.biomaterials.2012.09.052
18. Nguyen KT, West JL, 2002, Photopolymerizable Hydrogels for Tissue Engineering Applications. *Biomaterials*, 23: 4307–14. https://doi.org/10.1016/s0142-9612(02)00175-8
19. Annabi N, Tamayol A, Uquillas JA, *et al.*, 2014, 25th Anniversary Article: Rational Design and Applications of Hydrogels in Regenerative Medicine. *Adv Mater*, 26:85–124. https://doi.org/10.1002/adma.201303233
20. Jiang Y, Chen J, Deng C, *et al.*, 2014, Click Hydrogels, Microgels and Nanogels: Emerging Platforms for Drug Delivery and Tissue Engineering. *Biomaterials*, 35:4969–85. https://doi.org/10.1016/j.biomaterials.2014.03.001
21. Van Vlierberghe S, Dubruel P, Schacht EJ, 2011, Biopolymer-based Hydrogels as Scaffolds for Tissue Engineering Applications: A Review. *Biomacromolecules*, 12:1387–408. https://doi.org/10.1021/bm200083n
22. Collins MN, Birkinshaw CJ, 2013, Hyaluronic Acid Based Scaffolds for Tissue Engineering a review. *Rom J Morphol Embryol*, 92:1262–79. https://doi.org/10.1016/j.carbpol.2012.10.028
23. Sherman L, Sleeman J, Herrlich P, *et al.*, 1994, Hyaluronate Receptors: Key Players in Growth, Differentiation, Migration and Tumor Progression. *Curr Opin Cell Biol*, 6:726–33. https://doi.org/10.1016/0955-0674(94)90100-7
24. Prestwich GD, 2011, Hyaluronic Acid-based Clinical Biomaterials Derived for Cell and Molecule Delivery in Regenerative Medicine. *J Control Release*, 155:193–9. https://doi.org/10.1016/j.jconrel.2011.04.007
25. Gramlich WM, Kim IL, Burdick JA, 2013, Synthesis and Orthogonal Photopatterning of Hyaluronic Acid Hydrogels with Thiol-Norbornene Chemistry. *Biomaterials*, 34:9803–11. https://doi.org/10.1016/j.biomaterials.2013.08.089
26. Oudshoorn MH, Rissmann R, Bouwstra JA, *et al.*, 2007, Synthesis of Methacrylated Hyaluronic Acid with Tailored Degree of Substitution. *Polymer*, 48:1915–20. https://doi.org/10.1016/j.polymer.2007.01.068
27. Poldervaart MT, Goversen B, De Ruijter M, *et al.*, 2017, 3D Bioprinting of Methacrylated Hyaluronic Acid (MeHA) Hydrogel with Intrinsic Osteogenicity. *PLoS One*, 12:e0177628. https://doi.org/10.1371/journal.pone.0177628
28. Liu Y, Chan-Park MB, 2010, A Biomimetic Hydrogel Based on Methacrylated Dextran-graft-lysine and Gelatin for 3D Smooth Muscle Cell Culture. *Biomaterials*, 31:1158–70. https://doi.org/10.1016/j.biomaterials.2009.10.040
29. Lai JY, Li YT, 2010, Functional Assessment of Cross-linked Porous Gelatin Hydrogels for Bioengineered Cell Sheet Carriers. *Biomacromolecules*, 11:1387–97. https://doi.org/10.1021/bm100213f
30. Schuurman W, Levett PA, Pot MW, *et al.*, 2013, Gelatin-methacrylamide Hydrogels as Potential Biomaterials for Fabrication of Tissue-engineered Cartilage Constructs. *Macromol Biosci*, 13:551–61. https://doi.org/10.1002/mabi.201200471
31. Mũnoz Z, Shih H, Lin CC, 2014, Gelatin Hydrogels Formed by Orthogonal Thiol-Norbornene Photochemistry for Cell Encapsulation. *Biomater Sci*, 2:1063–72. https://doi.org/10.1039/c4bm00070f
32. Chen YC, Lin RZ, Qi H, *et al.*, 2012, Functional Human Vascular Network Generated in Photocrosslinkable Gelatin Methacrylate Hydrogels. *Adv Funct Mater*, 22:2027–39. https://doi.org/10.1002/adfm.201101662
33. Sun X, Lang Q, Zhang H, *et al.*, 2017, Electrospun Photocrosslinkable Hydrogel Fibrous Scaffolds for Rapid *In Vivo* Vascularized Skin Flap Regeneration. *Adv Funct Mater*, 27:1604617. https://doi.org/10.1002/adfm.201604617
34. Zhao X, Lang Q, Yildirimer L, *et al.*, 2016, Photocrosslinkable Gelatin Hydrogel for Epidermal Tissue Engineering. *PLoS One*, 5:108–18.
35. Zhao X, Sun X, Yildirimer L, *et al.*, 2017, Cell Infiltrative Hydrogel Fibrous Scaffolds for Accelerated Wound Healing. *Acta Biomater*, 49:66–77. https://doi.org/10.1016/j.actbio.2016.11.017
36. Pellá MC, Lima-Tenório MK, Tenório-Neto ET, *et al.*, 2018, Chitosan-based Hydrogels: From Preparation to Biomedical Applications. *Carbohydr Polym*, 196:233–45. https://doi.org/10.1016/j.carbpol.2018.05.033
37. He M, Han B, Jiang Z, *et al.*, 2017, Synthesis of a Chitosan-

based Photo-Sensitive Hydrogel and its Biocompatibility and Biodegradability. *Carbohydr Polym*, 166:228–35. https://doi.org/10.1016/j.carbpol.2017.02.072

38. Pei M, Mao J, Xu W, *et al.*, 2019, Photocrosslinkable Chitosan Hydrogels and their Biomedical Applications. *J Polym Sci*, 57:1862–71.
39. Elizalde-Peña E, Flores-Ramirez N, Luna-Barcenas G, *et al.*, 2007, Synthesis and Characterization of Chitosan-g-glycidyl Methacrylate with Methyl Methacrylate. *Eur Polym J*, 43:3963–9. https://doi.org/10.1016/j.eurpolymj.2007.06.004
40. Lin CC, Raza A, Shih HJ, 2011, PEG Hydrogels Formed by Thiol-ene Photo-Click Chemistry and their Effect on the Formation and Recovery of Insulin-Secreting Cell Spheroids. *Biomaterials*, 32:9685–95. https://doi.org/10.1016/j.biomaterials.2011.08.083
41. Hockaday L, Kang K, Colangelo N, *et al.*, 2012, Rapid 3D Printing of Anatomically Accurate and Mechanically Heterogeneous Aortic Valve Hydrogel Scaffolds. *Biofabricatio*, 4:035005. https://doi.org/10.1088/1758-5082/4/3/035005
42. Lim WS, Chen K, Chong TW, *et al.*, 2018, A Bilayer Swellable Drug-eluting Ureteric Stent: Localized Drug Delivery to Treat Urothelial Diseases. *Biomaterials*, 165:25–38. https://doi.org/10.1016/j.biomaterials.2018.02.035
43. Shin H, Olsen BD, Khademhosseini A, 2012, The Mechanical Properties and Cytotoxicity of Cell-laden Double-network Hydrogels Based on Photocrosslinkable Gelatin and Gellan Gum Biomacromolecules. *Biomaterials*, 33:3143–52. https://doi.org/10.1016/j.biomaterials.2011.12.050
44. Kaur M, Srivastava A, 2002, Photopolymerization: A review. *J Macromol Sci Part C Polym Rev*, 42:481–512.
45. Yan Q, Dong H, Su J, *et al.*, 2018, A Review of 3D Printing Technology for Medical Applications. *Engineering*, 4:729–42.
46. Colosi C, Shin SR, Manoharan V, *et al.*, 2016, Microfluidic Bioprinting of Heterogeneous 3D Tissue Constructs Using Low-viscosity Bioink. *Adv Mater*, 28:677–84. https://doi.org/10.1002/adma.201503310
47. Wadnap S, Krishnamoorthy S, Zhang Z, *et al.*, 2019, Biofabrication of 3D Cell-encapsulated Tubular Constructs Using Dynamic Optical Projection Stereolithography. *J Mater Sci Mater Med*, 30:1–10. https://doi.org/10.1007/s10856-019-6239-5
48. Xu H, Liu Q, Casillas J, *et al.*, 2020, Prediction of Cell Viability in Dynamic Optical Projection Stereolithography-based Bioprinting Using Machine Learning. *J Intell Manuf*, 2020:1–11. https://doi.org/10.1007/s10845-020-01708-5
49. Zhang K, Feng Q, Xu J, *et al.*, 2017, Self-assembled Injectable Nanocomposite Hydrogels Stabilized by Bisphosphonate-magnesium (Mg_2+) Coordination Regulates the Differentiation of Encapsulated Stem Cells Via Dual Crosslinking. *Adv Funct Mater*, 27:1701642. https://doi.org/10.1002/adfm.201701642
50. Zuo Y, Liu X, Wei D, *et al.*, 2015, Photo-cross-linkable Methacrylated Gelatin and Hydroxyapatite Hybrid Hydrogel for Modularly Engineering Biomimetic Osteon. 7:10386–94. https://doi.org/10.1021/acsami.5b01433
51. Shi D, Xu X, Ye Y, *et al.*, 2016, Photo-cross-linked Scaffold with Kartogenin-encapsulated Nanoparticles for Cartilage Regeneration. *ACS Nano*, 10:1292–9. https://doi.org/10.1021/acsnano.5b06663.s001
52. de Windt TS, Vonk LA, Slaper-Cortenbach IC, *et al.*, 2017, Allogeneic Mesenchymal Stem Cells Stimulate Cartilage Regeneration and are Safe for Single-stage Cartilage Repair in Humans Upon Mixture with Recycled Autologous Chondrons. *Stem Cells*, 35:256–64. https://doi.org/10.1002/stem.2475
53. Levato R, Webb WR, Otto IA, *et al.*, 2017, The Bio in the Ink: Cartilage Regeneration with Bioprintable Hydrogels and Articular Cartilage-derived Progenitor Cells. *Acta Biomater*, 61:41–53. https://doi.org/10.1016/j.actbio.2017.08.005
54. Yan S, Wang T, Feng L, *et al.*, 2014, Injectable *In Situ* Self-cross-linking Hydrogels Based on Poly (L-glutamic Acid) and Alginate for Cartilage Tissue Engineering. *Biomacromolecules*, 15:4495–508. https://doi.org/10.1021/bm501313t
55. Gao G, Schilling AF, Hubbell K, *et al.*, 2015, Improved Properties of Bone and Cartilage Tissue from 3D Inkjet-bioprinted Human Mesenchymal Stem Cells by Simultaneous Deposition and Photocrosslinking in PEG-GelMA. 37:2349–55. https://doi.org/10.1007/s10529-015-1921-2
56. Rao RR, Stegemann JP, 2013, Cell-based Approaches to the Engineering of Vascularized Bone Tissue. *Cytotherapy*, 15:1309–22. https://doi.org/10.1016/j.jcyt.2013.06.005
57. Peters EB, 2018, Endothelial Progenitor Cells for the Vascularization of Engineered Tissues. *Tissue Eng Part B Rev*, 24:1–24.
58. Zhai X, Ruan C, Ma Y, *et al.*, 2018, 3D-bioprinted Osteoblast-laden Nanocomposite Hydrogel Constructs with Induced Microenvironments Promote Cell Viability, Differentiation,

and Osteogenesis Both *In Vitro* and *In Vivo*. *Adv Sci* (*Weinh*), 5:1700550.
https://doi.org/10.1002/advs.201700550

59. Wenz A, Tjoeng I, Schneider I, *et al.*, 2018, Improved Vasculogenesis and Bone Matrix Formation through Coculture of Endothelial Cells and Stem Cells in Tissue-specific Methacryloyl Gelatin-Based Hydrogels. *Biotechnol Bioeng*, 115:2643–53.
https://doi.org/10.1002/bit.26792
60. Doschak MR, Kucharski CM, Wright JE, *et al.*, 2009, Improved Bone Delivery of Osteoprotegerin by Bisphosphonate Conjugation in a Rat Model of Osteoarthritis. *Mol Pharm*, 6:634–40.
https://doi.org/10.1021/mp8002368
61. Park D, Park CW, Choi Y, *et al.*, 2016, A Novel Small-molecule PPI Inhibitor Targeting Integrin αvβ3-osteopontin Interface Blocks Bone Resorption *In Vitro* and Prevents Bone Loss in Mice. *Biomaterials*, 98:131–42.
https://doi.org/10.1016/j.biomaterials.2016.05.007
62. Teno N, Masuya K, Ehara T, *et al.*, 2008, Effect of Cathepsin K Inhibitors on Bone Resorption. *J Med Chem*, 51:5459–62.
63. Arrighi I, Mark S, Alvisi M, *et al.*, 2009, Bone Healing Induced by Local Delivery of an Engineered Parathyroid Hormone Prodrug. *Biomaterials*, 30:1763–71.
https://doi.org/10.1016/j.biomaterials.2008.12.023
64. Rodan GA, Martin TJ, 2000, Therapeutic Approaches to Bone Diseases. *Science*, 289:1508–14.
65. Zhang Gand Suggs L J J A d d r, 2007, Matrices and scaffolds for drug delivery in vascular tissue engineering. *Adv Drug Deliv Rev*, 59:360–73.
https://doi.org/10.1016/j.addr.2009.08.002
66. Nomi M, Atala A, De Coppi P, *et al.*, 2002, Principals of Neovascularization for Tissue Engineering. *Mol Aspects Med*, 23:463–83.
https://doi.org/10.1016/s0098-2997(02)00008-0
67. An Y, Hubbell JA, 2000, Intraarterial Protein Delivery Via Intimally-adherent Bilayer Hydrogels. *J Control Release*, 64:205–15.
https://doi.org/10.1016/s0168-3659(99)00143-1
68. Kim HD, Lee EA, An YH, *et al.*, 2017, Chondroitin Sulfate-based Biomineralizing Surface Hydrogels for Bone Tissue Engineering. *ACS Appl Mater Interfaces*, 9:21639–50.
https://doi.org/10.1021/acsami.7b04114
69. Xin T, Mao J, Liu L, *et al.*, 2020, Programmed Sustained Release of Recombinant Human Bone Morphogenetic Protein-2 and Inorganic ion Composite Hydrogel as Artificial Periosteum. *ACS Appl Mater Interfaces*, 12:6840–51.
https://doi.org/10.1021/acsami.9b18496
70. Cui H, Zhu W, Nowicki M, *et al.*, 2016, Hierarchical Fabrication of Engineered Vascularized Bone Biphasic Constructs Via Dual 3D Bioprinting: Integrating Regional Bioactive Factors into Architectural Design. *Adv Healthc Mater*, 5:2174–81.
https://doi.org/10.1002/adhm.201600505
71. Boere KW, Visser J, Seyednejad H, *et al.*, 2014, Covalent Attachment of a Three-dimensionally Printed Thermoplast to a Gelatin Hydrogel for Mechanically Enhanced Cartilage Constructs. *Acta Biomater*, 10:2602–11.
https://doi.org/10.1016/j.actbio.2014.02.041
72. Dhawan A, Kennedy PM, Rizk EB, *et al.*, 2019, Three-dimensional Bioprinting for Bone and Cartilage Restoration in Orthopaedic Surgery. J Am Acad Orthop Surg, 27:e215–26.
https://doi.org/10.5435/jaaos-d-17-00632
73. Duchi S, Onofrillo C, O'Connell CD, *et al.*, 2017, Handheld Co-axial Bioprinting: Application to *In Situ* Surgical Cartilage Repair. *Scientific Reports*, 7:1–12.
https://doi.org/10.1038/s41598-017-05699-x
74. Galarraga JH, Kwon MY, Burdick JA, 2019, 3D Bioprinting Via an *In Situ* Crosslinking Technique towards Engineering Cartilage Tissue. *Sci Rep*, 9:1–12.
https://doi.org/10.1038/s41598-019-56117-3
75. Lam T, Dehne T, Krüger JP, *et al.*, 2019, Photopolymerizable Gelatin and Hyaluronic Acid for Stereolithographic 3D Bioprinting of Tissue-engineered Cartilage. *J Biomed Mater Res*, 107:2649–57.
https://doi.org/10.1002/jbm.b.34354
76. Abdollahiyan P, Oroojalian F, Mokhtarzadeh A, *et al.*, 2020, Hydrogel-Based 3D Bioprinting for Bone and Cartilage Tissue Engineering. 15:2000095.
https://doi.org/10.1002/biot.202000095
77. Askari M, Naniz MA, Kouhi M, *et al.*, 2021, Recent Progress in Extrusion 3D Bioprinting of Hydrogel Biomaterials for Tissue Regeneration: A Comprehensive Review with Focus on Advanced Fabrication Techniques. *Biomater Sci*, 9:535–73.
https://doi.org/10.1039/d0bm00973c
78. Cui X, Breitenkamp K, Finn M, *et al.*, 2012, Direct Human Cartilage Repair Using Three-dimensional Bioprinting Technology. *Tissue Eng Part A*, 18:1304–12.
https://doi.org/10.1089/ten.tea.2011.0543
79. Gao F, Xu Z, Liang Q, *et al.*, 2019, Osteochondral Regeneration with 3D-Printed Biodegradable High-strength Supramolecular Polymer Reinforced-gelatin Hydrogel Scaffolds. *Adv Sci*., 6:1900867.
https://doi.org/10.1002/advs.201900867

80. Genova T, Roato I, Carossa M, *et al.*, 2020, Advances on Bone Substitutes Through 3D Bioprinting. *Int J Mol Sci*, 21:7012. https://doi.org/10.3390/ijms21197012
81. Qiao H., Tang TJ, 2018, Engineering 3D Approaches to Model the Dynamic Microenvironments of Cancer Bone Metastasis. *Bone Res*, 6:1–12. https://doi.org/10.1038/s41413-018-0008-9
82. Ozbolat IT, Peng W, Ozbolat VJ, 2016, Application Areas of 3D Bioprinting. *Drug Discov Today*, 21:1257–71. https://doi.org/10.1016/j.drudis.2016.04.006
83. Ozbolat IT, Hospodiuk MJ, 2016, Current Advances and Future Perspectives in Extrusion-based Bioprinting. *Biomaterials*, 76:321–43. https://doi.org/10.1016/j.biomaterials.2015.10.076
84. Miri AK, Nieto D, Iglesias L, *et al.*, 2018, Microfluidics-Enabled Multimaterial Maskless Stereolithographic Bioprinting. *Adv Mater*, 30:e1800242. https://doi.org/10.1002/adma.201870201
85. Zhu W, Holmes B, Glazer RI, *et al.*, 2016, 3D Printed Nanocomposite Matrix for the Study of Breast Cancer Bone Metastasis. *Nanomedicine*, 12:69–79. https://doi.org/10.1016/j.nano.2015.09.010
86. Zhou X, Zhu W, Nowicki M, *et al.*, 2016, 3D Bioprinting a Cell-laden Bone Matrix for Breast Cancer Metastasis Study. *ACS Appl Mater Interfaces*, 8:30017–26. https://doi.org/10.1021/acsami.6b10673
87. Stichler S, Jungst T, Schamel M, *et al.*, 2017, Thiol-ene Clickable Poly(glycidol) Hydrogels for Biofabrication. *Ann Biomed Eng*, 45:273–85. https://doi.org/10.1007/s10439-016-1633-3
88. Murphy SV, Atala A, 2014, 3D Bioprinting of Tissues and Organs. *Nat Biotechnol*, 32:773–85. https://doi.org/10.1038/nbt.2958
89. Baxter FR, Bowen CR, Turner IG, *et al.*, 2010, Electrically Active Bioceramics: A Review of Interfacial Responses. *Ann Biomed Eng*, 38:2079–92. https://doi.org/10.1007/s10439-010-9977-6
90. Jiang L, Wang Y, Liu Z, *et al.*, 2019, Three-dimensional Printing and Injectable Conductive Hydrogels for Tissue Engineering Application. *Tissue Eng Part B Rev*, 25:398–411. https://doi.org/10.1089/ten.teb.2019.0100
91. Wei K, Zhu M, Sun Y, *et al.*, 2016, Robust Biopolymeric Supramolecular "Host Guest Macromer" Hydrogels Reinforced by *In Situ* Formed Multivalent Nanoclusters for Cartilage Regeneration. *Macromolecules*, 49:866–75. https://doi.org/10.1021/acs.macromol.5b02527.s001
92. Salzlechner C, Haghighi T, Huebscher I, *et al.*, 2020, Adhesive Hydrogels for Maxillofacial Tissue Regeneration Using Minimally Invasive Procedures. *Adv Healthc Mater*, 9:1901134. https://doi.org/10.1002/adhm.201901134
93. Khare D, Basu B, Dubey AK, 2002, Electrical Stimulation and Piezoelectric Biomaterials for Bone Tissue Engineering Applications. *Biomaterials*, 258:120280.
94. Wang Q, Chen X, Zhu J, *et al.*, 2008, Porous Li-Na-K Niobate Bone-substitute Ceramics: Microstructure and Piezoelectric Properties. *Mater Lettt*, 62:3506–8. https://doi.org/10.1016/j.matlet.2008.03.024
95. Zhang X, Zhang C, Lin Y, *et al.*, 2016, Nanocomposite Membranes Enhance Bone Regeneration Through Restoring Physiological Electric Microenvironment. *ACS Nano*, 10:7279–86. https://doi.org/10.1021/acsnano.6b02247.s001
96. Mestres G, Perez RA, D'Elía NL, *et al.*, 2019, Advantages of Microfluidic Systems for Studying Cell-biomaterial Interactions Focus on Bone Regeneration Applications. *Biomed Phys Eng Express*, 5:032001. https://doi.org/10.1088/2057-1976/ab1033
97. Kirillova A, Maxson R, Stoychev G, *et al.*, 2017, 4D Biofabrication Using Shape-morphing Hydrogels. *Adv Mater*, 29:1703443. https://doi.org/10.1002/adma.201703443

REVIEW ARTICLE

Fabrication and Biomedical Applications of Heart-on-a-chip

Qingzhen Yang[1,2,3,4], Zhanfeng Xiao[1,2], Xuemeng Lv[1,2], Tingting Zhang[5]*, Han Liu[6]

[1]The Key Laboratory of Biomedical Information Engineering of Ministry of Education, School of Life Science and Technology, Xi'an Jiaotong University, Xi'an, Shaanxi 710049, P.R. China
[2]Bioinspired Engineering and Biomechanics Center (BEBC), Xi'an Jiaotong University, Xi'an, Shaanxi 710049, P.R. China
[3]Micro-/Nano-technology Research Center, State Key Laboratory for Manufacturing Systems Engineering, Xi'an Jiaotong University, Xi'an, Shaanxi 710049, P.R. China
[4]Research Institute of Xi'an Jiaotong University, Hangzhou, Zhejiang 311215, P.R. China
[5]College of Mechanical and Electrical Engineering, Shaanxi University of Science and Technology, Xi'an, Shaanxi 710021, P.R. China
[6]Collaborative Innovation Center for Chinese Medicine and Respiratory Diseases Co-constructed by Henan Province and Education Ministry of P.R. China, Academy of Chinese Medical Sciences, Henan University of Chinese Medicine, Zhengzhou 450016, P.R. China

Abstract: Heart diseases have become the main killer threatening human health, and various methods have been developed to study heart disease. Among them, heart-on-a-chip has emerged in recent years as a method for constructing disease (or normal) models *in vitro* and is considered as a promising tool to study heart diseases. Compared with other methods, the advantages of heart-on-a-chip include the high portability, high throughput, and the capability to mimic microenvironments *in vivo*. It has shown a great potential in disease mechanism study and drug screening. In this paper, we review the recent advances in heart-on-a-chip, including the fabrication methods (*e.g.,* 3D bioprinting) and biomedical applications. By analyzing the structure of the existing heart-on-a-chip, we proposed that a highly integrated heart-on-a-chip includes four elements: Microfluidic chips, cells/microtissues, microactuators to construct the microenvironment, and microsensors for results readout. Finally, the current challenges and future directions of heart-on-a-chip are discussed.

Keywords: Heart-on-a-chip; Microfluidic chip; Disease model; In vitro culture; Drug screening

*Correspondence to: Tingting Zhang, College of Mechanical and Electrical Engineering, Shaanxi University of Science and Technology, Xi'an, Shaanxi 710021, P.R. China; tting.zhang@sust.edu.cn

Received: April 21, 2021; **Accepted:** May 25, 2021; **Published Online:** June 26, 2021

(This article belongs to the *Special Section*: *Bioprinting of 3D Functional Tissue Constructs*)

Citation*:* Yang Q, Xiao Z, Lv X, *et al*., 2021, Fabrication and Biomedical Applications of Heart-on-a-chip. *Int J Bioprint*, 7(3):370. http://doi.org/10.18063/ijb.v7i3.370

1. Introduction

Heart is one of the most important organs in human body. It provides power for blood circulation which supplies oxygen and nutrients to organs and removes metabolic waste. In recent years, with the change in dietary structure and the increase of life pressure, heart diseases have become the leading cause of death worldwide[1,2]. To study the pathogenesis of heart diseases and pursue the effective treatments, it is of need to establish the disease (or normal) models. Overall, animal model and cell culture are the two frequently used methods.

These two methods have their own advantages and limitations. For animal model, it is different with human being in physiological conditions and organ functionalities[3]. Thus, the results of animal experiments may not precisely predict the response and/or functionalities of humans. In addition, animal experiments have other limitations, such as time-

© 2021 Yang, *et al*. This is an Open Access article distributed under the terms of the Creative Commons Attribution License (https://creativecommons.org/licenses/by/4.0/), permitting distribution and reproduction in any medium, provided the original work is cited.

consuming investigations, high cost, and low efficiency. Moreover, there are ethical issues to consider when conducting research. In recent years, Society for the Prevention of Cruelty to Animals has been established around the world, which strongly opposes animal experiments. Therefore, research communities are under increasing public pressure as to whether animals can be used in experiments.

As to the Petri dish-based cell culture, it is now widely used due to the simple operation and good controllability. Despite its merits, there are still some drawbacks to this method. For instance, the morphologies are different for cells in human body and those in Petri dish. The cells *in vivo* usually assemble into three-dimensional (3D) structures, while cells in a petri dish lack the 3D scaffolds and thus form a two-dimensional (2D) flat structure. In addition, Petri dish is unable to provide the microenvironments that are required for cell growth and differentiation, and cannot well simulate the cell-cell and cell-extracellular matrix (ECM) interactions. Cells *in vivo* are usually subjected to some mechanical and electrical stimuli. These stimuli are of importance for the maturation and functionalities of cells. However, it is difficult to impose the stimuli in Petri dish.

Since these two methods are not satisfying, a novel method is required. With the advances of bio-fabrication, microfluidics, and biosensing techniques, organ-on-a-chip has emerged as a new technology. Organ-on-a-chip is a device for *in vitro* cell culture which utilizes microfluidic technology to create a highly controllable microenvironment for cells. Various organs-on-chips, for example, lung-on-a-chip, kidney-on-a-chip, intestine-on-a-chip, and even tumor-on-a-chip, have been developed for different biomedical applications[4]. Among them, heart-on-a-chip, as a method to construct heart models *in vitro*, has attracted considerable attention. Various fabrication methods have been developed and different applications, for example, drug screening, physiology study and disease modeling, have been proposed[5].

There are some well-written review papers on heart-on-a-chip[6-9]. However, most of them focused on the biomedical applications. In this paper, we review the recent advances of heart-on-a-chip from the viewpoint of biofabrication. By analyzing the structures of heart-on-a-chip, we found that a highly integrated heart-on-a-chip includes four elements: Microfluidic chips, cells/microtissues, microactuators for constructing the microenvironment, and microsensors for results detection. The fabrication methods for these elements are introduced in details, and the applications of heart-on-a-chip in the field of biomedical engineering are discussed. In the end, the challenges and possible solutions, as well as the future directions of heart-on-a-chip are summarized.

2. The structures of heart-on-a-chip

By reviewing the existing literature, we propose that a highly integrated heart-on-a-chip includes four elements: microfluidic chip, cells/microtissues, microactuators for physical/chemical stimuli, and microsensors for monitoring cells status (**Figure 1**). In practical experiments, a heart-on-a-chip may not include all these four elements, but the microfluidic chip and cells/microtissues are necessary. In recent years, with the advances in manufacturing technology (*e.g.,* 3D bioprinting), microactuators and microsensors have been integrated within heart-on-a-chip. The purpose of microactuators is to promote cardiac cells maturation and functionalization, while microsensors are to detect cells status. In the following, we introduce these four elements sequentially.

2.1. Microfluidic chips

Microfluidic chip is the major part of heart-on-a-chip, and it provides habitat for cells. To date, various materials and fabrication methods have been proposed for microfluidic chips.

(1) Materials of microfluidic chips

The traditional materials for microfluidic chips include glass, silicon, polydimethylsiloxane (PDMS), polymethyl methacrylate (PMMA), and papers[10]. Silicon and glass are compatible to the standard micro- or nano-fabrication methods (photolithography, etching, etc.). The advantages of silicon and glass include high precision, reproducibility, and resistance to organic solvents. As to the disadvantages, silicon has poor light transmittance, which renders direct observation of the cells difficult. As a polymer organic silicon compound, PDMS is the most popular material for microfluidic chips. Its main advantages are non-toxic, chemically inert, and optically transparent properties as well as simple to use and low cost. The major disadvantage of PDMS is that it has a high absorption rate for small molecule chemicals. If the heart-on-a-chip is used for drug screening, the absorption problem should be addressed. PMMA is a transparent thermoplastic, which has the advantage of high biocompatibility, low cost, superior mechanical strength, and transparency. Papers are also used for microfluidic chips. The merits include good biocompatibility, ease of fabrication, environmental friendliness, and self-powered feature[11].

With the advances in 3D bioprinting, some printable materials have been developed for microfluidic chips. Some representative materials include thermoplastic polyurethane (TPU)[12], polycaprolactone (PCL)[13,14], and silicone[15]. TPU is a versatile multiphase block copolymer. When heated, TPU becomes soft and

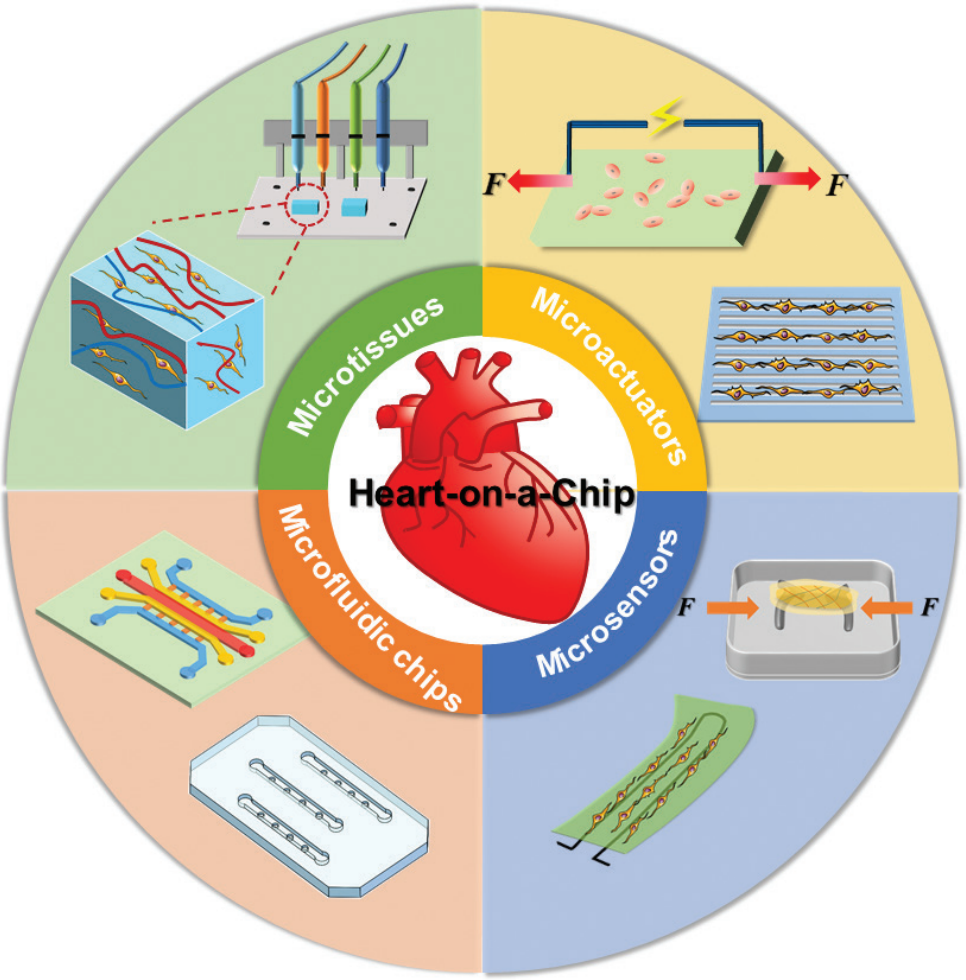


Figure 1. Structures of the heart-on-a-chip. A highly integrated heart-on-a-chip may include four components: microfluidic chips, microtissues, microactuators and microsensor.

easy to print. If the temperature decreases, it becomes flexible with elasticity[12]. The advantages include high transparency, resistance to chemical solvents, high strength, low melting point, and high abrasion resistance. PCL is a thermoplastic material which has been approved by the Food and Drug Administration (FDA)[14]. It has a low melting temperature (~60°C), thus it is suitable for 3D bioprinting[13]. Besides, the silicon material can be modified for fast crosslinking. The modified material is 3D printable and can be used for heart-on-a-chip.

(2) Fabrication of microfluidic chips

Various methods have been used to fabricate the microfluidic chips, including photolithography, soft lithography, laser etching, hot embossing, and machining process. As a well-developed technique, photolithography enables the micro/nano structures with a high resolution[16]. The extreme ultraviolet (EUV) lithography enables the fabrication of microstructures down to 10 nm[17]. However, the facility of photolithography is expensive. As to the soft lithography, the PDMS is poured on the pre-fabricated mold. After being cured and peeling off from the mold, the PDMS slab is then bonded to the glass substrate. Laser etching enables the fabrication of microstructures in polymers. Materials are sublimated due to high temperature from the laser, and the depth of microstructures can be controlled by the laser intensity. In hot embossing, the hot mold is pressed into thermoplastic materials, for example, PMMA. Under the high temperature and pressure, microstructures can be obtained in PMMA. This technique is rather straightforward and suitable for mass production. However, it may cause the deformation of microfluidic chips due to high temperature. Machining process is another fabrication method for microfluidic chips. The materials are precisely milled in a programmable manner with a machine tool. In this method, the resolution can reach up to tens of micrometers.

With the improvement of resolution, some researchers used 3D bioprinting to fabricate microfluidic chips[18]. In 3D bioprinting, the microfluidic chip is fabricated in a layer-by-layer manner. The major advantage of 3D bioprinting is that it is an integrated fabrication method, and enables 3D complex structures. Using 3D bioprinting, the microfluidic chip can be fabricated in one-step. The assembling errors in chip assembly can be avoided[19]. To date, various microfluidic chips have been fabricated with high definition and high quality.

2.2. Microtissues

The second component of heart-on-a-chip is the microtissues. According to the dimension, microtissue can be divided into 2D microtissue and 3D microtissue. Based on the cells in microtissue, it can be divided into single type of cells and co-culture of multiple types of cells (see **Table 1** for the details). Both dimension and cell types have significant influence on cell shape, alignment, expression of structural protein, and sarcomere length and beating.

(1) Cells in heart-on-a-chip

Cell type and source are the key parameters that may affect the performance of heart-on-a-chip. The adult heart is mainly composed of cardiomycytes (CMs), human cardiac fibroblasts (hCFs), endothelial cells, and others, which can perform different functions to make the heart work. Although CMs only account for ~33% of the total number of cells, they account for ~75% of the heart volume[20]. CMs are responsible for heart beating and considered as the most important cells. Thus, CMs are usually adopted in heart-on-a-chip. Usually, human cells are favorable since the purpose of heart-on-a-chip is to study heart disease of human beings. Unfortunately, it is difficult to obtain human cells directly. To date, the frequently used cells in heart-on-a-chip are animal's primary cells and/or commercial cell lines. The animal cells are different from human cells in term of species. One possible solution to the dilemma is the use of induced pluripotent stem cells (iPSCs) which offer an almost unlimited source of cells[21]. As a novel technique, deriving CMs from iPSCs are still unsatisfying as the cells are usually phenotypically immature. Improving the maturity of CMs is the challenging part of developing heart-on-a-chip.

(2) Fabrication of microtissues

As aforementioned, microtissues can be divided into 2D and 3D types. In 2D microtissues, cells are cultured in a planner layer. Patterning cells are an important task for 2D microtissues fabrication[22]. Micro-contact printing is the most frequently used technique for cell patterning[23,24]. In this method, the pattern of liquid biomaterials is realized on the surface of a substrate through conformal contact with the soft mold (**Figure 2A**)[25]. The area with liquid biomaterial (*e.g.* fibronectin and hyaluronic acid) is adhesive to living cells. Thus, cells proliferate on these patterning areas only. Gabriele *et al*. dipped fibronectin with PDMS mold and then transferred to the substrate[26]. Due to the good biocompatibility of fibronectin, cells tend to adhere and grow on the area with fibronectin. In this manner, they obtained 2D microtissues with well-controlled shape.

The tissues *in vivo* are usually in 3D morphology. It has been found that the 2D and 3D microtissues are different in protein expression and drug response. To

Table 1. Some representative microtissues in heart-on-a-chip

Features	Fabrication methods	Cells	Materials	Functionalities
Patterned microtissues	Soft lithography[22,27] Microcontact printing[22-25] Electrospinning[44] 3D bioprinting[28]	HUVECs[22] Rat CMs[24,25,28] Fibroblasts[24]	PAAm[22] Collagen[24] GelMA[28] MeTro[25]	To study the influence of stiffness on cell morphology[22] To promote the attachment, spreading, alignment, and intercellular communication[24,25,28]
Vascularized microtissues	3D bioprinting[30,34,100] Photocuring[32] Lithography[34]	HUVECs[30,34,98] iPSC-CMs[30] Rat CMs[32]	Alginate[30] GelMA[30,98] PEGDA[98], hydroxybutyl chitosan (HBC)[34]	To align cardiomyocytes that can contract synchronously[30,32]
Microtissues with multiple cells	3D bioprinting[31,33]	NIH/3T3[33], C2C12[33] iPSC-CMs[29,31] Endothelial cells[29]	GelMA[31,33] Alginate[31] Gelatin, Fibrinogen[29]	Biomimetic heterogeneous tissues[31,33] Multiple-organs-on-a-chip[29]

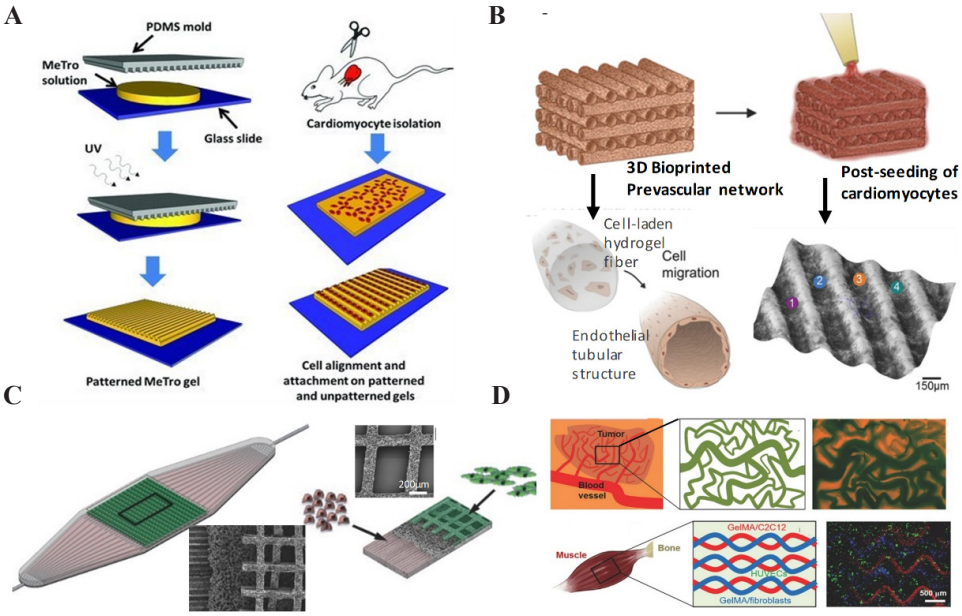


Figure 2. Microtissues in heart-on-a-chip. (A) 2D patterned microtissues by micro-contact printing (Republished with permission from Annabi N, Tsang K, Mithieux SM, *et al*., *Advanced Functional Materials*, © 2013 WILEY-VCH Verlag GmbH and Co. *KGaA,* Weinheim). (B) 3D vascularized microtissue by 3D bioprinting (Republished with permission from Colosi C, Shin SR, Manoharan V, *et al*., *Advanced Materials*, © 2015 WILEY-VCH Verlag GmbH and Co. KGaA, Weinheim.) (C) 3D hydrogel scaffold for the co-culture of CMs and vascular endothelial cells (Republished with permission from Morgan KY, Sklaviadis D, Tochka ZL, *et al*., *Advanced Functional Materials,* © 2016 WILEY-VCH Verlag GmbH and Co. KGaA, Weinheim.) (D) Microtissues with multiple cells by 3D bioprinting (Republished with permission from Miri AK, Daniel N, Luis I, *et al*., *Adv Mater*, ©2018 WILEY-VCH Verlag GmbH and Co. KGaA, Weinheim)

fabricate the 3D microtissues, various methods have been proposed, including photolithography, electrospinning, and 3D bioprinting. Among them, 3D bioprinting is considered a promising technique to fabricate 3D microtissues. The cell-laden bioinks are printed through the nozzle of a 3D printer. Bioinks are of great importance for 3D bioprinting of microtissues. So far, the most frequently used bioinks are hydrogels. Hydrogels have similar structure with ECM and porous properties as well as good diffusion of biomolecules. Thus, they are promising candidates for the fabrication of microtissues and simulation of the growth environment for cardiac cells *in vivo*[27]. Their stiffness is adjustable and the biocompatibility is good after modification.

Some researchers used 3D bioprinting to fabricate microtissues in heart-on-a-chip. Chen *et al*. prepared CMs-laden GelMA and fabricated the cardiac microtissues using 3D bioprinting[28]. The phonotype of cells is similar with the cells *in vivo*. Hydrogel based 3D bioprinting has shown a great potential in fabrication of microtissues. Due to the good biocompatibility, hydrogel-based microtissues provide ideal microenvironments for cell growth and proliferation. Recently, some researchers have attempted to print the microtissues together with microfluidic chips in one step. For example, Lewis *et al*. used multi-materials (six functional bioinks) and fabricated the heart-on-a-chip by 3D bioprinting technology[12]. Using this chip, the alignment of cells can be well controlled by fabricating some microgrooves in the chip.

(3) Multiple cells in heart-on-a-chip

Native tissues are generally composed of multiple cells, which are necessary to implement the complex functions. To better mimic the heart function, some researchers used multiple cells to fabricate the microtissues[29,30]. To fabricate the vascularized cardiac microtissues, Colosi *et al*. developed a 3D bioprinting platform with a coaxial printhead. The human umbilical vein endothelial cells (HUVECs)-laden bioink (including alginate and GelMA) was squeezed out of the printhead, and formed the 3D scaffold. Then, cardiomyocytes were seeded in the scaffold. After a few days of culture, the vascularized cardiac microtissues were obtained (**Figure 2B**)[31]. Morgan *et al.* fabricated polymer scaffold with multiscale porous structure and then co-cultured cardiomyocytes and HUVECs on the structure. They successfully obtained the vascularized cardiac microtissue (**Figure 2C**)[32]. Miri *et al*. developed a printing platform to fabricate the multi material heterogeneous hydrogel microstructures[33]. This platform can quickly switch between different nozzles that have loaded different hydrogels and cells, and thus, enable multi-material printing (**Figure 2D**). The system

provides a platform for high-resolution printing of microtissues.

Besides 3D bioprinting, some other methods have been employed to fabricate 3D cardiac microtissues. Fenech *et al*. used photolithography to fabricate the network of blood vessels with microvessel diameter ranging from 5 μm to 120 μm[34]. The microvessel caters to the needs of the large-scale cardiac tissues by providing nutrition and discharging waste. Bartholoma *et al*. have fabricated a scaffold-free functional cardiac spheroids which can perform spontaneous beating and synchronous contraction[35]. Since the fabrication process is simple, the cardiac spheroids have been widely used in drug screening.

2.3. Microactuators

The third component of heart-on-a-chip is the microactuators, which are used to impose external stimuli to cells/microtissues. In the native tissues, cells are subjected to various chemical, mechanical, and electrical cues, which significantly affect the cell behaviors. In heart-on-a-chip, the main function of microactuator is to stimulate the cells/microtissues to promote their maturation. In this section, we discuss the fabrication of microactuators for electrical and mechanical stimulation.

(1) Electrical stimulation microactuators

It is known that CMs are responsive to electrophysiological stimulation. Electrical stimulation can increase the percentage of cells that beat spontaneously and assist in cell synchronization and calcium processing. In a heart-on-a-chip, electrical stimulation is usually performed through electrodes that are in contact with cells[36]. A variety of materials have been applied to fabricate electrical actuators in heart-on-a-chip, including copper, graphite, titanium, silver, platinum, and alloys[37]. As a commonly used electrode, graphite has good machining performance, and is wear-resistant and low-cost. Margari *et al*. fabricated an engineered heart-on-a-chip which includes graphite electrodes and gold electrodes[38]. The hPSC-CMs were cultured on the electrodes and the CMs became mature after 14 days. Platinum and titanium electrodes are also used in heart-on-a-chip. Zhang *et al*. fabricated a 3D cylindrical platinum electrode, which can electrically stimulate the cells for a few weeks[39]. The advantage of using platinum and titanium is that they have high corrosion resistance.

Some metal electrodes may cause toxic reaction in the culture, and the electrodes may degrade due to the electrochemical reaction with the culture medium. An alternative solution is the indium tin oxide (ITO) film, which has good conductivity, optical transparency, stability, and non-toxicity. Kang *et al.* used ITO to electrically stimulate neonatal rat ventricular myocytes. It was found that electrical stimulation results in a well-organized sarcomere structure and upregulates the heart-specific gene expression[40]. Nieto *et al.* fabricated a chip and stimulated the H9C2 cells by depositing an aluminum film on soda lime glass with physical vapor deposition (PVD) method[41]. Recently, 3D bioprinting has been used to fabricate electrodes in heart-on-a-chip. Lin *et al.* 3D printed the microprobes with the conductive polymer poly (3,4-ethylenediox-ythiophene): polystyrene sulfonate (PEDOT: PSS)[42]. Adly *et al.* fabricated microelectrode arrays (MEAs) with a high resolution by ink-jet printing. In this method, the conductive material was deposited the substrate which was composed of PDMS, agarose, and gelatin[43].

In natural myocardial tissues, CMs show synchronous contraction through intercellular electrical communication, resulting in a strong contraction force. It has been found that it can promote electrical communication and maturation of myocardial tissues by adding conductive materials, for example, carbon nanotubes (CNTs), to cell culture scaffolds. The directional conduction of CNTs can regulate the alignment of CMs and improve their beating and contractility. Some researchers have fabricated CNTs or silk scaffolds by electrospinning and found that the materials can improve the maturity of CMs[44].

(2) Mechanical stimulation microactuators

In addition to the electrical stimulation, mechanical stimulation also plays an important role in heart. It has been found that the external mechanical forces can affect the alignment, phenotype, calcium concentration, and contractile properties of CMs[45]. In this section, we mainly discuss two types of mechanical stimuli, mechanical stress, and mechanical properties of substrate.

A variety of devices have been developed to impose mechanical stress to CMs with the purpose to mimic the physiological functions of heart. We would introduce two types of mechanical stress microactuators, the electromagnetic microactuators, and pneumatic microactuators. Electromagnetic microactuators are widely used due to its stability and high sensitivity. Li *et al.* fabricated a device to impose mechanical stress to cells. In their experiments, the magnetic particles were mixed to the cell-laden hydrogels. The electromagnetic microactuators were placed at the ends of hydrogel structures. In this manner, the non-contact electromagnetic force can be applied to the cells[46]. The force is well controlled in magnitude, frequency, and duration by the electromagnetic microactuators. This method was successful in promoting the maturation of CMs. As to the pneumatic actuators, Rasponi *et al.* have developed a heart-on-a-chip that can mimic the mechanical microenvironment of native CMs[47]. The chip includes

a pneumatic system that can impose uniform uniaxial cyclic strain to the 3D microtissues.

The substrate stiffness is another mechanical stimulus in heart-on-a-chip. In the native myocardial tissues, the mechanical property, for example, stiffness is spatially non-uniform which has been observed in the tissue slices[48]. The stiffness would affect the cells in growth, differentiation, gene expression, and protein secretion. It has been found that the CMs would have sarcomere in 48 h when cultured on the soft substrate. However, the sarcomere was not observed when cells were cultured on the medium stiffness substrate. Studies have been conducted to evaluate the effects of 2D substrate stiffness on CMs contraction rate, stress, and intracellular calcium concentration. Experimental results indicate that the contraction force of CMs *in vitro* would change with matrix stiffness in a time-dependent manner. Bajaj *et al*. cultured embryonic chicken CMs on PAAm gels with different stiffness. They have found that the stiffness of gels affects the beating frequency in 24 h[49].

Moreover, the surface morphology of substrate also affects the behavior of cells. In heart-on-a-chip, the microstructure on substrate can regulate the alignment of CMs, which is a critical factor influencing the contraction force. Lewis *et al*. fabricated a heart-on-a-chip by 3D bioprinting. In this chip, they fabricated microgroove structures on the surface of substrate. The CMs were cultured on the substrate surface and cells tend to orient along the grooves. By regulating the alignment of CMs, the contraction force would be enhanced since cells tend to contract along the same long axis[12].

Some researchers have simultaneously imposed the electrical and mechanical stimuli to cells. Murry *et al*. found that if both electrical and mechanical stimuli are imposed, the hESC-CMs can mature at a faster pace[50]. Later, they used hiPSC-CMs and collagen to construct the engineered cardiac microtissues and studied the effect of mechanical conditions and electrical stimulation on the maturation of cardiac tissue[51]. Rasponi *et al.* developed a biological reactor which can provide a uniform electric field and periodic uniaxial strain to the 3D cardiac microtissues[52].

2.4. Microsensors

Microsensors are the fourth elements in heart-on-a-chip. The function is to monitor the status of cells/microtissues in heart-on-a-chip. At the early stage, some biochemical reagents were used to stain cells to characterize their status and functionalities. The disadvantage is that this method is destructive to cells, and it is difficult to implement the real-time monitoring. In recent years, some researchers have begun to integrate microsensors in heart-on-a-chip to monitor the physiological status of cardiac cells noninvasively[53].

(1) Measurement of contraction force

One property of CMs is that it can generate contraction force. The contraction force is an important indicator of CMs status. The contraction of CMs is visible in the microscope, but it is difficult to quantify the contraction force by direct observation. The atomic force microscopy (AFM) and traction force microscopy (TFM) are capable to quantify the contraction force. However, it may affect behaviors of the cells[54]. Moreover, the instruments are expensive and complex to operate. Some researchers integrated microsensors in heart-on-a-chip to measure the contraction force of CMs (see **Table 2** for the details).

One commonly used method is to fabricate an elastic component in heart-on-a-chip. The CMs cultured on the elastic component would cause the visible deformation of the component[55-58]. The elastic component could

Table 2. Microsensors for contraction force measurement in heart-on-a-chip

Mechanism	Structures	Materials	Cells	Applications	Measured values
Visible deformation	Biowires[62,63,93] Cantilever[59,64] Micropillars[57] Helical structure[56]	POMaC[62] PDMS[59] Hydrogel[57,64]	iPSC-CMs[62,63] Rat CMs[59,64] HCFs[63]	Cell maturation[57,62] Drug screening [57,59,62,63] Disease model[63]	Contraction force 2.89-5.09 μN[64] ~40 μN[62] Contractile stress ~15.4 kPa[59] ~1.7 kPa[57]
Electrical sensors	Piezoelectric[69] Crack sensor[74] Piezoresistive[12,67,68]	AlN[69] Pt-PDMS[74] CNTs-PDMS[68] CB:TPU[12]	Rat CMs[12,67,72,74] iPSC-CMs[68,69]	Drug screening[9,12,67-69]	Contraction force ~107 nN[74] Contractile stress ~2.34 kPa[68] 7-15 kPa[12]
Structural color	Cantilever[56] Biological-Crawling robot[66]	GelMA[66]	Rat CMs[66]	Drug screening[56,66] Biological soft robots[66]	crawling speed 20 μm/s[66]

be in different shape, for example, film, cantilever, or micropillars. The contraction force of CMs would bend the elastic component, and the deformation is observed and recorded by a microscope. Then, the contraction force can be calculated by image processing. Parker *et al*. fabricated the PDMS films in a heart-on-a-chip, and they cultured cells on these films which are referred to as muscular thin films (MTFs)[59]. The deformation caused by the contraction force can be read out by the optical signal. Using this platform, they studied the influence of temperature and electrical stimulation on the contraction force (**Figure 3Ai**). Some researchers used micropillars to measure the contraction force. Cells cultured on the micropillars tend to adhere to the tips[60]. When the cell contracts, it would deflect the surrounding micropillars (**Figure 3Aii**)[61]. The micropillars can be fabricated by soft lithography or other methods. Another similar structure that can measure contraction force is the biowires[62,63]. In this method, the microtissues tend to enlace the two wires and the contraction force drags them to each other (**Figure 3Aiii**). Bashir *et al*. fabricated microcantilevers using 3D bioprinting with cross-linkable hydrogels. The cantilevers have similar mechanical properties with native myocardial tissues and can be used to measure the contraction force. Using this device, they studied the influence of substrate stiffness on the contraction force[64]. Chen *et al*. fabricated similar microsensors by 3D bioprinting. They obtained microcantilevers with CMs-laden GelMA hydrogel and measured the contraction force[28].

Another method to measure the contraction force is to use the structure coloration. Zhao *et al*. fabricated a heart-on-a-chip with thin films which was made of the material inverse opal structure GelMA hydrogel[65]. The material would change its color when subjected to external force. In this manner, the thin films performed as microsensors and the contraction of myocardial cells would cause a visible color change (**Figure 3Bi**). Such microsensors can be used to characterize the beating frequency of CMs. Zhao *et al*. also fabricated a micro-robot which was powered by the CMs. The materials of micro-robot include CNT and the inverse opal structure GelMA hydrogel (structure color material)[66]. The micro-robot can mimic the crawling behavior of a caterpillar (**Figure 3Bii**). The crawling speed and structural color are the indicators of myocardial tissues status.

The above-mentioned methods are referred to as direct methods. The contraction force-induced deformation is usually observed under a microscope, making it inconvenient to some extent since the heart-on-a-chip is usually laid in the incubator for culture. An alternative is to embed piezoelectric or piezoresistive materials into the microsensors. When the contraction force causes the deformation in the elastic component, the electrical voltage or electrical resistance would be changed. In other words, the contraction force is transferred to the electrical signal by the microsensors[67].

Sun *et al.* developed a deformable PDMS membrane with CNT (a piezoresistive material) embedded inside. They cultured hiPSC-CMs on the membrane. After a period of incubation, the cell begun to contract and the contraction force causes the change of electrical resistance of CNT (**Figure 3Ci**). This platform can continuously measure the contraction force and beating rate of CMs in a long term (14 days)[68]. Another choice is to use the piezoelectric material to measure the contraction force[69-71]. When the contraction force triggered the deformation, an electrical voltage (and thus a measurable current) is generated in the piezoelectric material. No external voltage is required for using this method.

The limitation of the piezoelectric and piezoresistive microsensors is that they have low sensitivity[69,72]. Crack-based microsensors may overcome this limitation[73]. Under the same contraction force, the sensitivity of crack-based microsensor is 900 times higher than that of piezoresistive microsensor. Lee *et al.* fabricated an integrated high-sensitivity crack microsensor within a PDMS cantilever. The contraction force of CMs leads to the deformation of cantilever and further causes the distance change in the crack[74]. When used in heart-on-a-chip, the crack-based microsensors have high sensitivity and accuracy (**Figure 3Cii**).

For the aforementioned microsensors in heart-on-a-chip, the fabrication is still challenging. 3D bioprinting is a powerful technique and can be used to fabricate the microsensors. Lewis *et al*. developed a multi-materials 3D bioprinting platform to fabricate the heart-on-a-chip[12]. They prepared six functional bioinks, including polyurethane (TPU), carbon black (CB), PDMS, and dextran, to print the chips. In this heart-on-a-chip, they integrated a flexible microsensor which performed well in monitoring the contraction of CMs. To fabricate the microsensors by 3D bioprinting, choosing the conductive material is a key task. Recently, a conductive polymer, poly(3,4-ethylenedioxythiophene): polystyrene sulfonate (PEDOT: PSS), has attracted considerable attention[42]. This material has shown excellent printability, high conductivity, high resolution (~30 μm), and good biocompatibility. This material is a promising candidate to fabricate the microsensors in heart-on-a-chip.

(2) Measurement of electrophysiological signals

Electrophysiological signal is another important indicator of CMs. Some researchers fabricated microsensors in heart-on-a-chip to detect the electrical activity of CMs. The planar MEA made of metal electrodes (gold or platinum) is a conventional tool to monitor the electrophysiology of CMs. Besides metal, some other conductive materials

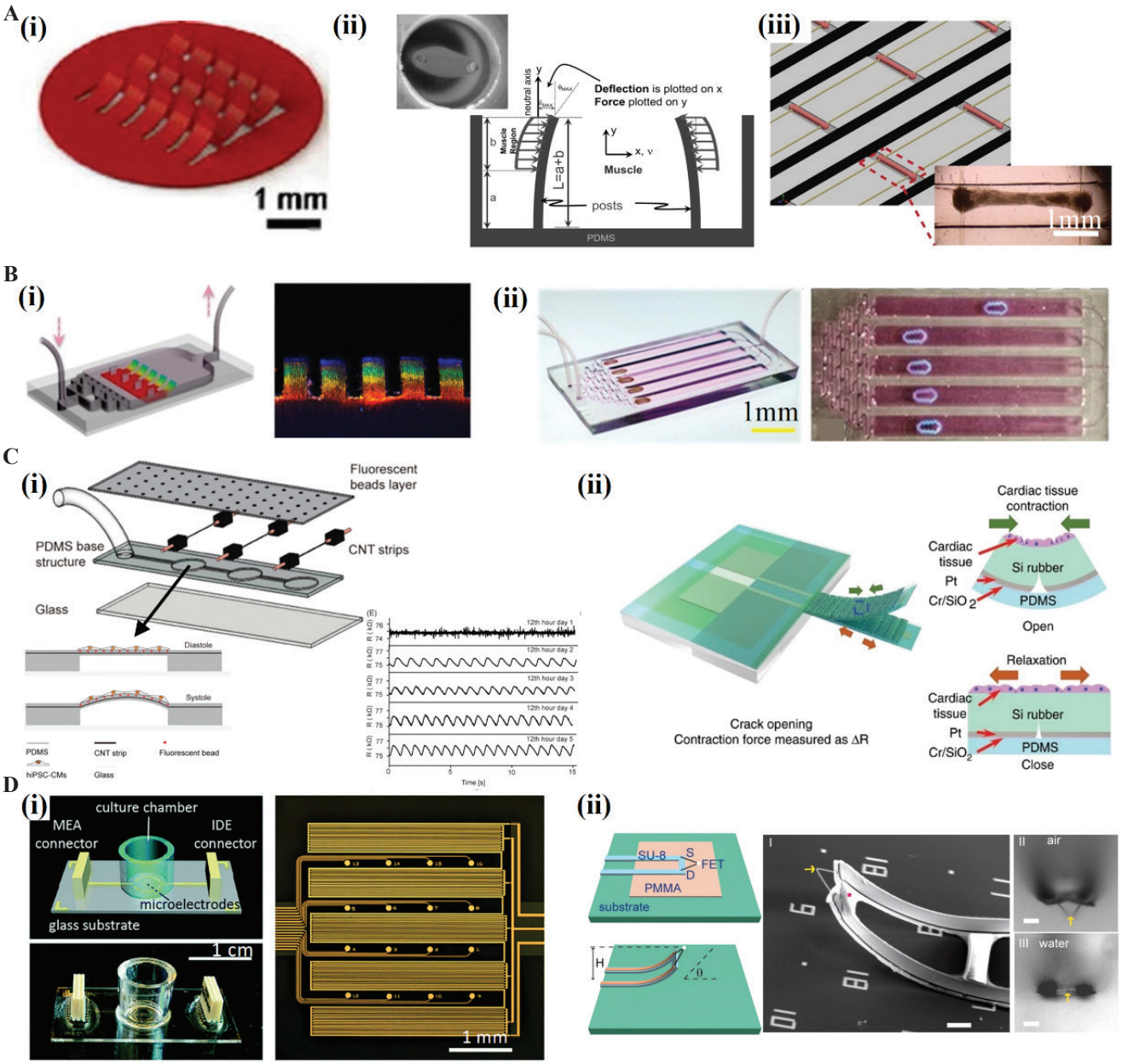


Figure 3. Microsensers in heart-on-a-chip. (A) Mechanical stress microsensors based on the visible deformation. The CMs can be cultured on different structures and result in the deformation. (i) MTFs (Reproduced from ref.[59] with permission from The Royal Society of Chemistry); (ii) micropillars (Republished with permission from Vandenburgh H, Shansky J, Benesch-Lee F, *et al*., Muscle Nerve, © 2008 WILEY-VCH Verlag GmbH and Co. KGaA, Weinheim). (iii) biowires (Republished with permission from Zhao Y, Wang EY, Davenport LH, *et al*., Adv Healthcare Mater, © 2019 WILEY-VCH Verlag GmbH and Co. KGaA, Weinheim). (B) Mechanical stress microsensors based on structure color. The microsensors can be designed to different structures. (i) MTFs (Republished with permission from Fu F, Shang L, Chen Z, *et al*., *Science Robotics*, 2018, 3(16): aar8580); (ii) microrobots. (Republished with permission from Sun L, Chen Z, Bian F, *et al*., 2020., Advanced Functional Materials, 2019, Weinheim) (C) Mechanical stress microsensors based on the electrical sensors. (i) Piezoresistive microsensors embedded inside the membrane (Adapted with permission from Wang L, Dou W, Malhi M, *et al*., 2018, Microdevice Platform for Continuous Measurement of Contractility, Beating Rate, and Beating Rhythm of Human-iPSCs-Cardiomyocytes inside a Controlled Incubator Environment. ACS Applied Materials and Interfaces, 10(25): 21173-83. Copyright (2018) American Chemical Society); (ii) crack-based microsensors (from ref.[74] licensed under Creative Commons Attribution 4.0 license) (D) Electrophysiology microsensors. (i) 2D MAE array for action potential and impedance readout (Reproduced from ref.[76] with permission from The Royal Society of Chemistry); (ii) 3D nanoelectrodes, scale bar = 5 μm (Tian B, Cohen-Karni T, Qing Q, *et al*., Science, 2010,329(5993): 830-4).

are also available for MEA. Offenhäusser *et al.* proposed a graphene-based MEA microsensors and monitored the extracellular action potential of CMs[75]. The MEA can detect local action potentials with high spatial resolution and high sensitivity, but failed to measure the contractility of CMs. Some researchers combined the MEA and interdigital electrode (IDE) together to measure the action potential, contraction force, beating rate, and other parameters (**Figure 3Di**)[76]. The MEA is an electrically stable, high-throughput, and non-invasive microsensor for recording the electrophysiology of CMs.

Sometimes, the microtissues in heart-on-a-chip are in 3D and thus 3D electrodes are required to measure the electrophysiological signals in the microtissues. To date, various 3D nanoelectrode structures have been developed, including nanotubes, nanopillars, and mushroom-shaped electrodes[77]. Lieber *et al*. fabricated a nanoscale field-effect transistor device which shows a high sensitivity in water and acid/alkali solution. They modified the transistor surface with phospholipid bilayers and implemented the real-time monitoring of intracellular potentials of single cell (**Figure 3Dii**)[77]. Abbott *et al.* fabricated nanoscale intracellular electrodes and realized a high-fidelity electrophysiological image for neonatal rat cardiomyocytes[78]. Some researchers used 3D plasma nanoelectrodes to record the electrical activities inside and outside the cells for a long term. Lieber *et al.* introduced a 3D nanoelectrode array that mimics the tissue scaffold. The device can simultaneously map the action potential in three dimensions in real time. This heart-on-a-chip with 3D nanoelectrode array can realize the monitoring of electrophysiological activity in the process of culture and development[79].

3. Biomedical applications of heart-on-a-chip

Heart-on-a-chip has found various applications, including physiology study, disease modeling, and drug screening. Compared with the traditional techniques, heart-on-a-chip can better mimic the cellular microenvironment and promotes the maturation of microtissues. In addition, heart-on-a-chip enables the real-time monitoring of the status of cells/microtissues. In this section, we discuss the applications of heart-on-a-chip in physiology study, disease modeling, and drug screening.

3.1. Physiology study

With the assistance of heart-on-a-chip, we can enhance our understanding in the physiological characteristics of heart. One feature of CMs is that they can rhythmically beat and are responsive to external stimuli such as force and electricity. Yasuda *et al*. used agarose material and fabricated a heart-on-a-chip with microchamber array[80]. They cultured single CM in each microchamber, and observed the beating cycle of CM. By changing the distance between two adjacent microchambers, they confirmed the clustering effect of CMs. Another feature of CMs is contraction, and the contraction force is an important indicator of cell physiological state. Varghese *et al*. fabricated a heart-on-a-chip, and studied the influence of electrical stimulation on the contraction force of CMs[81].

Some researchers fabricated heart-on-a-chip with the biowire structures. Two flexible wires fabricated from a poly(octamethylene maleate (anhydride) citrate) (POMaC) polymer are secured with adhesive glue. The chip was used to study the response of immature CMs to electrical stimulation. It was found that electrical stimulation could increase the microstructure of myofibrils, increase the electrical conduction, and change the properties of electrophysiology and calcium ion transients. The human circulatory system is composed of the heart and a complex network of blood vessels. Blood pressure is an important issue of blood circulation, and it can be studied by heart-on-a-chip. Sethu *et al.* designed a chip which can accurately simulate the hemodynamic stress, and they found the stress can promote the maturation of CMs[82]. Wu *et al.* developed a heart-on-a-chip to simulate the circulation system[83]. The chip includes four pump units representing the four heart chambers, and the pressure is controllable to study its influence on the cells (**Figure 4A**).

3.2 Disease modeling

Disease modeling is an important step in analyzing disease mechanisms and developing drugs for treatments[84]. Coronary heart disease refers to the stenosis or blockage of the vascular lumen caused by coronary atherosclerosis. Coronary heart disease may lead to the myocardial infarction in the later stage. For a better understanding of the coronary heart disease and for exploring effective treatments, Wang *et al*. designed a heart-on-a-chip in which the oxygen was well controlled to study the myocardial damage caused by hypoxia (**Figure 4B**)[85]. Liu *et al*. fabricated the heart-on-a-chip to model the non-uniform oxygen distribution. The model can mimic the blockage of coronary arteries and study the electrophysiological response of myocardial hypoxia[86]. For CMs, the activity of Ca^{2+} channels would affect the contraction. Elvassore *et al*. designed a heart-on-a-chip and found that the hypoxia would induce the reversible change of Ca^{2+} concentration in CMs[87].

Cardiac fibrosis could form a large number of fibrosis scar tissue, and lead to heart failure. Heart-on-a-chip can be used to simulate the cardiac fibrosis model by controlling the number of fibroblasts and the concentration of collagen in the engineered microtissues. Experimental results showed that increasing the fibroblast density can reduce the contraction force[12]. Some researchers used 3D hydrogel microtissues to model the cardiac fibroblasts[88].

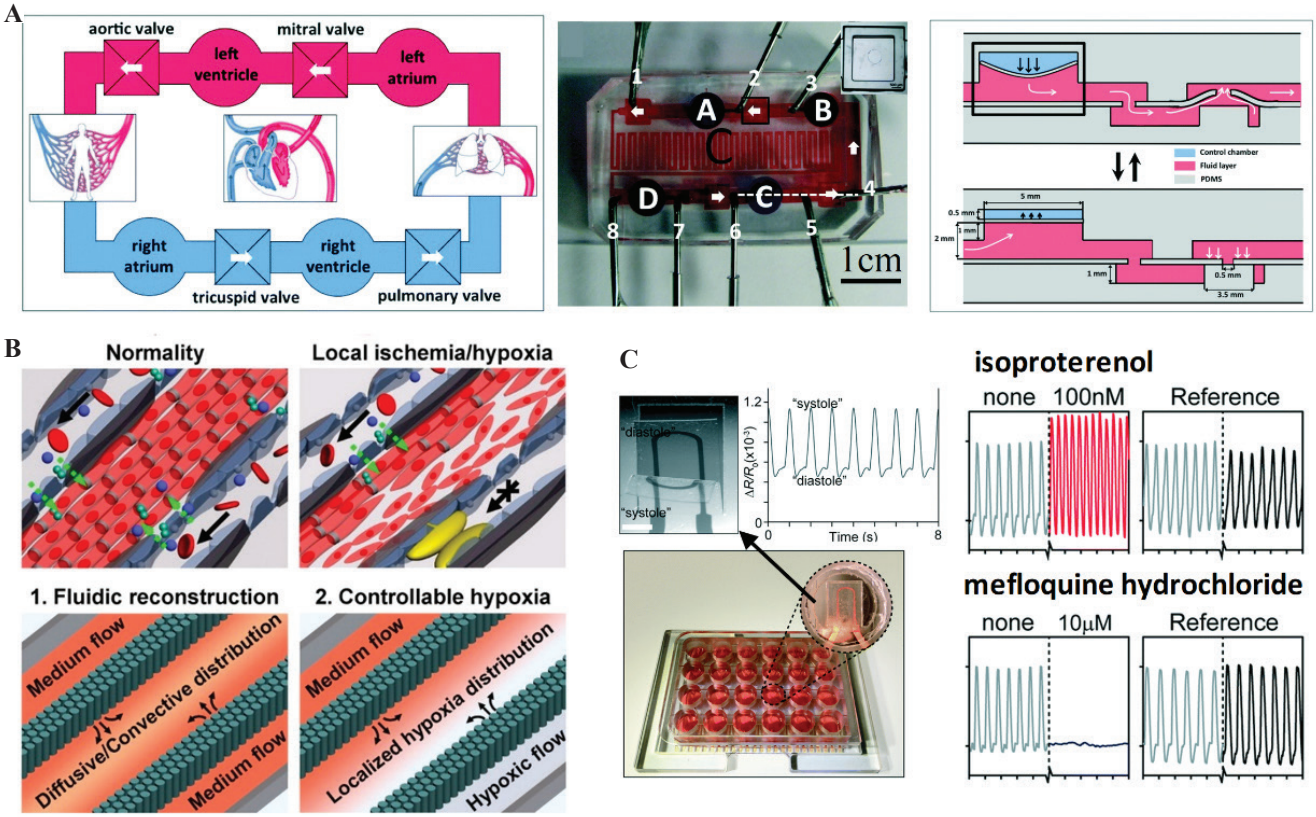


Figure 4. Biomedical applications of heart-on-a-chip. (A) Physiology study. The chip was composed of four microchambers to mimic the heart and the microfluidic channels to mimic the network of blood vessels. Its function is to study the working mechanism of circulatory system (Reproduced from ref. [83] with permission from The Royal Society of Chemistry). (B) Disease model. The heart-on-a-chip was designed to model the hypoxia-induced myocardial injury (Adapted with permission from (Ren L, Liu W, Wang Y, *et al*., 2013, Investigation of Hypoxia-Induced Myocardial Injury Dynamics in a Tissue Interface Mimicking Microfluidic Device. Analytical Chemistry, 85(1): 235-244). Copyright (2013) American Chemical Society.) (C) Drug screening. The high-throughput chip with iPSC-CMs microtissues was used to test the effect of isoproterenol and mefloquine hydrochloride (Reproduced from ref.[72] with permission from The Royal Society of Chemistry).

The advantage is that the microenvironment is close to the native tissues and the mechanical properties are controllable. These models in heart-on-a-chip can be used to study the pathology of cardiac fibrosis, and therefore, lay a basis for exploring the effective treatments.

Another cause of heart failure is the arrhythmia, which refers to the disturbed heartbeat rhythm caused by the abnormal cardiac electrical activity[89]. Heart-on-a-chip has been used to model the arrhythmia and related cardiovascular diseases. Healy *et al.* constructed a 3D *in vitro* arrhythmia model by heart-on-a-chip. They used the iPSCs-derived CMs and filamentous matrix to fabricate the 3D microtissues[90]. They studied the electrophysiological signals and contraction force related to arrhythmia. Using the chip, the response to a group of drugs was also investigated. In addition, there have been some studies using heart-on-a-chip to model other cardiovascular conditions, such as hypertension or hypotension and hypertrophy[91].

3.3. Drug screening

Drug screening is one of the most important applications of heart-on-a-chip. For some drugs, the side effect may cause heart damage or even heart failure. Thus, it is necessary to study the drug-induced cardiotoxicity. Heart-on-a-chip as an effective and accurate *in vitro* model can be used to evaluate cardiotoxicity. Parker *et al*. have found that the isopropylnoradrenaline has a positive influence on the contraction force of CMs using heart-on-a-chip[59]. Ren *et al*. fabricated a heart-on-a-chip for high-throughput drug screening[92]. They chose clinically approved doxorubicin and cyclophosphamide as model drugs to examine dose-dependent cardiotoxicity, and ivabradine and carbachol as candidates for ameliorating cardiotoxicity.

As discussed in the previous section, the 3D microtissues are different from 2D microtissues in morphology and functionality. Some researchers suggested to use 3D microtissues for drug response in heart-on-a-

chip. Compared with the 2D microtissues, the heart-on-a-chip with 3D microtissues is complex in structure and thus, the throughput is lower. However, the advantage is that the functionalities are close to native tissues and the maturation is improved. Nakayama *et al.* fabricated a heart-on-a-chip with 3D microtissues using 3D bioprinter. The cell spheroids were printed on the micropillar array, and the contraction force of the 3D microtissues was evaluated by measuring the micropillar deformation. The platform can be used for drug screening by adding drugs into the device and observing the response afterward. Chen *et al*. fabricated the 3D microtissues using 3D bioprinting, and monitored the concentration of calcium. They found that the isopropylnoradrenaline can affect the calcium concentration[28]. Zhao *et al*. designed a heart-on-a-chip with biowire structures, which can be used for drug screening and gene expression testing. This chip can record the contraction force and calcium concentration in real-time[93]. Paker *et al*. fabricated a heart-on-a-chip with 24 MTFs and each MTF can detect the contraction force and beating frequency of cardiomyocytes. Using this heart-on-a-chip, they tested the influence of 12 drugs (*e.g.* Isradipine, Nicardipine, Clofilium, and Flecainide) and demonstrated the application of this chip in drug screening (**Figure 4C**)[72]. Wan *et al.* fabricated a heart-on-a-chip with 3D microtissues and used it for cardiotoxicity studies of drugs (antibiotics, antidiabetic drugs, and anticancer drugs). Compared with the 2D model, the 3D microtissues performed better in drug screening. The results by 3D microtissues are consistent with clinical observations[5].

4. Summary and outlook

In this paper, we review the recent advances of heart-on-a-chip, including the history, structures, fabrication methods, and the biomedical applications. Collectively, we propose that a highly integrated heart-on-a-chip includes four elements: Microfluidic chip, cells/microtissues, microactuators, and microsensors. The microfluidic chip and microtissues are necessary for a heart-on-a-chip. The microactuators can be used to impose electrical and/or mechanical stimuli to cells. The microsensors are designed to monitor the performance of cells in heart-on-a-chip. Various methods have been proposed to fabricate heart-on-a-chip. We shed light on the 3D bioprinting which is a promising technique and can enable the one-step fabrication of heart-on-a-chip. 3D bioprinting has greatly improved the complexity, functionality, and efficiency of heart-on-a-chip. Heart-on-a-chip has found broad applications in biomedical engineering, including physiology study, disease modeling, and drug screening. At present, the development and applications of heart-on-a-chip are still in its early stage, and facing some challenges.

An important challenge for heart-on-a-chip is to better mimic the microenvironment of native cells[94]. The challenges include addressing the issues pertaining to cell alignment, multiple cells co-culture and external stimuli which are key factors to improve cell maturation and functionalities. They can be implemented by fabricating micro-patterned substrate, complex 3D scaffold, and vascularized tissues. It is still challenging to fabricate these structures. Perhaps, 3D bioprinting is a possible solution which has shown a great potential in biofabrication. To date, 3D bioprinting has enabled cell alignment, co-culture of multiple cells, and vascularized myocardial tissue. Nevertheless, precise regulation of cell microenvironment (especially the spatial-temporal anisotropic microenvironment) still needs further exploration.

There are considerable research on the microsensors in heart-on-a-chip[53]. However, the accuracy and sensitivity are still unsatisfying. PDMS as an elastic material is widely used in microsensors to measure conTFM. The modulus of PDMS is still high and thus the deformation caused by CMs is relatively small. For the microsensors based on optical method, it is complex to measure the contraction force. The strain microsensors can read out the contraction force directly, but the stability, linearity, and accuracy of the microsensors are not satisfying[7]. With the advances of wearable and flexible electronics, more microsensors have been invented. These microsensors could be used in heart-on-a-chip, and monitor the status of cells.

As a promising technique, 3D bioprinting has shown a great potential in fabricating highly integrated heart-on-a-chip in one step[95]. Using 3D bioprinting, it becomes possible to fabricate the microfluidic chip, microtissues, microactuators, and microsensors on the same platform. On the basis of 3D bioprinting, some researchers developed 4D bioprinting method[96]. In 4D bioprinting, smart materials were used and the printed objects can change their shapes or functionalities with time. This technique can be used to fabricate microactuators and impose mechanical stress to cells. For 3D/4D bioprinting, there are still challenges, such as on how to improve the resolution and develop novel materials with good printability and mechanical properties.

Another challenge for heart-on-a-chip is the commercialization. To ensure the physiological state of the cardiac cells, the storage and transportation should be considered which are necessary for the off-the-shelf use. One possible solution is to use the vitrifying method which is commonly used in reproductive medicine[97]. The chip together with the microtissues is frozen under a low temperature, and the physiological activity of the cells is paused. When it is ready to be used, the heart-on-a-chip is rewarmed to activate physiological activity of the cells. Such vitrifying process necessitates strict demands for the design and materials of heart-on-a-chip.

To sum up, the development of heart-on-a-chip is still in its early stage, and there are barriers to overcome in its commercialization and clinical applications. However, it is believed that heart-on-a-chip is a promising technique and has a great potential in various biomedical applications.

Acknowledgments

The work was financially supported by National Natural Science Foundation of China (51911530694, 11902245), the Key Research and Development Program of Shaanxi (2021GY-294), the Zhejiang Provincial Natural Science Foundation of China (LQ21E050009), and Beilin District Applied Technology Research and Development Projects in 2020 (GX2027).

Conflict of interest

The authors declare that they have no conflict of interest.

References

1. Yusuf SW, Cipolla C, Durand JB, *et al*., 2011, Cancer and Cardiovascular Disease. *Cardiol Res Pract*, 2011:943748.
2. Benjamin EJ, Muntner P, Alonso A, *et al*., 2020, Heart Disease and Stroke Statistics-2019 Update: A Report from the American Heart Association. *Circulation*, 141:E33. https://doi.org/10.1161/cir.0000000000000746
3. Denayer T, StöHr T, Roy MT, 2014, Animal Models in Translational Medicine: Validation and Prediction. *New Horiz Transl Med*, 2:5–11.
4. Chi CW, Lao YH, Ahmed AH, *et al*., 2020, High-Throughput Tumor-on-a-Chip Platform to Study Tumor-Stroma Interactions and Drug Pharmacokinetics. *Adv Healthc Mater*, 9:2000880. https://doi.org/10.1002/adhm.202000880
5. Lu HF, Leong MF, Lim TC, *et al*., 2017, Engineering a Functional Three-dimensional Human Cardiac Tissue Model for Drug Toxicity Screening. *Biofabrication*, 9:025011. https://doi.org/10.1088/1758-5090/aa6c3a
6. Zhang Y, Aleman J, Arneri A, *et al*., 2015, From Cardiac Tissue Engineering to Heart-on-a-chip: Beating Challenges. *Biomed Mater*, 10:034006. https://doi.org/10.1088/1748-6041/10/3/034006
7. Wei X, Zhuang L, Li H, *et al*., 2020, Advances in Multidimensional Cardiac Biosensing Technologies: From Electrophysiology to Mechanical Motion and Contractile Force. *Small*, 16:2005828. https://doi.org/10.1002/smll.202005828
8. Huang S, Yang Y, Qi Y, *et al*., 2018, Engineered Circulatory Scaffolds for Building Cardiac Tissue. *J Thorac Dis*, 10:S2312–28. https://doi.org/10.21037/jtd.2017.12.92
9. Zhao Y, Rafatian N, Wang E, *et al*., 2020, Towards Chamber Specific Heart-on-a-chip for Drug Testing Applications. *Adv Drug Deliv Rev*, 165–166:60–76. https://doi.org/10.1016/j.addr.2019.12.002
10. Guerzoni L, Tsukamoto Y, Gehlen DB, *et al*., 2019, A Layer-by-Layer Single-Cell Coating Technique To Produce Injectable Beating Mini Heart Tissues via Microfluidics. *Biomacromolecules*, 20:3746–54. https://doi.org/10.1021/acs.biomac.9b00786
11. Derda R, Laromaine A, Mannoto A, *et al*., 2009, Paper-supported 3D Cell Culture for Tissue-based Bioassays. *Proc Natl Acad Sci U S A*, 106:18457–62.
12. Lind JU, Busbee TA, Valentine AD, *et al*., 2017, Instrumented Cardiac Microphysiological Devices via Multimaterial Three-dimensional Printing. *Nat Mater*, 16:303. https://doi.org/10.1038/nmat4782
13. Kim BS, Jang J, Chae S, *et al*., 2016, Three-dimensional Bioprinting of Cell-laden Constructs with Polycaprolactone Protective Layers for Using Various Thermoplastic Polymers. *Biofabrication*, 8:035013. https://doi.org/10.1088/1758-5090/8/3/035013
14. Yi HG, Choi YJ, Kang KS, *et al*., 2016, A 3D-printed Local Drug Delivery Patch for Pancreatic Cancer Growth Suppression. *J Control Release*, 238:231–41. https://doi.org/10.1016/j.jconrel.2016.06.015
15. Kolesky DB, TRuby RL, Gladman AS, *et al*., 2014, 3D Bioprinting of Vascularized, Heterogeneous Cell-laden Tissue Constructs. *Adv Mater*, 26:3124–30. https://doi.org/10.1002/adma.201305506
16. Yashiro M, Oouchi T, Tsushima H, *et al*., 2017, Excimer Laser Gas Usage Reduction Technology for Semiconductor Manufacturing, *SPIE Adv Lithogr*, 10147:1014710. https://doi.org/10.1117/12.2257972
17. Randall JN, Owen JH, Lake J, *et al*., 2019, Next Generation of Extreme-Resolution Electron Beam Lithography. *J Vac Sci Technol*, 37:061605. https://doi.org/10.1116/1.5119392
18. He Y, Wu Y, Fu JZ, *et al*., 2016, Developments of 3D Printing Microfluidics and Applications in Chemistry and Biology: A Review. *Electroanalysis*, 28:1658–78. https://doi.org/10.1002/elan.201600043
19. He Y, Qiu J, Fu J, *et al*., 2015, Printing 3D Microfluidic Chips with a 3D SUGAR Printer. *Microfluid Nanofluidics*, 19:447–56. https://doi.org/10.1007/s10404-015-1571-7

20. Caulfield JB, Borg TK, 1979, The Collagen Network of the Heart. *Lab Invest*, 40:364–72.
21. Ramme AP, Koenig L, Hasenberg T, *et al*., 2018, Towards an Autologous iPSC-Derived Patient-on-a-Chip.
22. Grevesse T, Verseavel M, Circelli G, *et al*., 2013, A Simple Route to Functionalize Polyacrylamide Hydrogels for the Independent Tuning of Mechanotransduction Cues. *Lab Chip*, 13:777–80. https://doi.org/10.1039/c2lc41168g
23. Cimetta E, Pizzato S, Bollini S, *et al*., 2009, Production of Arrays of Cardiac and Skeletal Muscle Myofibers by Micropatterning Techniques on a Soft Substrate. *Biomed Microdevices*, 11:389–400. https://doi.org/10.1007/s10544-008-9245-9
24. Camelliti P, Gallagher JO, Kohl P, *et al*., 2006, Micropatterned Cell Cultures on Elastic Membranes as an *In Vitro* Model of Myocardium. *Nat Protoc*, 1:1379–91. https://doi.org/10.1038/nprot.2006.203
25. Annabi N, Tsang K, Mithieux SM, *et al*., 2013, Highly Elastic Micropatterned Hydrogel for Engineering Functional Cardiac Tissue. *Adv Funct Mater*, 23:4949–59. https://doi.org/10.1002/adfm.201300570
26. Versaevel M, Grevesse T, Gabriele S, 2012, Spatial Coordination Between Cell and Nuclear Shape within Micropatterned Endothelial Cells. *Nat Commun*, 3:671. https://doi.org/10.1038/ncomms1668
27. Mccain ML, Agarwal A, Nesmith HW, *et al*., 2014, Micromolded Gelatin Hydrogels for Extended Culture of Engineered Cardiac Tissues. *Biomaterials*, 35:5462–71. https://doi.org/10.1016/j.biomaterials.2014.03.052
28. Liu J, Miller K, Ma X, *et al*., 2020, Direct 3D Bioprinting of Cardiac Micro-Tissues Mimicking Native Myocardium. *Biomaterials*, 256:120204. https://doi.org/10.1016/j.biomaterials.2020.120204
29. Skardal A, Murphy SV, Devarasetty M, *et al*., 2017, Multi-Tissue Interactions in an Integrated Three-Tissue Organ-on-a-Chip Platform. *Sci Rep*, 7:8837.
30. Zhang YS, Arneri A, Bersini S, *et al*., 2016, Bioprinting 3D Microfibrous Scaffolds for Engineering Endothelialized Myocardium and Heart-on-a-Chip. *Biomaterials*, 110:45–59. https://doi.org/10.1016/j.biomaterials.2016.09.003
31. Colosi C, Shin SR, Manoharan V, *et al*., 2016, Microfluidic Bioprinting of Heterogeneous 3D Tissue Constructs Using Low-Viscosity Bioink. *Adv Mater*, 28:677–84. https://doi.org/10.1002/adma.201503310
32. Morgan KY, Sklaviadis D, Tochka ZL, *et al*., 2016, Multi-Material Tissue Engineering Scaffold with Hierarchical Pore Architecture. *Adv Funct Mater*, 26:5873–83. https://doi.org/10.1002/adfm.201601146
33. Miri AK, Daniel N, Luis I, *et al*., 2018, Microfluidics-Enabled Multimaterial Maskless Stereolithographic Bioprinting. *Adv Mater*, 30:1800242. https://doi.org/10.1002/adma.201800242
34. Fenech M, Girod V, Claveria V, *et al*., 2019, Microfluidic Blood Vasculature Replicas using Backside Lithography. *Lab Chip*, 19:2096106. https://doi.org/10.1039/c9lc00254e
35. Bartholomaand P, Gorjup E, Monz D, *et al*., 2005, Three-Dimensional *In Vitro* Reaggregates of Embryonic Cardiomyocytes: A Potential Model System for Monitoring Effects of Bioactive Agents. *J Biomol Screen*, 10:814–22. https://doi.org/10.1177/1087057105280070
36. Ronaldson-Bouchard K, Ma SP, Yeager K, *et al*., 2018, Advanced Maturation of Human Cardiac Tissue Grown from Pluripotent Stem Cells. *Nature*, 556:239–43. https://doi.org/10.1038/s41586-018-0016-3
37. Tandon N, Marsano A, Maidhof R, *et al*., 2011, Optimization of Electrical Stimulation Parameters for Cardiac Tissue Engineering. *J Tissue Eng Regen Med*, 5:E115–25. https://doi.org/10.1002/term.377
38. Valls-Margarit M, Iglesias-Garcia O, di Guglielmo C, *et al*., 2019, Engineered Macroscale Cardiac Constructs Elicit Human Myocardial Tissue-like Functionality. *Stem Cell Reports*, 13:207–20. https://doi.org/10.1016/j.stemcr.2019.05.024
39. Zhang N, Stauffer F, Simona BR, *et al*., 2018, Multifunctional 3D Electrode Platform for Real-Time *In Situ* Monitoring and Stimulation of Cardiac Tissues. *Biosens Bioelectron*, 112:149–55. https://doi.org/10.1016/j.bios.2018.04.037
40. Moon SH, Cho YW, Shim HE, *et al*., 2020, Electrically Stimulable Indium Tin Oxide Plate for Long-Term *In Vitro* Cardiomyocyte Culture. *Biomater Res*, 24:10. https://doi.org/10.21203/rs.3.rs-22137/v2
41. Oyunbaatar NE, Shanmugasundaram A, Jeong YJ, *et al*., 2020, Micro-Patterned SU-8 Cantilever Integrated with Metal Electrode for Enhanced Electromechanical Stimulation of Cardiac Cells. *Colloids Surf B Biointerfaces*, 186:110682. https://doi.org/10.1016/j.colsurfb.2019.110682
42. Yuk H, Lu B, Lin S, *et al*., 2020, 3D Printing of Conducting Polymers. *Nat Commun*, 11:1604.
43. Adly N, Weidlich S, Seyock S, *et al*., 2018, Printed Microelectrode Arrays on Soft Materials: From PDMS to Hydrogels. *NPJ Flex Electron*, 2:15.

https://doi.org/10.1038/s41528-018-0027-z

44. Zhao G, Zhang X, Li B, *et al*., 2020, Solvent-Free Fabrication of Carbon Nanotube/Silk Fibroin Electrospun Matrices for Enhancing Cardiomyocyte Functionalities. *ACS Biomater Sci Eng*, 6:1630–40. https://doi.org/10.1021/acsbiomaterials.9b01682
45. Stoppel WL, Kaplan DL, Black LD, 2016, Electrical and Mechanical Stimulation of Cardiac Cells and Tissue Constructs. *Adv Drug Deliv Rev*, 96:135–55. https://doi.org/10.1016/j.addr.2015.07.009
46. Mihic A, Li J, Miyagi Y, *et al*., 2014, The Effect of Cyclic Stretch on Maturation and 3D Tissue Formation of Human Embryonic Stem Cell-Derived Cardiomyocytes. *Biomaterials*, 35:2798–808. https://doi.org/10.1016/j.biomaterials.2013.12.052
47. Marsano A, Conficconi C, Lemme M, *et al*., 2016, Beating Heart on a Chip: A Novel Microfluidic Platform to Generate Functional 3D Cardiac Microtissues. *Lab Chip*, 16:599–610. https://doi.org/10.1039/c5lc01356a
48. Chinali M, Simone GD, Roman MJ, *et al*., 2005, Left Atrial Systolic Force and Cardiovascular Outcome. The Strong Heart Study. *Am J Hypertens*, 18:1570–6.
49. Bajaj P, Tang X, Saif TA, *et al*., 2010, Stiffness of the Substrate Influences the Phenotype of Embryonic Chicken Cardiac Myocytes. *J Biomed Mater Res Part A*, 95A:1261–9. https://doi.org/10.1002/jbm.a.32951
50. Hong SP, Song S, Cho SW, *et al*., 2017, Generation of PDGFRα+ Cardioblasts from Pluripotent Stem Cells. *Sci Rep*, 7:41840.
51. Ruan JL, Tulloch NL, Razumova MV, *et al*., 2016, Mechanical Stress Conditioning and Electrical Stimulation Promote Contractility and Force Maturation of Induced Pluripotent Stem Cell-Derived Human Cardiac Tissue. *Circulation*, 134:1557–67. https://doi.org/10.1161/circulationaha.114.014998
52. Visone R, Talò G, Occhetta P, *et al*., 2018, A Microscale Biomimetic Platform for Generation and Electro-Mechanical Stimulation of 3D Cardiac Microtissues. *APL Bioeng*, 2:046102. https://doi.org/10.1063/1.5037968
53. Cho KW, Lee WH, Kim BS, *et al*., 2020, Sensors in Heart-on-a-Chip: A Review on Recent Progress. *Talanta*, 219:121269. https://doi.org/10.1016/j.talanta.2020.121269
54. Plotnikov SV, Sabass B, Schwarz U, *et al*., 2014, High-Resolution Traction Force Microscopy. *Methods Cell Biol*, 123:367–94. https://doi.org/10.1016/b978-0-12-420138-5.00020-3
55. Polacheck W, William J, Chen CS, 2016, Measuring Cell-Generated Forces: A Guide to the Available Tools. *Nat Methods*, 13:415–23. https://doi.org/10.1038/nmeth.3834
56. Yu Y, Fu F, Shang L, *et al*., 2017, Bioinspired Helical Microfibers from Microfluidics. *Adv Mater*, 29:1605765. https://doi.org/10.1002/adma.201605765
57. Ma X, Dewan S, Liu J, *et al*., 2018, 3D Printed Micro-Scale Force Gauge Arrays to Improve Human Cardiac Tissue Maturation and Enable High Throughput Drug Testing. *Acta Biomat*, 95:319–27. https://doi.org/10.1016/j.actbio.2018.12.026
58. Tan JL, Tien J, Pirone DM, *et al*., 2003, Cells Lying on a Bed of Microneedles: An Approach to Isolate Mechanical Force. *Proc Natl Acad Sci U S A*, 100:1484–9. https://doi.org/10.1073/pnas.0235407100
59. Agarwal A, Goss JA, Cho A, *et al*., 2013, Microfluidic Heart on a Chip for Higher Throughput Pharmacological Studies. *Lab Chip*, 13:3599–608. https://doi.org/10.1039/c3lc50350j
60. Oyunbaatar NE, Shanmugasundaram A, Lee DW, 2019, Contractile Behaviors of Cardiac Muscle Cells on Mushroom-Shaped Micropillar Arrays. *Colloids Surf B Biointerfaces*, 174:103–9. https://doi.org/10.1016/j.colsurfb.2018.10.058
61. Vandenburgh H, Shansky J, Benesch-Lee F, *et al*., 2008, Drug-Screening Platform Based on the Contractility of Tissue-Engineered Muscle. *Muscle Nerve*, 37:438–47. https://doi.org/10.1002/mus.20931
62. Zhao Y, Wang EY, Davenport LH, *et al*., 2019, A Multimaterial Microphysiological Platform Enabled by Rapid Casting of Elastic Microwires. *Adv Healthc Mater*, 8:1801187. https://doi.org/10.1002/adhm.201801187
63. Mastikhina O, Moon BU, Williams K, *et al*., 2020, Human Cardiac Fibrosis-on-a-Chip Model Recapitulates Disease Hallmarks and Can Serve as a Platform for Drug Testing. *Biomaterials*, 233:119741. https://doi.org/10.1016/j.biomaterials.2019.119741
64. Chan V, Jeong JH, Bajaj P, *et al*., 2011, Multi-Material Bio-Fabrication of Hydrogel Cantilevers and Actuators with Stereolithography. *Lab Chip*, 12:88–98. https://doi.org/10.1039/c1lc20688e
65. Fu F, Shang L, Chen Z, *et al*., 2018, Bioinspired Living Structural Color Hydrogels. *Sci Robot*, 3:aar8580.
66. Sun L, Chen Z, Bian F, *et al*., 2020, Bioinspired Soft Robotic Caterpillar with Cardiomyocyte Drivers. *Adv Funct Mater*, 30:1907820.

https://doi.org/10.1002/adfm.201907820

67. Kim DS, Jeong YJ, Lee BK, *et al*., 2017, Piezoresistive Sensor-Integrated PDMS Cantilever: A New Class of Device for Measuring the Drug-Induced Changes in the Mechanical Activity of Cardiomyocytes. *Sens Actuators B Chem*, 240:566–72. https://doi.org/10.1016/j.snb.2016.08.167
68. Wang L, Dou W, Malhi M, *et al*., 2018, Microdevice Platform for Continuous Measurement of Contractility, Beating Rate, and Beating Rhythm of Human-Induced Pluripotent Stem Cell-Cardiomyocytes inside a Controlled Incubator Environment. *Acs Appl Mater Interfaces*, 10:21173–83. https://doi.org/10.1021/acsami.8b05407.s001
69. Coln EA, Colon A, Long CJ, *et al*., 2019, Piezoelectric bioMEMS Cantilever for Measurement of Muscle Contraction and for Actuation of Mechanosensitive Cells. *MRS Commun*, 9:1186–92. https://doi.org/10.1557/mrc.2019.129
70. Wang A, Liu Z, Hu M, *et al*., 2018, Piezoelectric Nanofibrous Scaffolds as *In Vivo* Energy Harvesters for Modifying Fibroblast Alignment and Proliferation in Wound Healing. *Nano Energy*, 43:63–71. https://doi.org/10.1016/j.nanoen.2017.11.023
71. Sakamiya M, Fang Y, Mo X, *et al*., 2020, A Heart-on-a-Chip Platform for Online Monitoring of Contractile Behavior Via Digital Image Processing and Piezoelectric Sensing Technique. *Med Eng Phys*, 75:36–44. https://doi.org/10.1016/j.medengphy.2019.10.001
72. Lind JU, Yadid M, Perkins I, *et al*., 2017, Cardiac Microphysiological Devices with Flexible Thin-Film Sensors for Higher-Throughput Drug Screening. *Lab Chip*, 17: 3692–703. https://doi.org/10.1039/c7lc00740j
73. Kang D, Pikhitsa PV, Choi YW, *et al*., 2014, Ultrasensitive Mechanical Crack-Based Sensor Inspired by the Spider Sensory System. *Nature*, 516:222–6. https://doi.org/10.1038/nature14002
74. Kim DS, Choi YW, Shanmugasundaram A, *et al*., 2020, Highly Durable Crack Sensor Integrated with Silicone Rubber Cantilever for Measuring Cardiac Contractility. *Nat Commun*, 11:535. https://doi.org/10.1038/s41467-019-14019-y
75. Kireev D, Seyock S, Lewen J, *et al*., 2017, Graphene Multielectrode Arrays as a Versatile Tool for Extracellular Measurements. *Adv Healthc Mater*, 6:1601433. https://doi.org/10.1002/adhm.201601433
76. Qian F, Huang C, Lin YD, *et al*., 2017, Simultaneous Electrical Recording of Cardiac Electrophysiology and Contraction on Chip. *Lab Chip*, 17:1732–9. https://doi.org/10.1039/c7lc00210f
77. Tian B, Cohen-Karni T, Qing Q, *et al.*, 2010, Three-Dimensional, Flexible Nanoscale Field-Effect Transistors as Localized Bioprobes. *Science*, 329:830–4. https://doi.org/10.1126/science.1192033
78. Abbott J, Ye T, Qin L, *et al.*, 2017, CMOS Nanoelectrode Array for All-Electrical Intracellular Electrophysiological Imaging. *Nat Nanotechnol*, 12:460–6. https://doi.org/10.1038/nnano.2017.3
79. Dai X, Zhou W, Gao T, *et al.*, 2016, Three-Dimensional Mapping and Regulation of Action Potential Propagation in Nanoelectronics-Innervated Tissues. *Nat Nanotechnol*, 11:776–82. https://doi.org/10.1038/nnano.2016.96
80. Kaneko T, Kojima K, Yasuda K, 2007, An On-Chip Cardiomyocyte Cell Network Assay for Stable Drug Screening Regarding Community Effect of Cell Network Size. *Analyst*, 132:892–8. https://doi.org/10.1039/b704961g
81. Aung A, Bhullar IS, Theprungsirikul J, *et al.*, 2016, 3D Cardiac Mu Tissues Within a Microfluidic Device with Real-Time Contractile Stress Readout. *Lab Chip*, 16:153–62. https://doi.org/10.1039/c5lc00820d
82. Mai-Dung N, Tinney JP, Yuan F, *et al.*, 2013, Cardiac Cell Culture Model As a Left Ventricle Mimic for Cardiac Tissue Generation. *Anal Chem*, 85:8773–9. https://doi.org/10.1021/ac401910d
83. Chen Y, Chan HN, Michael SA, *et al.*, 2017, A Microfluidic Circulatory System Integrated with Capillary-Assisted Pressure Sensors. *Lab Chip*, 17:653–62. https://doi.org/10.1039/c6lc01427e
84. Savoji H, Mohammadi MH, Rafatian N, *et al.*, 2019, Cardiovascular Disease Models: A Game Changing Paradigm in Drug Discovery and Screening. *Biomaterials*, 198:3–26. https://doi.org/10.1016/j.biomaterials.2018.09.036
85. Ren L, Liu W, Wang Y, *et al.*, 2013, Investigation of Hypoxia-Induced Myocardial Injury Dynamics in a Tissue Interface Mimicking Microfluidic Device. *Anal Chem*, 85:235–44. https://doi.org/10.1021/ac3025812
86. Liu H, Bolonduro OA, Hu N, *et al.*, 2020, Heart-on-a-Chip Model with Integrated Extra-and Intracellular Bioelectronics for Monitoring Cardiac Electrophysiology under Acute Hypoxia. *Nano Lett*, 20:2585–93. https://doi.org/10.1021/acs.nanolett.0c00076
87. Martewicz S, Michielin F, Serena E, *et al.*, 2012, Reversible

Alteration of Calcium Dynamics in Cardiomyocytes during Acute Hypoxia Transient in a Microfluidic Platform. *Integr Biol*, 4:153–64.
https://doi.org/10.1039/c1ib00087j

88. Sadeghi AH, Shin SR, Deddens JC, *et al.*, 2017, Engineered 3D Cardiac Fibrotic Tissue to Study Fibrotic Remodeling. *Adv Healthc Mater*, 6:1601434.
https://doi.org/10.1002/adhm.201601434
89. Tse G, 2016, Mechanisms of Cardiac Arrhythmias. *J Arrhythm*, 32:75–81.
90. Ma Z, Koo S, Finnegan MA, *et al.*, 2014, Three-Dimensional Filamentous Human Diseased Cardiac Tissue Model. *Biomaterials*, 35:1367–77.
https://doi.org/10.1016/j.biomaterials.2013.10.052
91. Brandão KO, Tabel VA, Atsma DE, *et al.*, 2017, Human Pluripotent Stem Cell Models of Cardiac Disease: From Mechanisms to Therapies. *Dis Model Mech*, 10:1039–59.
https://doi.org/10.1242/dmm.030320
92. Ren L, Zhou X, Nasiri R, *et al.*, 2020, Combined Effects of Electric Stimulation and Microgrooves in Cardiac Tissue-on-a-Chip for Drug Screening. *Small Methods*, 4:2000438.
https://doi.org/10.1002/smtd.202000438
93. Zhao Y, Rafatian N, Feric NT, *et al.*, 2019, A Platform for Generation of Chamber-Specific Cardiac Tissues and Disease Modeling. *Cell*, 176:913–27.e18.
94. Huang G, Li F, Zhao X, *et al.*, 2017, Functional and Biomimetic Materials for Engineering of the Three-Dimensional Cell Microenvironment. *Chem Rev*, 117:12764–850.
95. Yu F, Choudhury D, 2019, Microfluidic Bioprinting for Organ-on-a-Chip Models. *Drug Discov Today*, 24:1248–57.
https://doi.org/10.1016/j.drudis.2019.03.025
96. Gao B, Yang Q, Zhao X, *et al.*, 2016, 4D Bioprinting for Biomedical Applications. *Trends Biotechnol*, 34:746–56.
97. Shi M, Ling K, Yong KW, *et al.*, 2015, High-Throughput Non-Contact Vitrification of Cell-Laden Droplets Based on Cell Printing. *Sci Rep*, 5:17928.
https://doi.org/10.1038/srep17928
98. Bertassoni LE, Cecconi M, Manoharan V, *et al.*, 2014, Hydrogel Bioprinted Microchannel Networks for Vascularization of Tissue Engineering Constructs. *Lab Chip*, 14:2202–11.
https://doi.org/10.1039/c4lc00030g

RESEARCH ARTICLE

3D Printing of Layered Gradient Pore Structure of Brain-like Tissue

Na Pei[1,2], Zhiyan Hao[1,2], Sen Wang[1,2], Binglei Pan[1,2], Ao Fang[1,2], Jianfeng Kang[3], Dichen Li[1,2], Jiankang He[1,2], Ling Wang[1,2]*

[1]State Key Laboratory for Manufacturing System Engineering, Xi'an Jiaotong University, 710054, Xi'an, Shaanxi, China
[2]School of Mechanical Engineering, Xi'an Jiaotong University, 710054, Xi'an, ShanXi, China
[3]Jihua Laboratory, Foshan, 528000, Guangdong, China

Abstract: The pathological research and drug development of brain diseases require appropriate brain models. Given the complex, layered structure of the cerebral cortex, as well as the constraints on the medical ethics and the inaccuracy of animal models, it is necessary to construct a brain-like model *in vitro*. In this study, we designed and built integrated three-dimensional (3D) printing equipment for cell printing/culture, which can guarantee cell viability in the printing process and provide the equipment foundation for manufacturing the layered structures with gradient distribution of pore size. Based on this printing equipment, to achieve the purpose of printing the layered structures with multiple materials, we conducted research on the performance of bio-inks with different compositions and optimized the printing process. By extruding and stacking materials, we can print the layered structure with the uniform distribution of cells and the gradient distribution of pore sizes. Finally, we can accurately print a structure with 30 layers. The line width (resolution) of the printed monolayer structure was about 478 μm, the forming accuracy can reach 97.24%, and the viability of cells in the printed structure is as high as 94.5%.

Keywords: Brain-like model; Layered gradient structure; Integrated cell printing/culture equipment; 3D bio-printing

*Correspondence to: Ling Wang, State Key Laboratory for Manufacturing Systems Engineering, Xi'an Jiaotong University, Xi'an 710054, Shaanxi, China; menlwang@mail.xjtu.edu.cn

Received: March 22, 2021; **Accepted:** April 20, 2021; **Published Online:** June 15, 2021

(This article belongs to the *Special Section: Bioprinting of 3D Functional Tissue Constructs*)

Citation: Pei N, Hao Z, Wang S, *et al*., 2021, 3D Printing of Layered Gradient Pore Structure of Brain-like Tissue. *Int J Bioprint*, 7(3):359. http://doi.org/10.18063/ijb.v7i3.359

1. Introduction

According to the statistics from the World Health Organization, the burden of brain diseases throughout the world has exceeded that of cardiovascular diseases and cancer, accounting for 28%[1]. At present, the models used for brain pathology research and new drug development are mainly derived from animal models[2], which not only have long cycles but also display huge differences as compared to the human brain tissue[3], leading to a failure rate of drug development as high as 95%. In addition, the two-dimensional (2D) cell model is the main approach for pathological research, but due to lacking the interactions of cell-cell and cell-extracellular matrix (ECM), the neurons cultured on 2D cell culture dishes show significant deficiency[4-6]. Compared with the traditional tissue engineering methods, 3D bioprinting technology can be used to manufacture biomimetic tissue with complex structure through a highly automated manufacturing platform. Three-dimensional (3D) bioprinting technology has high precision and repeatability, which has great potential in achieving the envisioned goal of tissue-specific composition and localization of simulated cells and extracellular components[7]. The 3D bioprinting processes can be classified into five main categories: (i) Extrusion bioprinting[8,9], (ii) stereolithography bioprinting[10], (iii) inkjet bioprinting[11], (iv) laser-assisted bioprinting[12], and (v) microvalve-based bioprinting[13]. Extrusion-based bioprinting technology is the most commonly used bioprinting method because of its fast printing speed and a wide variety of bio-inks that can be printed.

© 2021 Pei, *et al*. This is an Open Access article distributed under the terms of the Creative Commons Attribution License (https://creativecommons.org/licenses/by/4.0/), permitting distribution and reproduction in any medium, provided the original work is cited.

Native tissues and/or organs possess complex hierarchical porous structures that confer highly-specific cellular functions[14]. The highly complex hierarchical porous structures are commonly found in most biological tissues such as skin[15-17], corneal[18], and even bone[19]. The importance of such hierarchical porous structures in native tissues has been critically reviewed elsewhere[20,21]. At present, 3D tissue engineering has been used to print the hierarchical porous structures in skin, blood vessels, esophagus, bladder, cartilage[22-28], and other tissues. Ng *et al*.[17] used a two-step drop-on-demand bioprinting strategy to manipulate the microenvironment to fabricate 3D biomimetic hierarchical porous collagen-based structures found in native skin tissue. The differences between the two manufacturing methods (3D bioprinting and manual-casting) are also compared. The results show that the two-step bioprinting strategy enables the homogeneous distribution of printed cells in a highly controlled manner as compared to the manual casting approach. However, there is a transition region between layers in the layered structure obtained by the 3D bioprinting method, while the aperture size in the transition region is uncontrollable. Nam *et al*.[29] used the dragging technique based on 3D extrusion method to manufacture the multi-layered hierarchical structure of the esophagus, it allowed the production of tubular structures with an adjustable line width and pore size. Moreover, their study also proved that porous structure can provide a more favorable environment for cell proliferation. However, the stretching properties vary depending on the viscosity of the material, and there are differences and limitations in pore size control for each self-supporting material. Sun *et al*.[30] incorporated biochemical stimulus with different growth factor releasing and biomechanical stimulus with small pore sizes to induce better chondrogenesis to create the dual-factor releasing and gradient-structured cartilage construct. The results indicated that the gradient scaffold group showed better chondroprotective effects with a significantly higher histological grading compared with the nongradient groups over the 24 weeks *in vivo*. However, the change of the pore size in this study was obtained by changing the spacing between the printed lines, which did not change the pore size in the printed structures.

Xu *et al*.[31] utilized a single type of hydrogel by changing the weight/volume ratio of Gelatin-methacryloyl (GelMA) to bioprint the bilayer tubular construct which has smaller pores in the inner layers (6% GelMA) and larger pores in the outer layers (4% GelMA). The results also indicated that the difference in pore sizes may have helped prevent each of these cell types from crossing their respective layers. Although the cells had a high survival rate after printing, the 3-(4,5-dimethylthiazol-2-yl)-2,5-diphenyltetrazolium bromide results showed that the cells in the printed structure almost did not proliferate after the 7 days of culture, which may be related to the printing inks in this research did not have the ability to make the cells growth rapidly. However, because of the complex composition and complicated structure of the brain tissue, it is rarely used in the brain.

The cerebral cortex is a layered gray matter covering the surface of the cerebral hemisphere. The lamellar structure is one of the most obvious characteristics of the cerebral cortex[32]. It has a typical structure with six layers and each has specific neurons. The six-layer structure is composed of the molecular layer (layer I), the external granule cell layer (layer II), the external pyramidal cell layer (layer III), the internal granule cell layer (layer IV), the internal pyramidal cell layer (layer V), and the multiform layer (layer VI). The thickness of the cortex in different functional areas ranges from 2 mm to 5.2 mm, and the thickness of each layer ranges from 200 μm to 1000 μm. The researchers believe that the gradient distribution of ECM or the soluble signal factors is likely to be the inducement of the directional growth and migration of neurons. They also studied the effects of gradient distribution of matrix hardness[33] and growth factors[34] on the directional growth of neurons. Various characteristic parameters of the natural cerebral cortex are the important basis to determine the target parameters of the brain-like cortex model with a layered gradient structure which we constructed in this study. Brain tissue has obvious biophysical characteristics, with the modulus of much lower than that of the heart, cartilage, etc. (the modulus of newborn brain tissue is about 110 Pa, and that of an adult brain tissue is about 500 – 1000 Pa)[35]. The porosity of the cerebral matrix has a greater influence on cell migration and metabolism[36-41]. Designing and manufacturing the brain-like model with similar pore size to natural tissues are more conducive to cell migration and nutrient exchange. Therefore, the manufacturing targets of the layered gradient structure that imitates the cerebral cortex are: (i) The bio-inks containing components with different concentration, (ii) the modulus of the printed structure which is as close as possible to 1000 Pa, and (iii) the appropriate internal pore size (30 – 150 μm) of the printed structure.

In this study, we have designed and built a set of integrated equipment for cell printing/culture, which can realize the target of printing a structure with multiple cells and multiple materials. This equipment can provide a suitable environment during the printing process for the cells to survive. Furthermore, this equipment also provides a long-term cultivation environment for the printed structure, which can solve the problem of separating the printed structure from the printing process to culture process in the traditional 3D printing method and can reduce the risk of cell contamination during the process

of transferring the printed structure to an incubator after printing. Moreover, we also optimize the printing process by adjusting the printing parameters of the bio-inks and the pre-processing and post-processing conditions of the bio-inks so that we can accurately control the compression modulus of the printed structure. Collagen is the main component of natural ECM, accounting for about 30% of the total protein of human body[14], which provides structural stability and strength to numerous tissues such as skin, bone, cartilage, or even teeth. Therefore, in this study, collagen was added to the bio-inks to increase the survival rate of the cells in printed structure. Then, the distribution of pore size in brain tissue was simulated by changing the concentration of collagen in bio-inks to alter the inner pore size of printing structure. Therefore, an artificial brain-like tissue model with a gradient distribution of pore size was constructed *in vitro*.

2. Materials and methods

2.1. Building an integrated cell printing/culture equipment

The integrated cell printing/culture equipment consists of both hardware and software. The hardware consists of three parts: Mobile control module, material extrusion module, and environment control module. The main components of the mobile control module and the material extrusion module were placed outside of the environment control module to avoid the corrosion of the precision components caused by humidity and other conditions in the printing environment. The software was based on the VC language which can realize the coordinated control of the mobile platform and the material extrusion module. QT5.8 programming software was used to write a set of graphical control software. We can achieve the goal of printing a brain-like layered structure with multiple bio-inks and multiple cells using multi-nozzles. Finally, the printed tissue can be cultured in the equipment after the printing process. Moreover, the environment within the equipment can be controlled to provide a suitable environment for the survival of cells, formation of bio-inks, and the culture of printed tissue. The integrated cell printing/culture equipment is shown in **Figure 1**, and the parameters of each part of this equipment are shown in **Table 1.**

2.2. Printing principle

Multiple nozzles were used to print the layered gradient brain-like structure by the extrusion method. Each nozzle contained a bio-ink with different compositions and different cells (**Figure 2B**), and all the nozzles printed the structure layer by layer in turn until the printing process was completed.

Table 1. Parameters of the integrated cell printing/culture equipment

Environment control module	Temperature		0 – 50±0.8°C
	Humidity		50 – 95%
	Oxygen concentration		0 – 5%
Material extrusion module	Channels		4
	Maximum stroke		90 mm
	Linear velocity range		7.49 μm/min – 79.4 mm/min
	Stroke resolution		0.165 μm
Motion control module	Stroke	X	150 mm
		Y	150 mm
		Z	150 mm
	Speed	X,Y	0 – 50 mm/s
	Reposition accuracy	X,Y,Z	10 μm
	Position Accuracy	X,Y,Z	20 μm

2.3. Preparation of the bio-inks

The bio-inks used for 3D cell printing needed to be both printable and biocompatible. Under certain conditions, gelatin and sodium alginate had higher viscosities which were easy to form and had good printing properties, but they were poorly biocompatible. Collagen and silk fibroin had good biocompatibility, but they were difficult to form and cannot print. Therefore, it was difficult to use a single biomaterial to meet the requirements of the printing. In this paper, gelatin and sodium alginate were mixed as the basic components of the bio-ink, and collagen was added as a regulating factor to form the final bio-ink, which has been proven to have good biocompatibility and printability.

The sodium alginate (medium viscosity, purity ≥98%) and gelatin (from pigskin, medium-strength) used in this experiment were purchased from Sigma company. Collagen was collagen type I, which was extracted from rat tail by our research group, and its concentration was 6 mg/ml. According to the preliminary experiment, we selected 6 wt% gelatin and 1 wt% sodium alginate as the basic bio-inks, and the collagen with different concentrations was added as the regulatory factor. By changing the concentration of collagen in the bio-ink (the concentrations of collagen are 1.5 mg/ml, 1 mg/ml, and 0.5 mg/ml, which are denoted as G6A1C1.5, G6A1C1, and G6A1C0.5, respectively), we could obtain the bio-inks that can print the layered gradient brain-like structure.

According to the characteristics of collagen that gelates at high temperature and of gelatin at low temperature, we developed a configuration process to mix the bio-inks (**Figure 3**).

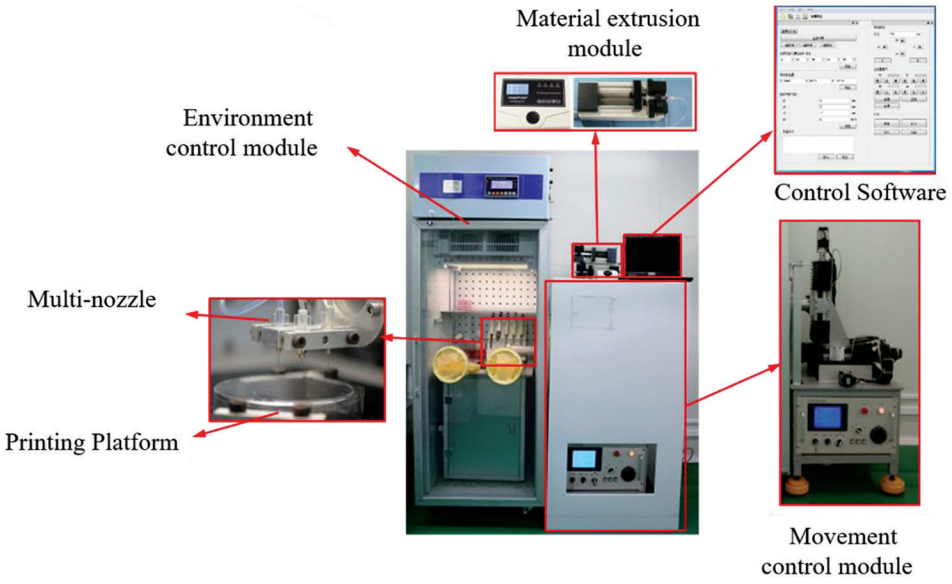


Figure 1. The integrated cell printing/culture equipment.

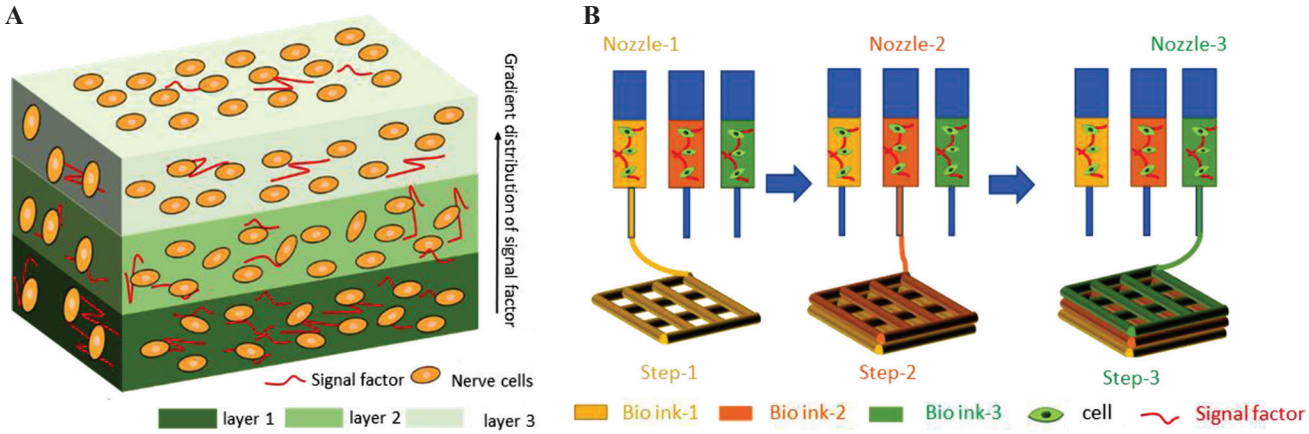


Figure 2. Printing a layered gradient structure that mimics the cortex. (A) Schematic diagram of the layered gradient brain-like model\ designed in the current study. (B) The printing principle of the layered gradient brain-like structure.

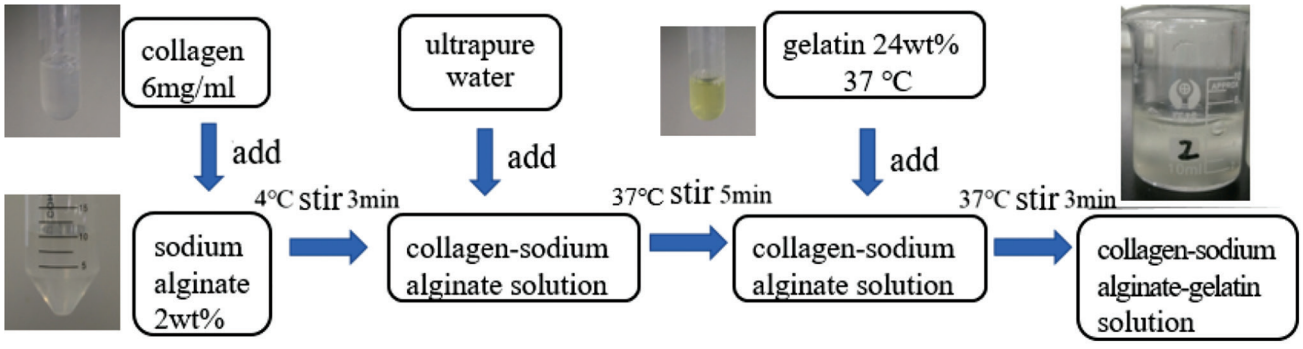


Figure 3. Configuration process of the bio-ink.

The pH value of the bio-inks was adjusted to 7.4 with 0.5M NaOH solution (Tianjin, Tianli), and then the U87 cells were mixed with the bio-inks to obtain the bio-inks with 1×10^6 cells/ml.

2.4. Determination of viscosity

The SNB-1 digital viscometer (Shanghai Nirun, measuring accuracy is ±1.0%) was used to measure the viscosity of the bio-ink. The bio-ink was placed in the metal measuring cylinder of the viscometer. After a series of rotor speed were set, respectively, the viscosity data of the bio-inks under the corresponding speed were recorded.

2.5. Test of compression modulus

The electronic universal testing machine (ETM103A, Shenzhen Wance Testing Equipment Company, China) was used to measure the compression modulus of the bio-ink. The loading speed was set to 1 mm/min, and the compression stroke was set to1.5 mm. Each sample was measured 3 times, and the number of samples is more than or equal to 3, and the variance analysis method was adopted for data analysis.

2.6. Observing the distribution and morphology of pore sizes

Scanning electron microscope (SEM, SU-8010, Japan) was used to analyze the micro-morphology of the internal pores of the printed structure. First, the printed structures were freeze-dried in a freeze-dryer (VFD2000, BIOCOOL, China) for 24 h. After the samples were taken out, the surface of the samples was sprayed with gold; finally, SEM was used to analyze the morphology and pore size of the printed structure.

2.7. Research on the printing parameters

The effects of needle diameter D, material extrusion rate u, and platform moving speed v on the performance of the printed structures were studied by designing orthogonal experiments. Three parameters for each variable were used and the L9 (3^4) orthogonal table (**Table 2**) was selected to design the orthogonal experiment. The printing effect of the printed structures was evaluated by two indexes: Line width and forming accuracy. The forming accuracy, A, of the printed structure was expressed by the following formula:

$$A = \left(1 - \left|\frac{l_1^2 - l^2}{l^2}\right|\right) \times 100\% \qquad (2.1)$$

where l, side length of design; l_1, average side length of the printed structure.

2.8. Determination of cell viability

The LIVE/DEAD®Viability/Cytotoxicity Kit reagent (L3224, Thermo, USA) was used to determine the viability of cells. Using a laser scanning confocal microscope (A1, Nikon, Japan) to observe the fluorescence image of cells, the living cells were labeled with green fluorescence, and the dead cells were labeled with red. Cell viability is expressed as the proportion of the stained green cells in the total number of stained cells. Image J software was used to count the number of the dead/living cells.

Table 2. Factor level table

Factor level	Experimental factors		
	Material extrusion rate μl/min	Platform movement speed mm/s	Needle diameter
	A	B	C
1	30	5	20G
2	60	10	23G
3	120	15	27G

2.9. Statistical analysis

Image J and Microsoft Excel 2010 were used for statistical analysis. Unless otherwise stated, all experiments were conducted independently for at least 3 times. The data were expressed as mean ± standard deviation. Statistical significance within the groups was tested by one-way analysis of variance (ANOVA) and statistical significance between the groups was tested by two-way ANOVA. $P < 0.05$ was considered statistically significant and the $P < 0.01$ was considered very significant.

3. Results

3.1. Influence of pre-treatment time at 4 on the performance of bio-inks

Pre-cooling the G6A1C1 bio-ink in a refrigerator at 4°C was used as the pre-treatment condition of the bio-ink and we studied the effect of the pre-cooling time on the performance of the printing ink. After the bio-inks were placed at 4°C for 0 min, 3 min, 6 min, 9 min, and 12 min, the viscosity of the mixed bio-inks increased rapidly with the increase of the pre-treatment time at low temperature (**Figure 4A**). When the bio-inks were placed at 4°C for 3 min and 6 min, the viscosity of the bio-inks was roughly the same. The viscosity of the bio-inks placed at 4°C for 9 min is about 10 times that of those for 6 min. With the increase of the pre-treatment time (**Figure 4A**), the shape of the extruded ink (**Figure 4B**) changed from spheroidal to linear. When the bio-ink was placed at 4°C for 9 min, the extruded ink was smooth with line shape, and the printed structure (**Figure 4C**) was regular with smooth surface. Therefore, placed the bio-ink at 4°C for 9 min was chosen as the appropriate pre-treatment time in this experiment.

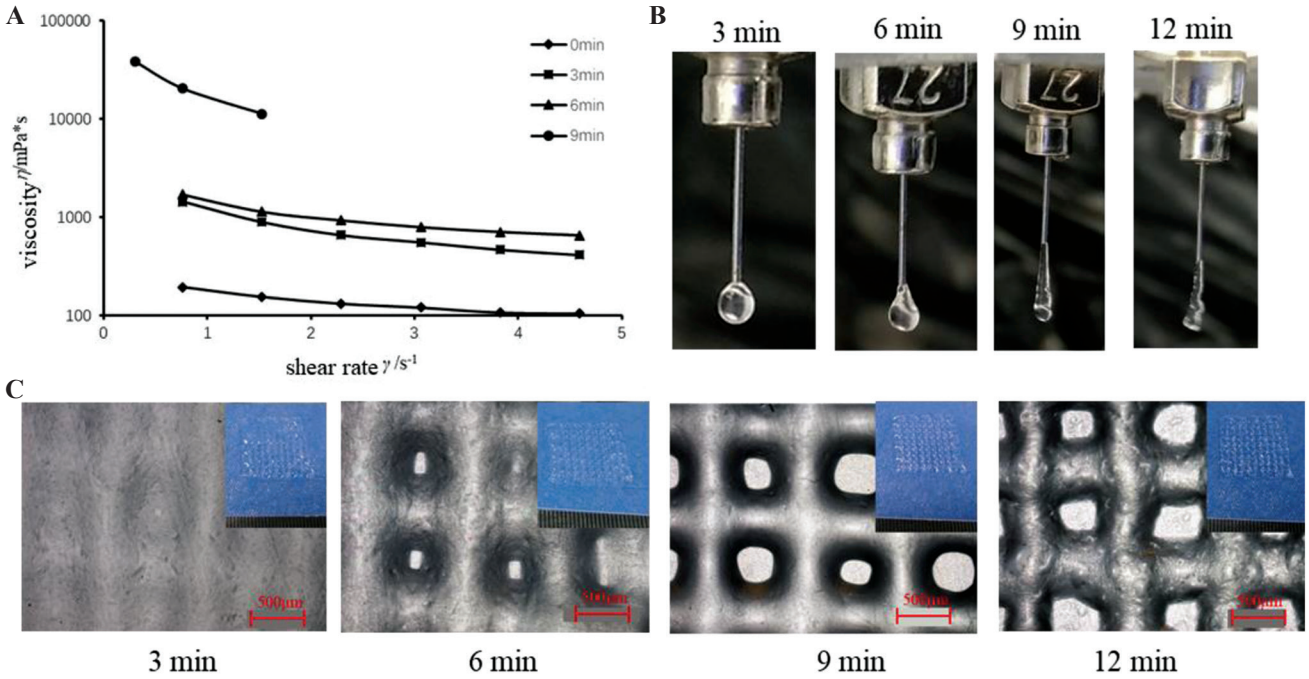


Figure 4. Effect of different pre-cooling time at 4°C on the performance of the G6A1C1 bio-inks. (A) Curve of viscosity and shear rate of the mixed bio-inks. (B) Outflow state of the bio-inks. (C) The micro-morphology of the printed structures printed by the bio-inks with different pre-cooling time.

3.2. Determining the printing parameters of the G6A1C1 bio-ink

The G6A1C1 bio-ink was used to print a single-layer grid structure with side length of 12 mm and spacing of 2 mm. The order of the influence of the printing parameters on the line width (**Table 3**) and forming accuracy (**Table 4**) of the printed structure was as follows: Needle diameter D > moving speed v > extrusion rate u. Needle diameter D ($P < 0.01$) and moving speed v ($P < 0.05$) had significant effects on the line width. These three factors had no significant effect on the forming accuracy.

According to the results of these two evaluation indexes, the optimal printing parameter for the G6A1C1 bio-ink to print the single-layer structure was chosen as follows: The diameter D of the needle was 27G, the moving speed v was 15 mm/s, and the extrusion rate u was 60 μl/min. When using this printing parameter to print a multi-layer structure, it was found that the extruded inks could not deposit continuously due to the fast-moving speed (**Figure 5D**). Therefore, it was necessary to optimize the printing parameters when printing a multi-layer structure. The continuity and stability of the printed multilayer structure can be guaranteed by reducing the moving speed (**Figure 6**). Therefore, according to the experimental results, the printing parameters of multi layer structure were determined as shown in **Table 5**.

Table 3. Range and variance analysis data of line width of the printed structure

Type of data processing	Factor A	Factor B	Factor C
Range analysis			
k1	730.73	856.53	1213.13
k2	761.60	786.60	559.40
k3	811.60	660.80	531.40
Range	80.87	195.73	653.73
Sequence	C>B>A		
Optimal levels	A1	B3	C3
Optimal combination	A1B3C3		
Variance analysis			
Mean-square value	4996.1	29513.9	446455.8
F value	5.397	31.883	482.298
Significance level (P value)	---(0.156)	*(0.030)	**(0.002)

3.3. Effect of post-processing on the performance of the printed structure

(1) Effect of temperature on the performance of the printed structures

G6A1C1 bio-ink was used to print a grid structure with 15 layers. The printed structure was immersed into a solution containing 1% $CaCl_2$ for 30 min at 20°C and 37°C, respectively. The compression modulus of the

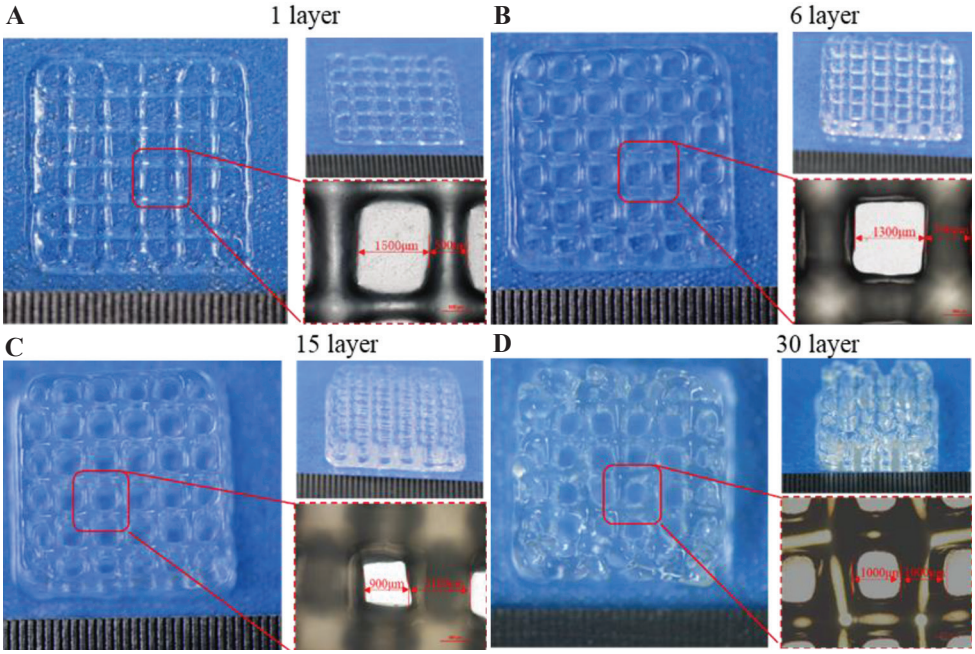


Figure 5. Effect of multi-layer structure printing with optimized single-layer printing parameters.

Table 4. Range and variance analysis data of forming precision

Type of data processing	Factor A	Factor B	Factor C
Range analysis			
k1	91.79	90.45	88.22
k2	95.57	93.34	94.91
k3	91.68	95.24	95.91
Range	3.90	4.79	7.69
Sequence	C>B>A		
Optimal levels	A2	B3	C3
Optimal combination	A2B3C3		
Variance analysis			
Mean-square value	16.06	19.00	56.93
F value	1.25	1.48	4.44
Significance level (*P* value)	---(0.444)	---(0.403)	---(0.184)

printed structure was 5.3 ± 1.3 kpa when treated at 20°C, and 8.1 ± 1.5 kpa while treated at 37°C. After the samples were freeze-dried and scanned by SEM, it was found that there were evenly distributed pores in the printed structure, and the average pore diameters of the pores were 46 ± 10 μm when treated at 20°C, and 44 ± 7 μm when treated at 37°C, and there was no significant difference between the pore sizes when the samples were treated at different temperatures. To meet the low elastic modulus of the cortical tissue, the post-treatment temperature was selected as 20°C in this experiment.

(2) Effect of the concentration of Ca^{2+} on the performance of the printed structure

G6A1C1 bio-ink was used to print a grid structure with 15 layers. In order to verify the effect of the concentration Ca2+ on the performance of the printed structure, we guaranteed that the soaking temperature was 37°C and the soaking time was 30 minutes. With the increase of the concentration of Ca^{2+}, the compression modulus of the printed structure (**Figure 7F**) also increased. The modulus of the printed structure treated with 5% $CaCl_2$ solution (9.57 ± 2.39kpa) was about twice as much as that treated with 0.1% $CaCl_2$ solution (5 ± 2.55 kpa). After freeze-drying, we found that with the increase of the concentration of Ca^{2+} (**Figure 7A-E**), the internal pore size of the printed structure gradually decreased. The internal pore size of the printed structure treated with 0.1% $CaCl_2$ solution (92.3 ± 7.4 μm) was about 5 times as much as that treated with 5% $CaCl_2$ solution. According to the characteristics of the pore size of the cortical tissue, 0.1% $CaCl_2$ solution was used for post-processing in this experiment.

3.4. Physical characterization of the layered structure

Three kinds of nozzles which contains the bio-inks in the order as follows: G6A1C1.5->G6A1C1->G6A1C0.5 were used in turn to print a layered structure. All bio-inks are printed with their optimized printing parameters, and after printing, the printed structure was immersed into a solution containing 0.1% $CaCl_2$ for 30 min at 20°C. It was found that the printed structure was complete and regular,

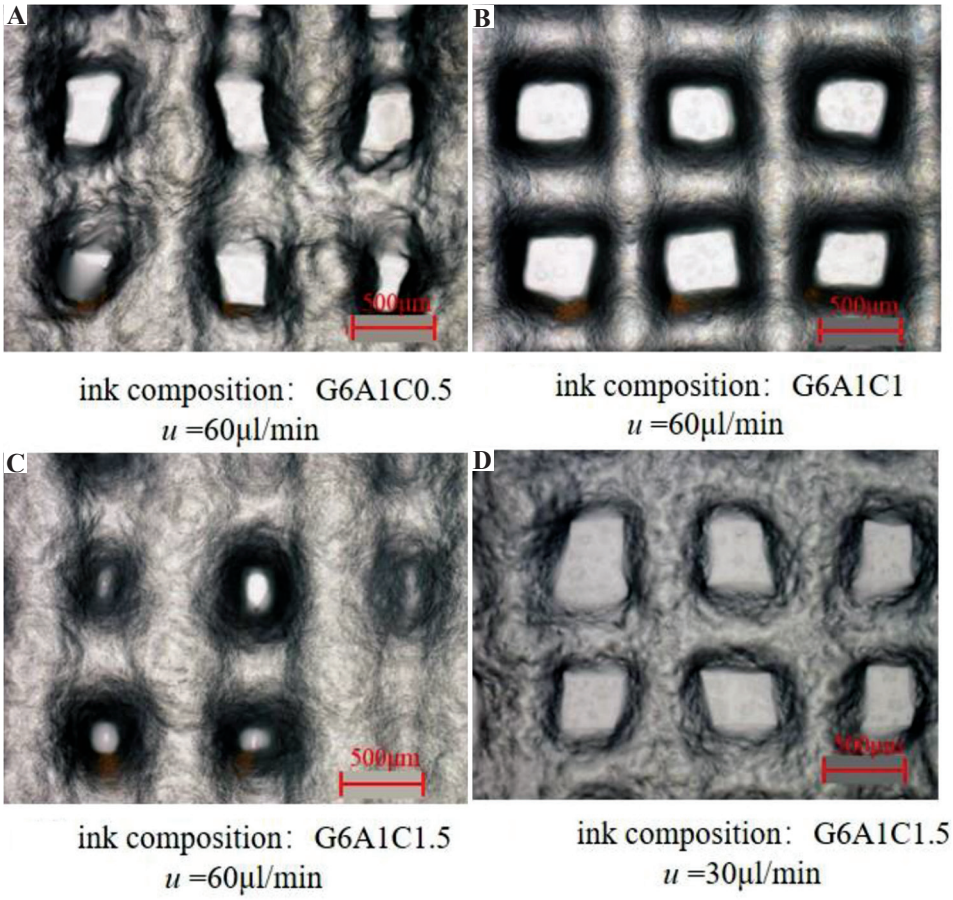


Figure 6. The use of different printing parameters to print the structure with different collagen concentrations in the ink.

which also has obvious layered characteristics and clear grid lines in the middle part (**Figure 8A**). The overall compression modulus (**Figure 8B**) of the total layered structure was 3.7 ± 0.8 kPa (n = 3). The pore size of the layered structure showed a clear gradient distribution (**Figure 8C**). With the decrease of the concentration of the collagen in the bio-inks, the size of the internal pore gradually decreased. The pore sizes of the top part printed with G6A1C1.5 bio-ink were larger than 100 μm when that of the middle part printed with G6A1C1 bio-ink were between 30 and 60 μm, and that of the bottom part printed with G6A1C0.5 bio-ink was the smallest, ranging from 20 μm to 30 μm.

3.5. Biological evaluation of the gradient structure

After the layered tissue was cultured in a cell incubator for 1 day, it was found that the grid structure remained intact (**Figure 9A**). Cells were evenly distributed inside of the printed structure, and most of the cells were living cells with a survival rate of 94.5%. With the increase of the culture days (**Figure 9C-E**), the number of the living cells increased significantly, which indicated that the cells can proliferate rapidly in this printed structure.

4. Discussion

In this study, a set of integrated equipment for cell printing/culturing was designed and built. The maximum printing volume of this system can reach 150 mm × 150 mm × 80 mm. It provided the installation location for multiple nozzles and can be used for printing with single nozzles, multiple nozzles, and coaxial nozzles. This equipment can also meet the requirements of hydrogel formation using various cross-linking forms. Most of the existing bio-printers, such as 3D Discovery and BioFactory manufactured by RegenHU company in Switzerland, and INKREDIBLE from CELLINK company in Sweden, are the open printing systems. During the printing process, the printing device needs to be placed on a clean bench to maintain a sterile environment. The integrated equipment for cell printing/culture designed in this paper can provide a sterile environment during the printing process to ensure that the cells cannot be contaminated. At the same time, the equipment can adjust the temperature and humidity of

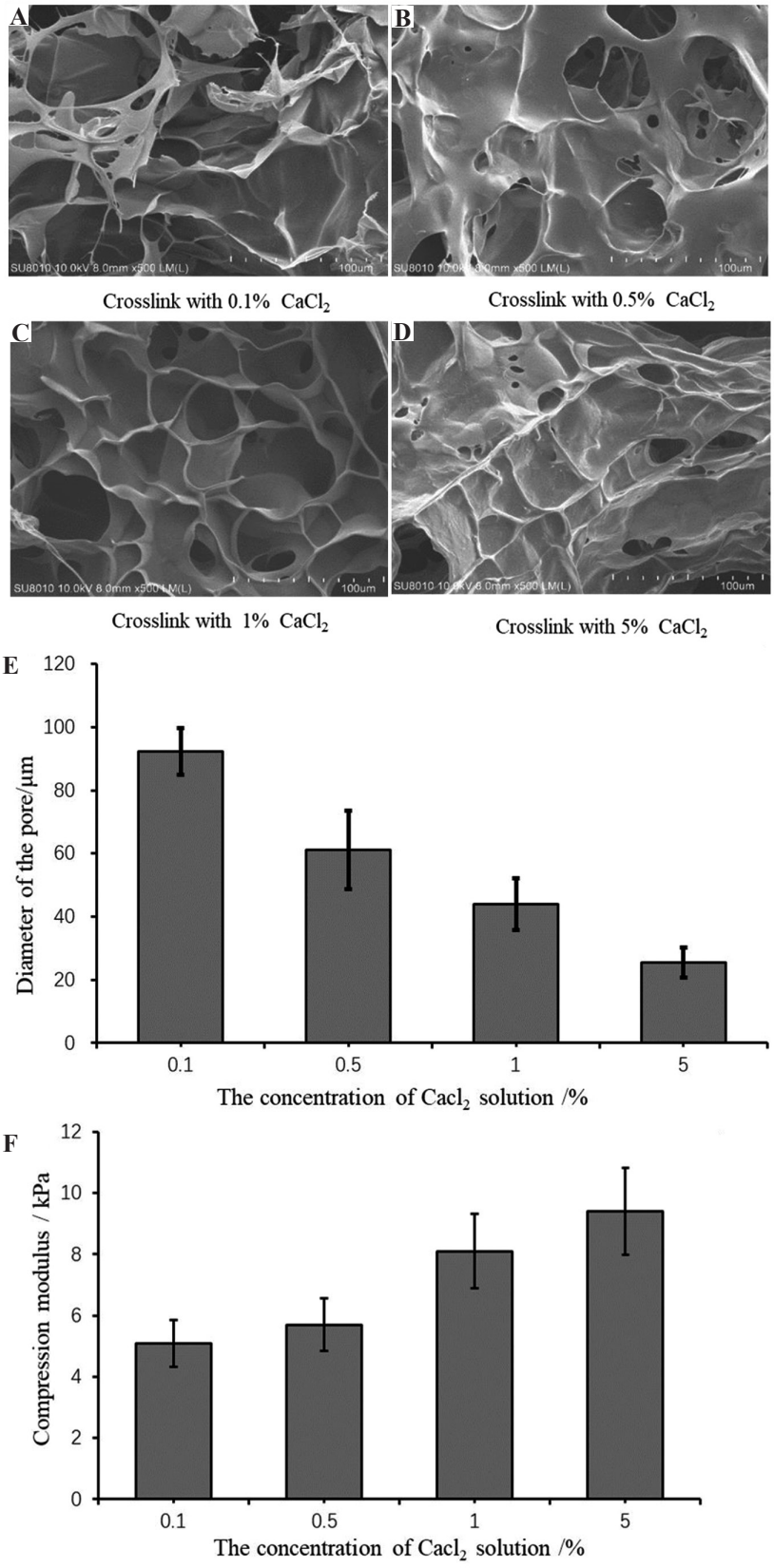


Figure 7. Effect of the concentration of Ca^{2+} on the performance of the printed structure. (A-D) scanning electron microscope image of the morphology of the internal pore of the printed structure. (E) The size of the internal pore of the printed structure. (F) Compression modulus of the printed structure when treated with the different concentration of Ca^{2+} solution.

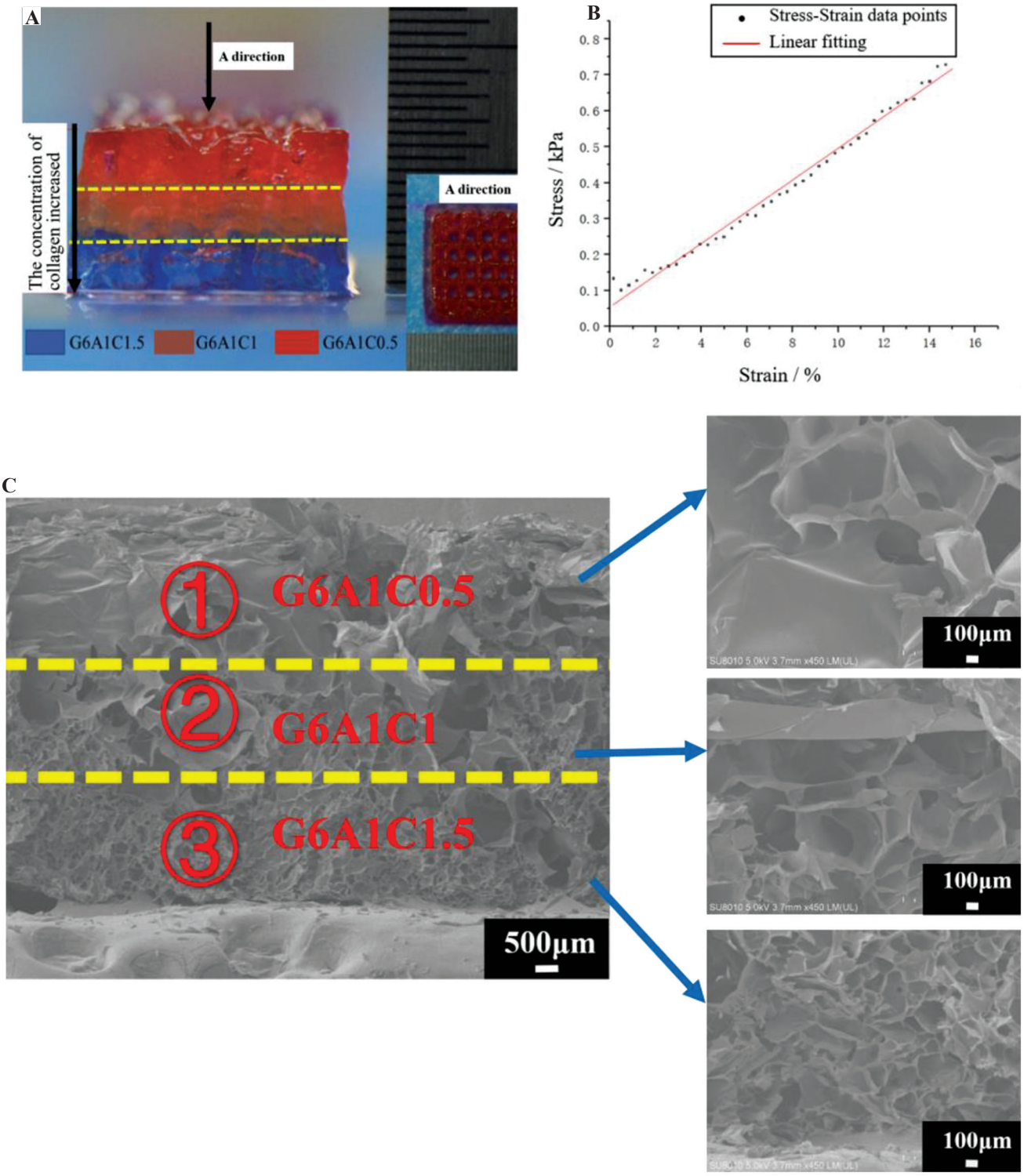


Figure 8. The macro and micro characteristics of the layered structure. (A) The macro-morphology of the layered structure. (B) The stress-strain diagram. (C) The scanning electron microscope image of the cross-section of the layered structure.

the printing room to meet the requirements of cell culture and solve the problem of separation between the printing process and the culture process in the traditional printing method. Meanwhile, the commercial biological 3D printers on the market are expensive, most of which cost between RMB 500,000 and 3 million. In this study, the overall cost of the self-made printing system was about 120,000 RMB, which can substantially reduce the research cost.

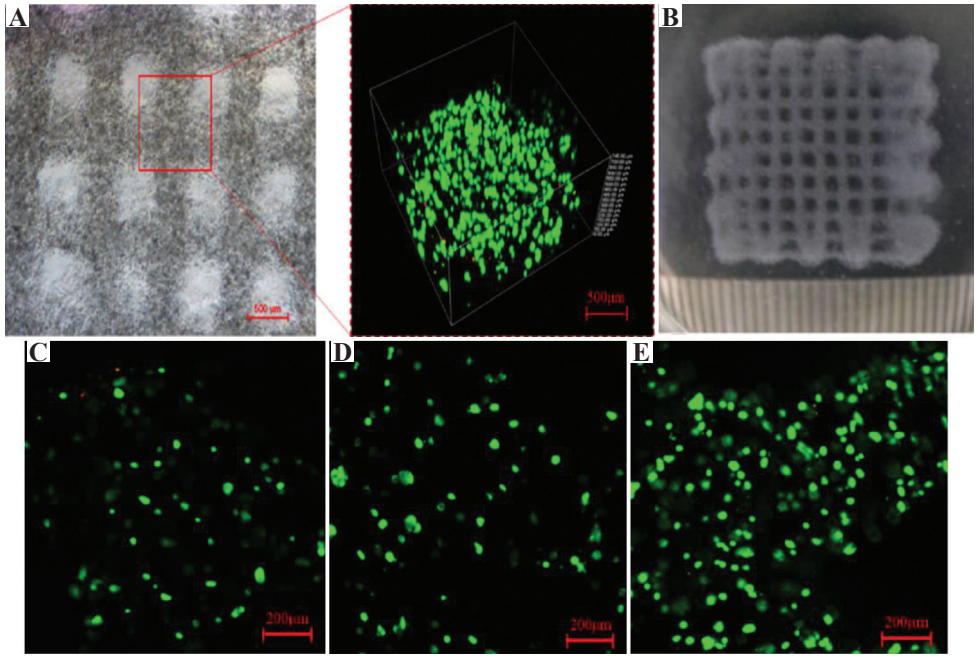


Figure 9. (A) The morphology of the layered structure and the distribution of cells inside of the layered structure which was cultured in a cell incubator for 1 day. (B) The macro morphology of the layered structure when cultured for 7 days. (C-E) The viability of cells in the layered structure when the structure was cultured for 1 day, 3 days, and 7 days, respectively. Green and red fluorescence denote living cells and dead cells, respectively.

Table 5. Printing parameters of bio-inks with different collagen concentration

Parameter type	Ink composition	Needle diameter D (μm)	Extrusion rate of the ink *u* (μl/min)	Moving speed of platform *v* (mm/s)
Top layer	G6A1C0.5	200 (27G)	60	10
Middle layer	G6A1C1	200 (27G)	60	10
Bottom layer	G6A1C1.5	200 (27G)	30	10

Due to the complexity of the brain structure, humans attempt to construct brain-like tissue models *in vitro* to study the structure and function of the brain. At present, Chwalek *et al*.[42] have used the molding method to produce a donut-shaped silk-collagen protein scaffold which can form a 3D neural network that has similar electrophysiological characteristics as normal neural tissue. Odawara *et al*.[43] developed a technique to form the directional fibers using collagen gel and also developed a 3D culture method in a polydimethylsiloxane micro-chamber. Finally, they proved that this method could generate a 3D neural network by accurately controlling the location of the cells. These studies built a 3D neural tissue model *in vitro* using the molding method. Although this method was simple to operate, had low requirements for forming, and did not require complex external conditions, it was difficult to manufacture complex structures, and at the same time, it was impossible to accurately control the density and spatial distribution of the nerve cells. Therefore, it was difficult to produce complex brain-like tissues that bear a high resemblance to the brain. Lee *et al*.[44] proposed a direct ink-jet 3D printing method with multi-layer collagen gel containing rat embryonic astrocytes and neurons. Gu *et al*.[45] proposed a direct printing method using a new bio-ink combining human neural stem cells to print a 3D porous grid structure. These methods can be used to construct 3D brain like tissue by 3D printing, but the brain like tissue constructed by these methods does not simulate the hierarchical structure and gradient characteristics of brain tissue, which verified the feasibility of using the printing method to construct brain-like tissues but lacked the simulation of the layered structure and gradient characteristics of brain tissues. Lozano *et al*.[46] used a peptide-modified gellan gum to prepare a three-layer brain-like layered structure by hand-held extrusion printing method. This study preliminarily simulated the layered structure with or without cells, but it was quite different from the continuous layered structure of natural brain tissue. Gu *et al*.[47] developed a novel and optically visible bio-ink for printing 3D neural tissue. The bio-inks can

maintain good molding accuracy after gelation. Then, the samples were stained to characterize the alive and dead cells, and it was found that there were many dead cells after 1 day of printing. Of note, the survival rate of the cells in the printed structure in our research was maintained at 94.5%. Vijayavenkataraman *et al*.[48] developed a biodegradable conductive hydrogel to provide a conductive environment for the proliferation and differentiation of neurons. However, nerve cells have extremely demanding requirements for the growth environment. The printing system constructed in this study cannot adjust the temperature and humidity in the printing environment during the printing process, thereby providing a sterile environment that is more suitable for the growth of nerve cell. In our research, we constructed a cell printing/culturing integrated operating system that can provide a suitable environment for cell growth during the printing process. Moreover, the overall modulus of the printed tissue constructed in our study is 3.7 ± 0.8 kPa, while the neurons prefer a softer substrate[49].

In view of the low elastic modulus and layered structure of the natural cerebral cortex, this paper proposed a method for manufacturing the layered structure with a gradient distribution of pore size. The density and position of cells in the printed structure can be precisely controlled by extrusion 3D printing technology. By controlling the different nozzles which contain different bio-inks to print the structure in turn, the layered structure can be manufactured. By changing the concentration of collagen in the bio-ink, it is possible to achieve the gradient change of pore size in the printed structure. As the collagen concentration increased from 0.5 mg/ml to 1.5 mg/ml, the pore size of the printed structure also showed a significant increase, thereby realizing the goal of manufacturing a layered structure with gradient pore sizes that mimic the cortex *in vitro*. At the same time, by changing the printing path, more complex tissue models can be printed *in vitro*.

At present, more and more studies have shown that changing the concentration of one or several biomaterials in the mixed bio-inks can change the internal pore size of the printed tissue so as to manufacture the gradient porous structure with heterogeneity. For example, Xu *et al*.[31] obtained smaller internal pore size by increasing the concentration of GelMA in hybrid bio-inks. Ng *et al*.[14] based on the principle of macroporous crowding and adopted the drop-on-demand technology to print the samples, their experimental results have indicated that the layered structures could be achieved by controlling the number of microporous-based bio-ink drops printed on each printed collagen layer. In this study, all parameters remained unchanged, with the exception of the collagen concentration in the mixed bio-ink. Fischer[50] proved that a higher concentration of collagen can lead to a smaller internal pores size of the structure. Therefore, this highlights that the change of pore size as mentioned in this paper is caused by the change of collagen concentration.

Based on the properties of collagen forming at high temperature and that of gelatin forming at low temperature, a set of ink mixing schemes has been developed to minimize the loss of the bio-inks during the mixing process as much as possible. This paper also focuses on the effect of the printing performance of the bio-inks by adjusting the printing parameters. By designing the orthogonal experiment, we found that the diameter of the needle had the most significant influence on the line width of the printed structure, and the moving speed has the second most significant impact. These findings can provide some guidance in the selection and optimization of the printing parameters in the future.

In this study, we have further studied and optimized the printing process. In the preliminary study, we determined that the pre-treatment time of the bio-inks at low temperature was a key parameter that affected the printing performance of bio-inks. When the pre-treatment time was 3 min or 6 min, the extrusion form of the bio-ink was spherical, and the printed grid structure appeared to adhere to each other. These phenomena indicated that the bio-ink tended to be at liquid state, which was mainly related to the characteristics of gelatin forming at low temperature. Thus, if the pre-treatment time was too short, the formation of gelatin would become incomplete, manifested by the collapse and adherence of printed structures. When the processing time was 12 min, the bio-ink had a rough surface morphology, indicating that the gelatin has been basically formed at this time and can be printed. However, at this time, the surface of the printed structure was too rough due to the over-molding. Based on these observations, we determined 9 min as the appropriate pre-treatment time at 4°C.

The main purpose of the post-processing in this study was to reduce the compression modulus of the printed structure and obtain a smaller aperture range (30 – 150 μm). The higher the concentration of Ca^{2+}, the greater the osmotic pressure between the printed tissue and the post-processed solution. The main reason of this phenomenon was that the increased concentration of Ca^{2+} would cause the printed tissue to be more fully cross-linked. Therefore, as the concentration of Ca^{2+} increased, the compressive modulus of the printed structure increased, and the pore size decreased. The total compression modulus of 3D brain-like nerve tissue printed by Gu *et al*.[45] was about 7.5 kPa, while that of the printed structure reported in this paper was about 3.7 kPa. The total compression modulus of the printed structure in our study was reduced by half compared to the results of Gu *et al*.[45], which was closer to that of natural brain tissue.

According to the layered characteristics of the brain tissue, in this paper, we developed a technology to print the layered structure with gradient distribution of pore size. This technology not only be used to manufacture brain-like tissue with layered structure, but also can be used to manufacture layered tissues widely existing in human body, such as cartilage, blood vessels and others. By changing and optimizing the cell type and cell density used in this printing process, we can construct the corresponding tissue/organ *in vitro*.

We encountered some problems in this study. A printed structure of <30 layers can maintain a more regular and complete structure, but when the printed structure had more than 30 layers, the edge of the printed structure began to appear defects, but the middle part could still maintain a better structure. In future research, we plan to further optimize the printing parameters and printing process to produce a structure with more layers. Although the cells possess a high survival rate and proliferation rate within the printed structure, they did not exhibit similar spreading and migration characteristics as in normal tissues. The biocompatibility of the bio-ink can be improved by modifying the material (RGD peptide modification) or adding bioactive factors (structural protein, glycoprotein, etc.) so as to further investigate the effect of special structure or signal factors (gradient distribution) on cell morphology and function expression.

5. Conclusion

In this study, we designed and built integrated cell printing/culture equipment for printing and culturing a 3D brain-like layered structure. This equipment provides a more affordable, integrated, and cell-friendly device for printing active organs and tissues *in vitro*. Gelatin, sodium alginate, and collagen were chosen as the raw materials of printing ink, and we developed a set of preparation scheme of the bio-inks. The optimum printing parameters of the bio-inks were determined by studying the printing process parameters such as material extrusion rate *u*, platform moving rate *v,* and needle diameter D. The pre-treatment and post-processing conditions of the bio-inks were also studied. By adjusting the collagen concentration of the bio-inks in each printing nozzle, the layered structure with gradient distribution of pore size could be produced. The forming accuracy of the printed single-layer structure reached 97.24%, and the survival rate of cells in the printed structure reached 94.5%. These gradient pore structures provide a more accurate 3D *in vitro* model for studying the complex structure and function of brain tissue.

Acknowledgments

The work was supported by the Program of the National Natural Science Foundation of China (51675411), and the Fundamental Research Funds for the Central Universities, and the Youth Innovation Team of Shaanxi Universities.

Conflicts of interest

We have no financial and personal relationships with other people or organizations that can inappropriately influence our work, there is no professional or other personal interest of any nature or kind in any product, service, and/or company that could be construed as influencing the position presented in, or the review of, this article.

Author contributions

J.H. is one of the guest editors of the Special Issue: Bioprinting of 3D Functional Tissue Constructs. The editorial and peer-review processes of this paper was exclusively handled by the editors of the journal without interference of any of the guest editors.

References

1. Muming Pu BX, 2016, Nao Ke Xue Yu Lei Nao Yan Jiu Gai Shu. [Brain Science and Brain-Inspired Intelligence Technology]. *J Chin Acad Sci*, 31:725–36.
2. Xiong Y, Mahmood A, Chopp M, 2013, Animal Models of Traumatic Brain Injury. *Nat Rev Neurosci*, 14:128–42. https://doi.org/10.1038/nrn3407
3. Huh D, Hamilton GA, Ingber DE, 2011, From 3D Cell Culture to Organs-on-Chips. *Trends Cell Biol*, 21:745–54. https://doi.org/10.1016/j.tcb.2011.09.005
4. Imamura Y, Mukohara T, Shimono Y, *et al.*, 2015, Comparison of 2D- and 3D-Culture Models as Drug-testing Platforms in Breast Cancer. *Oncol Rep*, 33:1837–43. https://doi.org/10.3892/or.2015.3767
5. Tian XF, Heng BC, Ge Z, *et al.*, 2008, Comparison of Osteogenesis of Human Embryonic Stem Cells within 2D and 3D Culture systems. *Scand J Clin Lab Invest*, 68:58–6. https://doi.org/10.1080/00365510701466416
6. Zhang D, Pekkanen-Mattila M, Shahsavani M, *et al.*, 2014, A 3D Alzheimer's Disease Culture Model and the Induction of P21-Activated Kinase Mediated Sensing in iPSC Derived Neurons. *Biomaterials*, 35:1420–8. https://doi.org/10.1016/j.biomaterials.2013.11.028
7. Ng WL, Chua CK, Shen YF, 2019, Print Me An Organ! Why We Are Not There Yet. *Prog Polym Sci*, 97:101145. https://doi.org/10.1016/j.progpolymsci.2019.101145
8. Ozbolat IT, Hospodiuk M, 2016, Current Advances and Future Perspectives in Extrusion-based Bioprinting. *Biomaterials*, 76:321–43. https://doi.org/10.1016/j.biomaterials.2015.10.076

9. Zhuang P, Ng WL, An J, *et al.*, 2019, Layer-by-layer Ultraviolet Assisted Extrusion-based (UAE) Bioprinting of Hydrogel Constructs with High Aspect Ratio for Soft Tissue Engineering Applications. *PLoS One*, 14:e0216776. https://doi.org/10.1371/journal.pone.0216776
10. Melchels FP, Feijen J, Grijpma DW, 2010, A Review on Stereolithography and its Applications in Biomedical Engineering. *Biomaterials*, 31:6121–30. https://doi.org/10.1016/j.biomaterials.2010.04.050
11. Saunders RE, Derby B, 2014, Inkjet Printing Biomaterials for Tissue Engineering: Bioprinting. *Int Mater Rev*, 59:430–48. https://doi.org/10.1179/1743280414y.0000000040
12. Koch LG, Unger C, Chichkov B, 2013, Laser Assisted Cell Printing. *Curr Pharm Biotechnol*, 14:91–7.
13. Ng WL, Lee JM, Yeong WY, *et al.*, 2017, Microvalve-based Bioprinting-process, Bio-inks and Applications. *Biomater Sci*, 5:632–47. https://doi.org/10.1039/c6bm00861e
14. Ng WL, Goh MH, Yeong WY, *et al.*, 2018, Applying Macromolecular Crowding to 3D Bioprinting: Fabrication of 3D Hierarchical Porous Collagen-based Hydrogel Constructs. *Biomater Sci*, 6:562–574. https://doi.org/10.1039/c7bm01015j
15. Tobin DJ, 2006, Biochemistry of Human Skin--our Brain on the Outside. *Chem Soc Rev*, 35:52–67. https://doi.org/10.1039/b505793k
16. Ng WL, Wang S, Yeong WY, *et al.*, 2016, Skin Bioprinting: Impending Reality or Fantasy? *Trends Biotechnol*, 34:689–99. https://doi.org/10.1016/j.tibtech.2016.04.006
17. Ng WL, Qi JT, Yeong WY, *et al.*, 2018, Proof-of-concept: 3D Bioprinting of Pigmented Human Skin Constructs. *Biofabrication*, 10:025005. https://doi.org/10.1088/1758-5090/aa9e1e
18. Meek KM, Knupp C, 2015, Corneal Structure and Transparency. *Prog Retin Eye Res*, 49:1–16.
19. Ferreira AM, Gentile P, Chiono V, *et al.*, 2012, Collagen for Bone Tissue Regeneration. *Acta Biomater*, 8:3191–200. https://doi.org/10.1016/j.actbio.2012.06.014
20. Yao HB, Fang HY, Wang XH, *et al.*, 2011, Hierarchical Assembly of Micro-/Nano-building Blocks: Bio-inspired Rigid Structural Functional Materials. *Chem Soc Rev*, 40:3764–85. https://doi.org/10.1039/c0cs00121j
21. Yang XY, Chen LH, Li Y, *et al.*, 2017, Hierarchically Porous Materials: Synthesis Strategies and Structure Design. *Chem Soc Rev*, 46:481–558. https://doi.org/10.1039/c6cs00829a
22. Levingstone TJ, Matsiko A, Dickson GR, *et al.*, 2014, A Biomimetic Multi-layered Collagen-based Scaffold for Osteochondral Repair. *Acta Biomater*, 10:1996–2004. https://doi.org/10.1016/j.actbio.2014.01.005
23. Tu DD, Chung YG, Gil ES, *et al.*, 2013, Bladder Tissue Regeneration Using Acellular Bi-layer Silk Scaffolds in a Large Animal Model of Augmentation Cystoplasty. *Biomaterials*, 34:8681–9. https://doi.org/10.1016/j.biomaterials.2013.08.001
24. Xu R, Luo G, Xia H, *et al.*, 2015, Novel Bilayer Wound Dressing Composed of Silicone Rubber with Particular Micropores Enhanced Wound Re-Epithelialization and Contraction. *Biomaterials*, 40:1–11. https://doi.org/10.1016/j.biomaterials.2014.10.077
25. Chung EJ, Ju HW, Park HJ, *et al.*, 2015, Three-layered Scaffolds for Artificial Esophagus Using Poly (Varepsilon-caprolactone) Nanofibers and Silk Fibroin: An Experimental Study in a Rat Model. *J Biomed Mater Res A*, 103:2057–65. https://doi.org/10.1002/jbm.a.35347
26. Mi HY, Jing X, Yu E, *et al.*, 2015, Fabrication of Triple-layered Vascular Scaffolds by Combining Electrospinning, Braiding, and Thermally Induced Phase Separation. *Mater Lett*, 161:305–8. https://doi.org/10.1063/1.4937310
27. Wang LR, Thissen H, Jane A, *et al.*, 2012, Screening Mesenchymal Stem Cell Attachment and Differentiation on Porous Silicon Gradients. *Adv Funct Mater*, 22:3414–23. https://doi.org/10.1002/adfm.201200447
28. Wu C H, Lee F K, Kumar SS, *et al.*, 2012, The Isolation and Differentiation of Human Adipose-derived Stem Cells Using Membrane Filtration. *Biomaterials*, 33:8228–39. https://doi.org/10.1016/j.biomaterials.2012.08.027
29. Nam H, Jeong HJ, Jo Y, *et al.*, 2020, Multi-layered Free-form 3D Cell-printed Tubular Construct with Decellularized Inner and Outer Esophageal Tissue-derived Bioinks. *Sci Rep*, 10:7255. https://doi.org/10.1038/s41598-020-64049-6
30. Sun Y, You Y, Jiang W, *et al.*, 2020, 3D Bioprinting Dual-factor Releasing and Gradient-structured Constructs Ready to Implant for Anisotropic Cartilage Regeneration. *Sci Adv*, 6:eaay1422. https://doi.org/10.1126/sciadv.aay1422
31. Xu L, Varkey M, Jorgensen A, *et al.*, 2020, Bioprinting Small Diameter Blood Vessel Constructs with an Endothelial and Smooth Muscle Cell Bilayer in a Single Step. *Biofabrication*, 12:045012.

https://doi.org/10.1088/1758-5090/aba2b6

32. Kato-Negishi M, Morimoto Y, Onoe H, *et al.*, 2013, Millimeter-sized Neural Building Blocks for 3D Heterogeneous Neural Network Assembly. *Adv Healthc Mater*, 2:1564–70. https://doi.org/10.1002/adhm.201300052
33. Sundararaghavan HG, Monteiro GA, Firestein BL, *et al.*, 2009, Neurite Growth in 3D Collagen Gels with Gradients of Mechanical Properties. *Biotechnol Bioeng*, 102:632–43. https://doi.org/10.1002/bit.22074
34. NjNbRU, 2008, Microfluidic Generation of Biomaterial Gradients for Control of Neurite Outgrowth. Graduate School New Brunswick Electronic Theses and Dissertations.
35. Hopkins AM, DeSimone E, Chwalek K, *et al.*, 2015, 3D *In Vitro* Modeling of the Central Nervous System. *Prog Neurobiol*, 125:1–25.
36. Bai H, Wang D, Delattre B, *et al.*, 2015, Biomimetic Gradient Scaffold from Ice-templating for Self-seeding of Cells with Capillary Effect. *Acta Biomater*, 20:113–119. https://doi.org/10.1016/j.actbio.2015.04.007
37. Rnjak-Kovacina J, Wise SG, Li Z, *et al.*, 2011, Tailoring the Porosity and Pore Size of Electrospun Synthetic Human Elastin Scaffolds for Dermal Tissue Engineering. *Biomaterials*, 32:6729–36. https://doi.org/10.1016/j.biomaterials.2011.05.065
38. Murphy CM, Haugh MG, O'Brien FJ, 2010, The Effect of Mean Pore Size on Cell Attachment, Proliferation and Migration in Collagen-glycosaminoglycan Scaffolds for Bone Tissue Engineering. *Biomaterials*, 31:461–6. https://doi.org/10.1016/j.biomaterials.2009.09.063
39. Lu H, Kawazoe N, Kitajima T, *et al.*, 2012, Spatial Immobilization of Bone Morphogenetic Protein-4 in a Collagen-PLGA Hybrid Scaffold for Enhanced Osteoinductivity. *Biomaterials*, 33:6140–6. https://doi.org/10.1016/j.biomaterials.2012.05.038
40. Engelmayr GC Jr., Cheng M, Bettinger CJ, *et al.*, 2008, Accordion-like Honeycombs for Tissue Engineering of Cardiac Anisotropy. *Nat Mater*, 7:1003–10. https://doi.org/10.1038/nmat2316
41. Pham QP, Shrma U, Mikos AG, 2006, Electrospun Poly(E-caprolactone) Microfiber and Multilayer Nanofiber/Microfiber Scaffolds: Characterization of Scaffolds and Measurement of Cellular Infiltration. *Biomacromolecules*, 7:2796–2805. https://doi.org/10.1021/bm060680j
42. Chwalek K, Tang-Schomer MD, Omenetto FG, *et al.*, 2015, *In Vitro* Bioengineered Model of Cortical Brain Tissue. *Nat Protoc*, 10:1362–73. https://doi.org/10.1038/nprot.2015.091
43. Odawara A, Gotoh M, Suzuki I, 2013, A Three-dimensional Neuronal Culture Technique that Controls the Direction of Neurite Elongation and the Position of Soma to Mimic the Layered Structure of the Brain. *RSC Adv*, 3:23620. https://doi.org/10.1039/c3ra44757j
44. Lee W, Pinckney J, Lee V, *et al.*, 2009, Three-dimensional Bioprinting of Rat Embryonic Neural Cells. *Neuroreport*, 20:798–803. https://doi.org/10.1097/wnr.0b013e32832b8be4
45. Gu Q, Tomaskovic-Crook E, Lozano R, *et al.*, 2016, Functional 3D Neural Mini-Tissues from Printed Gel-Based Bioink and Human Neural Stem Cells. *Adv Healthc Mater*, 5:1429–38. https://doi.org/10.1002/adhm.201670060
46. Lozano R, Stevens L, Thompson BC, *et al.*, 2015, 3D Printing of Layered Brain-like Structures Using Peptide Modified Gellan Gum Substrates. *Biomaterials*, 67:264–73. https://doi.org/10.1016/j.biomaterials.2015.07.022
47. Gu ET, Wallace GG, Crook JM, 2017, Engineering Human Neural Tissue by 3D Bioprinting. In: Biomaterials for Tissue Engineering. Methods in Molecular Biology. p129–38. https://doi.org/10.1007/978-1-4939-7741-3_10
48. Vijayavenkataraman S, Vialli N, Fuh JY, *et al.*, 2019, Conductive Collagen/Polypyrrole-b-polycaprolactone Hydrogel for Bioprinting of Neural Tissue Constructs. *Int J Bioprint*, 5:229. https://doi.org/10.18063/ijb.v5i2.1.229
49. Engler AJ, Sen S, Sweeney HL, *et al.*, 2006, Matrix Elasticity Directs Stem Cell Lineage Specification. *Cell*, 126:677–89. https://doi.org/10.1016/j.cell.2006.06.044
50. Fischer T, Hayn A, Mierke CT, 2019, Fast and Reliable Advanced Two-step Pore-size Analysis of Biomimetic 3D Extracellular Matrix Scaffolds. *Sci Rep*, 9:8352. https://doi.org/10.1038/s41598-019-44764-5

RESEARCH ARTICLE

Coaxial Electrohydrodynamic Bioprinting of Pre-vascularized Cell-laden Constructs for Tissue Engineering

Mao Mao[1,2], Hongtao Liang[1,2], Jiankang He[1,2]*, Ayiguli Kasimu[1,2], Yanning Zhang[1,2], Ling Wang[1,2], Xiao Li[1,2], Dichen Li[1,2]

[1]State Key Laboratory for Manufacturing Systems Engineering, Xi'an Jiaotong University, Xi'an 710049, China
[2]NMPA Key Laboratory for Research and Evaluation of Additive Manufacturing Medical Devices, Xi'an Jiaotong University, Xi'an 710049, China

Abstract: Recapitulating the vascular networks that maintain the delivery of nutrition, oxygen, and byproducts for the living cells within the three-dimensional (3D) tissue constructs is a challenging issue in the tissue-engineering area. Here, a novel coaxial electrohydrodynamic (EHD) bioprinting strategy is presented to fabricate thick pre-vascularized cell-laden constructs. The alginate and collagen/calcium chloride solution were utilized as the outer-layer and inner-layer bioink, respectively, in the coaxial printing nozzle to produce the core-sheath hydrogel filaments. The effect of process parameters (the feeding rate of alginate and collagen and the moving speed of the printing stage) on the size of core and sheath lines within the printed filaments was investigated. The core-sheath filaments were printed in the predefined pattern to fabricate lattice hydrogel with perfusable lumen structures. Endothelialized lumen structures were fabricated by culturing the core-sheath filaments with endothelial cells laden in the core collagen hydrogel. Multilayer core-sheath filaments were successfully printed into 3D porous hydrogel constructs with a thickness of more than 3 mm. Finally, 3D pre-vascularized cardiac constructs were successfully generated, indicating the efficacy of our strategy to engineer living tissues with complex vascular structures.

Keywords: Electrohydrodynamic bioprinting; Coaxial bioprinting; Vascularized tissues; Biofabrication; Core-sheath filaments

*Correspondence to: Jiankang He, State Key Laboratory for Manufacturing Systems Engineering, Xi'an Jiaotong University, Xi'an 710049, China; jiankanghe@mail.xjtu.edu.cn

Received: April 3, 2021; **Accepted:** May 14, 2021; **Published Online:** June 4, 2021

(This article belongs to the *Special Section*: *Bioprinting of 3D Functional Tissue Constructs*)

Citation: Mao M, Liang H, He J, *et al*., 2021, Coaxial Electrohydrodynamic Bioprinting of Pre-vascularized Cell-laden Constructs for Tissue Engineering. *Int J Bioprint*, 7(3):362. http://doi.org/10.18063/ijb.v7i3.362

1. Introduction

One of the most challenging problems in the tissue engineering area is to fabricate functional vasculature within the three-dimensional (3D) engineered tissue that provides enough nutrition and oxygen to the cells and transports the byproducts[1]. Cellular viability and function will be compromised, and necrosis may further occur without a capillary network within a few hundred microns of cells[2,3]. Thus, many approaches such as microreplication, photolithography, and sacrificial molding have been proposed to organize the endothelial cells in the spatially predefined organization, with an attempt to build microvessels within the cell-laden constructs[4-8]. It has been demonstrated that the endothelial cells in the spatially predefined organization can significantly improve the speed and extent of the vascularization after implantation, compared to that in a random distribution[9,10]. However, these engineering methods could only be used to fabricate constructs with relatively simple architectures and homogeneous cell-laden matrices, which make them difficult to recapitulate the intricate 3D structure and composition of natural tissues[11,12].

© 2021 Mao, *et al*. This is an Open Access article distributed under the terms of the Creative Commons Attribution License (https://creativecommons.org/licenses/by/4.0/), permitting distribution and reproduction in any medium, provided the original work is cited.

3D printing, mainly including the inkjet[13], extrusion[14], and vat polymerization-based processes[13-15], has evolved as a prevalent technology for producing 3D living tissue constructs with excellent controllability of geometrical shapes and complex microscale architectures. Especially, the inkjet or extrusion-based bioprinting approaches have been extensively explored over the past decade for creating 3D vascularized, heterogeneous cell-laden tissue constructs, owing to their remarkable advantages in wide suitability to various cell-laden bioinks and controllable positioning of the multicellular organization on demand[16-18]. However, as a consequence of the jetting or extrusion process through the printing nozzle, the cells would experience mechanical shear force inevitably, which has a negative effect on cell viability[19,20]. As smaller nozzles were usually employed to improve the printing resolution, the cell viability would further be challenged and clogging might occur when the viscous hydrogel was printed.

Electrohydrodynamic (EHD) printing, with inherent advantages in generating micro/nanoscale droplets or filaments, was recently explored to process cells-laden hydrogel for fabricating functional tissue constructs with high resolution and cell viability[21,22]. It is a novel hybrid inkjet printing combined with the electrospinning technique. When the electric field was applied on the printing nozzle, the bioink would be jetted out and the cells would experience a very low electrical current which would not cause notable damage to the cell integration, viability, and proliferation[23-25]. Since it was the electric force that pulled the bioink through the nozzle, the EHD cell printing process enabled to reduce the damage of shear stress on the printed cells which contributed to relatively high cell viability[26]. However, the nozzle-to-collector distance in these studies was over 600 μm to decrease the effect of high voltage on cell viability, and the size of the EHD-printed hydrogel filaments was larger than 200 μm[27,28]. To further improve the printing resolution, our group recently developed a novel EHD cell printing process by utilizing an insulating material to replace the conventional conductive or semiconductive material as the collecting substrate, which significantly reduced the electrical current on the bioink to microamperes (<10 μA)[29]. The feature size of the resultant hydrogel filament could be smaller than 100 μm while the cell viability was as high as 95%, implicating a potential strategy to build high-resolution living tissues. One limitation of this EHD cell printing process is that the height of the EHD-printed cell/hydrogel constructs was smaller than 145 μm, which resulted from the limited diffusion of calcium ions from the collecting substrate of agarose hydrogel to the deposited alginate filaments for crosslinking.

In this study, we integrated a coaxial nozzle into our house-made EHD cell printing system and explored its ability to fabricate thick pre-vascularized cell-laden constructs. When the collagen solution supplemented with calcium chloride ($CaCl_2$) in the inner layer and the alginate solution in the outer layer was pulled out of the coaxial nozzle by the electric force, instant crosslinking occurred when these bioink solutions met to form the core-sheath filaments. The width of the core and sheath hydrogel lines could be well modulated by changing the printing parameters such as the feeding rate of collagen solution and alginate solution as well as the moving speed of the substrate platform. Endothelialized lumen structure gradually formed along with the interface between the core and sheath lines when the endothelial cells were encapsulated into collagen solution as the inner-layer bioink. 3D porous hydrogel constructs with a thickness of more than 3 mm were successfully printed. As a concept of the study, we encapsulated endothelial cells and H9C2 cells into two layers of the coaxial nozzle, respectively, and successfully fabricated 3D pre-vascularized cardiac constructs.

2. Materials and methods

2.1. Materials and bioinks

Type I collagen derived from rat tail was prepared followed by previously described protocols and stored at 4°C. $CaCl_2$ and sodium hydroxide (NaOH) powder were purchased from Aladdin (Shanghai, China). Agarose powder with low melting temperature (87–89°C) was bought from Biowest (Spain). Alginate solution with a viscosity of 2000 mPa·S was prepared by dissolving alginate powder (Sigma, United Kingdom) into the cell culture medium with 10% (w/v) fetal bovine serum and 1% (w/v) antibiotic/antimycotic. 0.1 mol/L NaOH solution was prepared by dissolving NaOH powder into phosphate buffer saline (PBS) at room temperature. 3% (w/v) $CaCl_2$ solution was prepared by dissolving $CaCl_2$ powder into tris-buffered saline (TBS) at room temperature. 2% (w/v) flat agarose hydrogel was prepared by casting the boiling agarose solution with 3% (w/v) $CaCl_2$ into a petri dish at room temperature. Before the printing process, the pH of the collagen solution was adjusted to 7.2-7.6. GFP expressing human umbilical vein endothelial cells (GFP-HUVEC; ATCC, USA) and embryonic rat cardiomyocytes (H9C2; ATCC, USA) labeled with red cell tracker (Invitrogen, cat. no. C34552) were cultured in Dulbecco's Modified Eagle Medium (DMEM, Thermo) for printing cell-laden constructs.

2.2. EHD bioprinting setup

The EHD bioprinting setup is mainly composed of three key components: A high precision X-Y-Z moving stage (Xiamen Heidelstar, China), a voltage generator with high voltage (ZGF-30/5, Welldone, Shanghai, China), and a precision syringe pump system (TJ-2A, Longer Pump, Baoding, China). The coaxial printing nozzle (19G/26G) is mounted onto the Z-axis and connected with the high

voltage generator. The sheath and core layer of the coaxial nozzle is fed with alginate solution and collagen/$CaCl_2$ solution, respectively, by high-resolution syringes.

2.3. EHD bioprinting process

The process parameters of the applied voltage and nozzle-to-collector distance were fixed at 4.5 kV, 3.5 mm, 300 μm according to our previous studies[30]. When the high voltage syringe pumps run, alginate and collagen/$CaCl_2$ solution was simultaneously fed into the coaxial nozzle. Alginate was immediately cross-linked by the $CaCl_2$ solution when they met in the nozzle head. During the EHD bioprinting process, the printing room temperature should be lower than 16°C to avoid collagen solution gelling. After printing, the constructs were put into the cell culture incubator set at 37°C for 10 min for collagen solution gelling.

2.4. Optimization of EHD printing process parameters

The effects of the feeding rate of alginate and collagen solution and the moving speed of stage on the width of the printed core-sheath filaments were investigated when the applied voltage, the distance between nozzle and collecting substrate were fixed at 4.5 kV and 300 μm, respectively. Green fluorescent particles (Lumisphere, BaseLine, China) were added to the collagen solution to distinguish the core line from the sheath line in the hydrogel filaments. The bright-field and fluorescent images of the printed filaments were captured with an inverted fluorescence microscope (ECLIPSE Ti, Nikon, Japan), which were utilized to measure the size of the core line and sheath line.

2.5. Characterization of the lattice hydrogel with core-sheath filaments

A single layer of complex lattice hydrogel with core-sheath filaments was printed. To show the distribution of collagen and alginate hydrogel in the electrohydrodynamically printed core-sheath filaments, red and green fluorescent particles were added into the alginate and collagen solution, respectively. Hollow filaments were printed by replacing collagen solution with 3% (w/v) $CaCl_2$ solution. The fluorescent cross-section images of the printed hollow filaments were reconstructed using confocal microscope (Nikon, Japan). To evaluate the perfusability of the lattice hydrogel with hollow filaments, a syringe was connected to the opening of the hollow filament and a blue dye solution was injected; the process was recorded by a commercial camera.

2.6. Cell culture within the core-sheath filaments

The inner-layer bioink was prepared with GFP-HUVECs, collagen, and $CaCl_2$ at the final concentration of 2×10^6/mL, 0.3% (w/v) and 3% (w/v). The outer-layer bioink was 0.3% (w/v) pure alginate solution. Cellular morphology and distribution after different days in culture were characterized with an inverted fluorescence microscope and confocal microscope. The endothelialized filaments after 14 days in culture were captured using the digital camera (Nikon, Japan).

2.7. Fabrication of 3D hydrogel constructs

The EHD printing strategy was also employed to fabricate 3D complex lattice hydrogel by precisely stacking the filaments in a layer-by-layer manner. In this study, the macro/microscopic images of the 3D hydrogel constructs were captured with a digital camera and optical microscope. A confocal laser scanning microscope (OLS4000, Olympus, USA) was used to rebuild the 3D profiles of the printed constructs, which were used to quantify the height of constructs with different layers. The printed constructs with 5 layers were further freeze-dried in a lyophilizer (FD-1A-50, Biocool, Beijing, China) for 3 days. The microstructures were observed with a scanning electron microscope (SEM, SU8010, Hitachi, Japan).

2.8. Fabrication and characterization of cell-laden 3D constructs

To fabricate pre-vascularized 3D lattice constructs, the inner-layer bioink was prepared with GFP-HUVECs, collagen, and $CaCl_2$ at the final concentration of 2×10^6/mL, 0.3% (w/v) and 3% (w/v). The outer-layer bioink was 0.3% (w/v) pure alginate solution or 0.3% (w/v) alginate solution laden with red H9C2 cells at the final concentration of 2×10^6/mL. The bioprinted lattice constructs were cultured statically for different days. The proliferation of the printed cells was quantified using CCK-8 assay (Dojindo Molecular Technologies) on the culturing day of 1, 4, and 7. The cell viability was quantified by performing Live/Dead assay (Thermo Fisher Scientific).

2.9. Statistical analysis

All quantitative results were presented as mean ±standard deviation. Statistical significance was determined using one-way analysis of variance (ANOVA) followed by Tukey *post-hoc* test for multiple comparisons using SPSS statistical software. The differences were considered statistically significant if the p-value was <0.05 (*).

3. Results and discussion

3.1. EHD bioprinting of core-sheath hydrogel filaments

Figure 1 shows the EHD printing strategy integrated with a coaxial nozzle for fabricating the thick vascularized construct, assembled by the cross-linked core-sheath filaments. As illustrated in our previous study, an insulating

petri dish filled with 2% (w/v) agarose hydrogel was placed on the grounded stage as the collecting substrate to avoid the high electric current during the EHD printing process. The alginate and collagen/$CaCl_2$ solution were respectively controlled by two high-precision syringe pumps and loaded into the outer layer and inner layer of the coaxial nozzle. When the high voltage was applied, alginate solution and collagen/$CaCl_2$ solution would be pulled out of the coaxial nozzle simultaneously and the alginate solution would be instantly cross-linked by the calcium ions, resulting in core-sheath filaments deposited onto the collecting substrate under the control of the user-specific design. Multiple layers of constructs could be further printed by precisely stacking the core-sheath filaments in a layer-by-layer manner.

We then studied the effect of process parameters (feeding rate of alginate and collagen, moving speed of the printing stage) on the size of core and sheath within EHD printed filaments. Alginate solution and collagen/CaCl2/green fluorescent particles solution were loaded into the outer and inner layers of the coaxial nozzle, respectively. The size of the core line was characterized as the width of the bands with green fluorescent particles through the fluorescent images, while the size of the sheath line, defined as the external width of the filament, was measured in the same region through the bright-field images. **Figure 2A-E**

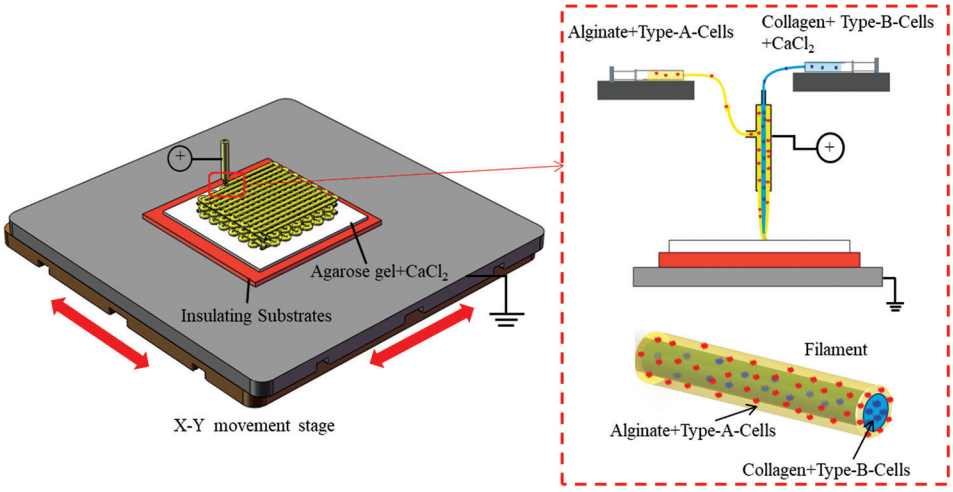


Figure 1. Schematic of EHD bioprinting strategy of core-sheath hydrogel filaments for generating cell-laden constructs.

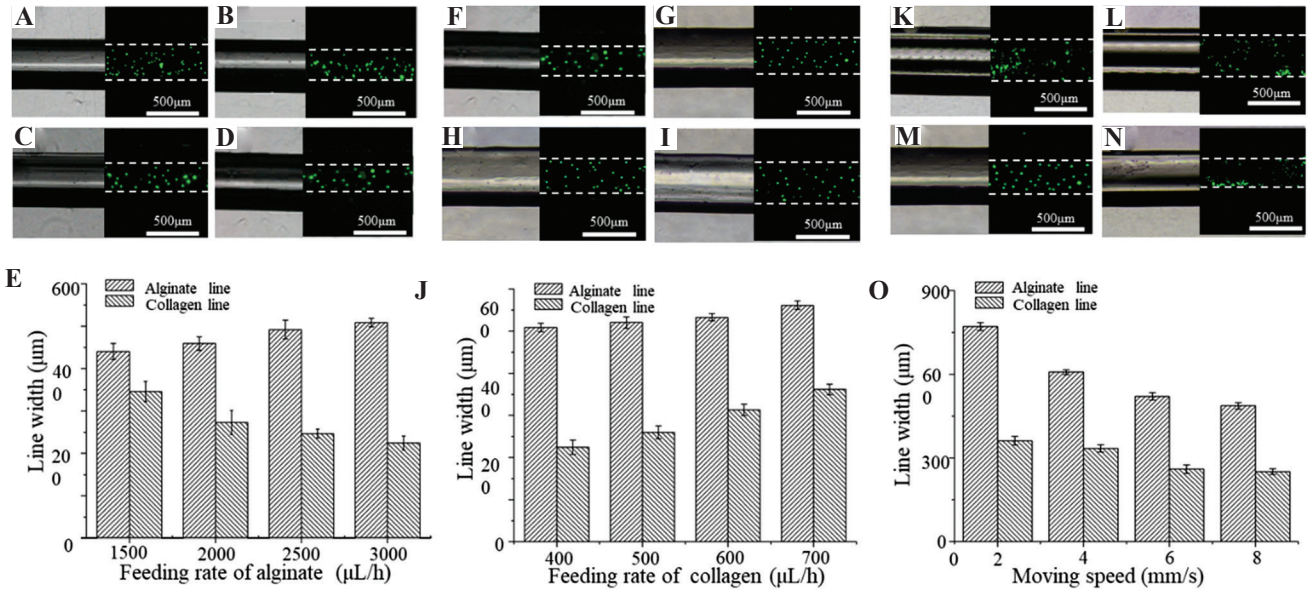


Figure 2. The effect of process parameters on the width of the EHD-bioprinted filaments. (A-E) The morphology and width of the core and sheath lines in the filaments as alginate feeding rate changed from 1500 μL/h to 3000 μL/h. (D-G) The morphology and width of the core and sheath lines in the filaments as collagen solution changed from 400 μL/h to 700 μL/h. (K-O) The morphology and width of the core and sheath lines in the filaments as moving speed changed from 2 mm/s to 8 mm/s.

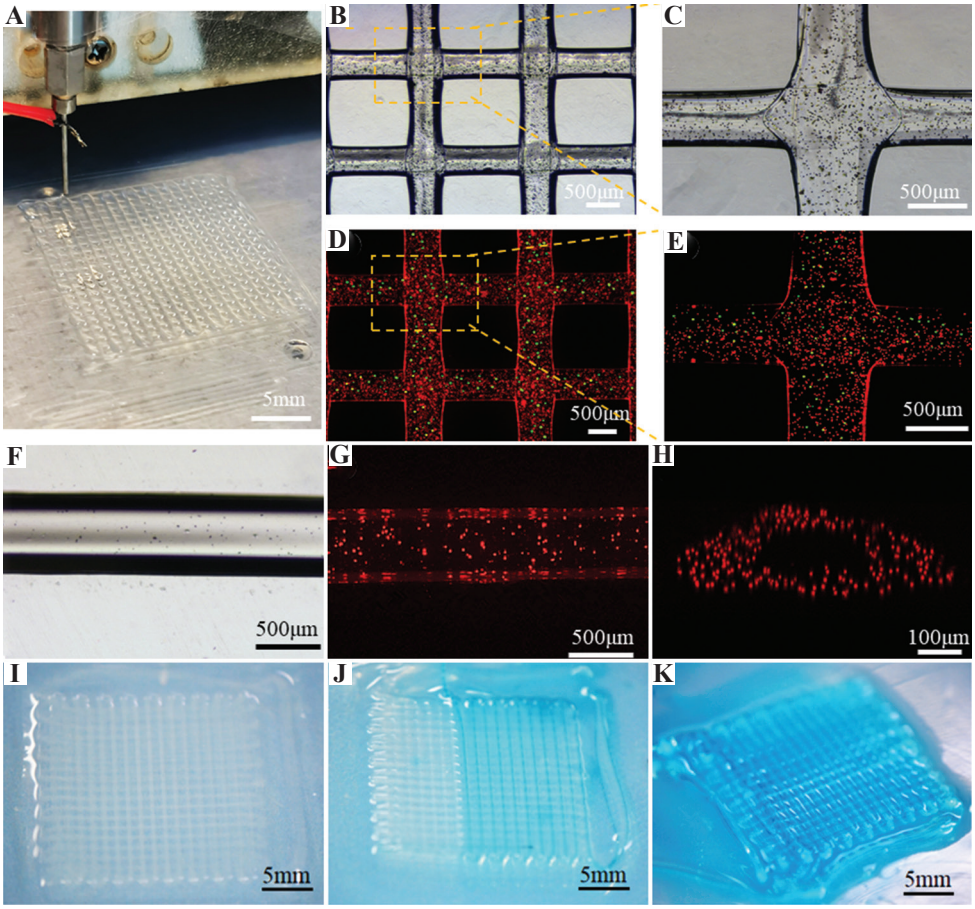


Figure 3. EHD bioprinting of lattice hydrogel with the core-sheath filaments. (A-C) The macroscopical and microscopical morphology of the lattice structures. (D and E) The core-sheath hydrogel filaments with green microbeads in the core line and red microbeads in the sheath line. The bright-field image (F) and fluorescent image (G) of the hollow hydrogel filament. (H) The cross-section of the 3D reconstructed models of hollow hydrogel filament. (I-K) Dye perfusion through the hollow filaments.

shows the effect of the feeding rate of alginate solution on the width of the EHD printed core-sheath filaments when the feeding rate of collagen solution and moving speed of stage were fixed at 400 μL/h and 6mm/s. It was found that the sheath-line width of the alginate filaments increased from 440 ± 18.79 μm to 508.75 ± 10.08 μm and the core-line width of the collagen filaments gradually decreased from 346 ± 23.63 μm to 224.5 ± 16.82 μm when the feeding rate of alginate of the solution changed from 1500 μL/h to 3000 μL/h (**Figure 2E**). **Figure 2F-I** shows the effect of the feeding rate of collagen solution on the width of the EHD printed core-sheath filaments when the feeding rate of alginate solution and moving speed fixed at 3000 μL/h and 6 mm/s. It was found that the sheath-line width of the alginate filaments increased from 508.75 ± 10.08 μm to 561.42 ± 10.14 μm and the core-line width of the collagen filaments increased from 224.5 ± 16.81 μm to 361.57 ± 12.37 μm when the feeding rate of collagen solution increased from 400 μL/h to 700 μL/h (**Figure 2G**). We then studied the effect of the moving speed of the printing stage on the width of the EHD printed core-sheath filaments when the feeding rate of alginate and collagen solution was fixed at 3000 μL/h and 500 μL/h (**Figure 2K-N**). It was found that when the moving speed of the printing stage increased from 2 mm/s to 8 mm/s, the width of the sheath and core line decreased from 771.5 μm to 486.86 μm and from 361.5 μm to 250.8 μm, respectively (**Figure 2O**). These results indicate that the size of the core and sheath within the EHD printed filaments could be modulated independently by changing the feeding rate of the solution in the outer and inner layers of the coaxial nozzle, while the higher moving speed of the printing stage leads to thinner sheath-core hydrogel filament. In the subsequent EHD bioprinting process, the feeding rate of alginate and collagen, as well as the moving speed of the stage, was set as 3000 μL/h, 500 μL/h, and 6 mm/s.

3.2. EHD bioprinting of the lattice hydrogel with core-sheath filaments

The presented EHD-bioprinting method was further employed to fabricate complex lattice hydrogel with core-

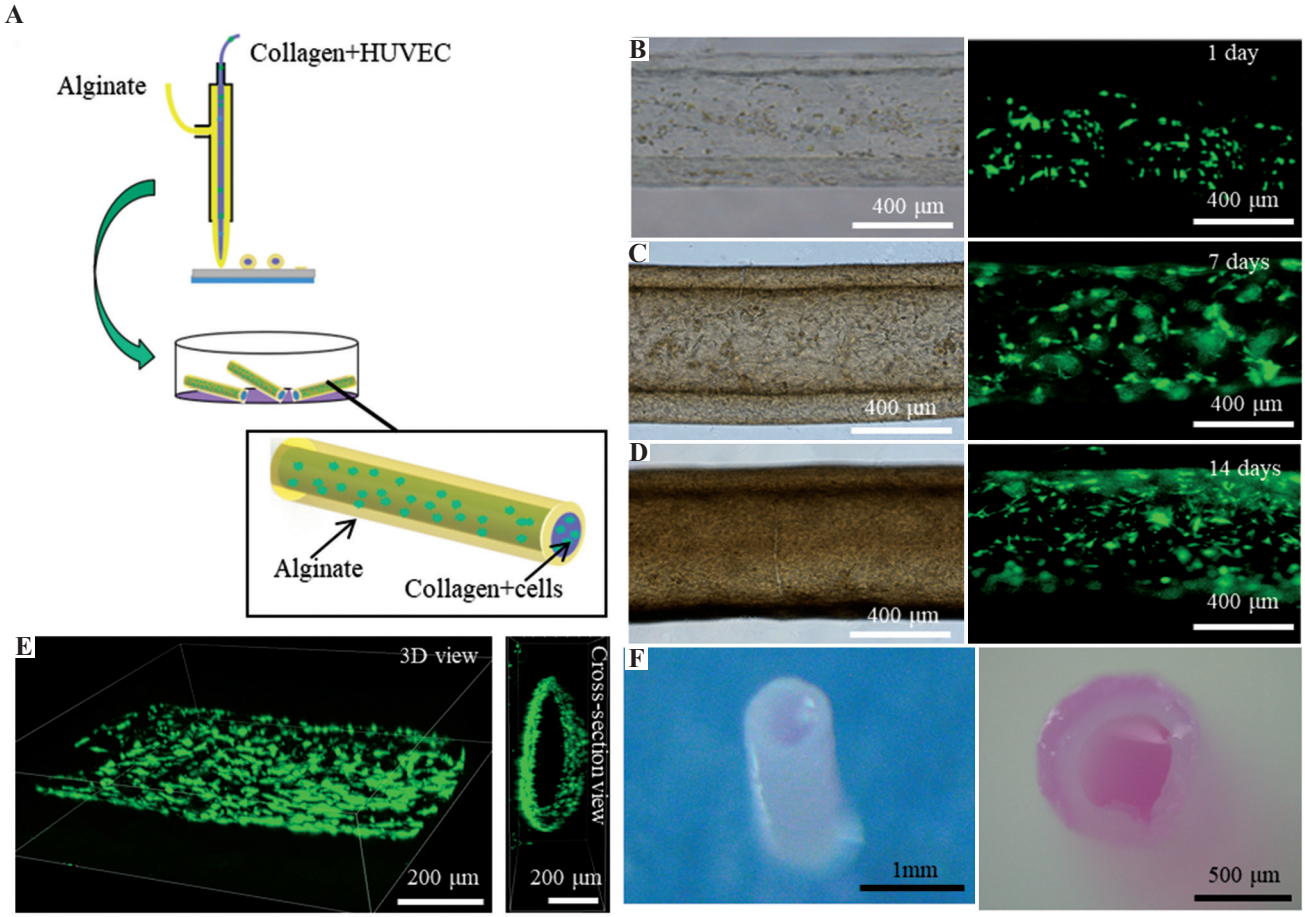


Figure 4. The growth of HUVECs in the core-sheath filaments. (A) The schematic of printing core-sheath filaments laden with HUVECs in the core collagen line. (B-D) The morphology of HUVECs within the filaments during 14 days in static culture. (E) The 3D structure of the formed circular vessel within the filament. (F) The morphology of the core-sheath filament after 14 days in culture.

sheath filaments (**Figure 3A**). Alginate/red fluorescent particles solution and collagen/$CaCl_2$/green fluorescent particles solution were loaded into the outer and inner layer of the coaxial nozzle, respectively. The EHD printed core-sheath filaments maintained excellent morphology and architecture during the printing of complex lattice structures, indicating its potential to fabricate 3D porous constructs for tissue engineering (**Figure 3B and C**). The green fluorescent particles mainly remained in the center of the red fluorescent area, indicating the well-formed core-sheath hydrogel filament with collagen core encapsulated by the alginate sheath without leakage (**Figure 3D and E**).

The collagen/$CaCl_2$/green fluorescent particles solution was replaced by the pure $CaCl_2$ solution to print the hollow hydrogel filaments with perfusable lumen structures. It was found that the printed alginate solution was cross-linked by the $CaCl_2$ solution to form a table hollow hydrogel filament (**Figure 3F**). Red fluorescent particles were uniformly distributed within the ring wall of the hollow filament and the lumen structure was well maintained, as shown in the top-view fluorescent image (**Figure 3G**) and cross-section of the 3D confocal profile (**Figure 3H**). This result demonstrated that the crosslinking between alginate solution and calcium ions occurred instantly when they met and the encapsulated cells would also be maintained uniformly during the printing process in future work. The perfusability of the lattice hydrogel assembled by the hollow filaments was then evaluated by a dye injection test. The blue dye solution could circulate rapidly through the hollow filaments with the predefined lattice pattern, suggesting that this printed lattice hydrogel with lumen filaments is well perfusable (**Figure 3I-K**).

3.3. Fabrication and characterization of the endothelialized lumen structure in the core-sheath filaments

To fabricate the endothelialized filaments, GFP-HUVECs were added into collagen/$CaCl_2$ solution as the inner-layer

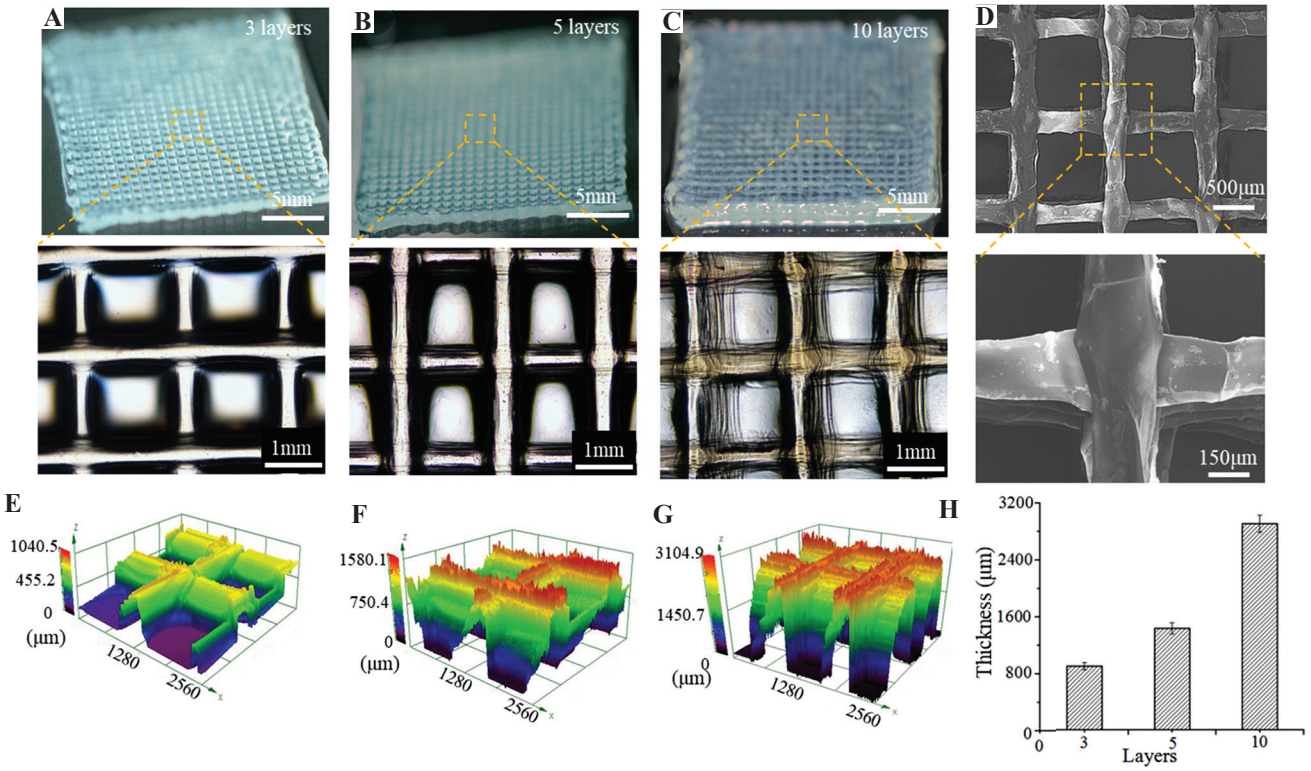


Figure 5. 3D porous hydrogel constructs with different layer numbers. (A-C) Macroscopical and microscopical images of the constructs with 3, 5, and 10 layers. (D) SEM images of the constructs with 5 layers after freeze-drying. (E-G) The 3D confocal profiles of the constructs. (H) Quantification of the thickness of the constructs.

bioink for EHD-bioprinting (**Figure 4A**). **Figure 4B-D** shows the morphology and distribution of HUVECs encapsulated in collagen gelation during 14 days in culture. It was found that the HUVECs maintained high viability and began to spread within the inner collagen layer after 2 days in culture. There was then a notable cell proliferation after 14 days in culture. It was interesting to observe that the cells migrated into the interface between the core and sheath hydrogel and formed a circular vessel along the filament instead of randomly distributing in the core (**Figure 4E**). This might be owing to the swelling and degradation of the collagen gel during the long culturing time, allowing for the movement of cells within the hydrogel filament. The endothelialized hydrogel filaments maintained good morphology during 14 days in culture (**Figure 4F**).

3.4. EHD-bioprinting of 3D porous hydrogel constructs

To investigate the feasibility of generating 3D porous hydrogel constructs, multilayer core-sheath filaments were further printed into lattice structures. **Figure 5A-C** shows the photo images and the corresponding microscopical images of the printed constructs with 3, 5, and 10 layers, indicating that the assembled core-sheath filaments maintained good line feature, predefined layout, and lattice structures during the printing process for all the groups. A substantial increase in the thickness of the constructs could be observed with more layers. **Figure 5D** shows SEM images of the printed lattice hydrogel constructs with 5 layers. It can be found that the neighboring layers were tightly merged, which still maintained structural integrity after freeze-drying. The diameter of the freeze-dried filaments was smaller than the printed hydrogel filaments due to water loss and shrinking during the freeze-drying process. The thickness of the printed constructs with different layers was characterized by 3D confocal profiles (**Figure 5E-G**). The measured thickness of the printed constructs increased from 894.35 ± 41.50 μm to 2893.85 ± 92.60 μm as the layer number increased from 3 to 10 (**Figure 5H**). The average height of each layer was about 290.75 ± 12.22 μm, which indicated that the printed core-sheath filaments in each layer could maintain good morphology and relatively stable thickness. These results indicated that this coaxial EHD bioprinting

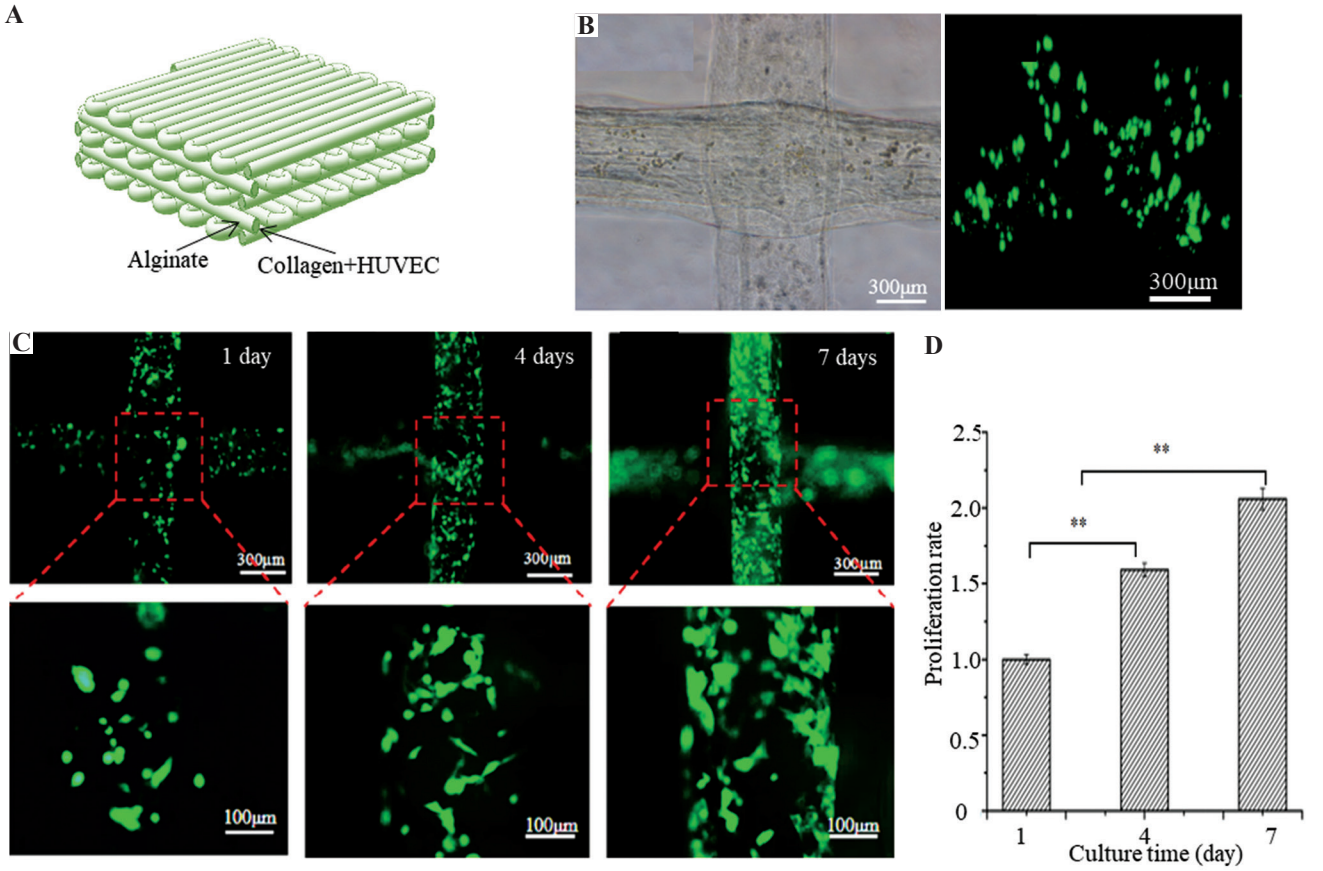


Figure 6. Engineering 3D vasculature within the lattice hydrogel. (A) The schematic of the hydrogel constructs laden with HUVECs within the core collagen bioink. (B) The bright-field image and 3D fluorescent profiles of the 3D lattice hydrogel laden with HUVECs after 3 hours in culture. (C) The growth of HUVECs within the lattices during 7 days in culture. (D) The proliferation of cells within 3D lattice hydrogel during 7 days in culture.

strategy might be employed to fabricate cell-laden 3D constructs for tissue engineering.

3.4. EHD bioprinting of pre-vascularized cell-laden constructs

Alginate and collagen/$CaCl_2$/HUVECs solution was utilized as the outer and inner-layer bioink, respectively, for EHD-bioprinting of pre-vascularized 3D lattice constructs (**Figure 6A**). **Figure 6B** shows the bioprinted lattice hydrogel with stable structures and the 3D fluorescent profiles of HUVECs encapsulated in the lattice hydrogel after 3 hours in culture. The spreading and proliferation of the encapsulated HUVECs within the filaments could be obviously observed during the static culture (**Figure 6C**). The constructs still maintained their morphological and structural features while the cell number was doubled after 7 days (**Figure 6D**), which demonstrated that the printed 3D porous lattice structures were beneficial to the mass transfer of the encapsulated cells. The results of live-dead staining indicated that the cell viability of the constructs increased from 92.5% to 96.3% after 7 days in culture. All these results indicated that the printed porous lattice hydrogel had a potential for engineering 3D vascularized constructs with predefined structures in the future.

As a proof of concept study we sought to employ the coaxial EHD bioprinting strategy for engineering pre-vascularized cardiac constructs by encapsulating H9C2 cells, a cardiac cell line, into alginate solution as the outer-layer bioink. **Figure 7B** shows the optical and fluorescence images of the cell-laden constructs after 1 day in culture, showing that HUVEC cells (green) were surrounded uniformly by the H9C2 cells (red) in 3D constructs. After 2 days in culture, all the cells maintained well viability and the HUVEC cells began to spread and became oriented along the filaments, showing that the coaxial EHD bioprinting strategy has the potential of engineering pre-vascularized cell-laden constructs.

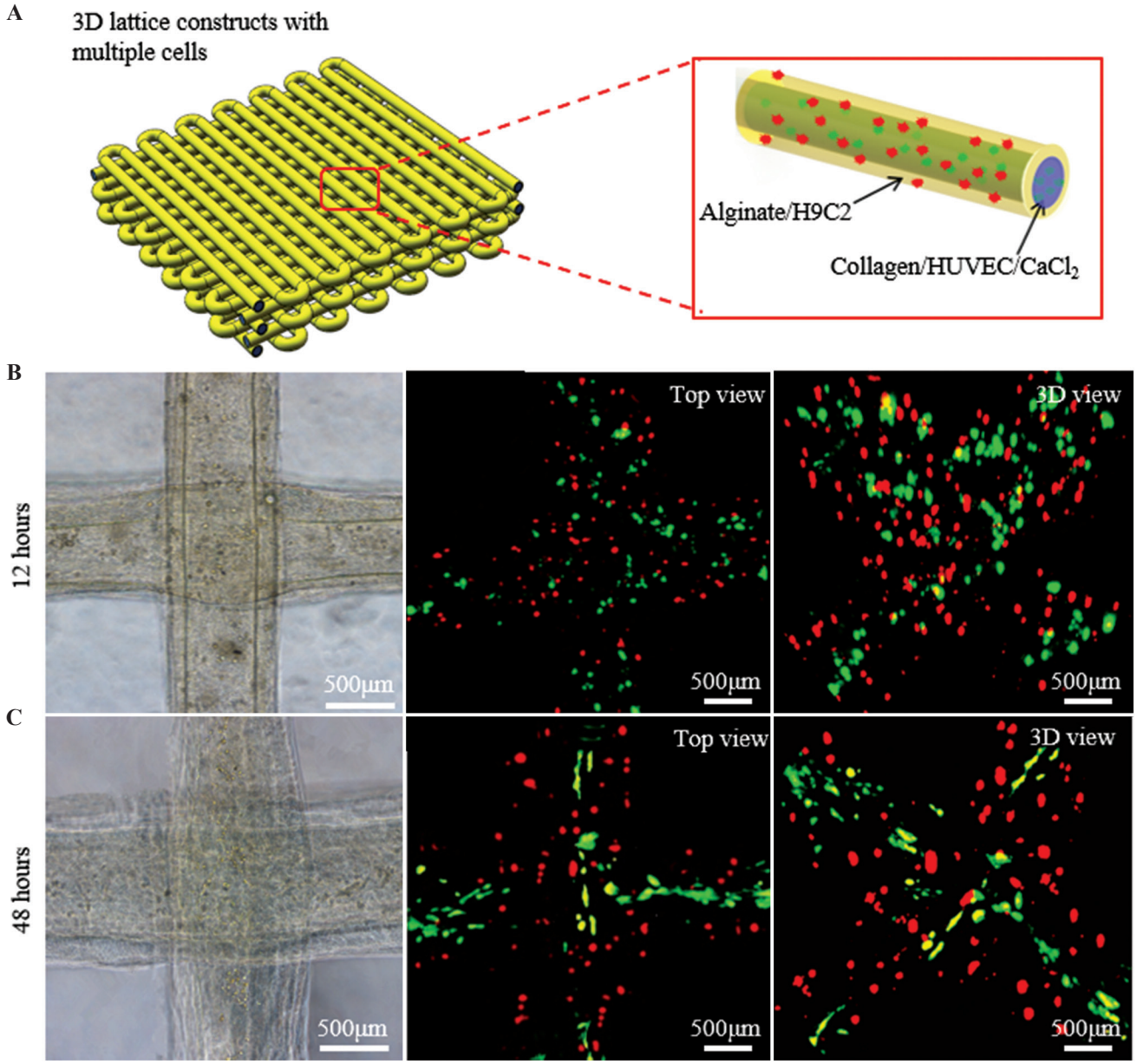


Figure 7. EHD bioprinting of pre-vascularized cardiac constructs. (A) The schematic of the hydrogel constructs laden with HUVECs and H9C2 cells within the core collagen and sheath alginate bioinks, respectively. (B and C) The morphology of the lattice structures and the growth of HUVECs (green) and H9C2 cells (red) within the hydrogel constructs during 48 h in culture.

4. Conclusion

In this study, a coaxial nozzle was introduced into the EHD bioprinting system to fabricate pre-vascularized constructs, which were assembled by the printed core-sheath hydrogel filaments. To stably print the filaments, some process parameters, such as feeding rate of alginate and collagen solution, and moving speed of stage were investigated. HUVECs were added into collagen solution as inner-layer bioink in the coaxial nozzle to generate endothelialized filaments. During cell culture, the cells gradually spread and migrated to the interface between the core collagen line and sheath alginate line and formed a biomimetic lumen vessel structure. 3D constructs with 3, 5, and 10 layers were printed, demonstrating that the hydrogel filaments in each layer maintained their morphology and enabled the formation of thick porous hydrogel construct of more than 3 mm. 3D constructs with HUVECs encapsulated into the core collagen filaments were electrohydrodynamically printed. The cells not only maintained high viability but also spread and proliferated during 7 days in static culture, indicating that the porous structures were beneficial to the nutrition

supply. Finally, GFP-HUVECs and H9C2 cells were mixed with inner-layer collagen and out-layer alginate solution, respectively, to fabricate 3D pre-vascularized cardiac constructs. It was noted that the HUVECs encapsulated in collagen gel were able to spread and align along the filaments surrounded by the H9C2 cells in the 3D constructs. These results demonstrate that this coaxial EHD bioprinting method has great potential to fabricate complex 3D tissues or organs with vascular network.

Acknowledgments

This work was financially supported by the National Key Research and Development Program of China (2018YFA0703000), the Key Research Project of Shaanxi Province (2020GXLH-Y-021), Guangdong Basic and Applied Basic Research Foundation (2020B1515130002), The Youth Innovation Team of Shaanxi Universities, and the Fundamental Research Funds for the Central Universities.

Conflict of interest

No conflict of interest were reported by the authors.

Author contributions

M.M. and H.L. designed the overall experimental plan and performed experiments. M.M. wrote the manuscript with support from H.L. and J.H., and co-authors A.K., Y.Z., L.W., and X.L. involved in the investigation and analysis of results. J.H. and D.L. supervised the project and conceived the original idea.

References

1. Zhu W, Qu X, Zhu J, *et al.*, 2017, Direct 3D Bioprinting of Prevascularized Tissue Constructs with Complex Microarchitecture. *Biomaterials*, 124:106–15. https://doi.org/10.1016/j.biomaterials.2017.01.042
2. Baranski JD, Chaturvedi RR, Stevens KR, *et al.*, 2013, Geometric Control of Vascular Networks to Enhance Engineered Tissue Integration and Function. *Proc Natl Acad Sci U S A*, 110:7586–91. https://doi.org/10.1073/pnas.1217796110
3. Bertassoni LE, Cecconi M, Manoharan V, *et al.*, 2014, Hydrogel Bioprinted Microchannel Networks for Vascularization of Tissue Engineering Constructs. *Lab Chip*, 14:2202–11. https://doi.org/10.1039/c4lc00030g
4. Qiu Y, Ahn B, Sakurai Y, *et al.*, 2018, Microvasculature-on-a-chip for the Long-term Study of Endothelial Barrier Dysfunction and Microvascular Obstruction in Disease. *Nat Biomed Eng*, 2:453–63. https://doi.org/10.1038/s41551-018-0224-z
5. Miller JS, Stevens KR, Yang MT, *et al.*, 2012, Rapid Casting of Patterned Vascular Networks for Perfusable Engineered Three-dimensional Tissues. *Nat Mater*, 11:768. https://doi.org/10.1038/NMAT3357
6. Mao M, Bei HP, Lam CH, *et al.*, 2020, Human-on-Leaf-Chip: A Biomimetic Vascular System Integrated with Chamber-Specific Organs. *Small*, 16:2000546. https://doi.org/10.1002/smll.202000546
7. He J, Mao M, Liu Y, *et al.*, 2013, Fabrication of Nature-Inspired Microfluidic Network for Perfusable Tissue Constructs. *Adv Healthc Mater*, 2:1108–13. https://doi.org/10.1002/adhm.201200404
8. Lenoir L, Segonds F, Nguyen KA, *et al.*, 2019, A Methodology to Develop a Vascular Geometry for *In Vitro* Cell Culture Using Additive Manufacturing. *Int J Bioprint*, 5:238. https://doi.org/10.18063/ijb.v5i2.238
9. Mirabella T, MacArthur JW, Cheng D, *et al.*, 3D-printed Vascular Networks Direct Therapeutic Angiogenesis in Ischaemia. *Nat Biomed Eng*, 1:0083. https://doi.org/10.1038/s41551-017-0083
10. Yao R, Alkhawtani AY, Chen R, *et al.*, 2019, Rapid and Efficient *In Vivo* Angiogenesis Directed by Electro-assisted Bioprinting of Alginate/Collagen Microspheres with Human Umbilical Vein Endothelial Cell Coating Layer. *Int J Bioprint*, 5:194. https://doi.org/10.18063/ijb.v5i2.1.194
11. Hasan A, Paul A, Vrana NE, *et al.*, 2014, Microfluidic Techniques for Development of 3D Vascularized Tissue. *Biomaterials*, 35:7308–25. https://doi.org/10.1016/j.biomaterials.2014.04.091
12. Ng WL, Chua CK, Shen YF, 2019, Print Me An Organ! Why We Are Not There Yet. *Prog Polym Sci*, 97:101145. https://doi.org/10.1016/j.progpolymsci.2019.101145
13. Li X, Liu B, Pei B, *et al.*, 2020, Inkjet Bioprinting of Biomaterials. *Chem Rev*, 120:10793–833. https://doi.org/10.1021/acs.chemrev.0c00008
14. Jiang T, Munguia-Lopez JG, Flores-Torres S, *et al.*, 2019, Extrusion Bioprinting of Soft Materials: An Emerging Technique for Biological Model Fabrication. *Appl Phys Rev*, 6:30. https://doi.org/10.1063/1.5059393
15. Ng WL, Lee JM, Zhou M, *et al.*, 2020, Vat Polymerization-based Bioprinting-Process, Materials, Applications and Regulatory Challenges. *Biofabrication*, 12:022001. https://doi.org/10.1088/1758-5090/ab6034
16. Kolesky DB, Homan KA, Skylar-Scott MA, *et al.*, 2016,

Three-dimensional Bioprinting of Thick Vascularized Tissues. *Proc Natl Acad Sci*, 113:3179–84. https://doi.org/10.1073/pnas.1521342113

17. Kolesky DB, Truby RL, Gladman AS, *et al.*, 2014, 3D Bioprinting of Vascularized, Heterogeneous Cell-laden Tissue Constructs. *Adv Mater*, 26:3124. https://doi.org/10.1002/adma.201305506
18. Feng F, He J, Li J, *et al.*, 2019, Multicomponent Bioprinting of Heterogeneous Hydrogel Constructs Based on Microfluidic Printheads. *Int J Bioprint*, 5:202. https://doi.org/10.18063/ijb.v5i2.202
19. Kang HW, Lee SJ, Ko IK, *et al.*, 2016, A 3D Bioprinting System to Produce Human-scale Tissue Constructs with Structural Integrity. *Nat Biotechnol*, 34:312–9. https://doi.org/10.1038/nbt.3413
20. Murphy SV, Atala A, 2014, 3D Bioprinting of Tissues and Organs. *Nat Biotechnol*, 32:773. https://doi.org/10.1038/nbt.2958
21. He J, Zhang B, Li Z, *et al.*, 2020, High-resolution Electrohydrodynamic Bioprinting: A New Biofabrication Strategy for Biomimetic Micro/Nanoscale Architectures and Living Tissue Constructs. *Biofabrication*, 12:042002. https://doi.org/10.1088/1758-5090/aba1fa
22. Huo H, Liu F, Luo Y, *et al.*, 2020, Triboelectric Nanogenerators for Electro-assisted Cell Printing. *Nano Energy*, 67:104150. https://doi.org/10.1016/j.nanoen.2019.104150
23. Gasperini L, Maniglio D, Motta A, *et al.*, An Electrohydrodynamic Bioprinter for Alginate Hydrogels Containing Living Cells. *Tissue Eng Part C Methods*, 21:123–32. https://doi.org/10.1089/ten.tec.2014.0149
24. Workman VL, Tezera LB, Elkington PT, *et al.*, 2014, Controlled Generation of Microspheres Incorporating Extracellular Matrix Fibrils for Three-Dimensional Cell Culture. *Adv Funct Mater*, 24:2648–57. https://doi.org/10.1002/adfm.201303891
25. Sampson SL, Saraiva L, Gustafsson K, *et al.*, Cell Electrospinning: An *In Vitro* and *In Vivo* Study. *Small*, 10:78–82. https://doi.org/10.1002/smll.201300804
26. Jayasinghe SN, Qureshi AN, Eagles PA, 2006, Electrohydrodynamic Jet Processing: An Advanced Electric-Field-Driven Jetting Phenomenon for Processing Living Cells. *Small*, 2:216–9. https://doi.org/10.1002/smll.200500291
27. Wang J, Huang R, Chen H, *et al.*, 2019, Personalized Single-Cell Encapsulation Using E-Jet 3D Printing with AC-Pulsed Modulation. *Macromol Mater Eng*, 304:1800776. https://doi.org/10.1002/mame.201800776
28. Yeo M, Ha J, Lee H, *et al.*, 2016, Fabrication of hASCs-laden Structures Using Extrusion-based Cell Printing Supplemented with an Electric Field. *Acta Biomater*, 38:33–43. https://doi.org/10.1016/j.actbio.2016.04.017
29. He J, Zhao X, Chang J, *et al.*, 2017, Microscale Electro-Hydrodynamic Cell Printing with High Viability. *Small*, 2017:1702626. https://doi.org/10.1002/smll.201702626
30. Liang HT, He JK, Chang JK, *et al.*, 2018, Coaxial Nozzle-assisted Electrohydrodynamic Printing for Microscale 3D Cell-laden Constructs. *Int J Bioprint*, 4:8. https://doi.org/10.18063/IJB.v4i1.127

RESEARCH ARTICLE

Elastic and Stretchable Double Network Hydrogel as Printable Ink for High-Resolution Fabrication of Ionic Skin

Kaiwen Chen†, Qiwei Ying†, Xingxing Hao†, Kai Sun, Huanan Wang*

Key State Laboratory of Fine Chemicals, School of Bioengineering, Dalian University of Technology, No. 2 Linggong Road, High-tech District, Dalian, 116024, P.R. China

†*These authors contributed equally to this work*

Abstract: A hydrogel that combines both printability and adaptability, high elasticity, and stretchability can provide ideal mechanical properties, and also render complex and accurate construction for ionic skin. However, it is extremely challenging. Here, we propose a colloidal-based double-network (DN) hydrogel as printable inks for high-precision fabrication of ionic skins. Particularly, polyacrylamide (PAAm), as the covalent network that can maintain the long-term material integrity, was combined with gelatin colloidal network to improve the injectability and printability of the resulting DN hydrogels. The DN design cooperatively provides the hydrogels with higher toughness values and deformability than what single colloidal or PAAm network can achieve. Further design of ionic skin based on capacitor microarray was demonstrated to serve as a sensitive and stable capacitor that can respond to external stimuli, thereby allowing to sense the body movements such as finger bending, laugh, and wrist pulse by translating mechanical changes into electric signals. Therefore, this study provides a novel strategy for the design and preparation of high-resolution ionic skins as the wearable sensor.

Keywords: Double-network hydrogel; Colloidal gel; 3D printing; Ionic skin; Capacitance microarray

*Correspondence to: Huanan Wang, Key State Laboratory of Fine Chemicals, School of Bioengineering, Dalian University of Technology, No.2 Linggong Road, High-tech District, Dalian, 116024, P.R.China; huananwang@dlut.edu.cn

Received: April 20, 2021 **Accepted:** May 25, 2021 **Published online:** June 25, 2021

(This article belongs to the *Special Section: Bioprinting of 3D Functional Tissue Constructs*)

Citation: Chen K, Ying Q, Hao X, *et al*., 2021, Elastic and Stretchable Double Network Hydrogel as Printable Ink for High-resolution Fabrication of Ionic Skin. *Int J Bioprint*, 7(3):377. http://doi.org/10.18063/ijb.v7i3.377

1. Introduction

Recently, various soft electronics have been developed to imitate skin's unique characteristics, such as mechanical adaptability and sensory capabilities[1]. These so-called "electronic skin" devices can convert external stimuli such as pressure[2], strain[3], and vibration[4] into reliable electronic signals, thus serving as ideal materials for the development of wearable devices and soft robotics. Although these electronic skins can sense various signals, they still show insufficient biocompatibility and mechanical adaptability which are caused by the potentially cytotoxic and rigid inorganic conductive materials. To this end, Whitesides *et al*. recently proposed the concept of "ionic skin" as biomimetic biosensor materials, in which mechanical signals can be converted into electric signals by using the soft, biocompatible, and ionically conductive hydrogels as the electronic conductors[5]. Unlike electronic skins composed of organic polymers and inorganic conductive materials, ionic skins typically consist of hydrophilic polymers dispersed in an aqueous salt solution that can transmit electrical signals through ions instead of electrons, resulting in physiological and mechanical properties comparable to natural skin tissues[6,7]. In general, the structure of the ionic skin is composed of a parallel plate capacitor and ionic hydrogel as the conductive layer. When the capacitor senses external stimuli (such as strain and pressure), the capacitance value will change. However, currently available ionic skins were

© 2021 Chen, *et al*. This is an Open Access article distributed under the terms of the Creative Commons Attribution License (https://creativecommons.org/licenses/by/4.0/), permitting distribution and reproduction in any medium, provided the original work is cited.

mostly based on chemically cross-linked hydrogels, such as polyacrylamide (PAAm). These hydrogels were inherently elastic, lack of stretchability and durability, and cannot adapt to the local movements of the human body[5]. Therefore, physically cross-linked hydrogels with self-healability and flexibility that can adapt to dynamic surfaces have been recently developed. However, these systems showed poor structural integrity, insufficient anti-fatigue properties, and plastic deformation under external force, which can compromise the materials stability and functionality of the ionic skins[8-11]. Therefore, it is still a challenge to develop hydrogel-based electronic sensors as ionic skins that feature the combined attributes of adaptability, high elasticity, and stretchability.

Gong *et al*. proposed double-network (DN) hydrogel, which typically combines a stable covalent network with a reversible non-covalent network, and has shown mechanical strength and toughness values orders of magnitude greater than what the can achieve separately[12-15]. Inspired by this concept, our group has developed DN hydrogels based on reversibly crosslinked colloidal network combined with a continuous phase of the permanently crosslinked network by covalent bonds. These hydrogels have shown significantly enhanced mechanical behavior, a high degree of stretchability and adaptability to local deformation or shear force[16]. Specifically, colloidal gels are based on a bottom-up assembly of micro- or nano-sized particles to form a porous but interconnected particulate network[17,18]. By introducing interparticle interactions such as electrostatic forces[19], magnetic forces[20], or hydrophobic interactions[21], and colloidal gels can develop shear-thinning and self-healing behavior, which are advantageous to applications in bioprinting, injectable scaffolds, or drug carriers.

Based on this design rationale, we hereby propose a DN colloidal hydrogel for the fabrication of ionic skins. Particularly, a binary composite hydrogel system composed of PAAm as the covalent network to maintain long-term material integrity in combination with a shear-thinning and self-healing gelatin colloidal network to improve the injectability and printability was developed, which allowed high-resolution fabrication of ionic skin with microscopic patterned microstructure by three-dimensional (3D) printing. The resulting DN ionic skin sensor can be rendered with high stretchability and elasticity, as well as enhanced sensitivity to forces and deformations, outperforming conventional bulk hydrogel-based ionic skins due to the specific microscale micro-architecture. The printed microarray in the current ionic skin devices can enable the sensing of the location where the external stress was applied with a resolution of millimeter-scale resolution (**Figure 1**). In general, we provide a novel approach for high-resolution fabrication of a new generation of ionic skin sensors with substantially higher stretchability and elasticity, which opens up a new avenue for the design and fabrication of degradable, implantable, and biocompatible smart electronics.

2. Materials and methods

2.1. Preparation of PAAm hydrogels

Acrylamide (AAm, 99%, Aladdin), N,N-methylene bis(acrylamide) (MBAA, 99%, Sigma-Aldrich), and 2-hydroxy-4'-(2-hydroxyethoxy)-2-methylpropiophenone (2959, >99%, Aladdin) were dissolved in 2 M NaCl solution at room temperature to obtain clear solution with different concentration of AAm (5 w/v%, 10 w/v% and 15 w/v%). The solution was further cross-linked by 365 nm ultraviolet (UV) lights (50 mW/cm^2, 60 s) to form PAAm hydrogels.

2.2. Preparation of colloidal hydrogels

Gelatin nanoparticles were prepared based on a previously reported two-step desolvation method[17]. Different mass fractions of gelatin nanoparticles (5%, 7.5%, 10%, and 15%) were dissolved in 2 M NaCl solution to obtain gelatin colloidal gels.

2.3. Preparation of DN hydrogels

For preparing the DN hydrogels, gelatin nanoparticles with a mass fraction of 10% were fully mixed with the solution which contained AAm as a monomer, MBAA as a crosslinking agent, and irgacure 2959 as a photo-initiator to obtain the colloidal gel. The AAm monomer in colloidal gel further was crosslinked by 365 nm UV lights (50 mW/cm^2, 60 s). The detailed parameters of hydrogels as listed in Table 1.

2.4. Scanning electron microscope (SEM)

The microstructure of hydrogels was observed by scanning electron microscopy (FEI, Quanta 450, USA). Specifically, the DN hydrogels were frozen and fractured at −80°C, and then freeze-dried to remove water. Then, the cross-sections of the hydrogel samples were coated with gold to increase the conductivity.

2.5. Rheology

The hydrogels were tested for rheological behavior using a discovery hybrid rheometer (DHR, TA instrument). The measurement was performed using a parallel plate fixture, and the gap distance was set to 1000 μm. The shear-thinning behavior of the colloidal gels was evaluated by a stepped flow test (shear rate was 0.1 – 100 1/s). The self-healing behaviors were quantitatively characterized by the change of storage modulus of the gels before/after destructive shearing (oscillatory strain sweep with an increased strain from 1 to 1000% and a frequency of 1 Hz for 200 s). The hydrogel samples were further

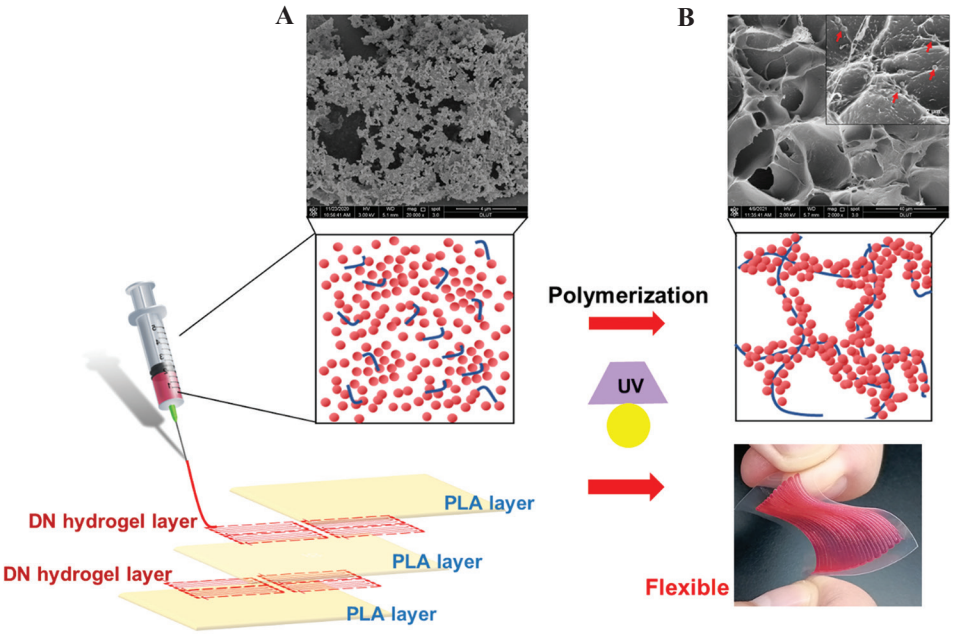


Figure 1. Design principle of gelatin/polyacrylamide (PAAm) double-network (DN) hydrogels for the preparation of ionic skin. The conductive layers were printed by gelatin nanoparticles in combination with AAm monomers, followed by photoinduced polymerization of PAAm, to obtain an elastic and flexible ionic skin. The dielectric layer was polylactic acid (PLA) film. The schematic diagram showing the mechanism of the formation of nanostructured gelatin colloidal network (A) and the DN hydrogels composed of gelatin nanoparticles and PAAm (B). Scanning electron microscope photographs showing the microstructures of pure gelatin colloidal gel and gelatin/PAAm DN hydrogels.

shaped by molding followed by secondary crosslinking by photo-induced polymerization of PAAm, in which the evolution of viscoelastic properties was determined by an oscillation time sweep (frequency of 1 Hz and strain of 0.5%). The inherent viscoelastic properties of the resulting hydrogels were characterized by an oscillation frequency sweep (0.1 to 100 rad/s at a constant strain of 0.5%).

2.6. Mechanical test

Compression and tensile test were performed using dumbbell-shaped and cylindrical-shaped specimens designed according to ISO standards and evaluated by a universal testing machine (E43, MTS instrument, USA) equipped with a 50 N sensor (25°C, 60% RH). The cyclic compression and tensile tests were carried out with a loading rate of 1 mm/min and samples were loaded to the initial deformation after being compressed to the strain of 0.75. The fracture energy (kJ/m^3) was calculated by the area below the tensile stress-strain curve used to characterize the work required to break a sample per unit volume. The elastic modulus was defined as the slope of the initial linear region of the stress-strain curve.

2.7. Printability and fidelity of DN hydrogels

To print the DN hydrogel, the hydrogel inks composed of gelatin nanoparticles and PAAm precursor solution were used to fabricate microstructures by a homemade extrusion-based bioprinter. Thereafter, the printed constructs were exposed to UV light to allow polymerization of PAAm. The injectability of the colloidal gels with different concentrations was evaluated by injecting force during the extrusion process by a universal testing machine (E43, MTS instrument, USA). Specifically, gelatin nanoparticles were weighed and mixed with 2 M NaCl solution (pH = 7.0) in 5 mL medical syringes (BD Plastipak™, orifice diameter of 400 μm) to obtain colloidal gels. After storing at 4°C for 2 h, the syringe was fixed vertically under the plate of the tensile bench, and a compressive force was applied to the plunger of the syringe at a constant velocity of 1 mm/min. The injection force was recorded as a function of the plunger travel time. In addition, the degree of material expansion after injection was evaluated by immediately recording photographs of the printed filaments from the nozzle of different diameters.

2.8. Fabrication of DN hydrogel-based ionic skin devices

To generate an ionic skin device with high resolution, we designed an electronic circuit with microarray printed by gelatin/PAAm DN hydrogel. Specifically, we used homemade 3D printing equipment, and 400 μm needle to further print DN hydrogel, and each sensor unit area is 7 mm × 7 mm, printing a total of 1 (1 × 1), 4 (2 × 2), and 49 (7 × 7) units of the ionic skin. To fabricate

a capacitor-based ionic skin, we first printed a hydrogel layer on a poly(lactic acid) (PLA) film layer, and hydrogel was further crosslinked to form a polymer network by 365 nm UV light. Then, we further printed a hydrogel layer on the top PLA layer and cured it with UV light, and the PLA film further covered as a dielectric layer and prevents evaporation of the hydrogel.

To further test the capacitance of capacitor-based ionic skin, we use an LCR meter (TH2830) at an AC voltage of 1 V and a sweeping frequency of 1 kHz. Capacitance changes were simultaneously detected with various stimuli on the prepared devices. The printed ionic skins were composed of five layers, of which the first, third, and fifth layers were PLA films (height: 50 μm), and the second and fourth layers were printed hydrogels.

3. Results and discussion

3.1. Mechanical properties of the DN hydrogels

The GNPs/PAAm DN hydrogels were prepared by directly mixing gelatin nanoparticles with flowable AAm monomer solution via multiple cycles of extrusion in a conventional medical syringe, followed by molding or printing into certain morphology that can be further photopolymerized to allow the solidification of the structures. Before triggering the polymerization of PAAm, we first evaluated the injectability and printability properties of pure nanostructured gelatin colloidal gels. By applying an increasing shear rate, the gelatin colloidal gels of different concentrations showed typical shear-thinning behavior as evidenced by a linear decrease in viscosity upon shearing (**Figure 2A**). Moreover, gelatin colloidal gels also showed a high degree of mechanical recovery after severe network destruction (or so-called self-healing behavior). As shown in **Figure 2B**, in the initial low strain region (0.5%), the colloidal gel showed the formation of a stable gel network as reflected by a higher value of G' than G". Subsequently, a higher shear strain (1 – 1000% for 1 min) led to network destruction and the transformation from a solid gel to a liquid-like material as reflected by G" higher than G'. On release of the destructive shear, gelatin colloidal gel immediately showed more than 70% of recovery of G' value as relevant to the initial G'. This can be attributed to the cohesive interactions between gelatin nanoparticles. Such shear-thinning and self-healing behavior rendered the colloidal gels printable and capable of blending with different components such as other types of micro-/nano-particles or flowable precursor solutions. To obtain a mechanically stable colloidal network, we prepared hydrogels containing gelatin nanoparticles with mass fraction ranging from 10 to 12 w/v% (corresponding to volume fraction above 0.5). Such highly packed colloidal systems can eliminate the effect resulting from the structural features of the particulate network on the mechanical properties of the resulting colloidal gels[22].

The gelatin/PAAm DN hydrogels not only maintained the shear-thinning and self-healing properties of the colloidal network but also exhibited enhanced gel elasticity after photopolymerization (G'~4 kPa) 3 times higher than before polymerization (**Figure 2C**). Further oscillatory frequency sweep tests revealed the frequency-independent behavior of the DN hydrogels as well as the colloidal gels; the DN gels had higher gel strength than the colloidal gels. In contrast, 10 w/v% PAAm hydrogels showed a more frequency-dependent behavior with the network moduli increasing gradually as a function of frequency (**Figure 2D**).

We further used conventional compression and tensile tests to characterize the mechanical properties of gelatin/PAAm DN hydrogels. On compression, the DN hydrogels initially showed a linear region with the stress increased linearly as strain increased (**Figure 3A**). After the linear region, the stress showed a sharp increase with increasing the compressive loading, with the compressive modulus E_c and strength σ_c of 31.1±4.6 and 270.1±15.7 kPa, respectively. Interestingly, we did not observe any yielding point even the compression strain was up to 95%, suggesting the considerable elasticity of the hydrogel matrix resulting from the DN design. In comparison, pure gelatin colloidal gels showed a similar elastic behavior at rather small deformation with the E_c = 32.9±4.5 and σ_c =15.7±1.8 kPa. However, gelatin colloidal gels can only resist 35% strain followed by an elastic fracture. Moreover, PAAm hydrogels showed a significantly weaker compressive modulus with E_c = 3.1±0.3 kPa as compared to both DN hydrogels and the colloidal gels.

Further tensile tests revealed almost purely elastic properties followed by an elastic fracture for the gelatin/PAAm DN hydrogels, evidenced by the highly linear stress-strain curve without showing any plastic deformation (**Figure 3B**). The tensile modulus E_t = 15.1±0.6 and tensile strength σ_t =27.8±1.3 kPa, respectively. Pure gelatin colloidal gel displayed a comparable tensile modulus E_t =14.1±3.1 but a considerably lower tensile strength σ_t =1.3±0.3 kPa as compared to DN hydrogels. In contrast, PAAm hydrogels showed the weakest mechanical properties with E_t = 2.3±0.4 and σt =2.5±0.2 kPa, respectively. Noticeably, the DN hydrogels also exhibited higher tensile fracture strain up to 1.74, slightly higher than PAAm (fracture strain of 1.21), but more than one order of magnitude higher than pure gelatin colloidal gels with yield strain of 0.11.

We further performed cyclic compression/tensile tests to explore the capacity of the DN hydrogels for anti-fatigue performance and energy dissipation on

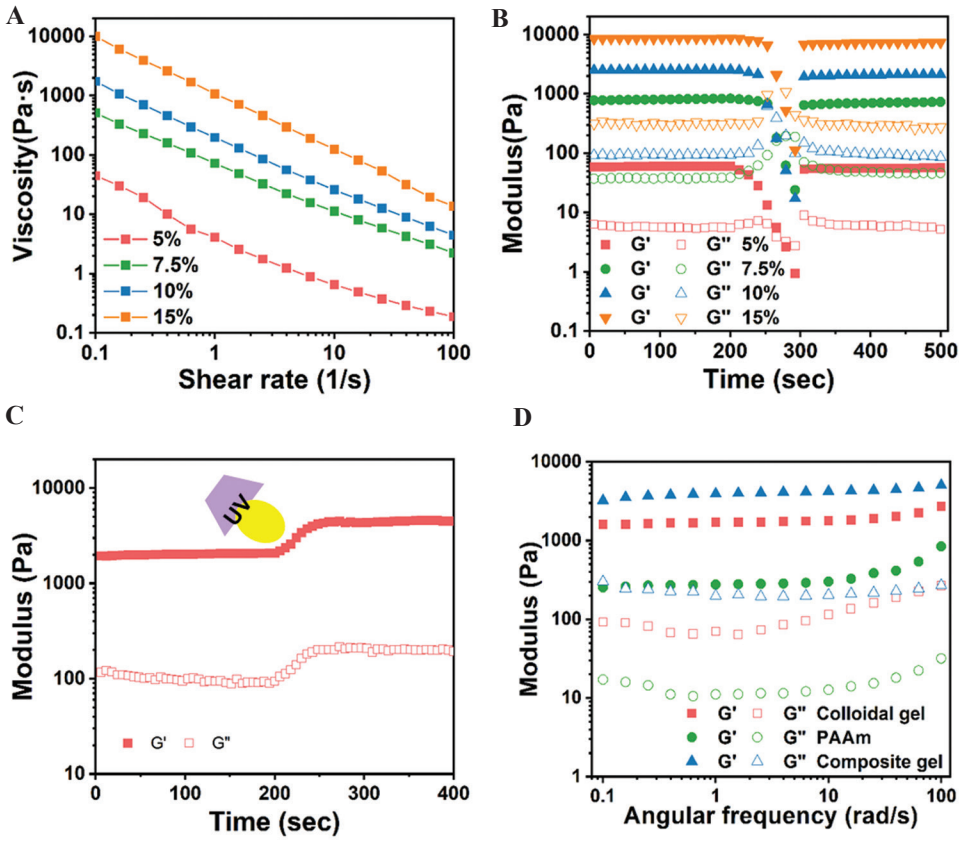


Figure 2. Viscoelastic properties of gelatin/polyacrylamide (PAAm) double-network (DN) hydrogels. (A) Shear-thinning behavior of the nanostructured gelatin colloidal gel of different concentrations (5, 7.5, 10, and 15 w/v%). (B) Evolution of modulus of the colloidal gel of different concentrations by applying the destructive shearing (oscillatory strain sweep with increasing strain from 1% to 1000% with a fixed frequency of 1 Hz) and the recovery (oscillatory time sweep at 0.5% strain and a frequency of 1 Hz for 200 s) on the release of destructive shearing. (C) Triggered photo-polymerization of gelatin/PAAm composite gels (time sweep at 0.5% strain and 1 Hz frequency), as reflected by the sharp increase of G' and G" values. (D) Frequency dependence of storage and loss modulus of pure gelatin colloidal gel (10 w/v% gelatin nanoparticles), PAAm (10w/v%), and gelatin/PAAm composite gel (10 w/v% gelatin nanoparticles, 10 w/v% PAAm).

loading. The gelatin/PAAm DN hydrogels can withstand the repetitive applications of the compressive stress of ~200 kPa and a compressive strain up to 0.75, and can rapidly recover to the original shape upon unloading during the cyclic compression test (**Figure 3C**). For the cyclic tensile tests, the DN hydrogels also showed a wide-range linear elasticity and capability to resist repetitive tensile stress of ~15 kPa and a tensile strain of 1 (**Figure 3D**). Similarly, we observed almost complete recovery to the original state on unloading and overlapped hysteresis loops even after 50 cycles of loading/unloading. These findings suggest that the DN hydrogels are highly elastic and anti-fatigue, which are of significant importance for the development of wearable devices that adapt to body movements[23,24].

We compared the current colloidal-based DN hydrogels with previously reported highly strong or tough hydrogels. Typical DN hydrogels achieve high robustness or toughness values through the combination of a permanent covalent network with a reversibly crosslinked non-covalent network to allow energy dissipation[14], thereby realizing gel mechanics outperforming what they can achieve individually. However, the preparation of conventional DN hydrogels was normally time-consuming and complicated, which restricted the precision manufacturing and wide-spreading applications[13]. Alternative strategy of introducing nanoparticles as the reinforcement components to the continuous polymer network was widely-used to prepare strong hydrogels as compared to the DN design, which normally confronted with the issue of network homogeneity of the disperse and continuous phases, and subsequent compromised mechanical properties[25]. In comparison, our DN design based on colloidal and polymeric networks combined the superior properties of both components, including ease of preparation, injectability, or moldability rendered by the reversibly crosslinked colloidal network, and high network mechanics and structural integrity resulting from the covalent PAAm network. Such combination allows us to fabricate these hydrogels into micro-meter scale

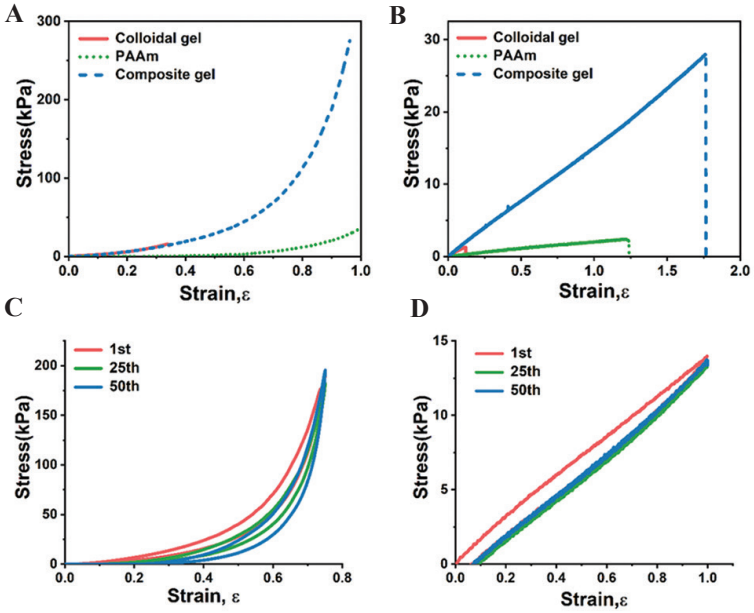


Figure 3. The mechanical properties of double-network (DN) hydrogels tested using conventional compressive and tensile tests. The stress-strain curves of (A) compressive and (C) tensile measurements at a strain rate of 0.021 1/s for the gelatin colloidal gel, polyacrylamide (PAAm), and gelatin/PAAm DN hydrogels. The hysteresis curves of DN hydrogels on (B) cyclic compressive and (D**)** tensile loading and unloading.

resolution through 3D printing meanwhile achieving outstanding gel mechanics through secondary crosslinking based on photo-polymerization of the polymer phase.

3.2. Printability of the DN hydrogels

We further evaluated the printability of the DN hydrogels as inks for 3D printing. Typically, we first assessed the injectability of the hydrogel inks by monitoring the compressive force for the extrusion of the inks using conventional medical syringes (**Figure 4A**). It was shown that gelatin hydrogel in with different colloid concentrations of 5, 7.5, and 10 w/v% can be easily extruded with a rather low compressive force (<20 N). In comparison, a higher colloid concentration (15w/v%) in the inks showed difficulty to extrude the inks out of the nozzle, with continuously increased compressive force up to 35 N. Moreover, images showing the shapes of the inks extruded out of the nozzles of the syringes showing different flow patterns during the injection (**Figure 4B**). Only inks containing 7.5-10 w/v% gelatin colloids still retained a noodle-like shape after injection, indicating the formation of stable flow during shear-thinning process. In contrast, both inks containing lower or higher concentrations of gelatin colloids formed drop-like shapes on injection. The former condition can be related to too dilute colloid concentration to allow fluent injection, while the latter can be related to too densely pack colloidal network that jammed in the syringe and led to poor injectability. We further observed the inks to expand when they were extruded out of the nozzle due to the release of shear stress, for which we can compare the change of the diameters of the injected strands as relative to the original nozzle diameter to evaluate the capacity of the inks to facilitate precise microfabrication. As a result, inks containing 10 w/v% colloids showed an expansion rate of ~120% when using a nozzle with a diameter of 200 μm, which was half to that of the 7.5 w/v% colloids (~240%) (**Figure 4C** and D). This can be explained by the tendency of the dilute colloidal components to stress-relax after being released from the confinement from the nozzle.

To demonstrate high-resolution printing using gelatin/PAAm DN hydrogel ink, we fabricated a connected circuit device using the hydrogel to form more than 49 patterned sub-units in a 50 mm × 50 mm area. A nozzle size of 400 μm was used, and resolution of the device preparation can reach up to 800 μm (**Figure 5A and B**). Such high-resolution construction of microarray architecture can allow high-degree sensitivity of the spatial location with the circuit area where pressure or deformation was applied. Moreover, we also printed an ear-shape construct using our DN hydrogel ink and observed that the sharp and rounded corners can be precisely fabricated, confirming the fidelity of the gelatin/PAAm DN hydrogel-based inks (**Figure 5C and D**).

3.3. 3D printed capacitance devices as wearable devices using the DN hydrogel

Typically, the hydrogel-based capacitor senses the pressure by the change in the relative area of conductive

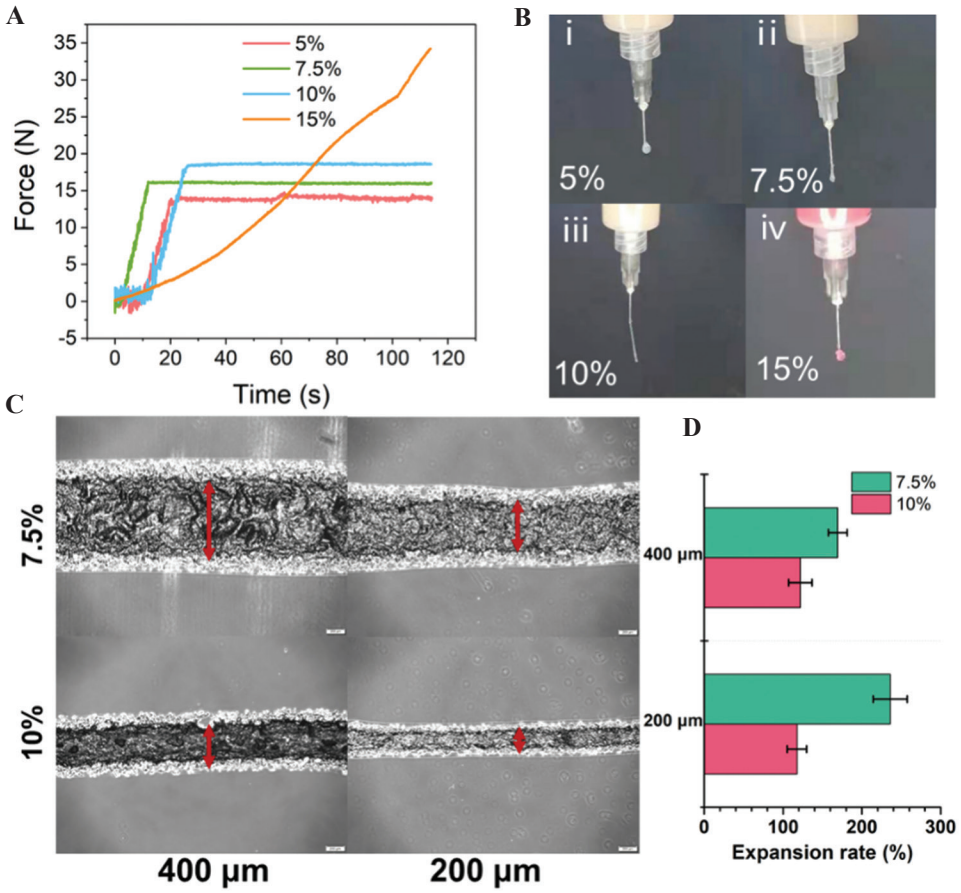


Figure 4. (A) Injectability of gelation colloidal gels (5, 7.5, 10, and 15 w/v % solid content) by measuring the compression force as a function of time during injection of the hydrogels using medical syringes. (B) Photographs showing the injectability of 5, 7.5, 10, and 15 w/v% gelatin colloidal gels during the injection test. (C) The light microscopic images showing the strands formed by gelatin colloidal gels (7.5, 10 w/v%) injected by syringes with different nozzle diameter (200 and 400μm). (D) Quantitative analysis of the expansion rate calculated by the ratio of the hydrogel strands after extrusion as relative to the original nozzle size.

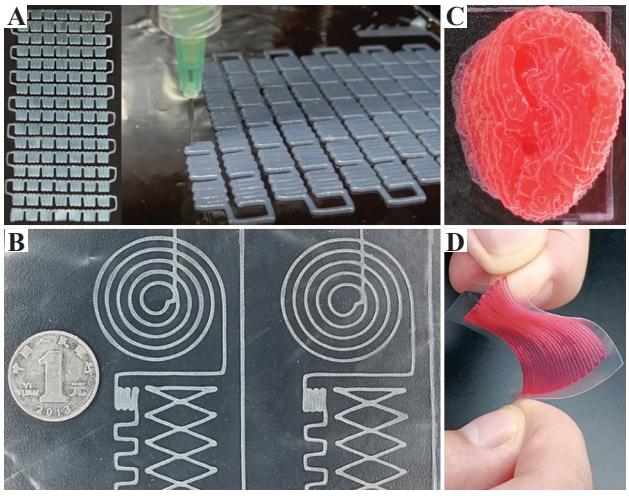


Figure 5. (A and B) Photographs showing the patterned electronic circuit printed by gelatin/polyacrylamide double-network (DN) hydrogel. (C) The ear-shaped construct was printed by DN hydrogel. (D) Image showing the high flexibility and stability of the printed patterned electronic circuit on a PLA film.

hydrogels. The relationship between deformation and capacitance in a parallel-plate capacitor can be explained by the equation $C = \varepsilon S/4\pi kd$, where C is the capacitance, ε is the dielectric constant, k is the electrostatic constant, S is the effective area of the conducting layer, and d is the thickness of the dielectric layer. Based on this theory, the expansion of the cross-section area of a hydrogel ionic skin can lead to increasing capacitance. Therefore, to prepare a capacitor as ionic skin, we printed a layer of electronic circuit array using DN hydrogels on the surface of a dielectric PLA film followed by printing another layer of electronic circuit array arranged orthogonally to the first printed layer (**Figure 6A**). Another two layers of PLA films were used as insulator layers to cover the conductive hydrogels and prevent the moisture from evaporation. To demonstrate the sensitivity of the ionic skins, we pressed the microarray using finger-touch or monitored complicated muscle movements. We used acrylic elastomer tape to adhesion the ionic skin to the finger. The two-layer ionic hydrogel's contact

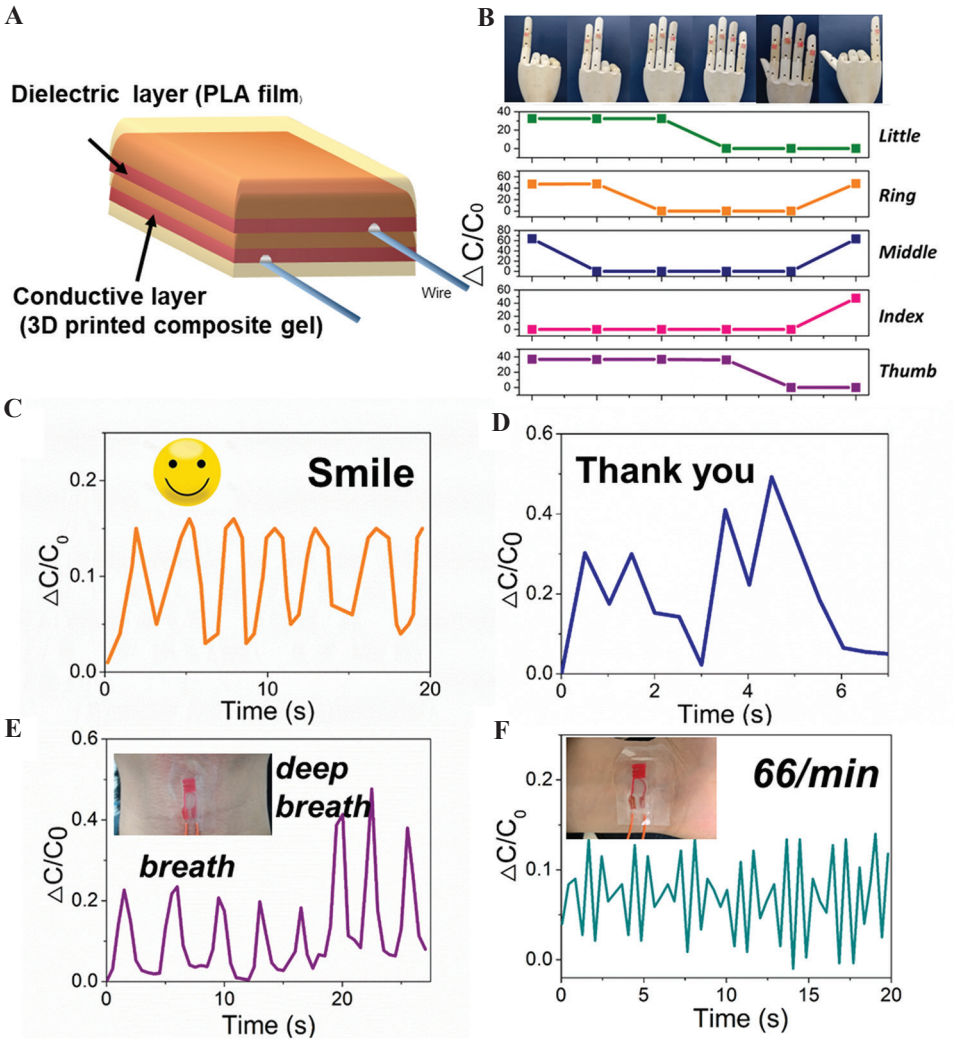


Figure 6. (A**)** Schematic design of the ionic skin developed in the current study. (B) The printed hydrogel sensors attached to a puppet hand and the real-time capacitance signals when different gestures were posed. Inserted images showing the corresponding gestures of the puppet hand. Real-time capacitance signals when the tester who wore the device (C) laughed, **(**D) said "thank you," and (E) took deep breaths. (F) Real-time capacitance signals of pulse when the sensor attaches to the tester's wrist.

area increased when the finger bending, leading to an increase in capacitance (**Figure 6B**). When the ionic skin was attached to the throat, it exhibited repeatable and characteristic signal peaks as the tester laughed or spoke (**Figure 6C and D**). The ionic skins also can distinguish between breathing and deep breathing by the degree of deformation on being worn on the chest of the tester (**Figure 6E**). Moreover, we also proved the application of this ionic skin as a sensor for wrist pulse. The capacitance changes showed periodic fluctuations according to the rhythm of pulse beating (**Figure 6F**). All these applications confirmed that these DN hydrogel-based ionic skins were promising candidates as highly sensitive pressure and strain sensors for wearable devices. To further evaluate the applications of the printed ionic skin in the flexible smart devices, a flexible touch screen panel (7×7 sensors, 5×5 mm^2 square per sensor unit) was fabricated to map the location of applied pressure with high resolution (**Figure 7A**). When one finger or two fingers touch the screen, the corresponding pressure peak mapping can be generated by measuring all the capacitance of the subunits (**Figure 7B**). Moreover, by placing cross- or box-shaped plastic devices on the touch screen panel's surface, we can locate the position and shapes of the devices placed.

For the development of a human-computer interaction monitor, a set of miniaturized functional chips were utilized, including printed ionic skin, data collector, control system, data transition, main control board, and output device (**Figure 8A**). The capacitance value of ionic skin will increase under external pressure, thus we can transfer the capacity signal to other signals,

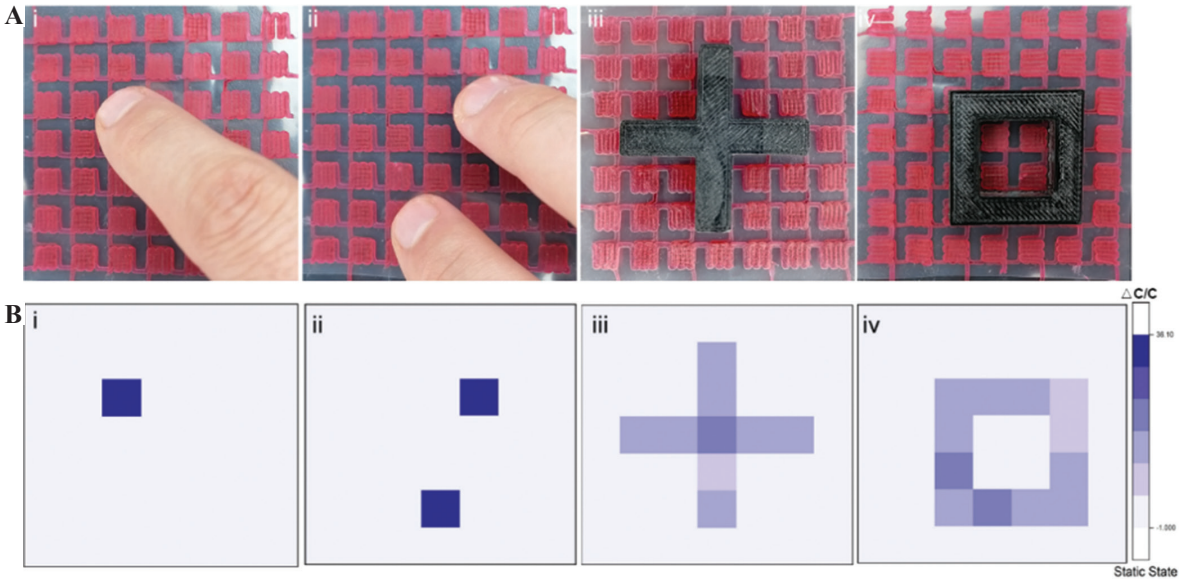


Figure 7. Sensitivity of the printed electronic circuit pattern. (A) Images showing the position of finger-touch (i, ii) and the placing of complex structures (iii, iv) on top of the printed ionic skin array, and (B) the corresponding capacitance signals based on the sensing of the different pressure mapping.

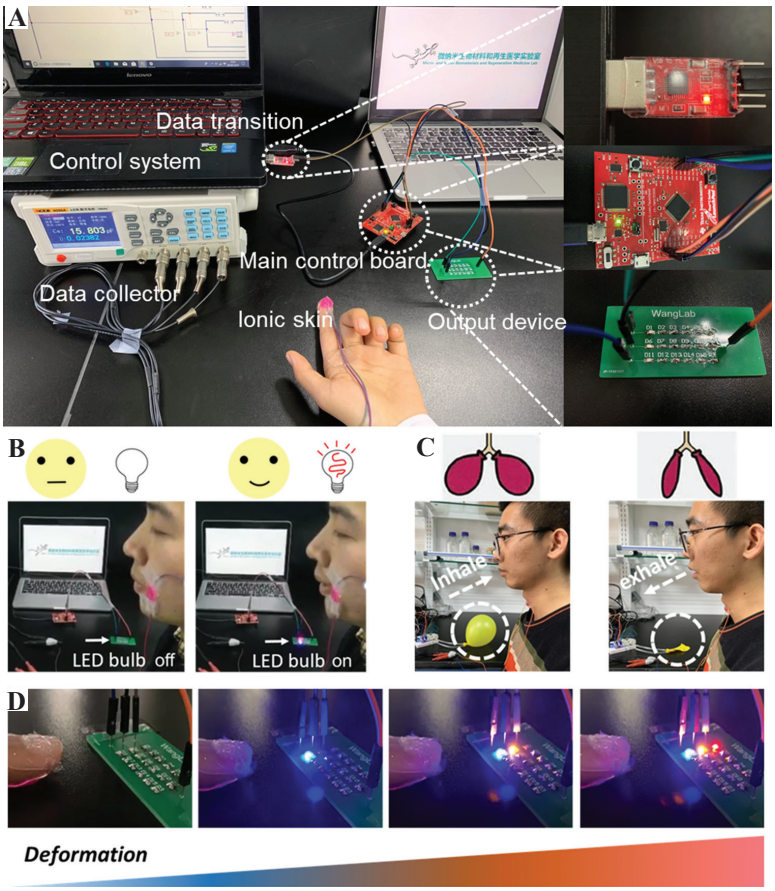


Figure 8. Human-computer interaction based on the ionic skin. (A) Human-computer interaction platform, including the printed ionic skin, data collector, control system, data transition, main control board, and output device. (B) The ionic skin device was attached to the tester's face, and controlled the LED bulb to turn on when the tester smiled **(**C) The ionic skin device was attached to the tester's throat, and controlled the inflation and deflation of the balloon when the tester was breathing. (D) The ionic skin device was attached to the finger to control different LED bulbs to turn on and off by different levels of pressure.

Table 1. Contents of DN hydrogel

Samples	AAM	GNPs	MBAA	2959	NaCl solution (2M)
5% colloidal gel	0 mg	150 mg	0 mg	0 mg	3 ml
7.5% colloidal gel	0 mg	225 mg	0 mg	0 mg	3 ml
10% colloidal gel	0 mg	300 mg	0 mg	0 mg	3 ml
15% colloidal gel	0 mg	450 mg	0 mg	0 mg	3 ml
5% PAAm hydrogel	150 mg	0 mg	1.5 mg	15 mg	3 ml
10% PAAm hydrogel	300 mg	0 mg	3 mg	15 mg	3 ml
15% PAAm hydrogel	450 mg	0 mg	4.5 mg	15 mg	3 ml
10% PAAm composite hydrogel	300 mg	300 mg	3 mg	15 mg	3 ml
15% PAAm composite hydrogel	450 mg	300 mg	4.5 mg	15 mg	3 ml

PAAm: Polyacrylamide; DN: Double-network

such as light and mechanical signals. As an example, the ionic skin was mounted on the tester's face, when the tester smiled, the capacity of ionic skin increased, and correspondingly controlled the LED bulb on and off (**Figure 8B**). Furthermore, by adhering the ionic skin to the tester's throat, we can control the inflation and deflation of a balloon by the inhalation and exhalation of the tester. For patients with breathing difficulties and breathing disorders, we suggested that this design can potentially test the inspiratory and expiratory volumes during breathing of the patients (**Figure 8C**). We further put the ionic skin on the fingertips of the tester and used the finger to compress the substrate with different levels of forces, through which the ionic skin can generate different degrees of deformation and capacitance values; this can be further converted to a readout signal. The increase of capacity signal can cause the LEDs to light up, and the number of lit LEDs corresponded to the degree of the applied pressure (**Figure 8D**).

4. Conclusion

In summary, we hereby presented the development of a novel class of DN hydrogels as printable skins for the fabrication of ions skin devices. The DN hydrogels were based on reversible gelatin colloidal network in combination with covalent PAAm network, which showed rapid, customized, and high-resolution fabrication of microscale constructs as ionic skins. The DN hydrogel displayed significantly enhanced elasticity and deformability which allow high adaptability of the resulting ionic skin devices to the body's movements. We further used the DN hydrogel to print microarray-based capacitors as ionic skins with high elasticity, stretchability, and sensitivity. The ionic skins exhibited high sensitivity to gentle finger-touch, body motion, and even wrist pulse-beating. We believe that this ionic skin can be potentially applied in the fields of human/machine interactions and wearable devices, and can promote the development of next-generation intelligent skin-mimicking sensors.

Acknowledgments

This work was supported by the National Key Research and Development Program of China (No.2018YFA0703000), National Natural Science Foundation of China (No. 31870957), and the Fundamental Research Funds for the Central Universities of China (No. DUT15RC(3)113).

Conflict of interest

The authors declare no conflict of interest.

Author contributions

K.C. and H.W. designed the study. K.C., Q.Y., and X.H. performed the experiments and analyzed the results. K.C., Q.Y., and H.W. wrote the manuscript. All authors commented on the manuscript.

References

1. Wang X, Dong L, Zhang H, *et al*., 2015, Recent Progress in Electronic Skin. *Adv Sci* (*Weinh*), 2:1500169. http://dx.doi.org/10.1002/advs.2015001691
2. Chortos A, Liu J, Bao Z, 2016, Pursuing Prosthetic Electronic Skin. *Nat Mater*, 15:937–50. http://dx.doi.org/10.1038/nmat46712
3. Jeon J, Lee HB, Bao Z, 2013, Flexible Wireless Temperature Sensors Based on Ni Microparticle-filled Binary Polymer Composites. *Adv Mater*, 25:850–5. http://dx.doi.org/10.1002/adma.2012040823
4. Chortos A, Bao Z, 2014, Skin-inspired Electronic Devices. *Mater Today*, 17:321–31. http://dx.doi.org/10.1016/j.mattod.2014.05.0064
5. Sun JY, Keplinger C, Whitesides GM, *et al*., 2014, Ionic Skin. *Adv Mater*, 26:7608–14. http://dx.doi.org/10.1002/adma.2014034415
6. Wen J, Tang J, Ning H, *et al*., 2021, Multifunctional Ionic Skin with Sensing, UV-Filtering, Water-Retaining, and Anti-

Freezing Capabilities. *Adv Funct Mater*, 31:2011176. http://dx.doi.org/10.1002/adfm.2020111766

7. Zhou Y, Wan C, Yang Y, *et al*., 2019, Highly Stretchable, Elastic, and Ionic Conductive Hydrogel for Artificial Soft Electronics. *Adv Funct Mater*, 29:1806220. http://dx.doi.org/10.1002/adfm.2018062207
8. Chen K, Lin Q, Wang L, *et al*., 2021, An All-in-One Tannic Acid-Containing Hydrogel Adhesive with High Toughness, Notch Insensitivity, Self-Healability, Tailorable Topography, and Strong, Instant, and On-Demand Underwater Adhesion. *ACS Appl Mater Interfaces*, 13:9748–61. http://dx.doi.org/10.1021/acsami.1c006378
9. Lei Z, Wu P, 2019, A Highly Transparent and Ultra-stretchable Conductor with Stable Conductivity during Large Deformation. *Nat Commun*, 10:3429. http://dx.doi.org/10.1038/s41467-019-11364-w9
10. Lei Z, Wang Q, Sun S, *et al*., 2017, A Bioinspired Mineral Hydrogel as a Self-Healable, Mechanically Adaptable Ionic Skin for Highly Sensitive Pressure Sensing. *Adv Mater*, 29:22. http://dx.doi.org/10.1002/adma.20170032110
11. Lei Z, Huang J, Wu P, 2019, Traditional Dough in the Era of Internet of Things: Edible, Renewable, and Reconfigurable Skin-Like Iontronics. *Adv Funct Mater*, 30:1908028. http://dx.doi.org/10.1002/adfm.20190801811
12. Sun JY, Zhao X, Illeperuma WR, *et al*., 2012, Highly Stretchable and tough Hydrogels. *Nature*, 489:133–6. http://dx.doi.org/10.1038/nature1140912
13. Gong JP, Katsuyama Y, Kurokawa T, *et al*., 2003, Double-Network Hydrogels with Extremely High Mechanical Strength. *Adv Mater*, 15:1155–8. http://dx.doi.org/10.1002/adma.20030490713
14. Gong JP, 2010, Why are Double Network Hydrogels so Tough? *Soft Matter*, 6:2583–90. http://dx.doi.org/10.1039/b924290b1.
15. Chen K, Feng Y, Zhang Y, *et al*., 2019, Entanglement-Driven Adhesion, Self-Healing, and High Stretchability of Double-Network PEG-Based Hydrogels. *ACS Appl Mater Interfaces*, 11:36458–68. http://dx.doi.org/10.1021/acsami.9b1434815
16. Mu Z, Chen K, Yuan S, *et al*., 2020, Gelatin Nanoparticle-Injectable Platelet-Rich Fibrin Double Network Hydrogels with Local Adaptability and Bioactivity for Enhanced Osteogenesis. *Adv Healthc Mater*, 9:e1901469. http://dx.doi.org/10.1002/adhm.20190146916
17. Wang H, Hansen MB, Lowik DW, *et al*., 2011, Oppositely Charged Gelatin Nanospheres as Building Blocks for Injectable and Biodegradable Gels. *Adv Mater*, 23:H119–H124. http://dx.doi.org/10.1002/adma.20100390817
18. Wang H, Boerman OC, Sariibrahimoglu K, *et al*., 2012, Comparison of Micro- vs. Nanostructured Colloidal Gelatin Gels for Sustained Delivery of Osteogenic Proteins: Bone Morphogenetic Protein-2 and Alkaline Phosphatase. *Biomaterials*, 33:8695–703. http://dx.doi.org/10.1016/j.biomaterials.2012.08.02418.
19. Du M, Liu P, Wong JE, *et al*., 2020, Colloidal Forces, Microstructure and Thixotropy of Sodium Montmorillonite (SWy-2) Gels: Roles of Electrostatic and van der Waals Forces. *Appl Clay Sci*, 195:105710. http://dx.doi.org/10.1016/j.clay.2020.10571019
20. Komarov KA, Yurchenko SO, 2020, Colloids in rotating electric and magnetic fields: Designing tunable interactions with spatial field hodographs. *Soft Matter*, 16:8155–68. http://dx.doi.org/10.1039/d0sm01046d20
21. Ruter A, Kuczera S, Gentile L, *et al*., 2020, Arrested Dynamics in a Model Peptide Hydrogel System. *Soft Matter*, 16:2642–51. http://dx.doi.org/10.1039/c9sm02244a21
22. Diba M, Wang H, Kodger TE, *et al*., 2017, Highly Elastic and Self-Healing Composite Colloidal Gels. *Adv Mater*, 29:11. http://dx.doi.org/10.1002/adma.2016046721
23. Huang H, Han L, Li J, *et al*., 2020, Super-stretchable, Elastic and Recoverable Ionic Conductive Hydrogel for Wireless Wearable, Stretchable Sensor. *J Mater Chem A*, 8:10291–300. http://dx.doi.org/10.1039/d0ta02902e22
24. Pan Z, Yang J, Li L, *et al*., 2020, All-in-one Stretchable Coaxial-fiber Strain Sensor Integrated with High-performing Supercapacitor. *Energy Storage Mater*, 25:124–30. http://dx.doi.org/10.1016/j.ensm.2019.10.02323
25. Haraguchi K, 2007, Nanocomposite Hydrogels. *Curr Opin Solid State Mater Sci*, 11:47–54. http://dx.doi.org/10.1016/j.cossms.2008.05.0013

RESEARCH ARTICLE

A Systematic Thermal Analysis for Accurately Predicting the Extrusion Printability of Alginate–Gelatin-Based Hydrogel Bioinks

Qi Li[1,2†], Bin Zhang[1,2†], Qian Xue[1,2], Chunxiao Zhao[1,2], Yichen Luo[1,2], Hongzhao Zhou[1,2*], Liang Ma[1,2*], Huayong Yang[1,2], Dapeng Bai[1,2]

[1]State Key Laboratory of Fluid Power and Mechatronic Systems, Zhejiang University, Hangzhou, 310058, People's Republic of China
[2]School of Mechanical Engineering, Zhejiang University, Hangzhou, 310058, People's Republic of China
[†]*These authors contributed equally to this work*

Abstract: Three-dimensional (3D) bioprinting has significant potential for addressing the global problem of organ shortages. Extrusion printing is a versatile 3D bioprinting technique, but its low accuracy currently limits the solution. This lack of precision is attributed largely to the complex thermal and dynamic properties of bioinks and makes it difficult to provide accurate estimations of the printed results. It is necessary to understand the relationship between printing temperature and materials' printability to address this issue. This paper proposes a quantitative thermal model incorporating a system's printing temperatures (syringe, ambient, and bioink) to facilitate accurate estimations of the printing outcomes. A physical model was established to reveal the relationship between temperature, pressure, and velocity in guiding the printing of sodium alginate–gelatin composite hydrogel (a popular bioink) to optimize its extrusion-based printability. The model considered the phenomenon of bioink die swells after extrusion. A series of extrusion experiments confirmed that the proposed model offers enhanced printing outcome estimations compared with conventional models. Two types of nozzles (32- and 23-gauge) were used to print several sets of lines with a linewidth step of 50 μm by regulating the extrudate's temperature, pressure, and velocity separately. The study confirmed the potential for establishing a reasonable, accurate open-loop linewidth control based on the proposed optimization method to expand the application of extrusion-based bioprinting further.

Keywords: 3D bioprinting; Pneumatic extrusion; Thermal effects; Temperature control; Printability

*Correspondence to: Hongzhao Zhou, State Key Laboratory of Fluid Power and Mechatronic Systems, Zhejiang University, Hangzhou, 310058, People's Republic of China; hz_zhou@zju.edu.cn; Liang Ma, State Key Laboratory of Fluid Power and Mechatronic Systems, Zhejiang University, Hangzhou, 310058, People's Republic of China; liangma@zju.edu.cn

Received: May 13, 2021; **Accepted:** May 26, 2021; **Published Online:** June 22, 2021

(This article belongs to the *Special Section: Bioprinting of 3D Functional Tissue Constructs*)

Citation: Li Q, Zhang B, Xue Q, *et al.,* 2021, A Systematic Thermal Analysis for Accurately Predicting the Extrusion Printability of Alginate–Gelatin-Based Hydrogel Bioinks. *Int J Bioprint*, 7(3):394. http://doi.org/10.18063/ijb.v7i3.394

1. Introduction

The three-dimensional (3D) bioprinting technique has the potential for creating functional tissues and organs *in vitro*, which could address the global shortage of human tissue/organ donation in the context of rising transplantation demands[1,2]. Over recent years, 3D bioprinting has become the focus of increasing attention due to its high efficiency, accuracy[3], and ability to fabricate scaffolds that provide 3D microenvironments, thereby avoiding the drawbacks associated with traditional two-dimensional monolayer cell culture[4]. In extrusion-based printing[5-10], syringes and pistons are used to extrude bioinks with viscosities of 30 – 10^7 mPa·s from nozzles to form complex 3D architectures that offer various benefits in cell culture[11]. The technique allows the low-cost and high-

© 2021 Li, *et al*. This is an Open Access article distributed under the terms of the Creative Commons Attribution License (https://creativecommons.org/licenses/by/4.0/), permitting distribution and reproduction in any medium, provided the original work is cited.

precision fabrication of cell-laden scaffolds with high cell viability[12]. Advancements based on this technology have been demonstrated, including mandible bones[7], liver tissue[13], cardiac patches[14], brain microenvironment[15], and multi-layered skin[16].

The differing properties of bioinks are a primary consideration in 3D bioprinting for fabricating different tissues/organs[17,18]. Extrusion-based bioprinting requires the use of biocompatible materials that must be fluid in the nozzle and solid after printing[19]. Increasingly, temperature-sensitive materials, such as gelatin, gelatin methacryloyl, collagen, and agarose, which are tunable in a sol–gel state through the alternation of temperatures, are becoming the focus of research attention[1,20]. Among these materials, a sodium alginate–gelatin composite hydrogel can be crosslinked just with divalent ions[21]. It is widely used because of its mild gelation, good printability, and high biocompatibility[3,22-28].

Bioink printability is critical to the *in vitro* reproduction of the complex micro-architectures of native tissues[29,30]. It is regarded as the ability to form complex 3D structures with high accuracy, integrity, and cell viability[27]. The intrinsic properties and printing parameters of bioinks affect their printability. Researchers have created several physical models to enhance this property that considers such variables, including pressure, the inner diameter (ID) of the nozzle, and the nozzle's moving velocity. However, as all these models ignore temperature, the experimental results in the original research could not be fitted accurately[31-33].

Many studies have found that temperature is a critical variable that affects printability[3,27,34]. When alginate–gelatin composite hydrogel is kept at 37°C, even low pressure and a fast printing velocity cause the width of the printed lines to increase, resulting in variations in width from those lines printed near the sol-gel transition temperature[3]. Ouyang *et al*. demonstrated that temperature affects the printing region in which the printability of a bioink is excellent[27]. Chen *et al.* found that the thermal parameters of a bioink obtained from a rheometer differed from those measured experimentally through a printing test. This disparity was attributed to the temperature difference between the two systems[34].

In addition, both the holding time and holding temperature have been proven to affect the viability of cells[25]. Although significant progress has been made in studying the printability of bioinks, a quantitative and comprehensive law is required to guide the printing process. Consequently, the printing capability of the 3D bioprinting technique remains compromised[22,23]. Furthermore, a lack of research regarding the thermal effects makes it challenging to construct large-scale tissue scaffolds using temperature-sensitive materials[7,9,34].

This study presents an optimization of the printability of extrusion-based bioprinting with a consideration of the thermal effects. A quantitative thermal model was established that considered the printing system's temperatures (nozzle, ambient, and bioink) to demonstrate the extrudate's thermal effects. The model can be applied for the precise regulation of extrudate temperature. A mathematical model revealing the relationship between the extrudate's temperature, pressure, velocity, and linewidth was established to optimize the printing process. The experimental results agreed reasonably well with the physical model, which outperformed conventional models. Nozzles with gauges (G) of 32 and 23 were used, and the temperature, pressure, and velocity of the extrudates were varied, respectively. Several sets of lines were fabricated using the established physical model with a linewidth step of 50 μm. The precise linewidth step control demonstrated by the proposed optimization model suggests it could guide soft biomaterials' fabrication with precise shape control and high cell viability.

2. Materials and methods

2.1. Bioprinting system design

As shown in **Figure 1A**, a customized bioprinter was produced comprising a temperature control module, a nozzle motion control module, and a bioink dispensing system.

Two nozzles with precise temperature control were installed on the x–y–z stage. The low-temperature (LT) module was tunable from 0°C to 70°C with individual temperature control for the nozzle tip. The high-temperature (HT) module was tunable from ambient temperature (AT) to 250°C. The temperature tuning range of the printing platform ranged between −5°C and 45°C. Since the AT has a significant impact on the printing process, this parameter was controlled using a temperature-adjustable (between 10°C and 40°C) chamber. The modules were designed to allow the precise temperature control of the bioink's flow path to produce a bioink with predictable thermal properties, a suitable viscoelastic modulus, and high cell activity[24,25,35]. The output pressure regulated by the pneumatic circuit was tunable from 1 kPa to 1 MPa with a resolution of 1 kPa.

Bioink properties must be controlled precisely to achieve excellent printability. A low-viscosity material will deform and collapse after printing, while a high-viscosity material will become clogged and excessively swollen. This study tested the rheological properties of the prepared bioink (**Figure 1B**). The obtained thermal parameters were entered into the established physical model. To achieve controllable deposition and to predict the printed linewidth, the model considered the pipe flow, the die swell, and the deposition stages.

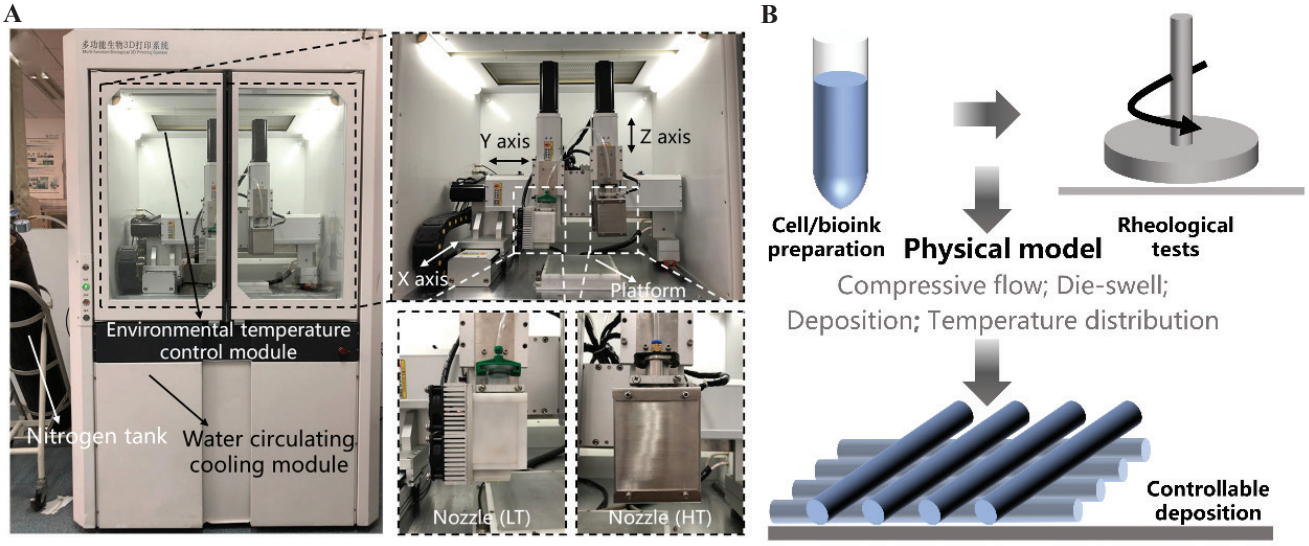


Figure 1. Schematic showing of the bioprinting system. (A) Diagram of the 3D bioprinter is composed of a temperature control module, a motion control module, and a dispensing module. (B) Schematic of the printing process. The rheological properties of the bioink are input into the mathematical model to realize the controllable deposition.

2.2. Sodium alginate–gelatin composite hydrogel preparation

The composite hydrogel comprised sodium alginate (Sigma-Aldrich, Shanghai, China), gelatin (from porcine skin, Sigma-Aldrich, Shanghai, China), and phosphate buffer saline (PBS) (GENOM, Hangzhou, China). The sodium alginate powder (2% w/v) and gelatin powder (10% w/v) were combined thoroughly in PBS by stirring at 60°C for 40 min at 400 r/min. The mixture was maintained at a temperature of 37°C to remove any bubbles before being transferred into a 30-cc syringe.

2.3. Rheological measurements

A rheological properties test was conducted using a rotational rheometer with a parallel plate measuring system (MCR302, Anton Paar, Austria). A 1 mm thick specimen was loaded onto the test plate and heated to 40°C before measurement. Then, it was cooled from 40°C to 10°C at increments of −2°C/min. The strain was set at 1% at a frequency of 1 Hz for the dynamic moduli measurements. As the power-law equation's coefficients remain almost constant in the shear rate range until the material is broken, the shear rate was set to 20 and 35 s^{-1} in the rotation measurement, respectively[31].

2.4. Composite hydrogel thermal analysis

The composite hydrogel's specific heat and isotropic thermal conductivities were measured using a thermal conductivity analyzer (TPS 2500S, Hot Disk, Sweden). The stainless steel and the polypropylene manufacturer kindly provided the properties of the materials, and the experimental temperature was measured using a k-type thermocouple (GM1312, Biaozhi, China). As the film coefficient varies according to environmental conditions, this study fitted the coefficient to 50 W/m^2°C, which was experimentally derived.

The temperature gradient of the model was simulated using Ansys 15.0 (ANSYS, USA) software, and **Table 1** summarizes the critical parameters used in the simulation. Two models were built using the SolidWorks (Dassault System, France) program using identical cylinder lengths of 13 mm and cylindrical nozzle IDs of 0.34 and 0.11 mm. The length of the nozzle exposed to the air was 5 mm, and a meshing size of 1×10^{-4} mm was used. The thermal effect analysis considered the effect of both heat conduction and convection, and thermal radiation was disregarded due to its negligible influence[36].

The study conducted four sets of simulations, as follows: (a) The transient temperature of the central material during heating/cooling, (b) the influence of syringe temperature, (c) the AT on the steady extrudate temperature, and (d) the transient temperature change of the extrudate during heating/cooling.

The simulation parameters were established as follows:

1. The temperature of the outer surface of the syringe was set to 19°C (lower than the AT of 20°C) and 31°C (higher than the AT), respectively. The initial temperature of the material was set to 21°C. Then, the central material's transient temperature change was simulated, and experiments with identical parameters were performed to verify the simulation results.
2. The outer surface temperature of the syringe was set to 19°C, 21°C, 23°C, 25°C, 27°C, 29°C, and

31°C, respectively. A steady extrudate temperature was simulated. The results were verified, and the film coefficient was fitted by experiments conducted under identical conditions.

3. The outer surface temperature of the syringe was set to a constant temperature of 27°C, while the AT was set to 20°C, 25°C, 30°C, 35°C, and 40°C, respectively. Then, a steady extrudate temperature was simulated.
4. The outer surface temperature of the syringe was set to a constant temperature of 27°C, which was identical to the initial temperature of the material. The AT was set to 20°C (lower than the nozzle temperature), 27°C (equal to the nozzle temperature), and 32°C (higher than the nozzle temperature), respectively. Then, the transient temperature change of the extrudate at the tip was simulated.

2.5. Printing parameters

This study's main focus was the linewidth as a printed outcome, which was measured using fluorescence microscopy (DM IL LED, Leica, Germany) and industrial microscopy (JC-2001G, Jingtuo, China). Two different types of nozzles were used; the 23-G nozzle was cylindrical with a 13-mm cylinder length and an ID of 0.34 mm, and the 32-G nozzle was cylindrical with a 13-mm cylinder length and an ID of 0.11 mm. The distance between the tip of the nozzle and the platform was set as the nozzle diameter's value to exclude its effect and produce continuous fibers[3].

1. The study conducted two sets of orthogonal experiments to determine the most suitable zone for well-defined printing lines. In these tests, the extrudate temperature, pressure, and velocity were varied separately.
2. To validate the physical model and to determine the coefficients, additional fiber extrusion experiments were conducted to investigate the effects of temperature, extrusion pressure, and nozzle velocity on the linewidth. Identical conditions were used except for the primary variable under investigation.
3. The observed results were used to determine the parameters for guiding the printing with a fixed linewidth step. The values at which the extrudate temperature, pressure, and velocity were set were calculated from the established physical model to acquire lines with a 50-μm linewidth step, respectively.

2.6. Cell culture and bioink preparation

According to the authors' previous research, sodium alginate–gelatin composite hydrogels are suitable for the *in vitro* fabrication of corneal substitutes[37-39]; this finding has received increasing attention over recent years. To test the effect of the printing process on cell viability, the cell-laden scaffold printing experiment used human keratocyte (HK) (ScienCell, CA, USA) cells. Cells were cultured in T25 flasks with Dulbecco's modified Eagle's medium/F12 (Life Technologies, USA) supplemented with 10% fetal bovine serum (Fisher Scientific, USA) and 1% penicillin-streptomycin (Life Technologies, USA) under a 5% CO_2 concentration. The culture media were replaced daily. The HKs were detached using Trypsin-EDTA (0.25%, Life Technologies, USA) and were centrifuged at 1,000 r/min for collection at a cell density of ca. 1.5×10^7 cells/mL.

The cells were suspended in growth media (ca. 1.5×10^7 cells/mL), centrifuged, and gently mixed into the sodium alginate–gelatin composite hydrogel at 37°C before being drawn into a sterilized commercial 30-cc syringe. The typical final concentrations of each component were as follows: 2% sodium alginate, 10% gelatin, and ca. 3×10^6 cells/mL.

2.7. Cell-laden scaffolds printing

For higher cell viability, the 23-G nozzle was used in the printing of cell-laden scaffolds[23]. The pressure and velocity were set to 130 kPa and 7 mm/s, respectively. To investigate the effect of temperature on cell viability, the extrudate temperature was regulated to 24°C, 27°C, and 30°C, respectively.

2.8. Cell viability assay

A Live/Dead cell viability/cytotoxicity assay kit (Thermo, USA) was used to determine cells' viability before and after printing. The assay solution was prepared by mixing 1-μL/mL Cal-AM and 2-μL/mL propidium iodide in PBS. Then, the mixture was added to the samples and was incubated (Thermo, USA) at 37°C for 20 min. After three 3-min washes with PBS, the samples were evaluated using fluorescence microscopy (Leica, Germany). For each sample, three fluorescent images were obtained from different areas. Live cells were shown in green, while dead cells were shown in red. The number of live and dead cells was counted using ImageJ (NIH, USA) software under the same thresholds. Cell viability was calculated as the number of living cells divided by the total number of cells.

2.9. Statistical analysis

The linewidth data were expressed as mean ± standard deviation. The inter-group variations were analyzed via a one-way ANOVA test in conjunction with Tukey's test using SPSS (IBM, USA) software.

3. Results and discussion

3.1. Rheological measurements

The rheological properties of the sodium alginate–gelatin composite hydrogel (**Figure 2**) were measured in a temperature sweep test, in which the temperature

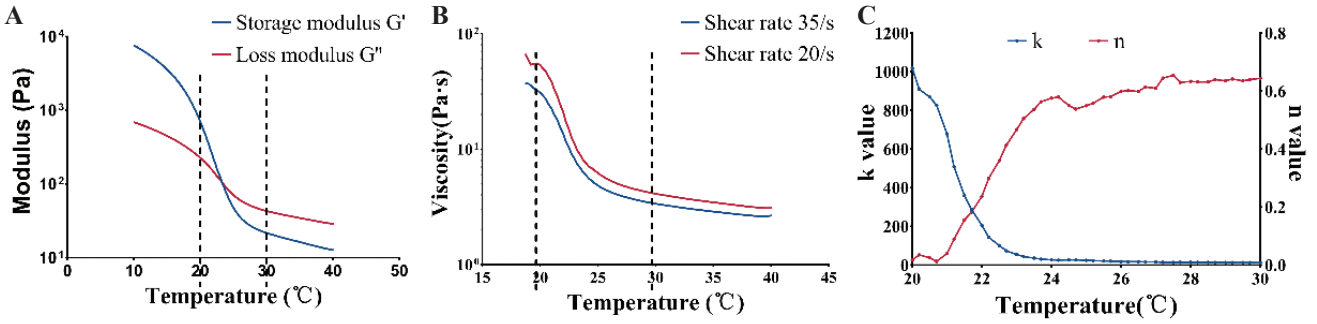


Figure 2. Rheological properties of the hydrogel. (A) Dynamic properties of 2% sodium alginate and 10% gelatin composite hydrogel. (B) Viscosity versus temperature characteristic of the hydrogel. (C) *k*, *n* value of the hydrogel.

was reduced from 40°C to 10°C. As the temperature decreased, the viscosity of the hydrogel increased, and the material's state was transformed from a liquid to a gel. A sol–gel transition was observed, during which the loss modulus of the hydrogel approached the storage modulus (**Figure 2A**)[24]. At temperatures between 20°C and 30°C, there was a noticeable change in viscosity (**Figure 2B**).

Achieving excellent printability with a bioink is possible only within a specific range of viscosity. The temperature range for a hydrogel with good printability lies in the phase transition zone, in which the viscosity of the bioink is sensitive to changes in temperature[24,27]. Usually, composite hydrogels are regarded as non-Newtonian fluids with viscoelastic properties and are often modeled using the power-law equation. The relationship between viscosity, shear stress, and shear rate can be described as follows:

$$\mu = k\gamma^{n-1} \tag{1}$$

$$\tau = k\ \dot{\gamma}^{n} \tag{2}$$

where μ is the apparent viscosity, τ is the shear stress, k is the flow consistency index, n is the flow behavior index, and $\dot{\gamma}$ is the shear rate. The parameters k and n are temperature sensitive and are determined from the experimental data shown in **Figure 2B** using the interpolation method. The results after interpolation are presented in **Figure 2C**. There is a sudden change in the values of k and n between 20°C and 30°C, which is in the sol–gel transition region. Following the transition, the values of k and n exhibit a smooth change. The curve's fluctuation could be attributed to the unsteady sol–gel transition state and experimental error.

3.2. Thermal analysis

As illustrated in **Figure 2**, the material's viscosity is affected significantly by the material's temperature, which is a factor that is closely related to the printing process. **Figure 3A** presents a schematic of a flowing hydrogel within a nozzle exposed to air, in which T_C is the controlled nozzle temperature, T_A is the AT, and T_E is the extrudate temperature. The temperature at the nozzle inlet and the AT are assumed to be both constant and controllable. For a specific extrusion rate, the temperature of the bioink inside the nozzle can be considered an isothermal system. Assuming there is no temperature gradient in the direction of the nozzle radius, the temperature differential (ΔT) along the nozzle length (ΔL) can be described, as follows:

$$\phi_{in} = \phi_{out} \tag{3}$$

$$\phi_{in} = \left(T_C - (T_C - \Delta T)\right)\lambda_s \frac{\pi(D_o^2 - D_i^2)}{4\Delta L} + \left(T_C - (T_C - \Delta T)\right)\lambda_h \frac{\pi D_i^2}{4\Delta L} \tag{4}$$

$$\phi_{out} = h\left(\frac{T_C + T_C - \Delta T}{2} - T_A\right)\pi D_o \Delta L, \text{and} \tag{5}$$

$$\Delta T = \frac{4hD_o\Delta L^2}{2hD_o\Delta L^2 + \lambda_s\left(D_o^2 - D_i^2\right) + \lambda_h D_i^2}\left(T_C - T_A\right) \tag{6}$$

where ϕ is the heat flux, D_i is the ID of the nozzle, D_o is the outer diameter of the nozzle, λ_s is the heat conductivity of the stainless steel, λ_h is the heat conductivity of the composite hydrogel, ΔL is the length differential of the nozzle exposed to the air, and h is the film coefficient. After integrating Eq. (6) along the length of the nozzle, the temperature difference between the controlled nozzle temperature (T_C) and the extrudate temperature (T_E) can be calculated. The steady temperature of the extruded material can be calculated using Eq. (6) irrespective of whether the AT is higher or lower than the syringe temperature. When the situation changes, only the

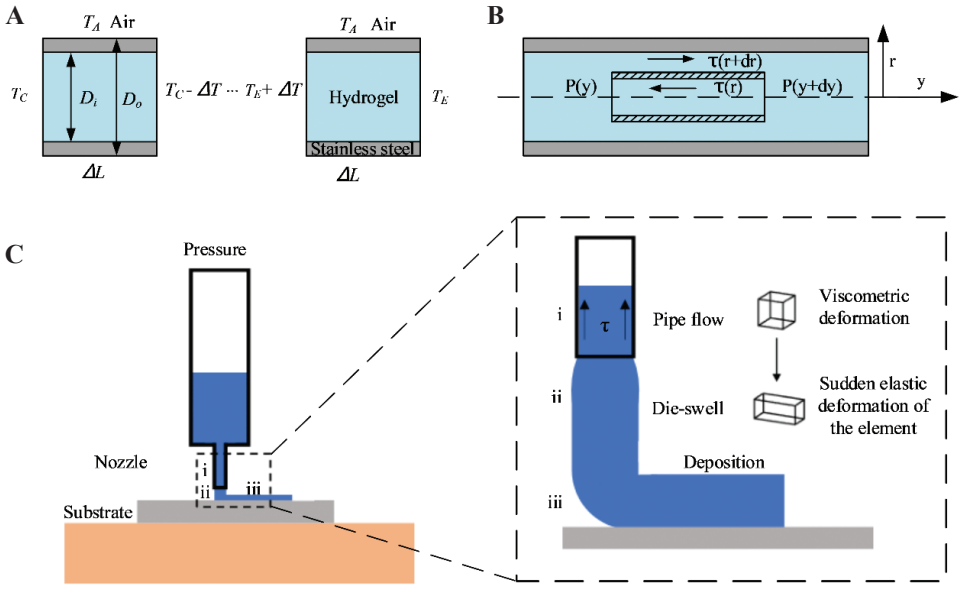


Figure 3. Schematic of nozzle exposed in the air with flowing hydrogel. (A) The temperature distribution. (B) The stress on the microelement. (C) Printing process.

direction of the heat flow will change. The steady-state means that the extrudate temperature, T_E, will always be between the temperatures of the syringe and the AT, that is, when the AT is lower than the syringe temperature, then $T_c \geq T_E \geq T_A$, while when the AT is higher than the syringe temperature, then $T_A \geq T_N \geq T_E$.

Four sets of analyses were conducted using ANSYS software to explore the temperature change during printing using the thermal parameters given in **Table 1**. **Figure 4** presents the simulation results.

The temperature of the composite hydrogel in the nozzle center increased from 21°C to 31°C and decreased from 21°C to 19°C gradually (**Figure 4B**). After more than 40 min of heating/cooling, the temperature reached a constant value; this phenomenon could be used as a criterion to determine whether a bioink is well heated or cooled. Because of the slight heat loss caused by the exposed nozzle, the hydrogel's steady stage in the syringe was not affected significantly by the nozzle's scaling. The results of one nozzle were plotted, and several sets of experiments verified the simulation results. There was a good agreement between the hydrogel's measured temperature in the center of the syringe and the heating and cooling processes' predicted temperature. This confirms that the thermal simulation is reasonably accurate.

The controlled syringe temperature was increased from 19°C to 31°C at a constant AT of 20°C (**Figure 4C**), and the temperature of the extrudate at the tip of the nozzle was measured. The film coefficient was determined (5 – 200 W/m^2°C in the native flow) using the experimental temperatures of the extrudate. After fitting, the film coefficient was set to 50 W/m^2°C. There was a good fit between the experimental and predicted temperatures, and it was found that the extrudate temperature rose as the controlled nozzle temperature increased. Because the large ID nozzle contained more materials that carried the syringe's thermal energy, the temperature was less susceptible to the AT; consequently, the 23-G nozzle produced a steeper slope.

The model was used to explore the influence of the AT on the steady temperature of the hydrogel extrudate (**Figure 4D**), and the simulation results confirmed that the AT had a significant effect on the extrudate's temperature. The influence of the AT on the extrudate's temperature was opposite to that of the syringe temperature. It was confirmed that the smaller (32-G) nozzle containing fewer materials was more vulnerable to the AT.

During the printing process, the flow of materials inside the nozzle was affected by the AT. To explore the transient change of the material's temperature, the AT was set to 19°C, 27°C, and 32°C, respectively (**Figure 4E**). The simulation revealed that the extrudate's temperature responses were relatively fast for both nozzles, reaching a steady-state within 10 s. A smaller ID corresponded to faster response in the simulation; furthermore, it demonstrated that a smaller nozzle was more vulnerable to the AT.

The experimental results are briefly summarized as follows: (a) The central material's temperature inside the syringe changed slowly and reached a constant temperature after more than 40 min of heating/cooling, (b) Nozzles with larger IDs were less susceptible to the AT and more vulnerable to the controlled syringe

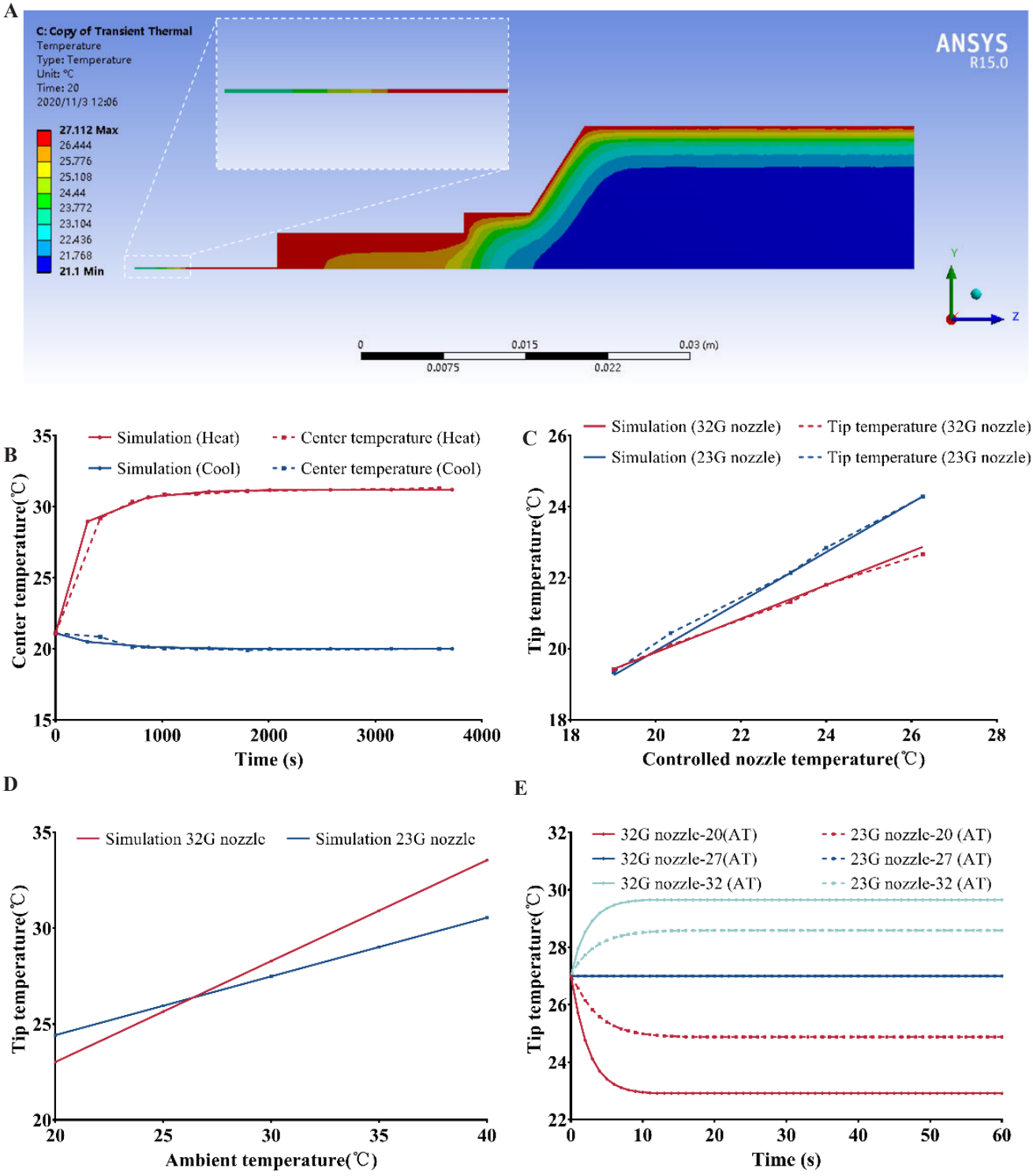


Figure 4. Results of the simulation. (A) The temperature distribution at 20 s in analysis for 32-G nozzle. (B) Transient change of the central material (n=9, P<0.0001, error=S.D.) (C) Steady change of the extrudate temperature versus the syringe temperature (n=9, P<0.0001, error=S.D.) (D) Steady change of the extrudate temperature versus the ambient temperature (E) Transient change of the extrudate temperature. established based on the proposed physical model.

temperature, and (c) there was a rapid change in extrudate temperature of under 10 s, which must be considered in the printing process.

3.3. Influence of multiple factors on printability

Often, a primary indicator of printability is the linewidth[31,40], which affects the porosity[41], cell viability,

and uniformity of the printed outcome[40,42,43]. This section explores the influence of temperature, pressure, and velocity on printability (as represented by linewidth). Both the power-law model and the die-swell phenomenon were considered before establishing a physical model for the a *priori* prediction of the linewidth.

Figure 3C shows there are three stages in the printing process. In the first, the bioink flows inside the nozzle with a viscoelastic fluid behavior. In the second, the bioink is extruded from the nozzle and swells due to shear stress's disappearance[44-48]. Here, the die-swell phenomenon causes a faster volume flow rate than in the first stage. In stage three, the extruded bioink accumulates on the receiving plate. The difference between the moving velocity of the nozzle and the extrusion velocity contributes to a secondary swell[31,43,49].

Figure 3B presents the first stage, in which the nozzle radius is *R,* and the length is *L*. The pressure drop across the nozzle is ΔP and the volume flow rate through the nozzle is *Q.* To simplify the calculation, the following assumptions are made based on past literature[31,33,43,47]: (a) The flow is isothermal and incompressible, (b) the length of the nozzle is adequate, (c) inertial effects in the flow are ignored, and (d) gravity, surface tension, and other body forces are also ignored.

The force equilibrium can be expressed as follows:

$$\frac{dP}{dy} = \frac{1}{r}\frac{d(r\tau)}{dr}, \text{and} \tag{7}$$

$$\iint r dr dP = \iint d(r\tau) dy \tag{8}$$

where P is the pressure, r is the radius, and τ is the shear stress. The left-hand side of Eq. (7) represents the pressure difference along the y axis, and the right-hand side shows the distribution of the shear stress along the r axis. After the integration concerning r and scale dP/dy with $\Delta P/L$, Eq. (9) is derived:

$$\tau = \frac{r}{R}\tau_{w,} \tag{9}$$

where τ_w is the wall shear stress, which is defined as $\tau_w = R\Delta P/2L$[49]. The shear rate, γ, can be defined as $\gamma = du/dr$, where $u(r)$ is the velocity. After substituting Eq. (9) into Eq. (2), the power-law formula can be rewritten as follows:

$$k\left(\frac{du}{dr}\right)^{n} = \frac{r}{R}\tau_w \tag{10}$$

After integrating Eq. (10) with respect to r, the function concerning the velocity and volume flow rate can be described in Eqs. (11) and (12):

$$u(r) = \left(\frac{\Delta P}{2kL}\right)^{\frac{1}{n}} \frac{R^{\frac{1}{n}+1} - r^{\frac{1}{n}+1}}{\frac{1}{n}+1} \text{ and} \tag{11}$$

$$Q = \int_0^R u(r) 2\pi r dr = \frac{\pi R^3}{\frac{1}{n}+3}\left(\frac{\Delta P R}{2kL}\right)^{\frac{1}{n}} \tag{12}$$

In the previous literature, Eq. (12) was regarded as the usual model for predicting the printability of bioinks[31-33]. During the second stage of the printing process, the extrudate's diameter emerging from the nozzle swells due to the release of the shear stress. The relationship between the diameter before and after extrusion can be expressed as Eq. (13)[44,46,49,50], below:

$$\frac{D_E}{d} = (1 + c\tau_w^2)^{\frac{1}{6}} \tag{13}$$

where D_E is the extrudate diameter, d is the ID, and c is the fitted shear coefficient. The radius of the extrudate, R_E, can be expressed as:

$$R_E = \left(1 + c\tau_w^2\right)^{\frac{1}{6}} R \tag{14}$$

After substituting Eq. (14) into Eq. (12), the volume flow rate of the bioink during the third stage can be written as:

$$Q_E = \frac{\pi n}{1+3n}\left(\frac{\Delta P}{2kL}\right)^{\frac{1}{n}}\left[\left(1 + c\left(\frac{R\Delta P}{2L}\right)^2\right)^{\frac{1}{6}} R\right]^{3+\frac{1}{n}} \tag{15}$$

During the third stage, the bioink is deposited on the substrate. Considering the moving velocity of the nozzle, v, and assuming that the cross section of the printed line is a part of a circle, which is determined by the contact angle, the linewidth can be expressed as Eq. (16):

$$D_p = \sqrt{\frac{1}{v}\frac{4\pi n}{1+3n}\left(\frac{\Delta P}{2kL}\right)^{\frac{1}{n}}\left[\left(1 + c\left(\frac{R\Delta P}{2L}\right)^2\right)^{\frac{1}{6}} R\right]^{3+\frac{1}{n}}}\, b \tag{16}$$

where b is the fitted shape coefficient influenced by the distance between the nozzle tip and the substrate and by the contact angle between the material and the slide (θ). Thus, the relationship between the printed hydrogel linewidth (D_p), pressure (ΔP), moving velocity of the nozzle (v), and extrudate temperature (T_E), which affects the flow consistency index (k)

and the flow behavior index (n), can be described by Eq. (16).

Experimental verification was conducted on the proposed physical model (**Figure 5**), and **Table 2** lists the printing conditions. The minimum change step is shown in brackets, for example, there is a change in nozzle temperature from 25°C to 29°C in increments of 1°C.

The plots of the overall phase diagrams of the printed filaments using the 32-G (ID=0.11 mm) and the 23-G (ID=0.34 mm) nozzles are shown in **Figures 5A–D.** The filaments were divided into four types. The first was a well-defined swollen filament with a linewidth greater than the nozzle diameter (denoted by the red dots), the second was an equivalent-diameter filament with a linewidth approximately similar to that of the nozzle diameter (green dots), and the third was a stretched filament with a linewidth narrower than the nozzle diameter (pink dots). The fourth type was an irregular filament with a standard deviation too large to be adapted (blue dots). For both nozzles, filaments' formation was shown to be

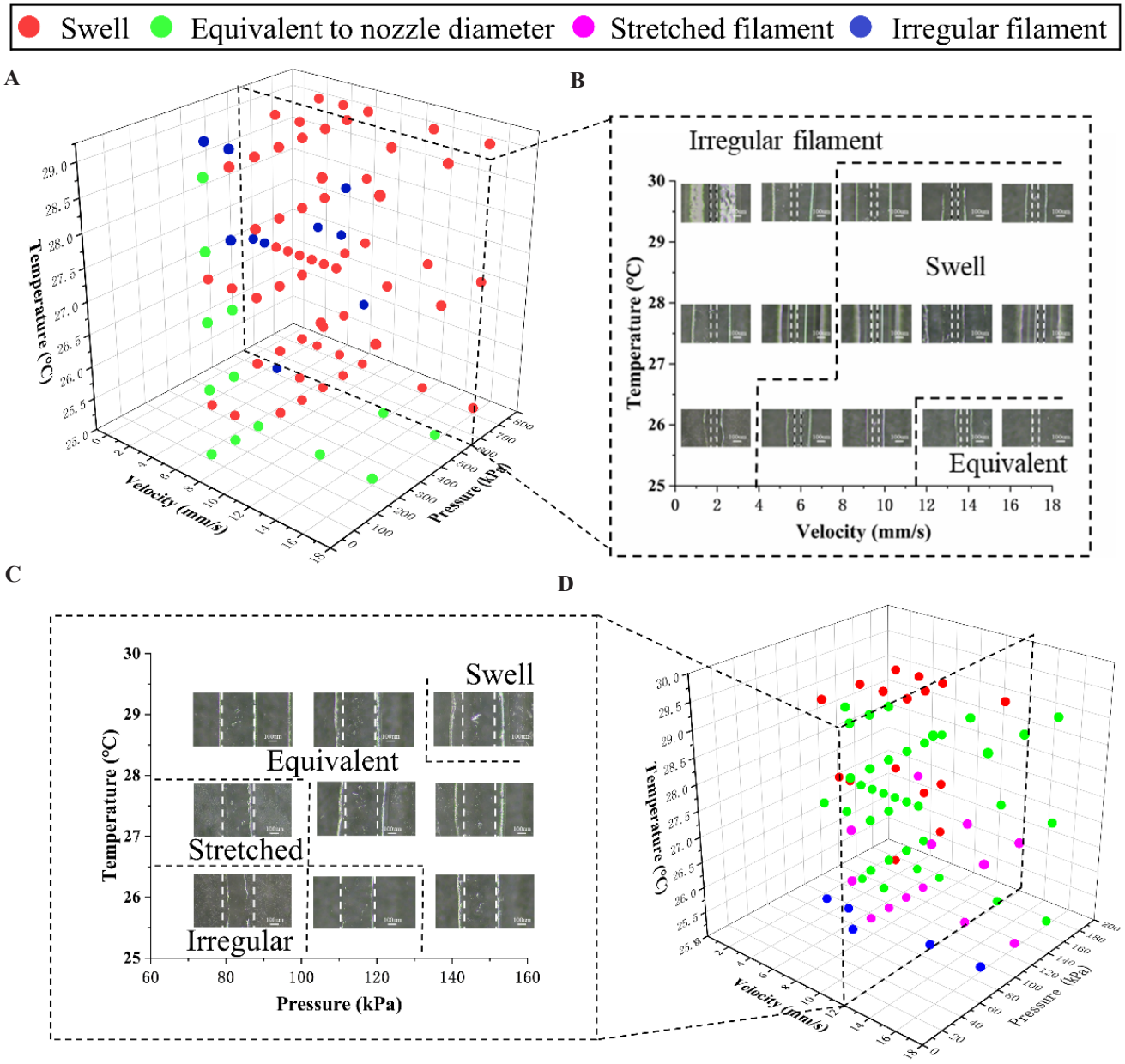


Figure 5. (A) Overall phase diagram of the printed filament using 32-G nozzle. (B) A typical two-dimensional phase diagram showing the influence of the velocity and the temperature on the linewidth. (C) Overall phase diagram of the printed filament using 23-G nozzle. (D) A typical two-dimensional phase diagram showing the influence of the pressure and the temperature on the linewidth (n=9, P<0.0001, error=S.D.).

a synergistic consequence of various factors, including pressure, velocity, and extrudate temperature. Forming stretched filaments with the small-diameter nozzle are challenging, although swollen or irregular filaments can be produced easily; this could be due to the high shear stress and long duration on the rheological properties of the material[51]. Conversely, the low shear stress and rapid flow time during extrusion make it easier for the larger diameter nozzle to form filaments of equivalent diameter.

Figures 5B and C summarize two representative sub-phase diagrams. In **Figure 5B**, the pressure was set to 600 kPa. Lower velocity and higher temperature result in irregular filaments; therefore, filaments of equivalent diameters can be printed at a relatively high velocity and at an appropriate temperature. The velocity in **Figure 5C** was set to 12 mm/s. Under low pressure and low temperature, discontinuous filaments can be produced easily. Therefore, the selection of appropriate temperature and pressure ranges results in producing the desired equivalent-diameter filaments.

To verify the proposed model, several experiments were conducted to determine the coefficient in Eq. (16). The relationships between temperature, pressure, and linewidth are shown in **Figure S1 (Supplementary File)**. **Figures 6A-D** present the fitted shear and shape coefficients. For each printing result, well-defined filaments were formed, and nine samples were measured. In terms of the inaccuracies in the diameters' measurement, the systematic errors in deriving the values of k and n and the error in regulating extrudate temperature could be the main reasons for the disparity between the experimental and predicted linewidths.

Figure S1A-E shows the lines printed with the 32-G nozzle at the controlled syringe temperatures of 25°C, 26°C, 27°C, 28°C, and 29°C, in which the predicted values of the proposed and conventional models are plotted. To predict the linewidth with consideration of the temperature change during extrusion, the predicted temperature of the extrudate was substituted into Eq. (16). The fitted shear coefficient, c, is shown in **Figure 6A.** The value of c was found to be almost linear with the temperature ($R^2 = 0.91$). As shown in **Figure 6C**, the shape coefficient, b, which can be influenced by the nozzle tip–substrate distance and the contact angle of the material, was found to be linear with the temperature ($R^2 = 0.97$).

The filaments printed at 25°C were discontinuous, which invalidated the results. Therefore, the linewidths

Table 2. Printing condition of each experiment

Group	Ambient temperature (T_A) (℃)	nozzle temperature (T_C) (℃)	Pressure (kPa)	Velocity (mm/s)
32-G	20 (constant)	25 – 29	100 – 800	1 – 16
0.11 mm I.D.		(1)	(100)	(3)
23-G	20 (constant)	25 – 29	70 – 170	1 – 16
0.34 mm I.D.		(1)	(20)	(3)

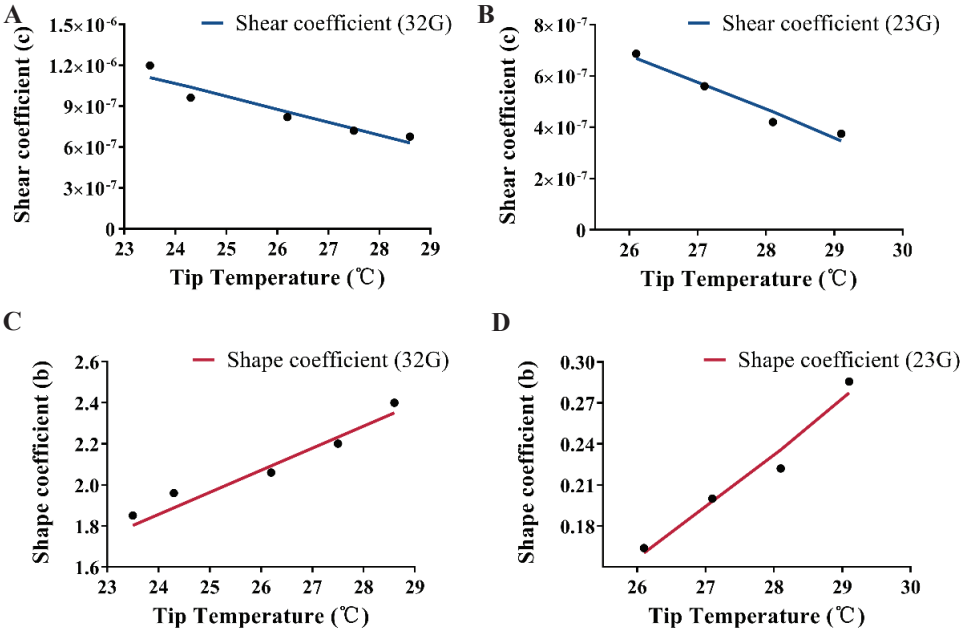


Figure 6. Shape coefficients and shear coefficients. (A) Shear coefficient c for 32-G nozzle. (B) Shear coefficient c for 23-G nozzle. (C) Shape coefficient b for 32-G nozzle. (D) Shape coefficient b for 23-G nozzle.

of the fibers printed at the controlled syringe temperatures of 26°C, 27°C, 28°C, and 29°C using the 23-G nozzle are plotted in **Figures S1F-I**. An almost linear relationship was also found between the value of *c* and the temperature, which is presented in **Figure 6(B)** ($R^2 = 0.96$). This was also the case for the relationship between the shape coefficient, *b*, and the temperature ($R^2 = 0.96$), as shown in **Figure 6D**.

The differences in coefficients *c* and *b* for different nozzles could be attributed to the nozzle diameter. The contact angle could be affected when the experimental linewidth was widened by the collapse of more materials extruded by the larger nozzle. A negative correlation was found between the shear coefficient, *c*, and the temperature. This could be attributed to the high temperature decreasing the viscosity of the material, thereby weakening the die-swell phenomenon. The increase in temperature decreased the material-slide contact angle, which increased the shape coefficient, *b*.

In **Figure S1**, the linewidths, predicted using the conventional model (Eq. [12]) at the extrudate temperature, do not match the experimental results ($R^2 = 0$); Chen *et al.* reported a similar conclusion[34]. However, when using *k* and *n*'s values at the predicted extrudate temperature and the proposed physical model, good agreement is found between the predicted and experimental linewidths ($R^2 > 0.8$ for each experimental set). Those results reveal that the extrudate temperature predicted by the syringe temperature and the AT, rather than by the syringe temperature alone, was similar to the actual printing temperature. And the physical model considering the die-swell phenomenon could describe the extrusion process more exactly. This could explain the difference between the predicted and experimental results reported in Chen *et al.*'s study[34].

When comparing the linewidths predicted by the proposed and conventional models, a deviation between two lines is evident for the 32-G nozzle but not for the 23-G nozzle. This could be attributed to differences in shear stress and flow duration. A greater pressure is required to force materials through the smaller diameter nozzle, which increases the wall shear stress and causes the extrudate to swell. For the larger nozzle (23-G), the deviation is decreased by the fast flow rate and the low shear stress.

The influence of the AT between 15°C and 40°C (data not shown) was also investigated. The significant difference between the predicted and printed linewidths suggests that the AT could result in different contact angles and collapse of the printed line, and it was demonstrated that the contact angle influences the measured linewidth[32,52].

During the third stage of the extrusion process, the mismatch between the nozzle's moving velocity and the extrusion velocity contributes to a secondary swell. For example, the printing condition was set to a pressure of 600 kPa for the 32-G nozzle and 130 kPa for the 23-G nozzle at a temperature of 27°C. The effect of nozzle velocity on linewidth is presented in **Figures S1J-K**. The faster the velocity, the thinner the linewidth. There was a gradual decline in the rate of change, as shown by Eq. (16). The derived shear coefficient, *c*, and the shape efficient, *b*, were substituted into the equation, and an approximation was found between the theoretical and experimental linewidths ($R^2 = 0.9807$ and 0.9421, respectively, for the 32-G and 23-G nozzles).

The above discussion results can be summarized as follows: (a) The formation of filaments is a synergistic consequence of various factors, including pressure, velocity, and extrudate temperature. (b) The predicted extrudate temperature (T_E), which was derived from the syringe temperature (T_C) and the AT (T_A), was close to the real extrudate temperature. (c) The modified model with consideration of the die-swell phenomenon was used to predict the printed linewidth. The results were superior to those of the ordinary model. (d) A reasonably accurate open-loop control could be established based on the proposed physical model.

3.4. Linewidth printing steps

The first step to printing 3D scaffolds is to use an appropriate linewidth, which can be achieved using the established physical model (Eq. [16]). The model describes the relationship between the extrudate's temperature, pressure, moving velocity, and linewidth. A series of lines with a stepped linewidth were printed using this model. The shape coefficient (*b*) and shear coefficient (*c*) were derived from **Figure 6**, and the AT was set to 25°C.

A series of experiments was conducted to modify the physical model's different parameters. Lines were printed using the 32-G and 23-G nozzles separately with a 50-μm linewidth step. **Figures 7A and B** show the fabricated lines, and a comparison between the printed and predicted linewidths is given in **Figures 7C-H**. The white dotted line denotes the outline of the printed lines.

With the 32-G nozzle, the initial linewidth was set to be equal to its nozzle diameter of 110 μm. The printed lines were expected to have linewidths of 110, 160, 210, 260, and 310 μm. In the first set of experiments, the printing pressure and velocity were maintained at 200 kPa and 8 mm/s, respectively. The extrudate temperature was controlled to 26.1°C, 27.3°C, 28.1°C, 28.7°C, and 29.3°C separately by changing the nozzle temperature, the values of which were determined by the thermal model and the simulation (Section 3.2). Then, the AT of 25°C and the thermal parameters (as given in **Table 1**) were substituted. In the second set of experiments, the

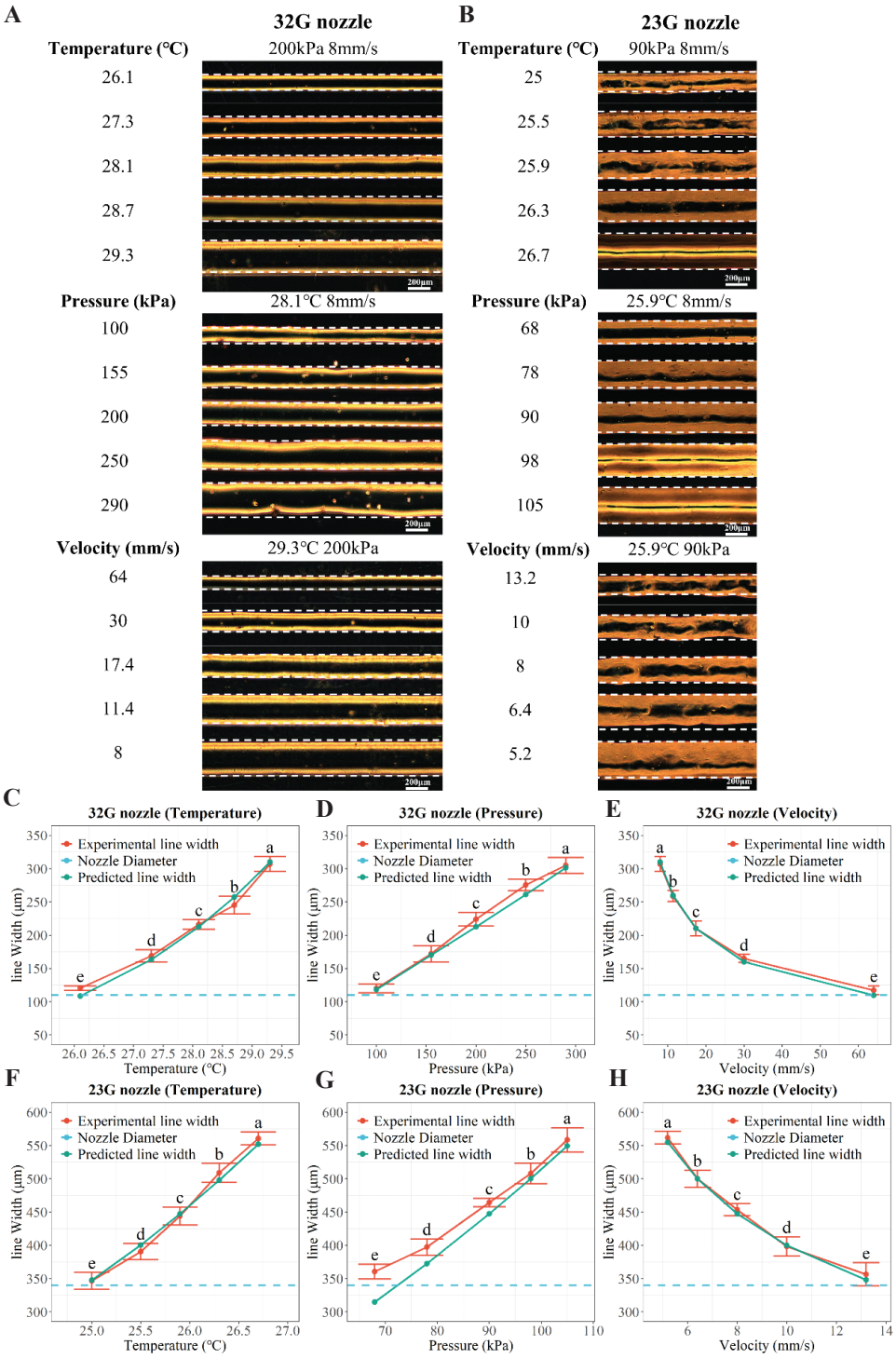


Figure 7. Linewidth gradient printing. (A) Lines printed using 32-G nozzle. (B) Lines printed using 23-G nozzle. (C-F) Comparison between the experimental linewidth and the predicted linewidth. (C) 32-G nozzle with variable extrudate temperature. (D) 32-G nozzle with variable pressure. (E) 32-G nozzle with variable velocity. (F) 23-G nozzle with variable temperature. (G) 23-G nozzle with variable pressure. (H) 23-G nozzle with variable velocity (n>9, P<0.0001, error=S.D.)

extrudate's temperature and velocity were set to 28.1°C and 8 mm/s, respectively. The printing pressure was set to 100, 155, 200, 250, and 290 kPa. The moving velocity was changed in the third set of experiments to 64, 30, 17.4, 11.4, and 8 mm/s, while the temperature and pressure of the extrudate were set separately to 29.3°C and 200 kPa. A comparison between the printed and predicted linewidths is given in **Figures 7C-E**. The R^2

values of these figures are 0.9744, 0.9757, and 0.9833, respectively (P<0.001).

In addition, the 23-G nozzle was used to verify the physical model and to print lines with a linewidth step. With a nozzle diameter of 340 μm, the linewidth gradient of the 23-G nozzle was 340, 390, 440, 490, and 540 μm. In the first set of experiments, the pressure and velocity were set at constants of 90 kPa and 8 mm/s, respectively. The extrudate's theoretical temperature was calculated according to Eq. (16) and was realized by regulating the nozzle temperature based on both Eq. (6) and the thermal simulation. The extrudate temperature was regulated separately at 25°C, 25.5°C, 25.9°C, 26.3°C, and 26.7°C. Then, in the second set of experiments, the pressure was set sequentially at 68, 78, 90, 98, and 105 kPa. The temperature and velocity of the extrudate were maintained at 25.9°C and 8 mm/s. In addition, in the third set of experiments, the velocity (as a controlled variable) was set to 13.2, 10, 8, 6.4, and 5.2 mm/s, respectively. The temperature and pressure of the extrudate were maintained as constants at 25.9°C and 90 kPa. **Figures 7F-H** plot the results of the three sets of experiments, and the separate R-square values of these results are 0.9724, 0.9661, and 0.9693, (P<0.001).

Lines with controllable linewidths were printed during six sets of experiments with a linewidth step of about 50 μm. The remarkably high R^2 values show that the applied parameters effectively fabricated lines with the expected linewidth. Compared with the lines printed by the 32-G nozzle, the lines printed by the 23-G nozzle (with a wider ID) were more difficult to control, which can be explained by Eq. (16). A larger diameter nozzle requires both lower pressure and velocity to print lines, thereby exacerbating the inherent error of the 3D bioprinter and increasing the difficulty in controlling the linewidth.

3.5. Cell-laden scaffold fabrication

In this study, printability was represented by the shape integrity and cell viability after printing. The rheological properties of the bioinks (in Section 3.1) and the physical models (in Section 3.3) provided the foundation for cell-laden bioprinting. The effect of pressure and nozzle type had been explored previously and had confirmed that higher shear stresses result in lower cell viability[23,27]. Therefore, the 23-G nozzle was adapted to investigate the influence of temperature on cell viability. Cell-laden scaffolds were fabricated at different temperatures using a bioink comprising sodium alginate–gelatin hydrogel and HKs with a cell density of 3×10^6/mL.

Three grid patterns were printed using the cell-laden bioink; to optimize printability, the study used the 23-G nozzle, 130 kPa of pressure, and a velocity of 7 mm/s. The extrudate temperature was regulated separately at 24°C (**Figures 8A-E**), 27°C (**Figures 8B-F**), and 30°C (**Figures 8C-G**). The LIVE/DEAD cell viability assay revealed the cells' viability after printing to be 89.21±4.09%, 91.83±2.05%, and 93.94±3.92%, as shown in **Figure 8D**.

The printing results revealed that the cell viability was almost identical in each experimental setup, although the shape fidelity changed significantly according to temperature. Shape fidelity was compromised when printing with bioink at a temperature higher than the gelation point of the ink. The minor change in cell viability could be due to the different lengths of time the cells remained in the syringe[25].

The criterion for selecting appropriate printing parameters using soft materials was described in Eq. (16). It was confirmed by the result of the fluorescent live/dead staining that the optimized printing process had no significant negative impact on cell viability. Ouyang *et al.* reported a similar conclusion[27].

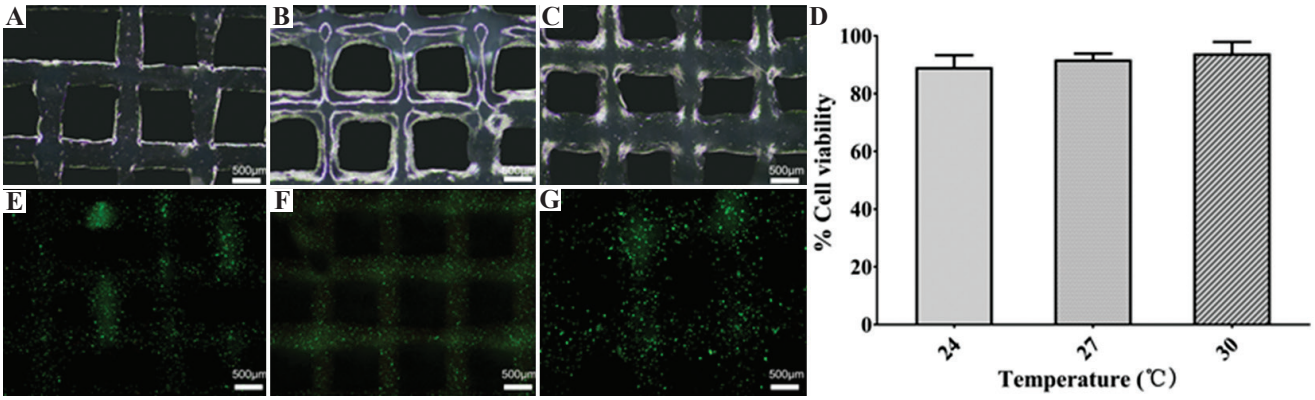


Figure 8. Cell-laden scaffolds: (A) Scaffolds printed in 24°C; (B) Scaffolds printed in 27°C; (C) Scaffolds printed in 30°C; (D) The viability of the cells printed in different temperature; (E) Live/dead staining images of scaffolds printed in 24°C; (F) LIVE/DEAD staining images of scaffolds printed in 27°C; (G) LIVE/DEAD staining images of scaffolds printed in 30°C (n=3, P>0.05, error=S.D.).

4. Conclusions

This study established a quantitative approach to evaluate a sodium alginate's printability–gelatin composite hydrogel using linewidth as a criterion. A quantitative thermal model was presented to facilitate precise temperature control with consideration of the syringe temperature, AT, and dispensing material temperature. A physical model was established that described the relationship between the temperature-sensitive indices, dispensing pressure, velocity, and linewidth. Subsequently, it was used to guide the accurate printing of lines with a 50-μm linewidth step. The cell-laden printing test results verified that cell viability in the gelatin–alginate temperature zone was not violated significantly by the printing process. Based on the proposed physical model, an open-loop control can be established to improve printability and expand the potential application of extrusion-based bioprinting.

Acknowledgments

We would like to thank the support by National Key Research and Development Program of China (2018YFA0703000), Key Research and Development Projects of Zhejiang Province (Grant No. 2017C01054), National Natural Science Foundation of China (Grant No. 51875518, No.51821093), and the Fundamental Research Funds for the Central Universities (Grant No. 2019XZZX003-02, 2020QNA4001).

Conflict of interest

There are no conflicts of interest to declare.

Author contributions

L.Q.: Experimental conception and design, acquisition of data, analysis and interpretation of data, paper drafting and revising; Z.B.: Experimental conception and design, paper drafting, and revising; X.Q: Experimental conception and design; Z.C.X.: Experimental conception and design; L.Y.C.: Experimental conception and design; Z.H.Z.: Supervise the work, paper drafting and revising, and final approval of paper; M.L.: Supervise the work, financial support, paper drafting and revising, and final approval of paper; Y.H.Y.: Financial support, administrative support, and final approval of paper; B.D.P.: Experimental conception and design.

References

1. Donderwinkel I, Hest JC, Cameron NR, 2017, Bio-inks for 3D Bioprinting: Recent Advances and Future Prospects. *Polym Chem*, 8:4451–71. https://doi.org/10.1039/c7py00826k.
2. Zhang B, Gao L, Ma L, *et al.*, 2019, 3D Bioprinting: A Novel Avenue for Manufacturing Tissues and Organs. *Engineering*, 5:777–94. https://doi.org/10.1016/j.eng.2019.03.009.
3. He Y, Yang F, Zhao H, *et al.*, 2016, Research on the Printability of Hydrogels in 3D Bioprinting. *Sci Rep*, 6:29977.
4. Michal S, Smadar C, 2003, Cardiac Tissue Engineering, *Ex Vivo*: Design Principles in Biomaterials and Bioreactors. *Heart Fail Rev*, 8:271–6.
5. Campbell J, McGuinness I, Wirz H, *et al.*, 2015, Multimaterial and Multiscale Three-Dimensional Bioprinter. *J Nanotechnol Eng Med*, 6:021005.
6. Holländer J, Hakala R, Suominen J, *et al.*, 2018, 3D Printed UV Light Cured Polydimethylsiloxane Devices for Drug Delivery. *Int J Pharm*, 544:433–42. https://doi.org/10.1016/j.ijpharm.2017.11.016.
7. Kang HW, Lee SJ, Ko IK, *et al.*, 2016, A 3D Bioprinting System to Produce Human-Scale Tissue Constructs with Structural Integrity. *Nat Biotechnol*, 34:312–9. https://doi.org/10.1038/nbt.3413.
8. Liu W, Zhang YS, Heinrich MA, *et al.*, 2017, Rapid Continuous Multimaterial Extrusion Bioprinting. *Adv Mater*, 29:1604630.
9. McElheny C, Hayes D, Devireddy R, 2017, Design and Fabrication of a Low-Cost Three-Dimensional Bioprinter. *J Med Device*, 11:041001. https://doi.org/10.1115/1.4037259.
10. Wang L, Xu ME, Luo L, *et al.*, 2018, Iterative Feedback Bio-Printing-Derived Cell-Laden Hydrogel Scaffolds with Optimal Geometrical Fidelity and Cellular Controllability. *Sci Rep*, 8:2802. https://doi.org/10.1038/s41598-018-21274-4.
11. Ahn G, Park JH, Kang T, *et al.*, 2010, Effect of Pore Architecture on Oxygen Diffusion in 3D Scaffolds for Tissue Engineering. *J Biomech Eng*, 132:104506.
12. Ng WL, Chua CK, Shen YF, 2019, Print Me An Organ! Why We Are Not There Yet. *Prog Polym Sci*, 97:101145. https://doi.org/10.1016/j.progpolymsci.2019.101145.
13. Nguyen DG, Funk J, Robbins JB, *et al.*, 2016, Bioprinted 3D Primary Liver Tissues Allow Assessment of Organ-Level Response to Clinical Drug Induced Toxicity *In Vitro*. *PLoS One*, 11:e0158674. https://doi.org/10.1371/journal.pone.0158674.
14. Park SJ, Kim RY, Park BW, *et al.*, 2019, Dual Stem Cell Therapy Synergistically Improves Cardiac Function And Vascular Regeneration Following Myocardial Infarction. *Nat Commun*, 10:3123. https://doi.org/10.1038/s41467-019-11091-2.

15. Ma L, Li Y, Wu Y, *et al.*, 2020, 3D Bioprinted Hyaluronic Acid-Based Cell-Laden Scaffold for Brain Microenvironment Simulation. *Biodes Manuf*, 3:164–74. https://doi.org/10.1007/s42242-020-00076-6.
16. Lee V, Singh G, Trasattijohn P, *et al.*, 2014, Design and Fabrication of Human Skin by Three-Dimensional Bioprinting. *Tissue Eng Part C Methods*, 20:473–84.
17. Peng W, Unutmaz D, Ozbolat IT, 2016, Bioprinting Towards Physiologically Relevant Tissue Models for Pharmaceutics. *Trends Biotechnol*, 34:722–32. https://doi.org/10.1016/j.tibtech.2016.05.013.
18. Zhang B, Luo Y, Ma L, *et al.*, 2018, 3D Bioprinting: An Emerging Technology Full of Opportunities and Challenges. *Biodes Manuf*, 1:2–13.
19. Gudapati H, Dey M, Ozbolat I, 2016, A Comprehensive Review on Droplet-Based Bioprinting: Past, Present and Future. *Biomaterials*, 102:20–42. https://doi.org/10.1016/j.biomaterials.2016.06.012.
20. Ying G, Jiang N, Yu C, *et al.*, 2018, Three-Dimensional Bioprinting of Gelatin Methacryloyl (GelMA). *Biodes Manuf*, 1:215–24. https://doi.org/10.1007/s42242-018-0028-8.
21. Ma L, Li Y, Wu Y, *et al.*, 2020, The Construction of *In Vitro* Tumor Models Based on 3D Bioprinting. *Biodes Manuf*, 3:227–36.
22. Alruwaili M, Lopez JA, McCarthy K, *et al.*, 2019, Liquid-phase 3D Bioprinting of Gelatin Alginate Hydrogels: Influence of Printing Parameters on Hydrogel Line Width and Layer Height. *Biodes Manuf*, 2:172–80. https://doi.org/10.1007/s42242-019-00043-w.
23. Chang R, Nam J, Sun W, 2008, Effects of Dispensing Pressure and Nozzle Diameter on Cell Survival from Solid Freeform Fabrication-Based Direct Cell Writing. *Tissue Eng Part A*, 14:41–8. https://doi.org/10.1089/ten.2007.0004.
24. Gao T, Gillispie GJ, Copus JS, *et al.*, 2018, Optimization of Gelatin-Alginate Composite Bioink Printability Using Rheological Parameters: A Systematic Approach. *Biofabrication*, 10:034106. https://doi.org/10.1088/1758-5090/aacdc7.
25. Zhao Y, Li Y, Mao S, *et al.*, 2015, The Influence of Printing Parameters on Cell Survival Rate and Printability in Microextrusion-Based 3D Cell Printing Technology. *Biofabrication*, 7:045002. https://doi.org/10.1088/1758-5090/7/4/045002.
26. Gong Y, Bi Z, Bian X, *et al.*, 2020, Study on Linear Bio-Structure Print Process Based on Alginate Bio-Ink in 3D Bio-Fabrication. *Biodes Manuf*, 3:109–21. https://doi.org/10.1007/s42242-020-00065-9.
27. Ouyang L, Yao R, Zhao Y, *et al.*, 2016, Effect of Bioink Properties on Printability and Cell Viability for 3D Bioplotting of Embryonic Stem Cells. *Biofabrication*, 8:035020. https://doi.org/10.1088/1758-5090/8/3/035020.
28. Kolan KC, Semon JA, Bromet B, *et al.*, 2019, Bioprinting with Human Stem Cell-Laden Alginate-Gelatin Bioink and Bioactive Glass for Tissue Engineering. *Int J Bioprint*, 5:204. https://doi.org/10.18063/ijb.v5i2.2.204.
29. Zhang Z, Jin Y, Yin J, *et al.*, 2018, Evaluation of Bioink Printability for Bioprinting Applications. *Appl Phys Rev*, 5:041304.
30. Yin J, Zhao D, Liu J, 2019, Trends on Physical Understanding of Bioink Printability. *Biodes Manuf*, 2:50–4.
31. Suntornnond R, Tan EY, An J, *et al.*, 2016, A Mathematical Model on the Resolution of Extrusion Bioprinting for the Development of New Bioinks. *Materials* (*Basel*), 9:756. https://doi.org/10.3390/ma9090756.
32. Lee JM, Yeong WY, 2014, A Preliminary Model of Time-Pressure Dispensing System for Bioprinting Based on Printing and Material Parameters. *Virtual Phys Prototyp*, 10:3–8. https://doi.org/10.1080/17452759.2014.979557.
33. Paxton N, Smolan W, Bock T, *et al.*, 2017, Proposal to Assess Printability of Bioinks for Extrusion-Based Bioprinting and Evaluation of Rheological Properties Governing Bioprintability. *Biofabrication*, 9:044107. https://doi.org/10.1088/1758-5090/aa8dd8.
34. Chen X, Li M, Ke H, 2008, Modeling of the Flow Rate in the Dispensing-Based Process for Fabricating Tissue Scaffolds. *J Manuf Sci Eng*, 130:021003. https://doi.org/10.1115/1.2789725.
35. Billiet T, Gevaert E, de Schryver T, *et al.*, 2014, The 3D Printing of Gelatin Methacrylamide Cell-Laden Tissue-Engineered Constructs with High Cell Viability. *Biomaterials*, 35:49–62. https://doi.org/10.1016/j.biomaterials.2013.09.078.
36. Mahmoudi Y, 2014, Effect of Thermal Radiation on Temperature Differential in a Porous Medium Under Local Thermal Non-Equilibrium Condition. *Int J Heat Mass Transf*, 76:105–21. https://doi.org/10.1016/j.ijheatmasstransfer.2014.04.024.
37. Zhang B, Xue Q, Hu HY, *et al.*, 2019, Integrated 3D Bioprinting-Based Geometry-Control Strategy for Fabricating Corneal Substitutes. *J Zhejiang Univ Sci B*, 20:945–59. https://doi.org/10.1631/jzus.b1900190.

38. Isaacson A, Swioklo S, Connon CJ, 2018, 3D Bioprinting of a Corneal Stroma Equivalent. *Exp Eye Res*, 173:188–93. https://doi.org/10.1016/j.exer.2018.05.010.
39. Kong B, Chen Y, Liu R, *et al.*, 2020, Fiber Reinforced GelMA Hydrogel to Induce the Regeneration of Corneal Stroma. *Nat Commun*, 11:1435.
40. Zhang B, Gao L, Gu L, *et al.*, 2017, High-resolution 3D Bioprinting System for Fabricating Cell-laden Hydrogel Scaffolds with High Cellular Activities. *Proc CIRP*, 65: 219–24. https://doi.org/10.1016/j.procir.2017.04.017.
41. Shao L, Gao Q, Xie C, *et al.*, 2020, Sacrificial Microgel-Laden Bioink-Enabled 3D Bioprinting of Mesoscale Pore Networks. *Biodes Manuf*, 3:30–9. https://doi.org/10.1007/s42242-020-00062-y.
42. Gong Y, Wang F, Al-Furjan MS, *et al.*, 2020, Experimental Investigation and Optimal 3D Bioprinting Parameters of SA-Gel Porous Cartilage Scaffold. *Appl Sci*, 10:768. https://doi.org/10.3390/app10030768.
43. Khalil S, Sun W, 2007, Biopolymer Deposition for Freeform Fabrication of Hydrogel Tissue Constructs. *Mater Sci Eng C*, 27:469–78. https://doi.org/10.1016/j.msec.2006.05.023.
44. Tanner RI, 2005, A Theory of Die-Swell Revisited. *J Nonnewton Fluid Mech*, 129:85–7.
45. Tanner RI, 1970, A Theory of Die-Swell. *J Polym Sci Part A-2 Polym Phys*, 8:2067–78.
46. Carreau PJ, Choplin L, Clermont JR, 1985, Exit Pressure Effects in Capillary Die Data. *Polym Eng Sci*, 25:669–76. https://doi.org/10.1002/pen.760251105.
47. Iwami K, Noda T, Ishida K, *et al.*, 2010, Bio Rapid Prototyping by Extruding/Aspirating/Refilling Thermoreversible Hydrogel. *Biofabrication*, 2:014108. https://doi.org/10.1088/1758-5082/2/1/014108.
48. Liang JZ, 2008, Effects of Extrusion Conditions on Die-Swell Behavior of Polypropylene/Diatomite Composite Melts. *Polym Test*, 27:936–40. https://doi.org/10.1016/j.polymertesting.2008.08.001.
49. Chin WC. Managed Pressure Drilling: Modeling, Strategy and Planning. Waltham: Gulf Professional Publishing; 2012. p. 315-85.
50. Allain C, Cloitre M, Perrot P, 1997, Experimental Investigation and Scaling Law Analysis of Die Swell in Semi-Dilute Polymer Solutions. *J Nonnewton Fluid Mech*, 73:51–66. https://doi.org/10.1016/s0377-0257(97)00051-7.
51. Cooke ME, Rosenzweig DH, 2021, The Rheology of Direct and Suspended Extrusion Bioprinting. *APL Bioeng*, 5:011502. https://doi.org/10.1063/5.0031475.
52. Quéré D, Azzopardi MJ, Delattre L, 1998, Drops at Rest on a Tilted Plane. *Langmuir*, 14:2213–6.

RESEARCH ARTICLE

Graphene Oxide-Embedded Extracellular Matrix-Derived Hydrogel as a Multiresponsive Platform for 3D Bioprinting Applications

Laura Rueda-Gensini, Julian A. Serna, Javier Cifuentes, Juan C. Cruz*, Carolina Muñoz-Camargo*

Department of Biomedical Engineering, Universidad de Los Andes, Bogotá, 11171, Colombia

Abstract: Decellularized extracellular matrices (dECMs) have shown enormous potential for the biofabrication of tissues due to their biomimetic properties that promote enhanced cellular interaction and tissue regeneration. However, biofabrication schemes requiring electrostimulation pose an additional constraint due to the insulating properties of natural materials. Here, we propose a methacryloyl-modified decellularized small intestine submucosa (SISMA) hydrogel, embedded with graphene oxide (GO) nanosheets, for extrusion-based 3D bioprinting applications that require electrostimulation. Methacryloyl biochemical modification is performed to enhance the mechanical stability of dECM constructs by mediating photo-crosslinking reactions, and a multistep fabrication scheme is proposed to harness the bioactive and hydrophilic properties of GO and electroconductive properties of reduced GO. For this, GO was initially dispersed in SISMA hydrogels by exploiting its hydrophilicity and protein adsorption capabilities, and *in situ* reduction was subsequently performed to confer electroconductive abilities. SISMA-GO composite hydrogels were successfully prepared with enhanced structural characteristics, as shown by the higher crosslinking degree and increased elastic response upon blue-light exposure. Moreover, GO was homogeneously dispersed without affecting photocrosslinking reactions and hydrogel shear-thinning properties. Human adipose-derived mesenchymal stem cells were successfully bioprinted in SISMA-GO with high cell viability after 1 week and *in situ* reduction of GO during this period enhanced the electrical conductivity of these nanostructures. This work demonstrates the potential of SISMA-GO bioinks as bioactive and electroconductive scaffolds for electrostimulation applications in tissue engineering and regenerative medicine.

Keywords: Extracellular matrix bioink; Graphene oxide; Reduced graphene oxide; Electroconductive hydrogel; Photocrosslinking

*Correspondence to: Juan C. Cruz, Biomedical Engineering Department, Universidad de Los Andes, Bogotá, 11171, Colombia; jc.cruz@uniandes.edu.co; Carolina Muñoz-Camargo, Department of Biomedical Engineering, Universidad de Los Andes, Bogotá, 11171, Colombia; c.munoz2016@uniandes.edu.co

Received: March 12, 2021; **Accepted:** April 20, 2021; **Published Online:** May 11, 2021

Citation: Rueda-Gensini L, Serna JA, Cifuentes J, *et al*., 2021, Graphene Oxide-Embedded Extracellular Matrix-Derived Hydrogel as a Multiresponsive Platform for 3D Bioprinting Applications. *Int J Bioprint*, 7(3):353. http://doi.org/10.18063/ijb.v7i3.353

1. Introduction

Decellularized extracellular matrices (dECMs) have gained significant attention over the past few decades as biomaterials for tissue engineering due to their promising potential as biomimetic scaffolds[1,2]. Composition-wise, dECMs hold a complex of structural proteins such as collagen, laminin, elastin, and fibronectin, which in native tissues grant adequate mechanical rigidity and structural stability for cellular growth, migration, and proliferation, and provide attachment sites for cell adhesion[1]. Additional proteins present in dECMs such as glycoproteins, proteoglycans, and bound growth factors mediate morphological organization and physiological function[3] while glycosaminoglycans (GAGs) provide an extremely hydrophilic environment essential for withstanding high compressive forces[4]. Although ECM composition varies depending on tissue function, its overall structure is similar for all tissues and, therefore, dECM hydrogels closely mimic the native cellular environment. Moreover, several studies have revealed that the presence and cumulative action

© 2021 Rueda-Gensini, *et al*. This is an Open Access article distributed under the terms of the Creative Commons Attribution License (https://creativecommons.org/ licenses/by/4.0/), permitting distribution and reproduction in any medium, provided the original work is cited.

of the bioactive molecules described above can promote regeneration processes and restore tissue homeostasis[5-7], underscoring the potential of dECM hydrogels for cellular scaffolding and advanced biomanufacturing applications above other natural materials.

Despite their great composition-wise resemblance to native tissues, solubilization procedures during dECM hydrogel preparation have shown to detrimentally alter the native structure of its fibrous proteins, mainly because of the use of proteolytic enzymes to aid matrix digestion[8]. This results in diminished biomechanical stiffness and higher biodegradability rate, which limits their prolonged functionality[9,10]. Specifically, temperature-dependent gelation, the principal crosslinking mechanism in dECM- and collagen-based hydrogels, is often not enough for maintaining structural stability within three-dimensional structures due to the weak forces (e.g., hydrogen bonds) holding together the digested components in the solubilized matrix[10]. As a result, dECM hydrogels usually need to be combined with other natural materials, such as hyaluronic acid, alginate, gelatin, chitosan, and silk fibroin, to facilitate alternative crosslinking mechanisms and improve their mechanical rigidity[11-13]. In this regard, the addition of crosslinking agents, such as glutaraldehyde and 1-ethyl-3-(3-dimethylaminopropyl) carbodiimide hydrochloride (EDC)/N-hydroxysulfosuccinimide (NHS), allows the formation of dense hydrogel networks[10,14]. However, unreacted reagents and reaction by-products from these approaches usually reduce the viability of the obtained hydrogel-based cellular constructs[15,16]. The biochemical modification of natural materials with methacryloyl groups has also emerged as a suitable alternative for photocrosslinking schemes[17], a method where material excipients are largely avoided for formulating the hydrogels and that favors crosslinking agents of low cytotoxicity[18-20]. In particular, improved mechanical stability has been reported in kidney- and bone-derived dECM bioinks upon methacryloyl modification, allowing tunable degrees of crosslinking with moderate ultraviolet or blue-light irradiation dosages[13,21]. Moreover, numerous biocompatible photoinitiators are commercially available to mediate this reaction (e.g., LAP, eosin Y, and riboflavin [RF])[13,20,22,23]. Therefore, methacryloyl modification of dECMs represents one of the most valuable avenues for the development of biomimetic hydrogels that closely recapitulate the biological and structural environment of native tissues and this, in turn, makes them suitable candidates for 3D bioprinting applications. In particular, these hydrogels can be precisely tuned for extrusion-based bioprinting (EBB) since their pseudoplastic rheological behavior facilitates their extrusion at high viscosity values, which are needed to achieve adequate shape fidelity and stability upon deposition[24]. EBB is one of the most adopted bioprinting technologies for the biofabrication of tissues and its advantages over other 3D bioprinting techniques have been extensively described elsewhere[25,26].

However, for the particular case of biomanufacturing tissues that require electrical stimulation to acquire their final biological function, dECM hydrogels face relevant limitations as building blocks, mainly because of their insulating properties[27]. Moreover, electrostimulation approaches have been reported to be beneficial in wound healing[28,29], bone regeneration[30,31], cell differentiation[32-34], and tissue maturation[35,36]. The incorporation of electroconductive nanostructured materials into hydrogels, such as graphene derivatives, gold nanoparticles, and carbon nanotubes, has shown great promise to alleviate these shortcomings[37]. Graphene, in particular, is a flexible nanomaterial made of sp^2 hybridized carbon atoms organized in a single two-dimensional layer, which generate a π-electron cloud responsible for electroconductivity[38]. However, due to its hydrophobic surface, the colloidal stability of graphene in hydrophilic media is highly limited. Consequently, its oxidized derivative, graphene oxide (GO), has attracted significant attention due to its superior hydrophilicity. This can be attributed to the presence of functional groups, such as hydroxyl and carboxyl moieties, which facilitate its dispersion in aqueous media. Moreover, they can promote protein adsorption from either culture media or cellular secretions, which improves overall cell-hydrogel interactions by increasing available cell anchoring sites[39,40]. However, the introduction of functional groups on GO disrupts the highly ordered carbon structures and results in reduced electroconductivity when compared to pristine graphene or reduced GO (rGO)[41]. Leveraging the bioactive and electroconductive properties of GO nanostructures is, therefore, a major challenge for the development of electroconductive hydrogels for tissue engineering applications.

Accordingly, the aim of this study is to develop an extrudable bioink based on methacryloyl-modified dECM and fully exfoliated GO nanosheets to render the potential for the electrostimulation of 3D bioprinted tissue constructs. We propose a fabrication scheme for the incorporation of GO that exploits both its bioactive and hydrophilic properties during the initial maturation stage of extruded constructs and simultaneously improves GO's electroconductivity upon *in situ* reduction. In particular, we harness the protein adsorption capacity of GO to induce homogeneous nanosheet dispersion within the dECM hydrogel, thus facilitating the formation of interconnected electrical networks and aiding initial cellular anchoring. The electro- and photo-addressable hydrogel obtained here, and the corresponding bioprinting scheme, hold much promise in the biofabrication of electrosensitive tissue constructs. Moreover, it may enable cell differentiation and tissue maturation processes by highly controllable electrostimulation strategies.

2. Materials and methods

2.1. Materials

Methacrylic acid (MA), EDC, NHS, dimethylformamide (DMF), picrylsulfonic acid, RF, formalin solution, TOX8 resazurin-based assay, rhodamine B, sodium bicarbonate, and low glucose Dulbecco's Modified Eagle Medium (DMEM) were purchased from Sigma-Aldrich (St. Louis, MO, USA). Sodium dodecyl sulfate was purchased from Santa Cruz Biotechnology (Dallas, TX, USA). Fetal bovine serum (FBS) and penicillin/streptomycin (P/S) were purchased from BioWest and hydrogen peroxide (H_2O_2), sodium chloride (NaCl), sodium hydroxide (NaOH), glacial acetic acid, sulfuric acid, phosphoric acid, potassium permanganate (K_2MnO_4), Tris-HCl, and hydrochloric acid (HCl) were purchased from PanReac AppliChem (Chicago, IL, USA), and graphite flakes from Graphene Supermarket (Ronkonkoma, NY, USA). Propidium iodide, AlexaFluor™ 488 Phalloidin, and Hoechst 3342 were purchased from Invitrogen (Waltham, MA, USA).

2.2. Isolation and decellularization of small intestinal submucosa (SIS)

Porcine small intestines were obtained from a local butcher shop and SIS was isolated and decellularized by following the protocol previously reported by Sánchez-Palencia and colleagues[42]. Briefly, the jejunum was thoroughly washed with tap water and the tunica mucosa and serosa muscularis layers were mechanically removed to isolate the SIS. For decellularization, isolated tissue samples were chemically treated with a proprietary solution consisting of H_2O_2, sodium hypochlorite, and autoclaved type II water for 15 min under constant agitation at room temperature (~23°C). Next, three successive washes with autoclaved type II water and one with sterile 1× phosphate-buffered saline (PBS) were performed to remove cellular and chemical remnants and for restoring ionic balance, respectively. Finally, the obtained membranes were dried at room temperature under laminar flow overnight and subsequently pulverized with the aid of a cryogenic mill (6875 Freezer/Mill, SPEX SamplePrep, Metuchen, NJ, USA). Dry SIS powder samples were then stored at −20°C until further use.

2.3. GO synthesis and characterization

GO synthesis was performed by following the Tour's methods with slight modifications[43]. Briefly, a solution prepared by mixing sulfuric acid and phosphoric acid at a 9:1 ratio was carefully poured into a flask containing graphite flakes and potassium permanganate. The resulting blend was then heated at 60°C and left for 12 h under constant vigorous magnetic stirring. Next, ice cold water and hydrogen peroxide (H_2O_2) were added to the blend and the obtained GO was washed successively by filtration with polyester fiber, centrifugation, and resuspension in a solution containing HCl, ethanol and type I water. The final pellet was resuspended in type II water and lyophilized for 24 h.

Adequate GO synthesis was confirmed through Raman spectroscopy by assessing the difference between excitation and emission intensity within a range of 0 and 3000 Raman shift (cm^{-1}). A point-wise laser excitation of 532 nm was shone at different locations along the synthesized GO sheets to evaluate homogeneity of the sample.

2.4. Pre-gel preparation and biochemical modification

Dry SIS powder was solubilized at 4 mg/mL in a solution containing 0.5 M acetic acid and porcine pepsin at a 1 mg/mL concentration. Solubilization was performed under constant vigorous magnetic stirring and at room temperature (~23°C) for 48 h. The free-amine groups present in the obtained SIS pre-gels were quantified by performing the 2,4,6-trinitrobenzene sulfonic acid (TNBSA) assay (see section 2.6).

Next, the obtained pre-gel was biochemically modified by covalently linking the C-terminal of MA to primary-amine residues present in fibrous structural protein backbones of SIS. This was accomplished by adapting the protocol reported by Gaudet *et al.*, which was developed for the biochemical modification of collagen[44]. Briefly, a working solution of MA (in a 1:20 molar excess with respect to free amines in SIS), EDC (1:1 molar ratio with MA) and NHS (1:1 molar ratio with MA) was prepared in DMF and heated for 15 min at 40°C under constant magnetic stirring for activating the terminal carboxyl groups of MA. The activated solution was then poured into the SIS pre-gel and the biochemical modification reaction was left for 24 h under constant magnetic stirring at 4°C. The resulting modified SIS (SISMA) pre-gel was dialyzed against 0.5 M acetic acid for 48 h and subsequently lyophilized for 24 h. The biochemically modified SIS samples were stored at −20°C and, if used for bioprinting experiments, sterilized by treatment with ethylene oxide (EtO).

2.5. Quantification of GO protein adsorption capacity

Dispersion of GO in acid solutions and biological buffers is very limited due to the presence of protonated carboxyl groups and surface charging that induces sheet agglomeration[45]. Consequently, its homogeneous incorporation into ECM and collagen-based hydrogels is a challenging task. To address this issue, we hypothesized

that the dispersion of GO would be improved by promoting protein adsorption before its incorporation into SIS and SISMA hydrogels. To test this hypothesis, GO's protein adsorption capacity was evaluated by quantifying the difference in protein concentration of cell culture media in the presence and absence of dispersed GO. Briefly, GO was dispersed at a concentration of 0.5 mg/mL in a DMEM cell culture media solution supplemented with 10% (v/v) FBS and 1% (v/v) P/S for 2 h at 4°C. The resulting solution was then centrifuged at 12,000 rpm for 5 min to isolate the GO from the medium, and protein concentration in the supernatant was finally quantified with the Quanti-Pro bicinchoninic acid assay Assay Kit (Sigma-Aldrich) and a bovine serum albumin standard curve **(Figure S1)**. The same procedure was conducted, as a control, for the same supplemented DMEM but in the absence of GO. Absorbance was measured at 562 nm with the aid of a microplate photometer (Multiskan™ FC, Thermo Scientific, Waltham, MA, USA) and protein adsorption on the GO sheets was calculated by implementing Equation 2.5.1.

$$Protein\ adsorption\ \% = \left(1 - \frac{A_{DMEM-GO}}{A_{DMEM}}\right) * 100 \qquad (2.5.1)$$

where $A_{DMEM-GO}$ is the absorbance measured from the supplemented DMEM in the presence of GO and A_{DMEM} is the absorbance from the supplemented DMEM alone.

2.6. Hydrogel preparation

A working solution (pH 8.5) consisting of DMEM supplemented with 10% (v/v) FBS, 1% (v/v) P/S, 0.1% (w/v) RF, and Tris-HCl 0.1 M was prepared. Next, GO was dispersed at a 0.5 mg/mL concentration in this working solution and left for 12 h at 4°C to promote protein binding. This was followed by resuspension of lyophilized SISMA at 40 mg/mL in a 0.02 M acetic acid solution aided by a spatula. This mixture was subsequently mixed at a 1:1 volume ratio with the working solution containing GO (SISMA-GO). For the hydrogels produced in the absence of GO, the same procedure was performed but with a working solution without the dispersed nanomaterial.

2.7. Quantification of functionalization efficiency

Since MA is conjugated to free-amine residues, these were quantified before and after biochemical modification as an indicator of reaction efficiency. This was achieved through a TNBSA assay according to the protocol described by Capella-Monsonís *et al.*[46]. Briefly, SIS and SISMA hydrogels were diluted in 0.1 M sodium bicarbonate (pH 8.5) to a final concentration of 0.2% (w/v), and 250 µL of a 0.01% (w/v) picrylsulfonic acid solution were then added to 500 µL of the diluted hydrogel sample. The blends were then mixed thoroughly with a benchtop vortex and incubated for 2 h at 37°C under constant agitation. Finally, 100 µL of each sample after incubation were transferred to a 96-well microplate and the absorbance was measured at 405 nm with the aid of a microplate photometer (Multiskan™ FC, Thermo Scientific, Waltham, MA, USA). The reaction product is highly chromogenic, meaning that a higher color intensity is associated with a higher concentration of primary amines. Finally, the reaction efficiency was calculated with Equation 2.7.1.

$$\%\ of\ functionalization = \left(1 - \frac{A_{SISMA}}{A_{SIS}}\right) * 100 \qquad (2.7.1)$$

where A_{SISMA} and A_{SIS} are the absorbance's of SISMA and SIS samples, respectively.

2.8. GO dispersion in SISMA

To evaluate if protein adsorption allowed proper GO dispersion within the hydrogel, serum proteins were fluorescently labeled with rhodamine B and exposed to GO such that, after dispersion, they can be imaged through confocal microscopy. Briefly, the carboxy terminal of rhodamine B was activated with EDC/NHS at 37°C for 15 min and subsequently added to a 10% (v/v) solution of FBS. The mixture was left to react for 24 h at room temperature (~23°C) under constant magnetic stirring. GO was then added at a concentration of 0.5 mg/mL and, after 2 h of exposure to the labeled proteins, it was thoroughly washed by several cycles of centrifugation and resuspension in type II water until the supernatant showed no traces of rhodamine B. Finally, protein-adsorbed GO was resuspended in type II water and mixed at a 1:1 volume ratio with a 40 mg/mL SISMA solution prepared in 0.02 M acetic acid. The samples were imaged at 559 nm with an Olympus FV1000 Confocal Microscope (Tokyo, Japan, Objective 10X) and particle count and area were later analyzed with the ImageJ® software. Z-stack reconstruction was also performed by capturing images at different positions throughout the hydrogel depth to assess the spatial distribution of GO sheets within the hydrogel.

2.9. Rheological evaluation

To assess the rheological response of the developed hydrogels, as well as the influence of photocrosslinking on their mechanical properties, flow sweep, temperature sweep, and time sweep experiments were performed on a Discovery Series Hybrid Rheometer-1 (TA Instruments, New Castle, DE, USA) using a parallel plate geometry with a 20 mm gap. Flow sweep experiments of SISMA and SISMA-GO hydrogels were conducted from 0.01 to

200 1/s at 1% strain and room temperature. The thermal response of these hydrogels was evaluated between 15°C and 37°C with a temperature ramp of 20°C/min, at 1% strain and 10 rad/s frequency. Finally, to compare the change in storage modulus upon photocrosslinking, time sweep assays were carried out before and after blue light irradiation (5 min at 62 mW/cm^2 constant intensity) under oscillatory mode, and constant strain of 1% and 10 rad/s.

Shear-thinning properties of the hydrogels were estimated by fitting the viscosity (η) versus shear rate (γ) plot to the power law regression model described by Equation 2.9.1.

$$\eta = K\gamma^{n-1} \quad (2.9.1)$$

K and n were recovered for all samples to assess shear thinning behavior[24].

2.10. Scanning electron microscopy (SEM) imaging of crosslinked structures

To evaluate the resulting hydrogel microstructure upon thermal- or photo-crosslinking, SISMA-GO samples were imaged through SEM. Gelation temperature was achieved after incubation of the samples for 15 min at 37°C. Photocrosslinking was achieved upon blue-light irradiation for 5 min at a constant intensity of 62 mW/cm^2. Samples were freeze dried and observed under vacuum conditions at 200× magnification with a 20 kV accelerating voltage (JSM 6490-LV, JEOL, Tokyo, Japan).

2.11. Isolation and *in vitro* culture of human adipose tissue-derived mesenchymal stem cells (hAD-MSCs)

For bioprinting experiments, hAD-MSCs were isolated following the protocol reported by Linero *et al.*[47] according to which residual adipose tissue (obtained from abdominoplasty procedures with the previous approval from the research ethics committee at the Universidad de Los Andes Act No. 942, 2018 and subsequent signing of patient informed consent) was subjected to mechanical distortion combined with enzymatic digestion. The isolated cells were subcultured until passage four using low glucose DMEM, supplemented with 10% (v/v) FBS and 1% (v/v) P/S. Their stem cell status was then characterized through flow cytometry (BD FACSCanto™ Flow Cytometer, BD Biosciences, San Jose, CA, USA) with the aid of a human mesenchymal stem cell validation kit (Human Mesenchymal Stem Cell Multi-Color Flow Kit, R&D Systems, Minneapolis, MN, USA) and data acquisition and analysis was done with the BD FACSDiva™ software version 6.1.3. Cells demonstrated positive expression of CD73, CD105, and CD90 as well as negative expression of all markers included in the negative marker cocktail. Quadrants have been set based on isotype controls **(Figure S2)**.

2.12. Biofabrication of cell-laden SISMA-GO constructs

After sterile SISMA and SISMA-GO hydrogels were successfully prepared, hAD-MSC in low glucose DMEM supplemented with 10% (v/v) FBS and 1% (v/v) P/S was homogeneously mixed at a 1:10 volume ratio with each hydrogel formulation to a final cell density of 4.5 × 10^6 cells/mL. The prepared bioink (i.e., hydrogel with embedded cells) was then loaded into a sterile printing cartridge. Bioprinting experiments were performed on an INKREDIBLE+ bioprinter (CELLINK AB, Gothenburg, Sweden). Printing parameters were manually optimized to achieve appropriate printing velocity and extrusion pressure according to the bioink's characteristics (i.e., viscosity, printability, and shape fidelity), as well as nozzle diameter for the intended construct geometry. In this regard, SISMA and SISMA-GO hydrogels achieved proper filament formation through a 25 G blunt needle nozzle at a constant pneumatic pressure of 10 kPa and 5 mm/s printing velocity. A 100 mm^2 squared construct with a 0.4 mm height was bioprinted with 10% infill density in a 6-well culture plate and was immediately crosslinked with 405 nm blue-light irradiation (62 mW/cm^2) for 1 min **(Figure S3)**. After photocrosslinking, 4 mL of cell medium were added to each well and the constructs were incubated for up to 7 days. The cell medium was refreshed every other day.

2.13. Cell viability, morphology and proliferation assessment

To assess the viability of hAD-MSCs embedded in SISMA and SISMA-GO constructs, nuclei and dead cell staining was performed with Hoechst 3342 and Propidium Iodide stains, respectively, at 2 h, 3 days, and 7 days after bioprinting. Accordingly, a working solution of the fluorophores was prepared at a 1:1000 ratio with 1× PBS each, and subsequently added to the culture medium at a 1:4 ratio. After 45 min, the medium was removed; the constructs were fixed with 4% (v/v) paraformaldehyde for 5 min and stored in PBS until microscopic observation. Confocal microscopy (Olympus FV1000, Tokyo, Japan) was used to visualize nuclei and dead cell locations with a 358 nm and 559 nm laser excitation, respectively. Emission channels were overlapped to identify live and dead cells, where live cells comprised locations with only nuclei being stained and dead cell locations with both nuclei and propidium iodide stained. Cell viability was assessed by stacking 25 images, captured from adjacent Z-planes separated by 2 μm each, and counting the live cells from the total

number of cells. Four different areas of each hydrogel were evaluated for statistical analysis.

Cell morphology changes were assessed in SISMA and SISMA-GO bioprinted constructs by staining F-actin filaments with AlexaFluor™ 488 Phalloidin and cell nuclei with Hoechst 3342 at day 0 and day 6. Briefly, tissues were fixed with 10% (v/v) formalin for 30 min and washed with 1× PBS 3 times to remove remnants of formalin. Cell membranes were then permeabilized with a 0.25% (w/v) solution of Triton-X in 1× PBS for 5 min and subsequently washed 3 times with 1× PBS. Finally, a working solution of AlexaFluor™ 488 Phalloidin and Hoechst 3342 was prepared at a 1:400 and 1:1000 ratios in 1× PBS, respectively, and then added to the constructs and incubated for 1 h. The stained constructs were washed 3 times with 1× PBS and immediately visualized with confocal microscopy using 488 nm and 358 nm laser excitations, respectively. Five images at a 20× magnification were captured and stacked from adjacent Z-planes, separated by 2 µm each, and emission channels were overlapped. Similarly, single-cell morphology was observed by capturing and stacking 45 images collected at 60× magnification.

Cell proliferation in SISMA and SISMA-GO constructs was also assayed by quantifying cell metabolic activity at days 0, 4, and 7 aided by a resazurin-based assay (TOX8). Reduced resazurin by viable cells emits red fluorescence and, therefore, the amount of dye conversion was fluorometrically measured. Accordingly, resazurin dye solution was added to the cell culture medium of each construct at a 10% (v/v) concentration and then incubated for 3 h. The medium was then removed and fluorescence intensity was quantified with a FluoroMax® fluorometer (Horiba, Kyoto, Japan) at 560 nm excitation. Fresh culture medium was added to the assayed constructs to continue incubation until the next measurement.

2.14. Characterization of GO reduced *in situ*

GO's *in situ* reduction was confirmed with Fourier Transform Infrared (FT-IR) spectroscopy and thermogravimetric analysis (TGA). Infrared spectra of graphite, GO, and rGO were recorded using an A250/D FT-IR (Bruker, Germany) within the range of 4000 – 400 cm^{-1} and spectral resolution of 2 cm^{-1}. The presence or absence of characteristic peaks of each material was analyzed to assess structural changes within these. TGA (TA Instruments) was also performed on these three materials from 30 to 800°C, with a temperature ramp of 10°C/min, to compare thermal stability differences that may arise from structural defects within these. Sample masses of 5 mg were used for this analysis. Reduction was further confirmed with Raman spectroscopy (0 – 3000 Raman shift [cm^{-1}]) of the bioprinted constructs after 3 days of incubation in DMEM culture medium supplemented with 0.5 mM ascorbic acid at 37°C. The treated constructs were lyophilized to avoid noise by water presence during data collection and point wise laser excitation of 532 nm was performed at different locations within the samples.

2.15. Electroconductivity of GO reduced *in situ*

Since GO was incorporated at a low concentration of 0.25 mg/mL, contacts between all GO sheets

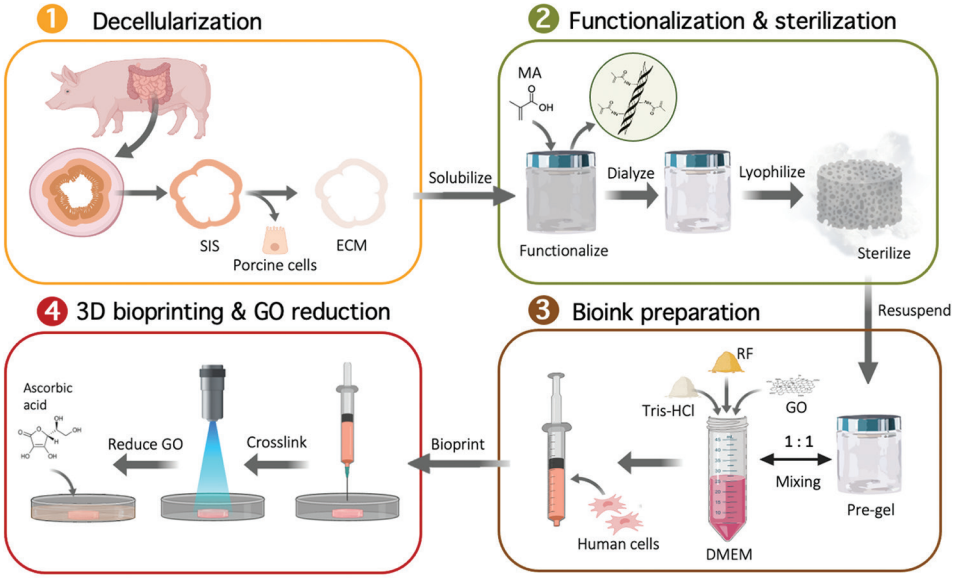


Figure 1. SISMA-graphene oxide (GO) composite bioink preparation and bioprinting schematic. The different steps in the preparation process are shown from small intestine submucosa dissection to bioprinting and tissue maturation with *in situ* reduction of GO (Created with BioRender.com).

are limited by their spatial distribution within the hydrogel. Therefore, considering that the hydrogel alone is not electroconductive, when a current is applied, it will only flow through interconnected networks at the microscale. However, such networks might not necessarily be all well connected. Since electric currents would be difficult to measure under the conditions of this scenario and present high variability, electroconductivity of the GO reduced *in situ* was measured by creating a densely packed rGO's squared sheet of 1 cm^2. For this, GO dispersed in DMEM culture medium supplemented with 0.5 mM ascorbic acid was incubated at 37°C for 3 days and subsequently centrifuged at 5000 rpm. The resulting pellet was lyophilized for 24 h and the obtained dry powder was resuspended in 96% (v/v) ethanol at a high concentration of 20 mg/mL to finally deposit it over a squared 1 cm^2 glass slide. To favor sheet formation by ethanol evaporation, the preparation was left overnight at room temperature. Then, variable currents (Keithley 2450 SourceMeter, SMU Instruments) were applied to the resulting sheet using the four-point probe method to measure the resulting voltage values. Resistance of the rGO sheet was calculated according to Ohm's law by fitting a linear regression of the measured values **(Figure S4)**. Conductivity was posteriorly calculated according to Equation 2.14.1.

$$C = \frac{L}{RA} \qquad (2.14.1)$$

where L is the thickness of the rGO sheet, A is the contact area of the sheet with the probes, and R is the previously calculated resistance of the sheet. This procedure was also performed for a GO sheet to estimate the possible effects of ascorbic acid and temperature treatment on the electroconductivity.

2.16. Statistical analysis

All experiments were performed in triplicate, unless otherwise stated and quantitative data are expressed as the mean ± standard deviation. Statistical analysis was performed with Student *t*-tests and $P < 0.05$ was considered as statistically significant.

3. Results and discussion

3.1. Preparation and functionalization of decellularized small intestine submucosa hydrogels

The SISMA-GO composite bioink was developed following the scheme shown in **Figure 1**. SIS was isolated from porcine intestines and subsequently decellularized with a sodium hypochlorite-based treatment (see section 2). Dry SIS powder was then solubilized with the aid of pepsin in an acidic solution to obtain a SIS pre-gel. Conjugation of carboxyl groups of MA to free amines present in the backbone of the ECM's proteins was later performed to confer photosensitive properties to the material in the presence of photoinitiator molecules. Considering that

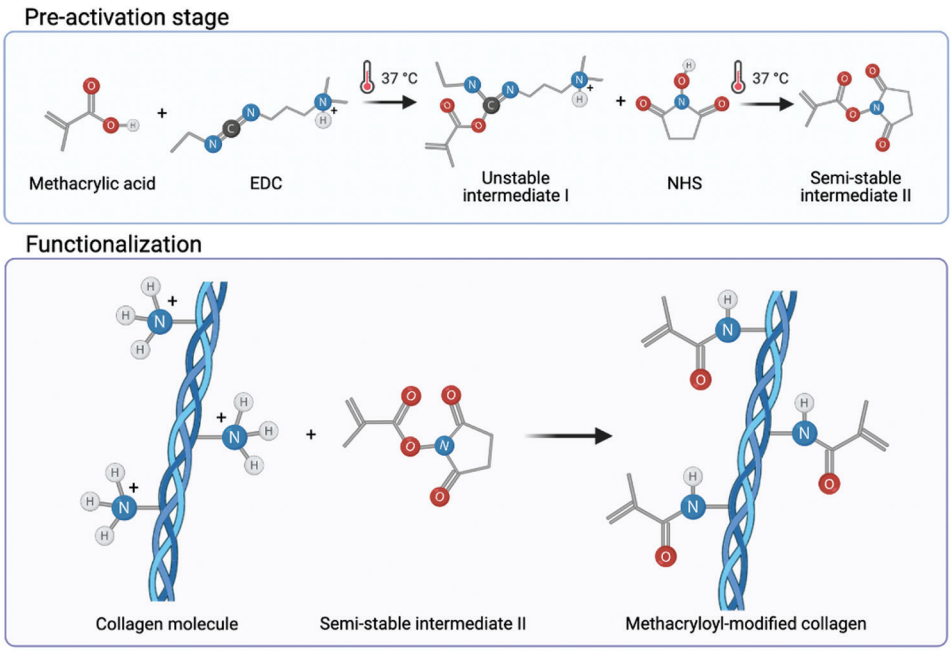


Figure 2. Proposed mechanism for the methacryloyl-modification of small intestinal submucosa collagen, as a general example of this modification on extracellular matrix proteins (Created with BioRender.com).

collagen is the main structural component of dECMs, the proposed mechanism for EDC/NHS mediated conjugation of MA to collagen backbones is shown in **Figure 2**, where EDC and NHS are zero-length crosslinkers that activate the nucleophilic reaction but are not included in the conjugation[48]. This is convenient since this biochemical modification involves no bulky elements that significantly modify the native dECM composition and, before cell embedding, the reaction by-products are eliminated with the aid of dialysis. ECM free amines were previously quantified with the TNBSA assay to determine the necessary reagent concentrations. An efficient biochemical conjugation reaction was demonstrated by an 81.5 ± 0.8% reduction in free-amine content after methacryloyl conjugation to SIS pre-gels (i.e., SISMA) **(Figure S5)**. This strongly suggests a high degree of functionalization when compared with previously reported values of other functionalization methods with MA[43,49,50], which ranged between 20% and 30%. Furthermore, it was comparable to other methods based on methacrylic anhydride, which reported values between 71% and 87%[13,51,52]. Dialyzed SISMA samples were then lyophilized and resolubilized to incorporate the GO nanosheets and the photoinitiator (i.e., RF). Moreover, a pH 8.5 DMEM solution supplemented with serum proteins and Tris-HCl buffer was added during the resuspension procedure to raise the pH of the hydrogel to 7 and to adjust the ionic balance for posterior cell incorporation.

3.2. GO synthesis and dispersion in SISMA hydrogels

GO nanosheets were successfully synthesized upon graphite exfoliation and oxidation procedures. However, the colloidal stability of GO in SISMA hydrogels was a special concern since previous studies have reported that GO forms aggregates in acidic media and biological buffers[53], two of the essential media for SISMA hydrogel preparation. The electrostatic repulsion between GO nanosheets has shown to be the main driving force for their colloidal stability[45], and this phenomenon is impaired at low pH due to the protonation of GO's carboxylic groups. Similarly, the sp^2-hybridized carbon backbone of GO has a high degree of surface planarity that facilitates electrostatic surface charging in the presence of electrolyte solutions, resulting in irreversible sheet aggregation[54]. Accordingly, we hypothesized that by coating GO surface with hydrophilic serum proteins from culture media, GO aggregation could be largely avoided. This would

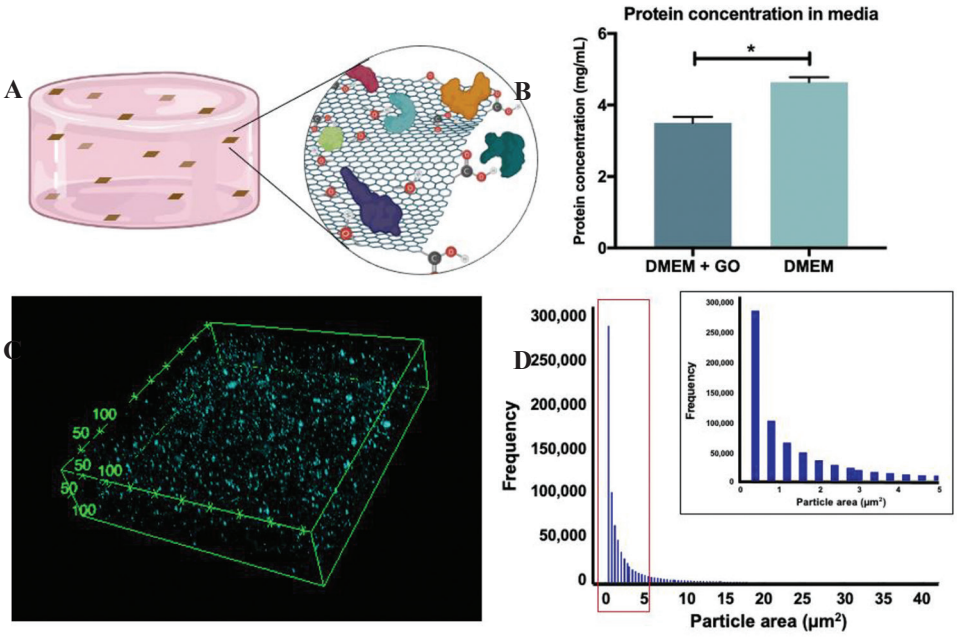


Figure 3. Graphene oxide (GO) protein adsorption and dispersion in composite hydrogels. (**A**) Schematic of hypothesized GO exfoliation in SISMA hydrogels as a result of exposure to serum proteins before dispersion (Created with BioRender.com). (**B**) Protein concentration in culture medium before and after the addition of GO. A statistically significant decrease is observed ($P < 0.05$, $n = 3$), which is attributed to serum protein adsorption on GO surface. (**C**) Confocal imaging of fluorescently labeled serum proteins adsorbed on GO shows a homogeneous dispersion within the hydrogel. Reference dimensions are in μm. (**D**) GO particle area distribution within the hydrogel seen as a right-tailed distribution centered at 0.386 μm^2.

lead to a superior exfoliation level within the hydrogel (**Figure 3A**). Protein adsorption on GO after exposure to culture media was confirmed by a 23.57 ± 3.51% decrease in medium protein concentration, as observed in **Figure 3B**. This corresponds to approximately 2.29 µg of serum proteins adsorbed per µg of GO. Nanocomposite exfoliation in SISMA hydrogels was then assessed by fluorescently labeling the serum proteins before its dispersion in SISMA. Confocal microscopy image reconstruction through z-stacking of the imaged GO-embedded hydrogels showed low aggregate formation and an overall homogeneous dispersion of GO nanosheets within the hydrogel (**Figure 3C**). Moreover, the particle area distribution within the hydrogel (**Figure 3D**) shows a right-tailed distribution centered at 0.386 μm^2 with a few out-of-distribution cases, indicating that low GO aggregation occurred. The high frequency at this specific area value may have been a result of the image resolution limits, which means that smaller GO sheets may exist within the hydrogel. This suggests that protein coating before dispersion may contribute to the adequate GO exfoliation levels observed in SISMA hydrogels. Our exfoliation strategy is advantageous with respect to previous methods as it does not require any alterations to GO's chemical structure with complex surface modification strategies[55-57]. We aimed at avoiding this functionalization approach because altering the surface groups of GO could hinder the reduction efficiency after bioprinting. Moreover, it avoids rough exfoliation methods, such as long periods of sonication[58,59], which can alter protein structure within bioactive hydrogels[60].

3.3. Characterization of SISMA-GO hydrogel crosslinking

The microscopic structural morphology of SISMA-GO composite hydrogels after thermal gelation and photo-crosslinking was evaluated through SEM imaging (**Figure 4A**). Fibrillar patterns resembling the hierarchical organization of collagen fibrils in native tissues were observed in thermally crosslinked hydrogels (yellow arrows). Self-assembling of collagen into fibers has been previously reported upon an increase in temperature, a process that is mediated by hydrogen bonding between collagen fibrils[61]. However, as shown in the magnified view (**Figure 4A**, right panel), the hydrogel is highly porous, a characteristic of weak crosslinking mechanisms[62]. On the contrary, fiber arrangement on photo-crosslinked hydrogels exhibits a much less porous structure (i.e., higher crosslinking degree), but is much more disorganized. This could be a result of the differences in crosslinking dynamics between both methods. In the presence of blue-light irradiation (405 nm), RF degrades and generates free radicals that destabilize the double bonds in methacryloyl moieties of the functionalized ECM and, as a consequence, induce covalent crosslinking between adjacent proteins[63]. Since at the moment of covalent bond formation collagen fibers were not aligned, SISMA hydrogels exhibited no observable hierarchical

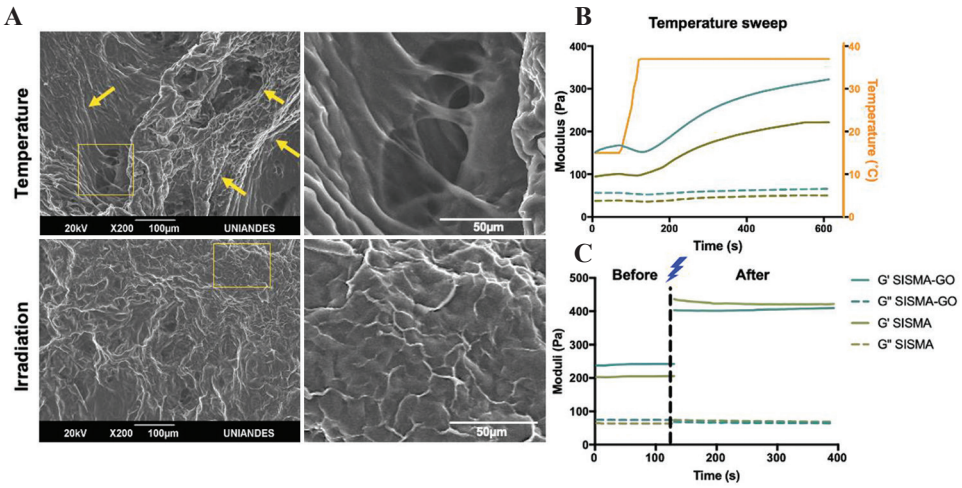


Figure 4. Thermal and photo-induced crosslinking of SISMA-graphene oxide (GO). **(A)** SEM images of composite hydrogels crosslinked with temperature and with blue-light irradiation. Thermal gelation showed alignment of collagen fibers but a highly porous structure, while photo-crosslinking showed a more disordered but less porous structure. **(B)** Temperature sweep experiments in SISMA-GO and SISMA hydrogels showed slow temperature-induced gelation profiles, as demonstrated by a similar increase in their storage moduli (G'). **(C)** Time sweeps before and after irradiation demonstrated a higher increase in G' than with the temperature stimulus, and negligible effect of GO on photocrosslinking.

structure even after incubation at 37˚C. This is probably because upon this thermal stimulus the formed covalent bonds have limited rotation for their 3D rearrangement.

Thermal- and photo-induced crosslinking of SISMA-GO hydrogels was further compared by evaluating their rheological behavior in the presence of both stimuli (**Figure 4B** and **C**). SISMA hydrogels were also assessed as a control to ensure that the presence of GO led to no detrimental impact on the crosslinking dynamics. Both crosslinking mechanisms effectively increased the storage moduli (G') in both hydrogels while the loss moduli (G'') remained unchanged. This confirms that both mechanisms increase the elastic response of the hydrogels and, consequently, their structural stability. Moreover, there is no crossover between G' and G'' curves during crosslinking, which indicates that the hydrogels exhibit a predominantly elastic behavior over time. This is particularly important in hydrogels intended for EBB, since it is crucial for assuring filament formation during extrusion, and for maintaining shape fidelity upon deposition[24]. However, while the temperature stimulus increased G' values of SISMA-GO to 300 Pa after 5 min, blue-light irradiation led to a value of about 400 Pa after 1 min, confirming that photo-stimulation yields faster and stronger crosslinking dynamics.

Moreover, since the formed covalent bonds during photo-stimulation are expected to produce more stable structures than the weak hydrogen bonds formed during thermal-stimulation, we evaluated both the soluble and gel fractions of thermally and photo-crosslinked SISMA-GO constructs as a function of mass loss over time, such that their stability can be estimated. After a 24-h incubation period, their gel fractions approached 69.32 ± 3.41% and 90.39 ± 1.92%, respectively **(Figure S6)**. These results suggest that photo-crosslinked SISMA-GO constructs exhibit a much slower degradation rate and are, therefore, more structurally stable over time. Likewise, swelling tests confirmed that, upon incubation, irradiated SISMA-GO constructs only swell up to 27.90 ± 4.88% of their initial weight, and this value remains unchanged after the first 8 h of incubation **(Figure S7)**. This confirms that the formed covalent bonds limit excessive hydrogel swelling and maintain stable hydrogel structures over time.

3.4. 3D bioprinting of cell-laden constructs

Before incorporating hAD-MSCs into the composite hydrogel, we conducted several tests to ensure it presented the required bioink behavior. Manual extrusion tests were carried out to select the adequate SISMA concentration that allowed a stable filament formation during the process (**Figure 5A**). Based on these results, a grid-like pattern was deposited with a 3D bioprinter to evaluate the shape fidelity of the concentration that granted the best filament formation (20 mg/mL). A defined construct outline with sharp edges was observed, which adequately maintained its shape during the bioprinting process and before photocrosslinking (**Figure 5B**, left panel). Similarly, an 8-layered cubic construct was successfully bioprinted (**Figure 5B**, right panel), which further demonstrates the suitability of our bioink for maintaining deposited patterns during the additive manufacturing of multilayered 3D constructs. Flow sweep experiments depicted in **Figure 5C** show that SISMA and SISMA-GO hydrogels presented the characteristic shear-thinning behavior of bioinks with superior printability, in which a decrease in viscosity occurs upon the application of a shearing force[64]. After fitting the data to a power law model **(Figure S8)**, the obtained *n* coefficients from Equation 2.9.1 were 0.208 and 0.223 for SISMA and SISMA-GO hydrogels, respectively, indicating a pseudoplastic behavior with strong shear-thinning (close to $n = 2$)[24]. This is important since high shear stress values predominate during the extrusion process and shear thinning fluids attenuate the perceived stress by cells by stress-relaxation mechanisms that ultimately help maintaining high cell viability[65]. Again, there was no observable difference between the shear-thinning behavior of SISMA-GO and SISMA hydrogels, meaning that GO shows no significant impact on the rheological response of the produced bioinks.

hAD-MSCs were embedded and bioprinted in SISMA-GO hydrogels to evaluate the biocompatibility of the materials and the suitability of the proposed bioprinting scheme. In addition, the proposed ascorbic acid-based scheme for *in situ* reduction was also performed on day 3 to assess whether any change was observable on construct viability. Cell viability was assessed with nuclei (blue) and dead cell (red) staining, where nuclei signal alone marked live cells and dual staining (seen as magenta) marked dead cells **(Figure S9)**. Since propidium iodide has been reported to interact with GO sheets[66], spots with only red staining were disregarded as they correspond to GO-PI complexes. The bioprinted constructs exhibit high cell viability at all measured time points, with a slight decrease on day 3 but a prompt recovery by day 7 (**Figure 6D**). This small drop may be attributed to unreacted by-products from the photocrosslinking reaction, since excess free radicals may induce the formation of reactive oxygen species, which have shown to induce DNA damage and compromise cell viability[67]. The ascorbic acid supplementation on day 3 may have also contributed to the observed drop. Despite this, a timely recovery was observed and high cell viability (96.9 ± 0.9%) was achieved 1 week after bioprinting, confirming that neither GO incorporation nor the proposed reduction scheme compromises cellular survival. In addition, embedded hAD-MSCs in both SISMA and SISMA-GO constructs transitioned from rounded to elongated morphology after 6 days of incubation (**Figure 5E**), which suggests

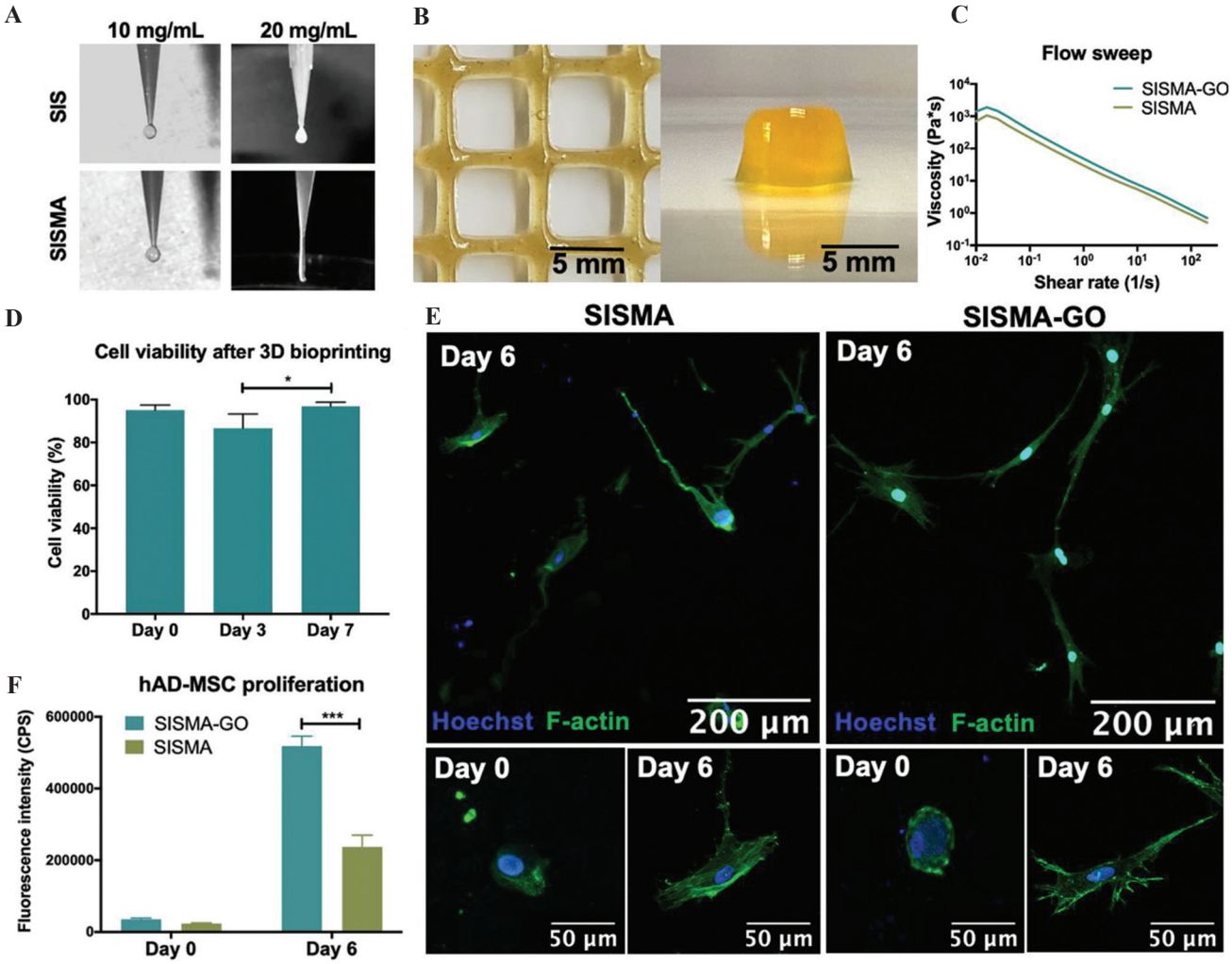


Figure 5. SISMA-graphene oxide (GO) bioprinting. Adequate filament formation during extrusion aided by a 3D bioprinter (**A**) and shape fidelity upon deposition (**B**) was observed for SISMA-GO composite hydrogels, highlighting their suitability for bioprinting applications. (**C**) Flow sweep experiments of SISMA-GO and SISMA hydrogels depict an appropriate shear-thinning behavior, with no observable difference in the presence of GO. (**D**) Cell viability of human adipose tissue-derived mesenchymal stem cells (hAD-MSC) 2 h, 3 days, and 7 days after bioprinting indicates high biocompatibility with SISMA-GO hydrogels ($n = 4$). (**E**) Confocal microscopy images of hAD-MSCs embedded in bioprinted SISMA and SISMA-GO constructs with stained nuclei in blue and stained F-actin filaments in green. Elongated morphologies are observed after 6 days of incubation, indicating the presence of cell-matrix interactions that mediate cell adhesion and spreading. (**F**) hAD-MSC proliferation in SISMA and SISMA-GO constructs, as measured by resazurin reduction as a consequence of metabolic activity.

the formation of cell-matrix interactions that mediate cell adhesion (i.e., cell-matrix adhesion complexes)[68]. Moreover, as observed in the magnified images of day 6 (**Figure 5**, bottom panel), hAD-MSCs in SISMA-GO constructs exhibit a greater amount of filopodia than in SISMA constructs, indicating that the presence of GO likely aids in cell adhesion. Notably, GO nanosheets also favored hAD-MSCs proliferation, as evidenced by the increased proliferation rate when compared to SISMA constructs (**Figure 5F**). This is consistent with the previous reports where proteins adsorbed on GO surfaces have been shown to favor integrin-based cell adhesion by providing anchoring sites that facilitate cell migration, proliferation and function[69].

3.5. Improved electroconductivity of GO reduced *in situ*

Several GO reduction methods have been reported that yield high reduction efficiencies, usually by employing high temperatures and by adding strong acids or bases at high concentrations[70]. However, these methods are not compatible with our biofabrication scheme due to their high cytotoxicity, especially considering that we need an *in situ* reduction of GO to harness its bioactive effects during the initial maturation stages of the bioprinted constructs. As a result, we propose an alternative reduction scheme based on ascorbic acid exposure and incubation at 37°C, to maintain high levels of electroconductivity without detrimentally affecting cell viability. Ascorbic acid concentration was selected according to previously reported values that are non-cytotoxic for mesenchymal stem cells[71]. GO reduction was evaluated after 3 days of exposure to ascorbic acid to subsequently assess the electroconductive potential of the bioinks. As observed in **Figure 6A**, after 3 days of incubation, the construct displays a much darker color (characteristic of rGO) in comparison to the color immediately after printing. The reduced weight loss profile of rGO when compared to GO (~20% difference) observed with TGA experiments (**Figure 6B**) suggests that the improved thermal stability may be a result of a decrease in GO's surface functional groups with our method. Similarly, FT-IR spectroscopy analysis of GO and rGO sheets (**Figure 6C**) showed that carboxyl (1721 cm^{-1}) and hydroxyl (1364 cm^{-1}) peaks in rGO were strongly diminished, but epoxy peaks (1215 and 1051 cm^{-1}) were conserved[72], suggesting a partial reduction was achieved. Moreover, Raman spectra of graphite, GO and rGO (**Figure 6B**) display the characteristic G and D peaks, where G represents the degree of sp^2 hybridization and D represents structural disorder (increases with surface modification)[73]. When comparing GO to graphite spectra, a clear increase in the D peak intensity is observed, which indicates disruptions in the sp^2-hybridized structure as a result of the presence of superficial carboxyl and hydroxyl groups. This, in turn, is an indicator of correct oxidation of the carbon structure, especially because the structural

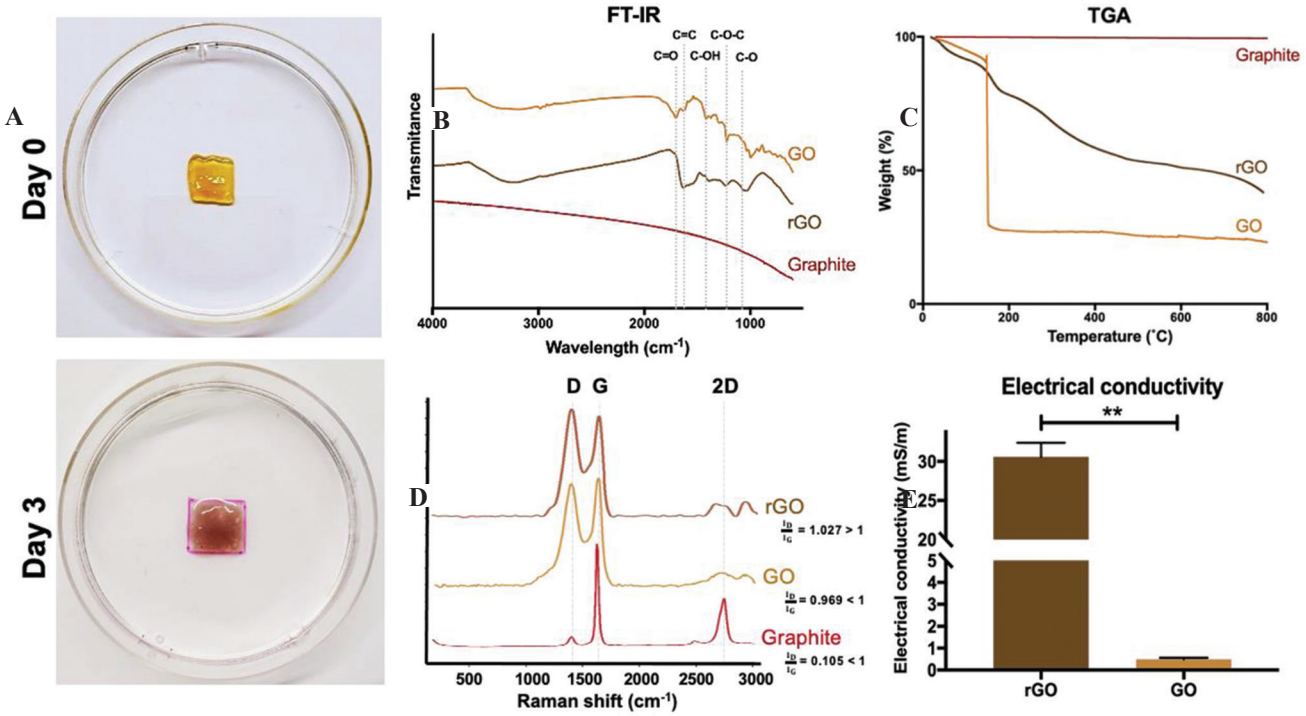


Figure 6. *In situ* reduction of graphene oxide (GO). (**A**) SISMA-GO constructs before and after 3-days incubation with ascorbic acid show hydrogel darkening attributed to GO reduction. (**B**) FTIR analysis confirms the elimination of carboxyl and hydroxyl peaks upon ascorbic acid incubation, and a (**C**) decreased thermal degradation rate is observed with thermogravimetric analysis. (**D**) Raman spectra of graphite, GO and GO after incubation in ascorbic acid (reduced GO [rGO]) present an increase in D peak intensity (I_D) with surface modifications and it surpasses G peak intensity (I_G) after ascorbic acid-based reduction. I_D/I_G ratios are indicative of structural disorder. (**E**) Improved electrical conductivity of rGO sheets with respect to GO, as measured with the four-point probe method.

disorder ratio (I_D/I_G) is <1, which is typical of oxidized graphene[73]. The observed D peak intensity in the rGO spectrum surpasses that of the G peak, which indicates that incubation with ascorbic acid increased structural disorder. This structural disorder ratio above 1 has been reported for rGO because previously oxidized structures fail to recover the original carbon backbone of graphene[74]. Moreover, the process permanently destroys some functional groups, thereby affecting the carbon backbone even further[74].

To further characterize GO's reduction, the conductivity of GO before and after incubation with ascorbic acid was assessed with the four-point probe method. As shown in **Figure 6C**, ascorbic acid-based reduction significantly increased the electroconductivity of GO sheets by nearly two orders of magnitude (i.e., from 0.49±0.04 mS/m to 30.59±1.27 mS/m). We decided to measure electroconductivity on the rGO sheets directly, instead of the composite hydrogel, to isolate the effect of the reduction from that of electrolytes in the culture medium and avoid measurement variabilities due to the localized electrical percolation networks[75]. This is a promising result for the intended electrostimulation applications since increased electroconductivity within the sheets may help direct electrical currents through the bioink. However, despite the large increase in conductivity with respect to GO, rGO sheets still exhibit a lower conductivity than those reported for rGO by other reduction methods[76-78]. This was an expected result due to the mild temperature and acid concentration used during the process to maintain viability unaffected. Nonetheless, considering electrostimulation studies have been performed in hydrogels without conductive materials due to the conductivity of cell culture medium (1,700 mS/m[79]) and that of cell surfaces (10^{-2} – 10^{-5} mS/m[80,81]), the presence of rGO sheets could enhance previous efficiencies by aiding the electrical connectivity and directing currents within the hydrogel. This is specifically advantageous if currents are applied during early maturation stages, since cells are yet to form interconnected networks themselves.

4. Conclusions

Tailoring the mechanical and biological properties of biomaterials for the biofabrication of tissues with specific maturation profiles has been an ongoing research focus for their translation to medical scenarios. The herein developed photocrosslinkable nanocomposite bioink showed great promise for 3D bioprinting applications, considering that it can be directly printed with little composition modifications and without the need of other excipient materials. The limited modification to the overall ECM composition enabled by methacryloyl modification maximizes its bioactive and biomimetic advantages, while also enhancing its mechanical properties upon the formation of stable interconnected crosslinked networks. This integrates two of the most important aspects for recapitulating the environment of native tissues and, in turn, for bioink formulation. In addition, GO incorporation followed by its *in situ* reduction harnessed the bioactivity and hydrophilicity of GO to improve its colloidal stability within the bioink, and once it was stably dispersed, improved its electroconductive properties by two orders of magnitude. As such, its bioactive, mechanically stable, and electroconductive properties are a clear advantage above previous bioink formulations.

The enhanced electrical conductivity of rGO sheets increases the potential of SISMA-GO for the biofabrication of tissues that require electrostimulation while avoiding current limitations of electroconductive hydrogels, such as cytotoxicity and poor dispersibility[82]. As such, it could contribute significantly to the development of electrosensitive tissues (e.g., skeletal muscle, cardiac muscle, and neural tissue), directing differentiation profiles (e.g., chondrogenesis[83], and osteogenesis[84]), and tissue regeneration[85]. Future work will be focused on optimizing the *in situ* reduction procedure to further improve the observed electroconductivity, and assessing its direct contribution to different electro stimulation applications. This work paves the way for exploiting the potential of SISMA-GO within the field of electrosensitive tissue engineering and regenerative medicine.

Author contributions

L.R. and J.A.S. performed most of the experiments and J.C performed experiments related to nanomaterial characterization. L.R. analyzed the data and wrote the manuscript with contributions from J.A.S., review and editing, L.R., J.C.C., and C.M.-C.; supervision, J.C.C. and C.M.-C.; project administration, J.C.C. and C.M.-C.; funding acquisition, J:C:C ans C.M.-C.

Funding sources

This work was funded by the Department of Biomedical Engineering and by the Vice-Chancellor for Research and Creation at Universidad de los Andes. Publishing expenses was funded by Convocatoria CI-001 Publica tus conocimientos o expone tus nuevas creaciones by the Vice-Chancellor for Research and Creation at Universidad de los Andes.

Conflict of interest

The authors declare no conflicts of interest.

References

1. Kim B, Das S, Jang J, *et al*., 2020, Decellularized Extracellular Matrix-based Bioinks for Engineering Tissue and Organ-specific Microenvironments. *Chem Rev*, 120:10608–61.

2. Ng W, Chua C, Shen Y, 2019, Print Me An Organ! Why We Are Not There Yet, *Prog Polym Sci*, 97:101145.
3. Frantz C, Stewart KM, Weaver VM, 2010, The Extracellular Matrix at a Glance, *J Cell Sci*, 123:4195–200.
4. Schaefer L, Schaefer RM, 2009, Proteoglycans: From Structural Compounds to Signaling Molecules, *Cell Tissue Res*, 339:237–46.
5. Kim BS, Kim H, Gao G, *et al*., 2017, Decellularized Extracellular Matrix: A Step Towards the Next Generation Source for Bioink Manufacturing. *Biofabrication*, 9:034104.
6. Kohane DS, Langer R, 2008, Polymeric Biomaterials in Tissue Engineering. *Pediatr Res*, 63:487–91.
7. Badylak SF, 2002, The Extracellular Matrix as a Scaffold for Tissue Reconstruction. *Semin Cell Dev Biol*, 13:377–83.
8. Saldin LT, Cramer MC, Velankar SS, *et al*, 2017, Extracellular Matrix Hydrogels from Decellularized Tissues: Structure and Function. *Acta Biomater*, 49:1–15.
9. Pouliot RA, Young BM, Link PA, *et al.* Porcine Lung-Derived Extracellular Matrix Hydrogel Properties Are Dependent on Pepsin Digestion Time. *Tissue Eng C Methods*, 26:332–46.
10. Yang C, 2012, Enhanced physicochemical properties of collagen by using EDC/NHS-crosslinking. *Bull Mater Sci*, 35:913–8.
11. Curley CJ, Dolan EB, Otten M, *et al*., 2018, An Injectable Alginate/Extra Cellular Matrix (ECM) Hydrogel Towards Acellular Treatment of Heart Failure. *Drug Deliv Transl Res*, 9:1–13.
12. Choi B, Kim S, Lin B, *et al*., 2014, Cartilaginous Extracellular Matrix-Modified Chitosan Hydrogels for Cartilage Tissue Engineering. *ACS Appl Mater Interfaces*, 6:20110–21.
13. Ali M, Kumar A Pr, Yoo JJ, *et al*., 2019, A Photo-Crosslinkable Kidney ECM-Derived Bioink Accelerates Renal Tissue Formation. *Adv Healthc Mater*, 8:1800992.
14. Sionkowska A, Skopinska-Wisniewska J, Gawron M, *et al*., 2010, Chemical and Thermal Cross-linking of Collagen and Elastin Hydrolysates. *Int J Biol Macromol*, 47:570–7.
15. Davidenko N, Schuster CF, Bax DV, *et al.*, 2015, Control of Crosslinking for Tailoring Collagen-based Scaffolds Stability and Mechanics. *Acta Biomater*, 25:131–42.
16. Reddy N, Reddy R, Jiang Q, 2015, Crosslinking Biopolymers for Biomedical Applications. *Trends Biotechnol*, 33:362–9.
17. O'Connell CD, Zhang B, Onofrillo C, *et al.*, 2018, Tailoring the mechanical properties of gelatin methacryloyl hydrogels through manipulation of the photocrosslinking conditions. *Soft Matter*, 14:2142–51.
18. Ashwin S, Reed G, Michael M, 2016, Myelinated 3D Neural Culture Platform as a Physiological Model of Diabetic Peripheral Neuropathy. *Front Bioeng Biotechnol*, 4:02188.
19. Williams CG, Malik AN, Kim TK, *et al*., 2005, Variable Cytocompatibility of Six Cell Lines with Photoinitiators Used for Polymerizing Hydrogels and Cell Encapsulation. *Biomaterials*, 26:1211–8.
20. Diamantides N, Wang L, Pruiksma T, *et al.*, 2017, Correlating Rheological Properties and Printability of Collagen Bioinks: The Effects of Riboflavin Photocrosslinking and pH. *Biofabrication*, 9:034102.
21. Parthiban SP, Athirasala A, Tahayeri A, *et al*., 2020, BoneMA Synthesis and Characterization of a Methacrylated Bone-derived Hydrogel for Bioprinting of Vascularized Tissues. *BioRxiv*, 2020:974063.
22. Kim SH, Yeon YK, Lee JM, *et al.*, 2018, Precisely Printable and Biocompatible Silk Fibroin Bioink for Digital Light Processing 3D Printing. *Nat Commun*, 9:1620.
23. Poldervaart MT, Goversen B, de Ruijter M, *et al.*, 2017, 3D Bioprinting of Methacrylated Hyaluronic Acid (MeHA) Hydrogel with Intrinsic Osteogenicity. *PLoS One*, 12:e0177628.
24. Paxton N, Smolan W, Böck T, *et al*., 2017, Proposal to Assess Printability of Bioinks for Extrusion-based Bioprinting and Evaluation of Rheological Properties Governing Bioprintability. *Biofabrication*, 9:044107.
25. Li J, Chen M, Fan X, *et al*, 2016, Recent Advances in Bioprinting Techniques: Approaches, Applications and Future Prospects. *J Transl Med*, 14:271.
26. Derakhshanfar S, Mbeleck R, Xu K, *et al*., 2018, 3D Bioprinting for Biomedical Devices and Tissue Engineering: A Review of Recent Trends and Advances. *Bioact Mater*, 3:144–56.
27. Agarwala S, 2020, Electrically Conducting Hydrogels for Health care: Concept Fabrication Methods, and Applications. *Int J Bioprint*, 6:273.
28. Thakral G, LaFontaine J, Najafi B, *et al*., 2013, Electrical Stimulation to Accelerate Wound Healing. *Diabetic Foot Ankle*, 4:22081.
29. Ashrafi M, Alonso-Rasgado T, Baguneid M, *et al*., 2017, The Efficacy of Electrical Stimulation in Lower Extremity Cutaneous Wound Healing: A Systematic Review. *Exp Dermatol*, 26:171–8.
30. Meng S, Rouabhia M, Zhang Z, 2012, Electrical Stimulation Modulates Osteoblast Proliferation and Bone Protein Production through Heparin-Bioactivated Conductive Scaffolds. *Bioelectromagnetics*, 34:189–99.
31. Leppik L, Zhihua H, Mobini S, *et al*., 2018, Combining Electrical Stimulation and Tissue Engineering to Treat Large

Bone Defects in a Rat Model. *Sci Rep*, 8:6307.

32. Chen C, Bai X, Ding Y, *et al*., 2019, Electrical Stimulation as a Novel Tool for Regulating Cell Behavior in Tissue Engineering. *Biomater Res*, 23:25.
33. Fu C, Pan S, Ma Y, *et al*., 2019, Effect of Electrical Stimulation Combined with Graphene-oxide-based Membranes on Neural Stem Cell Proliferation and Differentiation. *Artif Cells Nanomed Biotechnol*, 47:1867–76.
34. Kwon HJ, Lee GS, Chun H, 2016, Electrical Stimulation Drives Chondrogenesis of Mesenchymal Stem Cells in the Absence of Exogenous Growth Factors. *Sci Rep*, 6:39302.
35. Sadeghian RB, Ebrahimi M, Salehi S, 2017, Electrical Stimulation of Microengineered Skeletal Muscle Tissue: Effect of Stimulus Parameters on Myotube Contractility and Maturation. *J Tissue Eng Regen Med*, 12:912–22.
36. Hirt MN, Boeddinghaus J, Mitchell A, *et al.*, 2014, Functional Improvement and Maturation of Rat and Human Engineered Heart Tissue by Chronic Electrical Stimulation. *J Mol Cell Cardiol*, 74:151–61.
37. Ashtari K, Nazari H, Ko H, *et al.*, 2019, Electrically Conductive Nanomaterials for Cardiac Tissue Engineering. *Adv Drug Deliv Rev*, 144:162–79.
38. Javadi M, Gu Q, Naficy S, *et al.*, 2017, Conductive Tough Hydrogel for Bioapplications. *Macromol Biosci*, 18:1700270.
39. Zhou X, Cui H, Zhang LG, *et al.*, 2017, 3D Bioprinted Graphene Oxide-incorporated Matrix for Promoting Chondrogenic Differentiation of Human Bone Marrow Mesenchymal Stem Cells. *Carbon*, 116:615–24.
40. Ku SH, Park CB, 2013, Myoblast Differentiation on Graphene Oxide. *Biomaterials*, 34:2017–23.
41. Liu Y, Zhang B, Xu Q, *et al.*, 2018, Development of Graphene Oxide/Polyaniline Inks for High Performance Flexible Microsupercapacitors via Extrusion Printing. *Adv Funct Mater*, 28:1706592.
42. Sánchez-Palencia DM, D'Amore A, González-Mancera A, *et al*., 2014, Effects of Fabrication on the Mechanics Microstructure and Micromechanical Environment of Small Intestinal Submucosa Scaffolds for Vascular Tissue Engineering. *J Biomech*, 47:2766–73.
43. Marcano DC, Kosynkin DV, Berlin JM, *et al.*, 2010, Improved Synthesis of Graphene Oxide. *ACS Nano*, 4:4806–14.
44. Gaudet ID, Shreiber DI, 2012, Characterization of Methacrylated Type-I Collagen as a Dynamic Photoactive Hydrogel. *Biointerphases*, 7:25.
45. Shih CJ, Lin S, Sharma R, *et al*., 2011, Understanding the pH-Dependent Behavior of Graphene Oxide Aqueous Solutions: A Comparative Experimental and Molecular Dynamics Simulation Study. *Langmuir*, 28:235–41.
46. Capella-Monsonís H, Coentro JQ, Graceffa V, *et al*., 2018, An Experimental Toolbox for Characterization of Mammalian Collagen Type I in Biological Specimens. *Nat Protoc*, 13:507–29.
47. Linero I, Chaparro O, 2014, Paracrine Effect of Mesenchymal Stem Cells Derived from Human Adipose Tissue in Bone Regeneration. *PLoS One*, 9:e107001.
48. Hermanson GT, 2013, Zero-Length Crosslinkers. In: Bioconjugate Techniques, Elsevier, Amsterdam, Netherlands, p259–73.
49. Lim KS, Schon BS, Mekhileri NV, *et al.*, 2016, New Visible-Light Photoinitiating System for Improved Print Fidelity in Gelatin-Based Bioinks. *ACS Biomater Sci Eng*, 2:1752–62.
50. Yoon HJ, Shin SR, Cha JM, *et al.*, 2016, Cold Water Fish Gelatin Methacryloyl Hydrogel for Tissue Engineering Application. *PLoS One*, 11:e0163902.
51. Drzewiecki KE, Parmar AS, Gaudet ID, *et al.*, 2014, Methacrylation Induces Rapid Temperature-Dependent, Reversible Self-Assembly of Type-I Collagen. *Langmuir*, 30:11204–11.
52. Ravichandran R, Islam MM, Alarcon EI, *et al.*, 2016, Functionalised Type-I Collagen as a Hydrogel Building Block for Bio-orthogonal Tissue Engineering Applications. *J Mater Chem B*, 4:318–26.
53. Tang H, Zhang S, Huang T, *et al*., 2020, Effects of pH and Electrolytes on the Sheet-to-Sheet Aggregation Mode of Graphene Oxide in Aqueous Solutions. *Environ Sci Nano*, 7:984–95.
54. Hong BJ, Compton OC, An Z, *et al*., 2011, Successful Stabilization of Graphene Oxide in Electrolyte Solutions: Enhancement of Biofunctionalization and Cellular Uptake. *ACS Nano*, 6:63–73.
55. Cha C, Shin SR, Gao X, *et al.*, 2013, Controlling Mechanical Properties of Cell-Laden Hydrogels by Covalent Incorporation of Graphene Oxide. *Small*, 10:514–23.
56. Huang CT, Shrestha LK, Ariga K, *et al*., 2017, A Graphenepolyurethane Composite Hydrogel as a Potential Bioink for 3D Bioprinting and Differentiation of Neural Stem Cells. *J Mater Chem B*, 5:8854–64.
57. Li Z, Shen J, Ma H, *et al.*, 2012, Preparation and Characterization of pH and Temperature-Responsive Hydrogels with Surface-functionalized Graphene Oxide as the Crosslinker. *Soft Matter*, 8:3139.
58. Sayyar S, Murray E, Thompson BC, *et al.*, 2015, Processable conducting graphene/chitosan hydrogels for tissue engineering. *J Mater Chem B*, 3:481–90.

59. Liu S, Mou S, Zhou C, *et al.*, 2018, Off-the-Shelf Biomimetic Graphene OxideCollagen Hybrid Scaffolds Wrapped with Osteoinductive Extracellular Matrix for the Repair of Cranial Defects in Rats. *ACS Appl Mater Interfaces*, 10: 42948–58.
60. Rahman MM, Byanju B, Grewell D, *et al*., 2020, High-power Sonication of Soy Proteins: Hydroxyl Radicals and their Effects on Protein Structure. *Ultrason Sonochem*, 64:105019.
61. Fratzl P, 2008, Collagen: Structure and mechanics an introduction. In: Collagen. Springer, United States, p1–13.
62. Mane NC, Ponrathnam S, 2016, Effect of Chemical Crosslinking on Properties of Polymer Microbeads: A Review. *Can Chem Trans*, 3:473–85.
63. Huang R, Choe E, Min DB, 2006, Kinetics for Singlet Oxygen Formation by Riboflavin Photosensitization and the Reaction between Riboflavin and Singlet Oxygen. *J Food Sci*, 69:C726–32.
64. Jiang T, Munguia-Lopez JG, Flores-Torres S, *et al*., 2019, Extrusion Bioprinting of Soft Materials: An Emerging Technique for Biological Model Fabrication. *Appl Phys Rev*, 6:011310.
65. Wilson SA, Cross LM, Peak CW, *et al*., 2017, Shear-Thinning and Thermo-Reversible Nanoengineered Inks for 3D Bioprinting. *ACS Appl Mater Interfaces*, 9:43449–58.
66. Liu F, Gao Y, Li H, *et al*., 2014, Interaction of Propidium Iodide with Graphene Oxide and its Application for Live Cell Staining. *Carbon*, 71: 190–5.
67. Mironi-Harpaz I, Wang DY, Venkatraman S, *et al*., 2012, Photopolymerization of Cell-encapsulating Hydrogels: Crosslinking Efficiency Versus Cytotoxicity. *Acta Biomater*, 8:1838–48.
68. Lock JG, Wehrle-Haller B, Strömblad S, 2008, Cell-Matrix Adhesion Complexes: Master Control Machinery of Cell Migration. *Semin Cancer Biol*, 18:65–76.
69. Kumar S, Parekh SH, 2020, Linking Graphene-based Material Physicochemical Properties with Molecular Adsorption Structure and Cell Fate. *Commun Chem*, 3:8.
70. Singh RK, Kumar R, Singh DP, 2016, Graphene Oxide: Strategies for Synthesis Reduction and Frontier Applications. *RSC Adv*, 6:64993–5011.
71. Choi KM, Seo YK, Yoon HH, *et al.*, 2008, Effect of Ascorbic Acid on Bone Marrow-derived Mesenchymal Stem Cell Proliferation and Differentiation. *J Biosci Bioeng*, 105:586–94.
72. Khalili D, 2016, Graphene Oxide: A Promising Carbocatalyst for the Regioselective Thiocyanation of Aromatic Amines Phenols, Anisols and Enolizable Ketones by Hydrogen Peroxide/KSCN in Water. *New J Chem*, 40:2547–53.
73. Wu JB, Lin ML, Cong X, *et al*., 2018, Raman Spectroscopy of Graphene-Based Materials and its Applications in Related Devices. *Chem Soc Rev*, 47:1822–73.
74. Muzyka R, Drewniak S, Pustelny T, *et al*., 2018, Characterization of Graphite Oxide and Reduced Graphene Oxide Obtained from Different Graphite Precursors and Oxidized by Different Methods Using Raman Spectroscopy. *Materials*, 11:1050.
75. Marsden AJ, Papageorgiou DG, Vallés C, *et al.*, 2018, Electrical Percolation in Graphene-polymer Composites. *2D Materials*, 5:032003.
76. Rao S, Upadhyay J, Polychronopoulou K, *et al*., 2018, Reduced Graphene Oxide: Effect of Reduction on Electrical Conductivity. *J Compos Sci*, 2:25.
77. Mohan VB, Brown R, Jayaraman K, *et al*., 2015, Characterisation of Reduced Graphene Oxide: Effects of Reduction Variables on Electrical Conductivity. *Mater Sci Eng B*, 193:49–60.
78. Kim M, Lee C, Jang J, 2013, Fabrication of Highly Flexible Scalable, and High-Performance Supercapacitors Using Polyaniline/Reduced Graphene Oxide Film with Enhanced Electrical Conductivity and Crystallinity. *Adv Funct Mater*, 24:2489–99.
79. Lang Q, Wu Y, Ren Y, *et al*., 2015, AC Electrothermal Circulatory Pumping Chip for Cell Culture. *ACS Appl Mater Interfaces*, 7:26792–801.
80. Adams TN, Turner PA, Janorkar AV, *et al*., 2014, Characterizing the Dielectric Properties of Human Mesenchymal Stem Cells and the Effects of Charged Elastin-Like Polypeptide Copolymer Treatment. *Biomicrofluidics*, 8: 054109.
81. Cho S, Thielecke H, 2008, Electrical Characterization of Human Mesenchymal Stem Cell Growth on Microelectrode. *Microelectron Eng*, 85:1272–4.
82. Walker BW, Lara RP, Mogadam E, *et al*., 2019, Rational Design of Microfabricated Electroconductive Hydrogels for Biomedical Applications. *Prog Polym Sci*, 92:135–57.
83. Barlian A, Judawisastra H, Alfarafisa NM, *et al*, 2018, Chondrogenic Differentiation of Adipose-derived Mesenchymal Stem Cells Induced by L-Ascorbic Acid and Platelet Rich Plasma on Silk Fibroin Scaffold. *PeerJ*, 6:e5809.
84. Kumar A, Nune KC, Misra RD, 2016, Understanding the Response of Pulsed Electric Field on Osteoblast Functions in Three-dimensional Mesh Structures. *J Biomater Appl*, 31:594–605.
85. Ross CL, 2016, The Use of Electric Magnetic, and Electromagnetic Field for Directed Cell Migration and Adhesion in Regenerative Medicine. *Biotechnol Prog*, 33:5–16.

RESEARCH ARTICLE

A Dual-sensitive Hydrogel Based on Poly(Lactide-co-Glycolide)-Polyethylene Glycol-Poly(Lactide-co-Glycolide) Block Copolymers for 3D Printing

Yang Zhou[1], Yuecheng Cui[1], Li-Qun Wang[1,2]*

[1]MOE Key Laboratory of Macromolecular Synthesis and Functionalization, Department of Polymer Science and Engineering, Zhejiang University, Hangzhou 310027, P. R. China
[2]Hangzhou Medsun Biological Technology Co., Ltd, Hangzhou Economic and Technological Development Area, Hangzhou 310027, P. R. China

Abstract: The thermo-sensitive hydrogel formed by triblock copolymers of polyethylene glycols and aliphatic polyesters serves as a promising candidate for bioink due to its excellent biodegradability and biocompatibility. However, the thermo-crosslinking alone cannot achieve a robust hydrogel to support the 3D printed constructs without collapse. Herein, a photo-crosslinkable group was introduced into the triblock copolymers to achieve a dual-sensitive hydrogel. A triblock copolymer poly(lactide-co-glycolide)-polyethylene glycol-poly(lactide-co-glycolide) decorated with acrylate group in the chain end was prepared. The obtained aqueous solutions of the copolymers could transform into hydrogels with excellent shear thinning properties and rapid elastic recovery properties spontaneously on the increase of temperature. The resulted thermogels also allowed for photo-crosslinking by exposure to ultraviolet radiation, with storage modulus dramatically increased to stable the printed constructs. Through a two-step crosslinking strategy, complicated tissue-like constructs with high shape fidelity can be printed using the dual-sensitive inks. Moreover, the mechanical strength, swelling ratio, and printability of the hydrogels can be tuned by varying the substitution rate of the acrylate group without compromising the inks' extrudability. We expect that the dual-sensitive hydrogels may be used as bioinks to print large constructs for applications in tissue engineering.

Keywords: 3D bioprinting; Dual-sensitive hydrogels; Poly(lactide-co-glycolide)-polyethylene glycol-poly(lactide-co-glycolide); Injectable hydrogels

*Correspondence to: Li-Qun Wang, Department of Polymer Science and Engineering, Zhejiang University, Hangzhou 310027, P. R. China; lqwang@zju.edu.cn

Received: April 29, 2021; **Accepted:** June 22, 2021; **Published online**: June 29, 2021

Citation: Zhou Y, Cui YC, Wang LQ, 2021, A Dual-sensitive Hydrogel Based on Poly(Lactide-Co-Glycolide)-Polyethylene Glycol-Poly(Lactide-Co-Glycolide) Block Copolymers for 3D Printing. *Int J Bioprint*, 7(3):389. http://doi.org/10.18063/ijb.v7i3.389

1. Introduction

Three-dimensional (3D) bioprinting is an emerging technology in the field of tissue engineering. The ability to rapidly create complicated biomimetic structures with high accuracy through layer-by-layer deposition make it a promising tool for patient-specific treatments[1-3]. Among several printing strategies, inkjet printing and laser-assisting bioprinting have high print resolutions but can only deal with nonviscous liquid[4,5]; stereolithography (STL) is fast but needs lots of ink to form a vat[6]; extrusion printing is the most widely used due to its easy implementation and ability to print large constructs[4,7]. Various biomaterials including synthetic and natural polymers have been reported as printing hydrogels, such as poly(ethylene glycol) (PEG)[3,8], collagen[9], gelatin[10], sodium alginate[11], silk fibroin[12-14], hyaluronic acid[15-17], and decellularized extracellular matrix[18]. Nevertheless, the number of compounds used as inks is still limited[6]. It is necessary to develop new inks to expand the inks library for further applications of 3D bioprinting.

© 2021 Zhou, *et al*. This is an Open Access article distributed under the terms of the Creative Commons Attribution License (https://creativecommons.org/licenses/by/4.0/), permitting distribution, and reproduction in any medium, provided the original work is properly cited.

Aqueous solutions of some ABA triblock copolymers, consisting of hydrophobic A and hydrophilic B blocks, will undergo a reversible sol-gel-sol transition with the increase of temperature[19-22]. One of the most commonly used copolymers is comprised of PEG as hydrophilic blocks and aliphatic polyester as the hydrophobic units. The polyester blocks can be poly(lactide-co-glycolide) (PLGA)[21,23], poly(caprolactone-co-lactide) [19,24], poly(caprolactone-co-glycolide) (PCGA) [25], polycaprolactone[20] and so on. At low temperatures, the triblock copolymers self-assemble into "flower-like" micelles and the solutions behave like liquid[26]. When the temperature is elevated, micelles aggregate to form a percolated network through hydrophobic interactions, resulting in a gel at the macroscopic level[22,27]. With many parameters such as block length of PEG and polyester[28], molecular weight distribution[21,23], end group[29], and even addition agent[28] can be used to adjust the sol-gel transition behavior. For their fast sol-gel transition between room and body temperature, these thermogels have been demonstrated potential applications as injectable hydrogels in drug delivery systems[30,31], tissue engineering[32,33], and prevention of post-operative adhesion[24].

We believe the thermal-sensitive copolymers hydrogel may serve as a promising candidate for bioink because of its excellent biodegradability and biocompatibility[34]. However, an ideal ink should fulfill certain rheological and mechanical requirements to achieve good extrudability as well as high shape fidelity. That is, it is required that the inks not only can be extruded easily as a smooth and uniform filament but also can maintain sufficient mechanical strength to support the printed structure without collapse[20,22]. Although the thermogels can be extruded as a fiber[35], their mechanical strength is still too weak to support large complicated objects. Therefore, it is desired to improve the mechanical strength of the hydrogel to meet the need of 3D printing.

At present, the introduction of new cross-linking mechanisms such as host-guest interaction[15,36,37], metal ions coordination[38], photopolymerization[10,39,40], chemical coupling reaction[41,42], and enzyme-catalyzed reaction[16,43,44] is the most common way to enhance the physical strength of inks. The thermo-sensitive physical hydrogel could also be strengthened through the formation of new crosslinks. For example, Ohya's group decorated the triblock copolymer PCGA-PEG-PCGA with succinimide ester groups at the termini and then crosslinked with polyamines. However, the modified copolymers were insoluble in water and a crosslinking agent was needed to form a covalent network. Most importantly, nearly no improvement on modulus was observed due to the low reaction efficacy[25]. Thus, it is desired to provide the thermogels with a more effective crosslinking to enhance their physical strength. The photopolymerization crosslinking system, which has been used to improve the printability of polymers such as gelatin[45], sodium alginate[46], silk fibroin[14], hyaluronic acid[15,17], and PEG[3,41,47], is a good choice due to its rapid solidification and controllable gelation by ultraviolet (UV) radiation.

In this study, the thermo-sensitive and photo-sensitive hydrogels based on triblock copolymers PLGA-PEG-PLGA were explored as inks. To obtain the dual-sensitive hydrogels, the copolymers were first synthesized by ring-opening polymerization, followed by esterification of the hydroxyl group with acrylic acid (**Figure S1**). The thermo-induced gelation was used to adjust the rheological properties of the hydrogels, yielding a printable ink that could hold its predesigned shapes during extrusion. Afterward, the printed scaffolds were fixed by UV photopolymerization crosslinking with the enhancement of physical strength. A variety of constructs, including a human nose, were successfully printed with high shape fidelity through the two-step crosslinking strategy. Moreover, by mixing with unmodified copolymers (**Figure 1A**), the mechanical properties, swelling ratio, and printability of inks could be easily tailored without compromising their extrudability. It is believed that this dual-sensitive hydrogel can be used as bioinks for printing large tissue-like constructs in the future.

2. Materials and methods

2.1. Materials

PEG with a number-average molecular weight of 1500 Da (PEG1500) was purchased from Sigma-Aldrich (St. Louis, USA). The monomers *L*-lactide and glycolide were gifted by Medsun (Hangzhou, China). *N,N'*-dicyclohexylcarbodiimide (DCC), 4-dimethylaminopyridine (DMAP), acrylic acid, and tin 2-ethylhexanoate [$Sn(Oct)_2$] were obtained from Aladdin (Shanghai, China). The photoinitiator, lithium phenyl-2,4,6-trimethylbenzoylphosphinate (LAP) was received from TCI (Tokyo, Japan). Anhydrous diethyl ether, methylene dichloride (DCM), and other chemicals were all chemical regent grade and bought from Shanghai Chemical Reagents Co. (Shanghai, China). PEG1500 was dehydrated before the experiments, and other reagents were all used as received.

2.2. Synthesis of the triblock copolymer

The triblock copolymers PLGA-PEG-PLGA were synthesized by ring-opening copolymerization of L-LA and GA in the presence of PEG1500 as an initiator and $Sn(Oct)_2$ as a catalyst (**Figure S1**). The detailed synthesis procedure of P1 was shown as following. Dehydrated PEG1500 (7.5 g, 5 mmol), *L*-LA (11.4027 g, 68.69 mmol), GA (9.1855 g, 68.69 mmol), and $Sn(Oct)_2$ (3 – 5 drops) were weighed and added to a 250-mL round-bottom flask.

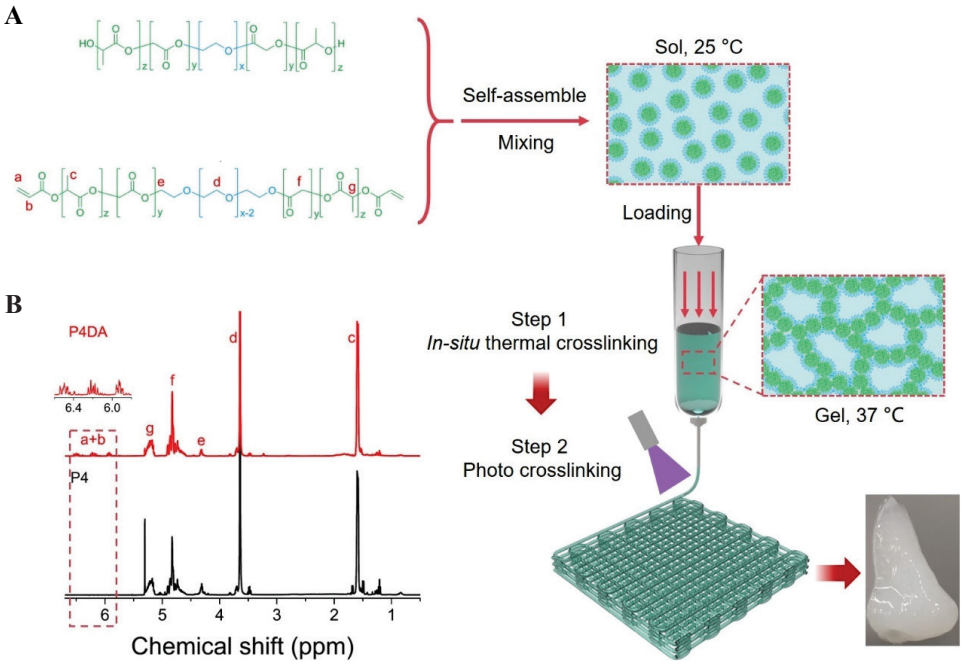


Figure 1. (A) Schematic of the 3D printing process through the dual-sensitive hydrogel inks. (B) ^{1}H-NMR spectra of P4 and P4DA.

Next, the flask was kept under reduced pressure at 60°C for 30 min to remove residual air and then filled with dry argon. With stirring, polymerization was carried out under argon protection at 160°C for 8 h. After cooling to room temperature, the crude product was dissolved in DCM (10 mL) and purified by reprecipitation using cold diethyl ether as a poor solvent. Then, the precipitate was dried in vacuo at r.t. for 3 days to yield the product. P2, P3, and P4 with different PLGA lengths were all acquired using similar procedures by varying the feed ratio.

P4DA was synthesized by esterification of P4 and acrylic acid as described in **Figure S1**. Firstly, P4 (21.08 g, 5 mmol) was dissolved in 30 mL DCM and transferred to a 250 mL flask. Then, DCC (3.095 g, 15 mmol) and DMAP (0.1832 g, 1.5 mmol) dissolved in 20 mL DCM were added to the flask and the solution was cooled to about 0°C in an ice-water bath under argon. At last, acrylic acid was added drop wise in 20 min through an addition funnel with a pressure-equalization arm. The reaction solution was stirred at 0°C for 2 h and further reacted at r.t. for 20 h. A small amount of water was added to stop the reaction and exhaust remained DCC. The reaction mixture was filtered by suction filtration to remove dicyclohexylurea. The filtrate was concentrated to 20 mL and precipitated 3 times using an excess of cold ethyl ether. After drying in vacuo for 3 days, the product was stored at −24°C.

2.3. Structural characterization

The ^{1}H-NMR spectra were recorded on an NMR spectrometer (Bruker, DMX-400MHz). $CDCl_3$ was used as deuterated solvent and the concentration of copolymer was 10 mg/mL. The number-average molecular weights of PLGA (M_n) can be calculated from ^{1}H-NMR spectra. The weight-average molecular weights (M_w) and polydispersity index (Đ) of copolymers were measured by GPC (TSK, D40). Tetrahydrofuran was used as mobile phase at a flow rate of 1.0 mL/min at 40°C and calibrated with polystyrene standards. The Fourier-transform infrared (FTIR) spectra of P4 and P4DA were scanned on an FTIR spectrometer (Thermo Scientific, Nicolet 6700) in the range of 4000-400 cm^{-1}. KBr pellets painted with samples were used for testing. The absorbance of P4 and P4DA was recorded on a UV spectrophotometer (Shimadzu, UV-1800) in the range of 200 – 400 nm. The copolymers were dissolved in water at a concentration of 0.05 wt.%.

2.4. Preparation of copolymer solutions

Unless otherwise specified, all the samples were prepared using deionized water here. To obtain copolymer solutions, a given volume of water was added to a vial with copolymer, followed by stirring with a magnetic stir bar below 30°C. The dissolution process lasted for 2 – 3 days until the polymer was completely dissolved and homogeneous solutions were achieved. For printing experiments, a series of solutions were prepared by blending P1 and P4DA. The total copolymer concentration was fixed at 25 wt.%, while the fraction of P4DA was varied. The prepared solutions were named DA00, DA20, DA40, DA60, and DA100, where the number referred to wt.% of P4DA in the total polymer. All the samples were

kept at 4°C before use. LAP was added as an initiator with a dosage of 0.003 wt.%.

2.5. Vial-inverting test

The sol-gel transition of the copolymer aqueous solutions was examined by the vial-inverting method. The vials containing 1 mL solution were immersed in a water bath. The temperature was adjusted from 25 to 55°C with an increment of 1°C/step. Samples were equilibrated for 10 min at each temperature and then the state was confirmed. If no flow was noticed in 20 s after the vial was inverted, the state of the solution was regarded as "gel," otherwise a "sol" state would be recorded.

2.6. Rheological analysis

(1) Sol-gel transition

A rotational rheometer (TA, DHR) was used to investigate the sol-gel-sol transition of the copolymer solutions and the properties of the hydrogel. Temperature sweep experiments were performed to examine the phase transition phenomenon using a cone-plate geometry (1.985°, 40 mm diameters, 0.05 mm gap). About 0.7 mL solution was added between two plates at 25°C. Then, the margin of the plate was covered with lowly viscous oil to prevent vaporization of the solvent. The temperature was increased from 25 to 55°C at a rate of 2°C/min. The controlled stress and frequency were 1.0 Pa and 6.28 rad/s, respectively.

(2) Extrudability

After adding to the plate, all the samples were then kept at 37°C for 5 min before measurement. To characterize the shear thinning nature of the hydrogel, the shear rate was logarithmically increased in a range of 0.1 – 100 s^{-1} and the viscosity was recorded. The elastic recovery behavior was measured by alternating 1% and 100% strain for 100 s at 6.28 rad/s angular frequency. The thixotropic property of the ink was proved using a three-stage steady-state flow test. At the first and the third stage, a shear rate of 0.1 s^{-1} was applied for 100 s. The shear rate was set to 100 s^{-1} and lasted for 5 s during the second stage.

(3) Mechanical properties

To compare the physical strength of hydrogels after photo-crosslinking, the samples were made into disks with 20 mm diameter and 1 mm thick by exposure to UV light (375 nm) for 300 s at 37°C. The disks were then tested on a parallel-plate (20 mm, 1.0 mm gap) fixture. A frequency sweep (1% strain, 0.1 – 50 rad/s angular frequency) was performed to examine the mechanical properties.

2.7. Tensile tests

A commercial tensile tester (Instron 3343) was used to measure tensile modulus of samples. After photo-crosslinked, the hydrogel was then cut into dumbbell-shaped specimens (gauge length, 12 mm; width, 2 mm; and thickness, 1 mm). All the experiments were conducted with a 50 N load cell and a stretch rate of 10 mm/min. At least three specimens were tested for each sample to get reliable data.

2.8. Swelling ratio

The water absorption properties were evaluated using the conventional gravimetric method. For this purpose, the inks were made into cylinder samples (4 mm height, 5 mm diameter) by exposure to UV light at 37°C for 5 min. The hydrogels were then immersed in 5 mL deionized water at 37°C for 48 h. After that, samples were taken out and the surface water was wiped carefully with filter papers, the swollen hydrogels were weighted and noted as W_s. Then, those samples were lyophilized and the dry weight (W_r) was recorded. Similar studies were conducted in triplicates, and the swelling ratio (s_r) was calculated using the equation.

$$s_r = \frac{W_s - W_d}{W_d} \times 100\%$$

2.9. Degradation properties

To study the degradation properties of the dual-sensitive hydrogel, 0.5 mL solution was added to a vial and then exposed to UV light for 5 min at 37°C. After gelation, 1 mL phosphate buffer saline (PBS) containing 0.02 mg lipase was added. The degradation experiments were conducted at 37°C and PBS was refreshed every day. At specific time intervals, the residual samples were taken out and freeze-dried. The weight was recorded and the weight loss to the original weight of samples before incubation was seen as the degradation rate. All the experiments were performed in triplicates and the average value was used for analysis.

2.10. Printing experiments

(1) Preparations before printing

The printing was performed in a commercial microextrusion 3D bioprinter (Regenovo, Bio-Architect®-Pro) with a temperature-controlled syringe and print bed. The control of the printer was achieved through software (Bio-Architect v2.2) on a personal computer. First, a printing model was designed in 3D computer-aided design and saved as STL files. Those files were imported to the software, and then the walking path was generated automatically according to the printing parameters. To print, inks were loaded into 10 mL syringes and store at 4°C for 2 h to remove bubbles. After those syringes were mounted onto the printing apparatus, equilibrating at 37°C for 15 min was required to make sure the inks stay at a

gel state. Blunt-tipped stainless-steel needles were used here to reduce the influence of environmental temperature. During the printing process, the temperature of the syringe and print bed was controlled at 37°C and an UV light lamp (UltraFire, 501 B) was applied to photo-crosslink the inks.

(2) Assessment of printability

To assess and compare the printability of inks, lattice structures ($20 \times 20 \times 0.5$ mm^3) were printed onto a glass plate. The printing speed was set at 10 mm/s here and the pressure was adjusted between 0.05 MPa and 0.55 MPa according to the situation. Various needle size (0.16, 0.21, 0.31, 0.41, and 0.51 mm) and line interval (0.8, 1.0, 1.2, 1.6 mm) were used to optimize the printing parameters. Images were captured by a digital microscope (Dino-lite, FC-OC1) immediately after the printing was completed. The line width and square area of grids were measured in ImageJ. Diffusion rate (D_r) was calculated according to previous research by He *et al*.[48]

$$D_r = \frac{A_t - A_e}{A_t} \times 100\%$$

where A_t is the theoretical area of a square and A_e is the experimentally measured area of the square.

(3) Printing of large constructs

Centimeter-scale structures cuboid ($20 \times 20 \times 4$ mm^3), pyramid ($20 \times 20 \times 10$ mm^3), and human nose ($28 \times 18 \times 10$ mm^3) were printed using DA40. We designed the models of cuboid and pyramid, and the human nose structure was retrieved from an open-source website (https://www.thingiverse.com/thing:306031) with a slight modification.

2.11. *In vitro* cell viability analysis

Human primary fibroblasts in cell culture medium with copolymers at 5 mg/mL were added to a 96-well plate at a cell density of 500 cells/well. Subsequently, the cells were incubated for 3 days at 37°C in the presence of 5% CO_2. To evaluate the cell viabilities, a cytotoxicity assay kit (KeyGEN BioTECH, China) was used to stain the cells. Briefly, the cell culture medium was removed and washed with PBS for 3 times. 1 mL PBS containing 0.5 μL calcein AM and 0.5 μL PI was added to the samples. The samples were then incubated for 45 min at room temperature. At last, a fluorescence microscope (Leica, Germany) was used to observe live/dead fibroblasts.

3. Results and discussion

3.1. Synthesis and structure characterization of the triblock copolymer

The triblock copolymers were synthesized through ring-opening polymerization of LA and GA using PEG1500 as an initiator. Here, four copolymers with different PLGA lengths, P1, P2, P3, and P4, were prepared and investigated. Their molecular weight and molecular weight distribution were characterized using ^{1}H NMR and GPC. Detailed data for the four copolymers are listed in **Table 1**. To obtain the dual-sensitive hydrogels, all the copolymers were then reacted with acrylic acid, while only P4 with a shorter PLGA length could result in a soluble polymer due to the end-group effect[29]. To verify the success of the acylation, the ^{1}H NMR spectrum of P4DA and its precursor was showed and compared (**Figure 1B**). Different from P4, three new peaks were observed between 5.8 and 6.6 ppm in the spectrum of P4DA, corresponding to the three protons of acryloyl. This observation indicated that the hydroxy end groups were replaced with acryloyl groups, and the degree of substitution was calculated to be 102%. This conclusion was also supported by emerging characteristic peaks related to acryloyl in IR and UV absorption spectrums (**Figure S2**).

3.2. Thermo-sensitive sol-gel transition of copolymer solutions

Initially, the vial-inverting test was used to examine the sol-gel behavior (**Figure 2A**), with the results displayed in **Figure 2B**. The phase transition diagram showed a gel window of "U" shape, representing a sol-gel-sol process. P1 showed a gelation temperature range from 33 to 46°C, and its critical gelation concentration (CGC) was around 16 wt.%. With the decrease of molecular weight, P2 and P3 got a narrower gel window and a higher CGC (**Table 1**) due to less hydrophobicity of the polyester block. Although P4 was quite hydrophilic and soluble even at high temperature and high concentration, P4DA underwent sol-gel-sol transition with a gel window located at 37 – 52°C. Their differences in the macroscopic gelation behavior are associated with the increased hydrophobicity induced by new end groups. To be a bioink, it is necessary for a hydrogel to possess a wider gel window and a lower CGC; so that P1 and P4DA were chosen for further studies.

The sol-gel transition behavior was also investigated with rheological measurements. Typical results of temperature sweeps for P1 and P4DA are shown in **Figure 2C**. Both the storage modulus (G') and loss modulus (G'') raised rapidly from low values to a peak around body temperature and then tended to decrease. There were two crossover points in curves of G' and G'', the first intersection implied a transition of sol-gel and the second one was believed to be a gel-sol transition. The temperatures at the two intersection points were remarked as T_{gel} and T_{sol}, respectively. T_{gel} and T_{sol} of P4DA were determined to be 38.8 and 49.2°C, which was in agreement with previous results (**Figure 2B**).

Whereas the results of P1 (34.5 and 38.0°C) shown obvious differences with those in the phase diagram (35 and 43°C). This situation was likely due to a continuous increase of system viscosity even G' was overtaken by G'' after 38.0°C.

The salting-out effect of the photoinitiator (LAP) on the sol-gel transition behavior of P1 and P4DA was also examined. As shown in **Figure S3**, T_{gel} and T_{sol} of the P4DA were found to be decreased once LAP was added to the solutions. In addition, G' and G'' of P4DA dropped sharply when the temperature was elevated above T_{sol}, indicating a gel-precipitation process instead of a gel-sol transition (**Figure S3B**). In contrast, the sol-gel transition behavior of P1 was much less affected by the salting-out effect than that of P4DA, and no gel-precipitation transition was observed (**Figure S3A**).

A mixing strategy was employed to prepare a series of samples with different P4DA content to evaluate the extent of photo-crosslinking on the printability of inks. For this purpose, six samples of DA00, DA20, DA40, DA60, DA80, and DA100 were prepared by blending P1 with P4DA, the number represented the fraction of P4DA in the total copolymer. All of those samples were then evaluated with rheological tests, and the calculated T_{gel} and T_{sol} are shown in **Figure 2E**. Both T_{gel} and T_{sol} were linearly increased with the fraction of P4DA, and

Table 1. Molecular characterization and gelation information of synthesized triblock copolymers

Samples	M_n [a]	LA/GA[a]	Đ[b]	CGC/wt %[c]	Gel window/°C[c]
P1	2102-1500-2102	1/0.97	1.27	16	35 – 43
P2	1790-1500-1790	1/1.00	1.33	22	39 – 41
P3	1495-1500-1495	1/1.00	1.23	32	-
P4	1345-1500-1345	1/0.97	1.23	-	-
P4DA	1627-1500-1627	1/0.99	1.25	22	42 – 48

[a]Number-average molecular weight (M_n) and the molar ratio of lactide/glycolide (LA/GA) were calculated from ^{1}H NMR spectroscopy. [b]Molar-mass dispersity (Đ) was measured via GPC. [c]Critical gelation concentration (CGC) was acquired from phase diagrams and the gel window showed a gelation temperature range at concentration of 25 wt.%

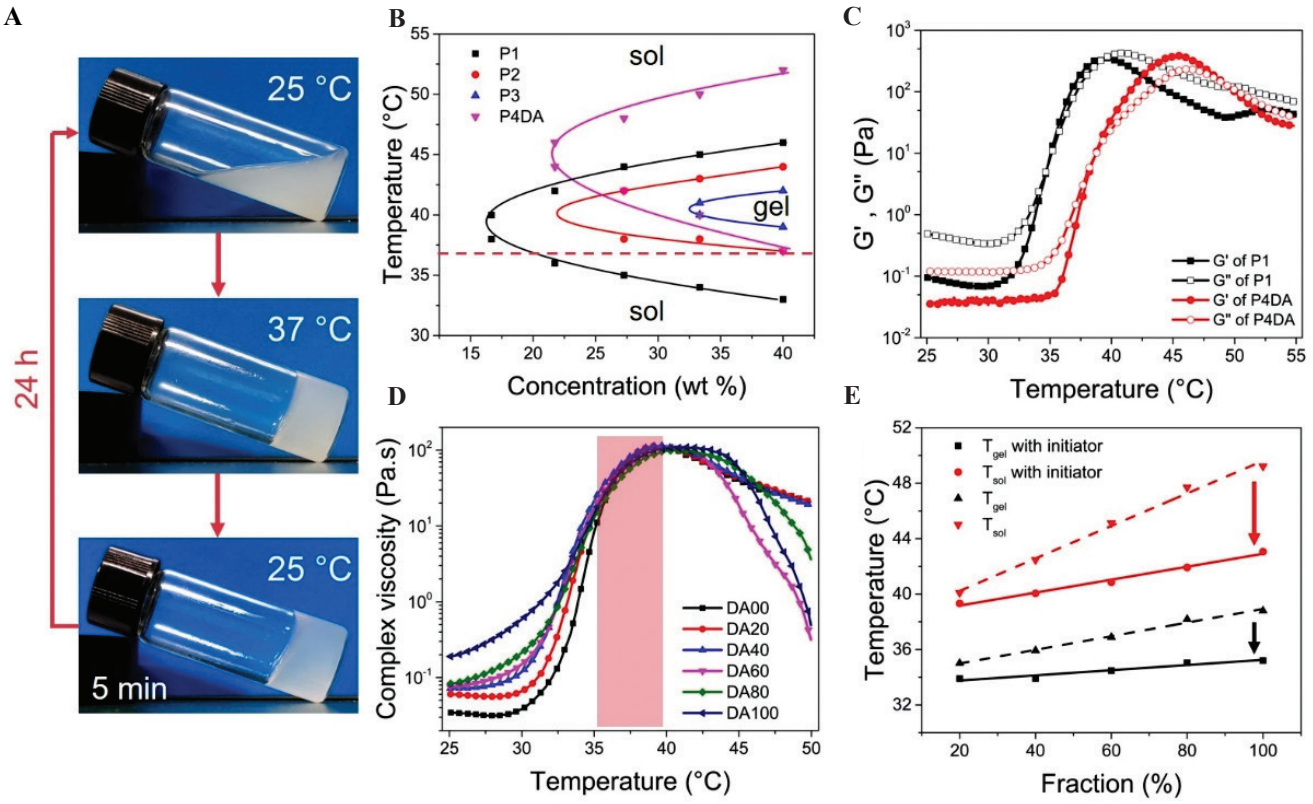


Figure 2. Thermo-sensitive sol-gel phase transition of samples. (A) Photographs of sample state at different temperature. (B) Phase diagrams of P1, P2, P3, and P4DA. (C) Storage modulus and loss modulus of P1 and P4DA as a function of temperature. (D) Complex viscosity of DA00, DA20, DA40, DA60, DA60, and DA100 with addition of photoinitiator as a function of temperature. (E) T_{gel} and T_{sol} of DA20, DA40, DA60, DA60, and DA100 with and without addition of photoinitiator.

so did the influence of salt-out effect on the transition temperature. More importantly, we found that all the samples showed similar curves in temperature sweeps (from 33 to 40°C) regardless of hydrogels composition (**Figure 3D**). The results indicated that the mechanical and other properties of the inks can be easily tuned by varying the fraction of P4DA without compromising its extrudability.

3.3. Assessment of extrudability

Through the temperature-induced sol-gel transition, the complex viscosity (above 10 Pa·s) of all the samples reached the requirement for a filament formation in the gelation temperature range from 35.2 to 39.1°C, **Figure 3D**[49]. To ascertain whether the thermogels were capable of printing, DA40 was loaded and extruded from a needle. As displayed in **Figure 3F**, filaments with a smooth and uniform morphology were extruded continuously from the printing nozzle when the printing temperature was set at 37°C. In contrast, only droplets were formed at the nozzle tip at 25°C. This result indicated that the extrudability of inks could be easily modulated by temperature. To achieve better printing results, all the printing experiments were conducted at 37°C.

The responsiveness of viscosity to shear rate was examined with rheological characterization. The flow curve of all samples demonstrated a linear decrease in viscosity with the increase of shear rate (**Figure 3A**), indicating their shear-thinning behavior. All the samples showed viscosity above 200 Pa·s at a shear rate of 0.01 s^{-1}, and it decreased to 0.05 Pa·s when the shear rate was increased to 100 s^{-1}.

Besides the shear-thinning properties, the rapid elastic recovery from disruption also contributed to high shape fidelity. Accordingly, elastic recovery tests were carried out using DA40 as a model with alternating low (1%) and high (100%) strain at 100 s intervals (**Figure 3B**). At a low strain of 1%, G' of hydrogel was greater than G'', implying a solid behavior, whereas a sharp drop was observed when the hydrogel was subjected to a high strain of 100%, and G' was surpassed by G''. After removal of applied high strain, G' of hydrogel instantly recovered to its initial value. The recovery of hydrogels remained unchanged after five cycles. Furthermore, a three-stage steady-flow test was set to simulate conditions before, during, and after the printing process (**Figure 3C**). At the first stage, the hydrogel showed a viscosity around 200 Pa·s with a low shear rate (0.1 s^{-1}) representing flow behavior in the barrel. A high shearing rate (100 s^{-1}) was followed to simulate the extrusion of inks, and the viscosity dropped sharply to 1 Pa·s at this stage. When high shearing force was removed as inks were extruded

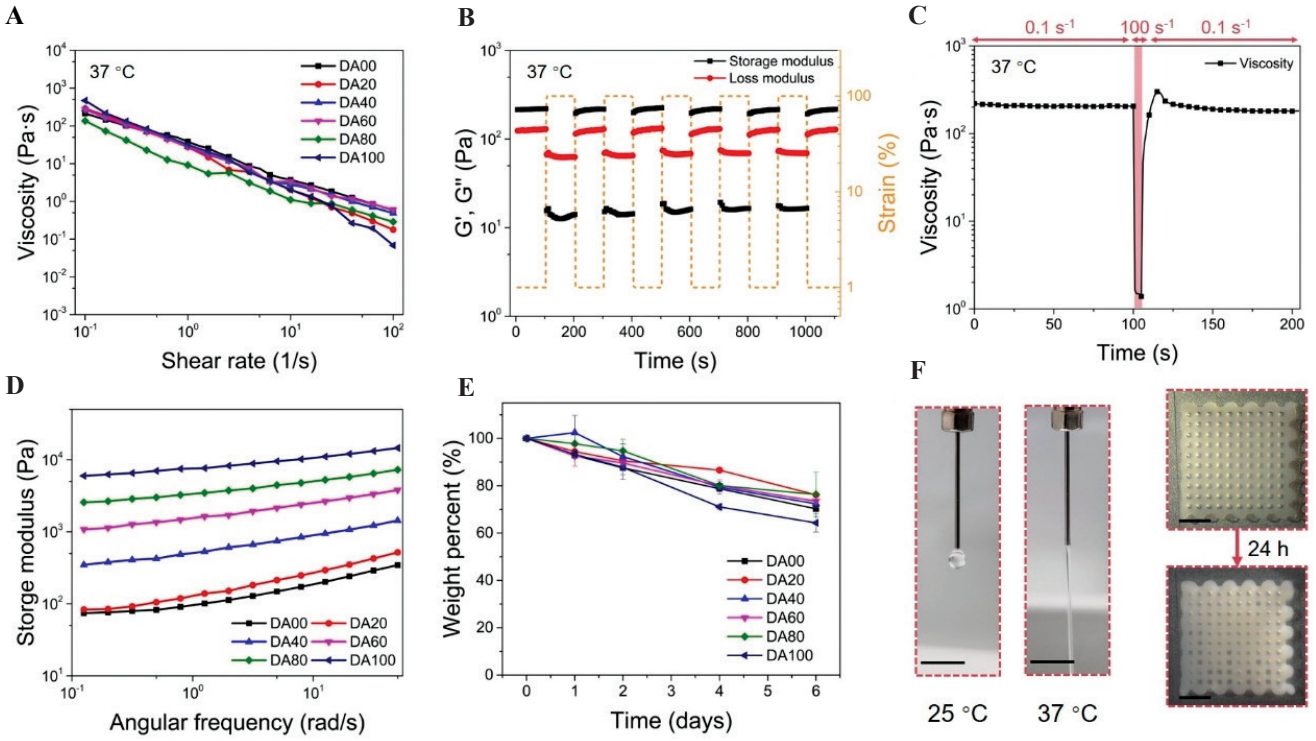


Figure 3. (A) Viscosity of DA00, DA20, DA40, DA60, DA60, and DA100 as a function of shear rate at 37°C. (B) Elastic recovery properties of DA40 at 37°C. (C) Shear recovery properties of DA40 at 37°C. (D) Storge modulus of DA00, DA20, DA40, DA60, DA60, and DA100 after photo-crosslinking as a function of frequency. (E) Degradation profiles of DA00, DA20, DA40, DA60, DA60, and DA100 at 37°C in PBS containing 0.02 mg lipase. (F) Effect of temperature on the filament formation of ink. (G) Photographs of printed construct with DA40 before and after immersing in water for 24 h (Scale bar: 5 mm).

out from the needle, viscosity bounced back to 180 Pa·s within 5 s, which was 90% recovery of its initial viscosity.

The above results suggested that the hydrogels possessed excellent shear-thinning and rapid recovery properties, which were mainly attributed to the reversible nature of physical bonding. Another worry on the thermo-sensitive inks was that the solid hydrogels would transform back into solutions at low environmental temperatures. But fortunately, the thermogels exhibited a slow de-gelling process; the viscosity of the system remained unchanged in 5 min even after the temperature was dropped from 37 to 25°C (**Figure 2A**). The self-supporting filament in the filament collapse experiments[50] also demonstrated that the inks could hold the printed constructs before the photo-crosslinking was constructed (**Figure 4G**).

3.4. Properties of the dual-sensitive hydrogel

Successful printing is dependent not only on the extrudability of inks but also on the ability to support the printed constructs. However, the thermo-sensitive hydrogel was a physical hydrogel with weak mechanical strength. The maximum value of G' in temperature sweep was only 500 Pa (**Figure 2C**), indicating poor shape retention of the hydrogels. To compare the mechanical strength of hydrogels after photo-crosslinking, G' of all samples was evaluated using frequency sweep tests. In **Figure 3D**, G' (at 1 rad/s) was increased from 90.7 Pa of DA00 to 7493.1 Pa of DA100, indicated that the mechanical strength was enhanced by the introduction of photo-crosslinking. Furthermore, this was also confirmed by the results of tensile tests, DA100 reached a tensile modulus of 21.9 kPa (**Figure S4**) but DA00 was too weak to form a specific shape for tests. In addition, the storage and tensile modulus tended to be higher when more P4DA was formulated into the inks. Therefore, by varying the fraction of P4DA in the inks, the hydrogels' mechanical strength can be tuned to satisfy a range of applications.

The swelling properties of the samples were investigated by immersing them in deionized water. DA00 (848.2%) and DA20 (844.26%) had a high swelling ratio because of the lack of effective covalent network formation. However, the swelling ratio of DA40 was decreased (771.7%), which was attributed to a denser hydrogel mesh formed by chemical crosslinking. As the fraction of P4DA further increased, the swelling ratio of DA60, DA80, and DA100 was decreased to 559.7%, 451.3%, and 430.0%, respectively. The higher swelling ratio of physical hydrogels was associated with low structural stability[51]. The reduced water absorption of dual-sensitive hydrogels vouched for good shape retention under cell culture over a long time (**Figure 3G**). The enzymatic degradation properties of the hydrogels were then evaluated. As displayed in **Figure 3E**, all the samples showed close degradation profiles regardless of the fraction of P4DA, implying that the excellent biodegradation properties of thermogels were not affected by the introduction of the covalent network.

3.5. Printing of the dual-sensitive hydrogel inks

To evaluate the printability of the dual-sensitive hydrogel inks, lattice structure was printed with DA00, DA20, DA40, DA60, DA80, and DA100. As shown in **Figure 4A**, multi-layer grids printed with DA00 and DA20 collapsed, square holes in the structure transformed into circular ones due to diffusion of filaments, showing their poor shape retention. In contrast, constructs with the well-defined structure were obtained in experiments of DA40, DA60, DA80, and DA100. And their diffusion rate, a parameter to evaluate ink's shape fidelity[48] was around 35%, much lower than that of DA00 (97.20%) and DA20 (78.80%). In addition, diameters of filament (line width) were used to quantitatively assess the printability of different inks. DA00 and DA20 showed an unacceptable line width (1.37 and 0.93 mm), which was three-fold larger than the needle diameters (0.31 mm). Nevertheless, the line width of DA40, DA60, DA80, and DA100 was, respectively, determined to be 0.44, 0.47, 0.46, and 0.53 mm, which was quite close to the diameters of needle. There was no doubt that the printability of the inks was improved by the addition of P4DA, which was attributed to enhanced mechanical strength due to the formation of covalent networks. Therefore, inks with P4DA fraction above 40 wt.% were expected to be used in further experiments.

Next, DA40 was chosen as a model to explore the influence of printing parameters on the inks' printability. The needles with different diameters were used to print the inks. The results showed that the inks could be extruded from all needles with diameters from 0.16 mm to 0.53 mm (**Figure 4B**). However, the smaller the diameters of the needle, the higher pressure was needed to extrude the inks. Besides, all the results showed a line width larger than their needle diameters (**Figure 4E**), which was attributed to the spreading of the weak thermo-sensitive hydrogel before photo-crosslinking. Filament interval, representing the distance a strand needed to span between filaments from the previous layer, is another important printing parament. As shown in the filament collapse study (**Figure 4G**), a sagging filament was observed between a large gap, which would result in poor shape fidelity. However, details of the printed constructs would disappear when a small interval was chosen due to diffusion of filament into the deep part of the construct (**Figure 4C and F**). For better printing results, a needle with 0.31 mm diameter and a filament interval of 1.2 mm was chosen for further experiments. With optimized parameters, a 10-layer lattice was printed and displayed in **Figure 4H**. The printed grid exhibited high shape fidelity; moreover, it could be held by hands, demonstrating the ink's ability to print large structures.

It is a challenge to print intricate 3D architectures of a soft hydrogel due to the lack of mechanical strength. To demonstrate the inks' ability to print centimeter-scale objects with high shape fidelity, a variety of constructs were printed. The printing was carried out using DA 40 with the optimized printing parameters. First, we printed a cuboid with the dimension of 20 × 20× 4 mm^3, the pictures in **Figure 5A** revealed high shape retention. And fusion of subsequent two layers was observed in the side view. Then, a more complicated pyramid (20 × 20 × 10 mm^3) was printed without collapsing (**Figure 5B**). At last, a self-supporting anatomical-size human nose (18 × 28 × 10 mm^3) was printed (**Figure 5C**). The printed construct showed high structural similarity to its 3D digital model in details, and no collapse was observed throughout the experiment.

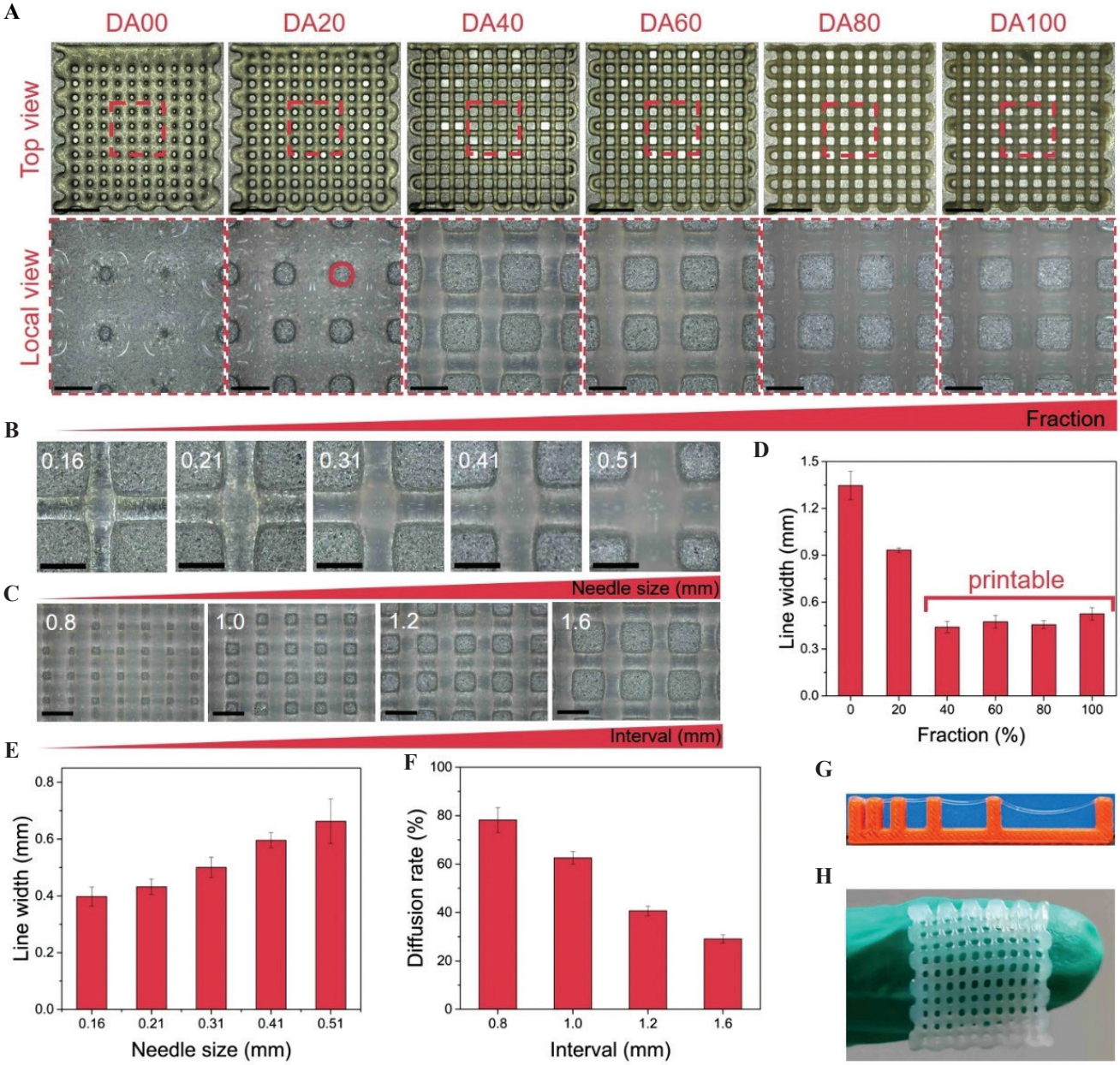


Figure 4. Printing of the dual-sensitive hydrogels inks. (A) Images of printed grids with DA00, DA20, DA40, DA60, DA60, and DA100 (scale bars in top view: 5 mm, in local view: 1 mm). Images of printed structures with DA40 using (B) different nozzle size and (C) different filament interval (scale bars: 1 mm). (D) Line width of DA00, DA20, DA40, DA60, DA60, and DA100 in printed lattices. (E) Line width of DA40 in printed lattices with different needle size. (F) Diffusion rate of DA40 in printed lattices with different filament interval. (G) Photograph of printed strand on a construct with pillars. (H) Photograph of a printed multi-layers construct moved by hands.

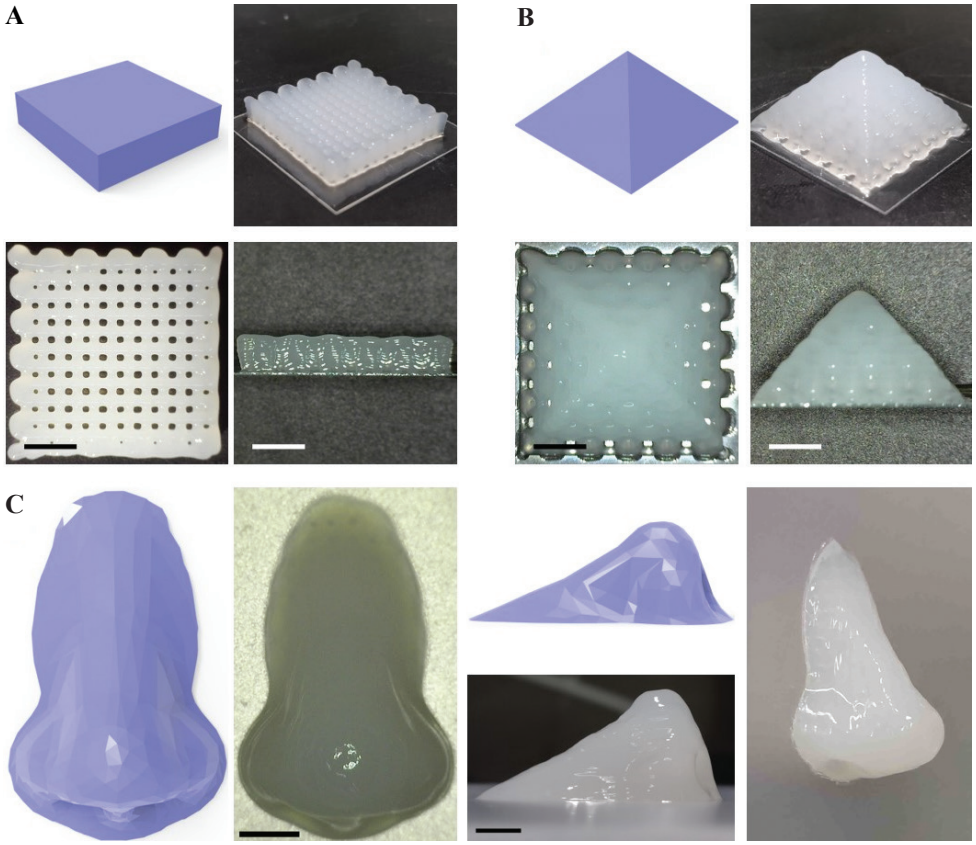


Figure 5. Images of printed constructs. (A) Cuboid (20 × 20 × 4 mm^3). (B) Pyramid (20 × 20 × 10 mm^3). (C) Human nose (28 × 18 × 10 mm^3). Scale bars: 5 mm.

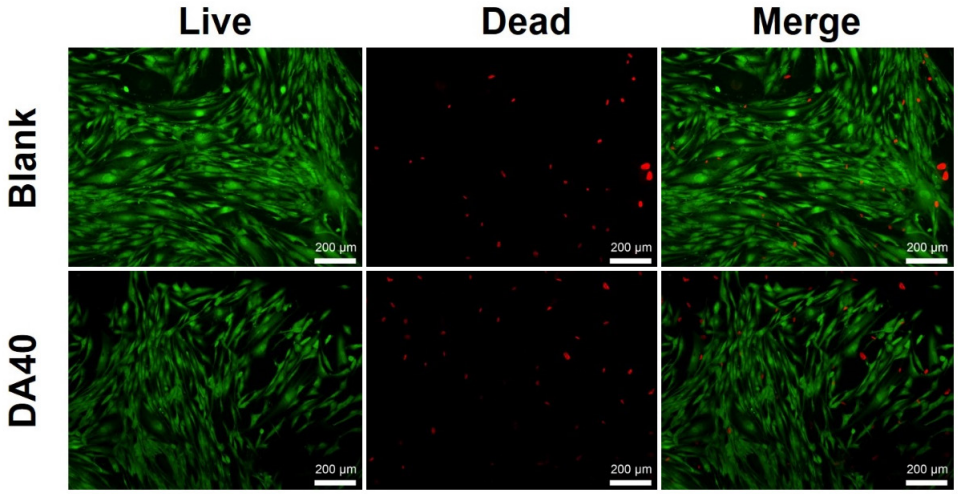


Figure 6. Fluorescent microscopic images of fibroblast cultured with DA40 (5 mg/mL) and with medium only.

3.6. *In vitro* cell viability analysis

Biocompatibility is also an important factor to evaluate a bioink; a cell viability test was performed using human primary fibroblasts to estimate the cell cytotoxicity of the copolymers. Live/dead staining was used to determine the cell viability over 3 days of culture. Fluorescence microscopy images (**Figure 6**) showed that 90% of cells were viable, which was similar to that in the blank control (92%). This result showed that the copolymers possess good cell compatibility, indicating that the inks may be printed to biodegradable scaffold for tissue engineering.

4. Conclusions

In summary, a thermo-sensitive and photo-sensitive hydrogel based on the triblock copolymers PLGA-PEG-PLGA was developed for 3D printing. Aqueous solutions of the copolymers exhibited thermo-induced sol-gel transition accompanied by the increase of the viscosity. The resulted hydrogels showed excellent shear-thinning properties and fast elastic recovery properties, which rendered the thermogels with good extrudability while maintaining the predesigned structures. Furthermore, the thermogels allowed for UV photopolymerization to stabilize the printed scaffolds, with storage modulus dramatically increased. Through a two-step crosslinking strategy, complicated constructs with high shape fidelity can be printed. Moreover, the self-supporting printed scaffolds could be picked up by hand. The synthesis process of the dual-sensitive hydrogels was simple and low-cost, meaning that large-scale production in industrial manufacture was possible. The dual-sensitive hydrogels were expected to be promising bioinks, development of cell-laden inks and their applications in tissue engineering will be explored in future studies.

Acknowledgments

This work was financially supported by the National Key Research and Development Program of China (2017YFC1103400).

Conflict of interest

All authors declare that they have no conflicts of interest.

Author contributions

Y. Z. designed the experiments. Y. Z. and Y. C. performed the experiments and analyzed the results. Y. Z. wrote the manuscript. L. W. supervised the work and revised the manuscript.

References

1. Noor N, Shapira A, Edri R, *et al.*, 2019, 3D Printing of Personalized Thick and Perfusable Cardiac Patches and Hearts. *Adv Sci*, 6:1900344. https://doi.org/10.1002/advs.201900344
2. Kang HW, Lee SJ, Ko IK, *et al.*, 2016, A 3D Bioprinting System to Produce Human-scale Tissue Constructs with Structural Integrity. *Nat Biotechnol*, 34:312–9. https://doi.org/10.1038/nbt.3413
3. Grigoryan B, Paulsen SJ, Corbett DC, *et al.*, 2019, Multivascular Networks and Functional Intravascular Topologies within Biocompatible Hydrogels. *Science*, 364:458–64.
4. Bedell ML, Navara AM, Du Y, *et al.*, 2020, Polymeric Systems for Bioprinting. *Chem Rev*, 120:10744–92.
5. Li X, Liu B, Pei B, *et al.*, 2020, Inkjet Bioprinting of Biomaterials. *Chem Rev*, 120:10793–833.
6. Valot L, Martinez J, Mehdi A, *et al.*, 2019, Chemical Insights Into Bioinks for 3D Printing. *Chem Soc Rev*, 48:4049–86. https://doi.org/10.1039/c7cs00718c
7. Murphy SV, Atala A, 2014, 3D Bioprinting of Tissues and Organs. *Nat Biotechnol*, 32:773–85. https://doi.org/10.1038/nbt.2958
8. Jin Y, Liu C, Chai W, *et al.*, 2017, Self-Supporting Nanoclay as Internal Scaffold Material for Direct Printing of Soft Hydrogel Composite Structures in Air. *ACS Appl Mater Interfaces*, 9:17456–65. https://doi.org/10.1021/acsami.7b03613
9. Lee A, Hudson AR, Shiwarski DJ, *et al.*, 2019, 3D Bioprinting of Collagen to Rebuild Components of the Human Heart. *Science*, 365:482–7.
10. Yin J, Yan M, Wang Y, *et al.*, 2018, 3D Bioprinting of Low-Concentration Cell-Laden Gelatin Methacrylate (GelMA) Bioinks with a Two-Step Cross-linking Strategy. *ACS Appl Mater Interfaces*, 10:6849–57. https://doi.org/10.1021/acsami.7b16059.s001
11. Colosi C, Shin SR, Manoharan V, *et al.*, 2016, Microfluidic Bioprinting of Heterogeneous 3D Tissue Constructs Using Low-Viscosity Bioink. *Adv Mater*, 28:677–84. https://doi.org/10.1002/adma.201503310
12. Singh YP, Bandyopadhyay A, Mandal BB, 2019, 3D Bioprinting Using Cross-Linker-Free Silk-Gelatin Bioink for Cartilage Tissue Engineering. *ACS Appl Mater Interfaces*, 11:33684–96. https://doi.org/10.1021/acsami.9b11644
13. Schacht K, Jungst T, Schweinlin M, *et al.*, 2015, Biofabrication of Cell-Loaded 3D Spider Silk Constructs. *Angew Chem Int Ed*, 54:2816–20. https://doi.org/10.1002/anie.201409846
14. Kim SH, Yeon YK, Lee JM, *et al.*, 2018, Precisely Printable and Biocompatible Silk Fibroin Bioink for Digital Light Processing 3D Printing. *Nat Commun*, 9:1620. https://doi.org/10.1038/s41467-018-04517-w
15. Highley CB, Rodell CB, Burdick JA, 2015, Direct 3D Printing of Shear-Thinning Hydrogels into Self-Healing Hydrogels. *Adv Mater*, 27:5075–9. https://doi.org/10.1002/adma.201501234
16. Petta D, Armiento A R, Grijpma D, *et al.*, 2018, 3D Bioprinting of a Hyaluronan Bioink through Enzymatic-and Visible Light-Crosslinking. *Biofabrication*, 10:044104.

https://doi.org/10.1088/1758-5090/aadf58

17. Shi L, Carstensen H, Hölzl K, *et al.*, 2017, Dynamic Coordination Chemistry Enables Free Directional Printing of Biopolymer Hydrogel. *Chem Mater*, 29:5816–23. https://doi.org/10.1021/acs.chemmater.7b00128.s001
18. Pati F, Jang J, Ha DH, *et al.*, 2014, Printing Three-Dimensional Tissue Analogues with Decellularized Extracellular Matrix Bioink. *Nat Commun*, 5:3935. https://doi.org/10.1038/ncomms4935
19. Nielsen JE, Zhu K, Sande SA, *et al.*, 2017, Structural and Rheological Properties of Temperature-Responsive Amphiphilic Triblock Copolymers in Aqueous Media. *J Phys Chem B*, 121:4885–99. https://doi.org/10.1021/acs.jpcb.7b01174.s001
20. Bae SJ, Suh JM, Sohn YS, *et al.*, 2005, Thermogelling Poly (Caprolactone-b-Ethylene Glycol-b-Caprolactone) Aqueous Solutions. *Macromolecules*, 38:5260–5. https://doi.org/10.1021/ma050489m
21. Chen L, Ci T, Li T, *et al.*, 2014, Effects of Molecular Weight Distribution of Amphiphilic Block Copolymers on Their Solubility, Micellization, and Temperature-Induced Sol-Gel Transition in Water. *Macromolecules*, 47:5895–903. https://doi.org/10.1021/ma501110p
22. Cui S, Yu L, Ding J, 2019, Thermogelling of Amphiphilic Block Copolymers in Water: ABA Type Versus AB or BAB Type. *Macromolecules*, 52:3697–715. https://doi.org/10.1021/acs.macromol.9b00534
23. Chen L, Ci T, Yu L, *et al.*, 2015, Effects of Molecular Weight and Its Distribution of PEG Block on Micellization and Thermogellability of PLGA-PEG-PLGA Copolymer Aqueous Solutions. *Macromolecules*, 48:3662–71. https://doi.org/10.1021/acs.macromol.5b00168
24. Zhang Z, Ni J, Chen L, *et al.*, 2011, Biodegradable and Thermoreversible PCLA-PEG-PCLA Hydrogel as a Barrier for Prevention of Post-Operative Adhesion. *Biomaterials*, 32:4725–36. https://doi.org/10.1016/j.biomaterials.2011.03.046
25. Yoshida Y, Kawahara K, Inamoto K, *et al.*, 2016, Biodegradable Injectable Polymer Systems Exhibiting Temperature-Responsive Irreversible Sol-to-Gel Transition by Covalent Bond Formation. *ACS Biomater Sci Eng*, 3:56–67. https://doi.org/10.1021/acsbiomaterials.6b00581.s001
26. Vidyasagar A, Ku SH, Kim M, *et al.*, 2017, Design and Characterization of a PVLA-PEG-PVLA Thermosensitive and Biodegradable Hydrogel. *ACS Macro Lett*, 6:1134–9. https://doi.org/10.1021/acsmacrolett.7b00523
27. Cui S, Yu L, Ding J, 2018, Semi-Bald Micelles and Corresponding Percolated Micelle Networks of Thermogels. *Macromolecules*, 51:6405–20. https://doi.org/10.1021/acs.macromol.8b01014
28. Jeong B, Bae YH, Kim SW, 1999, Thermoreversible Gelation of PEG-PLGA-PEG Triblock Copolymer Aqueous Solutions. *Macromolecules*, 32:7064–9. https://doi.org/10.1021/ma9908999
29. Yu L, Zhang H, Ding J, 2006, A Subtle End-Group Effect on Macroscopic Physical Gelation of Triblock Copolymer Aqueous Solutions. *Angew Chem Int Ed*, 45:2232–5. https://doi.org/10.1002/anie.200503575
30. Zhou X, He X, Shi K, *et al.*, 2020, Injectable Thermosensitive Hydrogel Containing Erlotinib-Loaded Hollow Mesoporous Silica Nanoparticles as a Localized Drug Delivery System for NSCLC Therapy. *Adv Sci*, 7:2001442. https://doi.org/10.1002/advs.202001442
31. Ci T, Shen Y, Cui S, *et al.*, 2017, Achieving High Drug Loading and Sustained Release of Hydrophobic Drugs in Hydrogels through *In Situ* Crystallization. *Macromol Biosci*, 17:1600299. https://doi.org/10.1002/mabi.201600299
32. Ni P, Ding Q, Fan M, *et al.*, 2014, Injectable Thermosensitive PEG-PCL-PEG Hydrogel/acellular Bone Matrix Composite for Bone Regeneration in Cranial Defects. *Biomaterials*, 35:236–48. https://doi.org/10.1016/j.biomaterials.2013.10.016
33. Zhang Z, Lai Y, Yu L, *et al.*, 2010, Effects of Immobilizing Sites of RGD Peptides in Amphiphilic Block Copolymers on Efficacy of Cell Adhesion. *Biomaterials*, 31:7873–82. https://doi.org/10.1016/j.biomaterials.2010.07.014
34. Yu L, Ding J, 2008, Injectable Hydrogels as Unique Biomedical Materials. *Chem Soc Rev*, 37:1473–81. https://doi.org/10.1039/b713009k
35. Park MH, Joo MK, Choi BG, *et al.*, 2012, Biodegradable Thermogels. *Acc Chem Res*, 45:424–33.
36. Song KH, Highley C B, Rouff A, *et al.*, 2018, Complex 3D-Printed Microchannels within Cell-Degradable Hydrogels. *Adv Funct Mater*, 28:1801331. https://doi.org/10.1002/adfm.201801331
37. Wang Z, An G, Zhu Y, *et al.*, 2019, 3D-Printable Self-Healing and Mechanically Reinforced Hydrogels with Host-Guest Non-Covalent Interactions Integrated Into Covalently Linked Networks. *Mater Horiz*, 6:733–42. https://doi.org/10.1039/c8mh01208c
38. Wlodarczyk-Biegun MK, Paez JI, Villiou M, *et al.*, 2020, Printability Study of Metal Ion Crosslinked PEG-Catechol Based Inks. *Biofabrication*, 12:035009. https://doi.org/10.1088/1758-5090/ab673a

39. Chimene D, Peak CW, Gentry JL, *et al.*, 2018, Nanoengineered Ionic-Covalent Entanglement (NICE) Bioinks for 3D Bioprinting. *ACS Appl Mater Interfaces*, 10:9957–68. https://doi.org/10.1021/acsami.7b19808
40. Pi Q, Maharjan S, Yan X, *et al.*, 2018, Digitally Tunable Microfluidic Bioprinting of Multilayered Cannular Tissues. *Adv Mater*, 30:1706913. https://doi.org/10.1002/adma.201706913
41. Rutz AL, Gargus ES, Hyland KE, *et al.*, 2019, Employing PEG Crosslinkers to Optimize Cell Viability in Gel Phase Bioinks and Tailor Post Printing Mechanical Properties. *Acta Biomater*, 99:121–32. https://doi.org/10.1016/j.actbio.2019.09.007
42. Rutz AL, Hyland KE, Jakus AE, *et al.*, 2015, A Multimaterial Bioink Method for 3D Printing Tunable, Cell-Compatible Hydrogels. *Adv Mater*, 27:1607–14. https://doi.org/10.1002/adma.201405076
43. Mehrotra S, de Melo BA, Hirano M, *et al.*, 2020, Nonmulberry Silk Based Ink for Fabricating Mechanically Robust Cardiac Patches and Endothelialized Myocardium-on-a-Chip Application. *Adv Funct Mater*, 30:1907436. https://doi.org/10.1002/adfm.201907436
44. Sakai S, Mochizuki K, Qu Y, *et al.*, 2018, Peroxidase-Catalyzed Microextrusion Bioprinting of Cell-laden Hydrogel Constructs in Vaporized ppm-Level Hydrogen Peroxide. *Biofabrication*, 10:045007. https://doi.org/10.1088/1758-5090/aadc9e
45. Yue K, Trujillo-de Santiago G, Alvarez MM, *et al.*, 2015, Synthesis, Properties, and Biomedical Applications of Gelatin Methacryloyl (GelMA) Hydrogels. *Biomaterials*, 73:254–71. https://doi.org/10.1016/j.biomaterials.2015.08.045
46. Kirillova A, Maxson R, Stoychev G, *et al.*, 2017, 4D Biofabrication Using Shape-Morphing Hydrogels. *Adv Mater*, 29:1703443. https://doi.org/10.1002/adma.201703443
47. Peak CW, Stein J, Gold KA, *et al.*, 2018, Nanoengineered Colloidal Inks for 3D Bioprinting. *Langmuir*, 34:917–25. https://doi.org/10.1021/acs.langmuir.7b02540
48. He Y, Yang F, Zhao H, *et al.*, 2016, Research on the Printability of Hydrogels in 3D Bioprinting. *Sci Rep*, 6:29977.
49. Ouyang L, Yao R, Zhao Y, *et al.*, 2016, Effect of Bioink Properties on Printability and Cell Viability for 3D Bioplotting of Embryonic Stem Cells. *Biofabrication*, 8:035020. https://doi.org/10.1088/1758-5090/8/3/035020
50. Ribeiro A, Blokzijl MM, Levato R, *et al.*, 2017, Assessing Bioink Shape Fidelity to Aid Material Development in 3D Bioprinting. *Biofabrication*, 10:014102. https://doi.org/10.1088/1758-5090/aa90e2
51. Xu C, Lee W, Dai G, *et al.*, 2018, Highly Elastic Biodegradable Single-Network Hydrogel for Cell Printing. *ACS Appl Mater Interfaces*, 10:9969–79. https://doi.org/10.1021/acsami.8b01294

RESEARCH ARTICLE

3D Topology Optimization and Mesh Dependency for Redesigning Locking Compression Plates Aiming to Reduce Stress Shielding

A. A. Al-Tamimi*

Industrial Engineering Department, College of Engineering, King Saud University, Riyadh 11421 Saudi Arabia

Abstract: Current fixation plates for bone fracture treatments are built with biocompatible metallic materials such as stainless steel, titanium, and its alloys (e.g., Ti6Al4V). The stiffness mismatch between the metallic material of the plate and the host bone leads to stress shielding phenomena, bone loss, and healing deficiency. This paper explores the use of three dimensional topology-optimization, based on compliance (i.e., strain energy) minimization, reshaping the design domain of three locking compression plates (four-screw holes, six-screw holes, and eight-screw holes), considering different volume reductions (25, 45, and 75%) and loading conditions (bending, compression, torsion, and combined loads). A finite-element study was also conducted to measure the stiffness of each optimized plate. Thirty-six designs were obtained. Results showed that for a critical value of volume reductions, which depend on the load condition and number of screws, it is possible to obtain designs with lower stiffness, thereby reducing the risk of stress shielding.

Keywords: Bone plates; Finite element analysis; Mesh dependency; Stress shielding; Topology optimization.

*Correspondence to: Abdulsalam Al-Tamimi, Industrial Engineering Department, College of Engineering, King Saud University, Riyadh 11421 Saudi Arabia; aaaltamimi@ksu.edu.sa

Received: January 5, 2021; **Accepted:** June 30, 2021; **Published Online:** July 1, 2021

Citation: Al-Tamimi AA., 2021, 3D Topology Optimization and Mesh Dependency for Redesigning Locking Compression Plates Aiming to Reduce Stress Shielding. *Int J Bioprint.* 7(3):339.http://doi.org/10.18063/ijb.v7i3.339

1. Introduction

Bone fractures represent a critical healthcare problem. In USA, number of fracture cases is predicted to increase from 2.1 million in 2005 to around three million in 2025[1]. Bone fixation implants are considered one of the riskiest implants[2], as the UK's National Health Service (NHS) reported over 11,000 revision operations for failed implants in 2016[3].

Fractures are often surgically treated with bone fixation devices such as internal fixators, external fixators, and intramedullary pins[4]. Internal fixations, the focus of this research, are usually applied to fixate the fractured bone through restoring the bone segments into its original functionality and anatomy. Since the introduction of the first metallic internal fixations in 1895 by Lane, different designs were developed and introduced in the market[5]. At present, the Locking Compression Plate (LCP) is the most commonly used fixation plate due to its hybrid design consisting of a conventional screwing system and a Locking Head Screw system[6]. LCP allows a gap between the bone and the implant to achieve callus formation and is more suitable for osteoporotic fractures[6].

Internal fixations (e.g., plates and screws) are built using biocompatible metallic materials such as stainless steel (i.e., 316L) and titanium-based alloys (e.g., Ti-6Al-4V). Such metallic materials present Young's modulus of around 120 GPa for Ti-6Al-4V and 190 GPa for 316L stainless steel, significantly higher than that for cortical bone (around 20 GPa)[7-9]. This large difference is one of the main causes of the stress shielding phenomenon characterized by the lack of mechanical stimulation of the bone through disruption of load distribution across in the bone-plate construct. This phenomenon affects the bone remodeling process, causing implant loosening and bone loss.

Different methods have been explored to reduce the stress shielding effect through the change of built material (e.g., functionally graded materials) and/or design

© 2021 Al-Tamimi. This is an Open Access article distributed under the terms of the Creative Commons Attribution License (https://creativecommons. org/licenses/by/4.0/), permitting distribution and reproduction in any medium, provided the original work is cited.

modifications (e.g. lattice structure, internal hollow, or porous structures)[10,11]. However, the fabrication of functionally graded structures is complex and expensive, while design modifications usually require laborious and costly iterative steps performed by expert technicians. Recently, we proposed a novel design method to minimize stress shielding using topology optimization (TO)[12]. Results-focused on two-dimensional (2D) topologies, considering tensile loads on the plates, loads on the holes simulating the screw and combination of both, and a maximum volume reduction of 75%. The approach allowed to obtain designs of lightweight plates with reduced equivalent stiffness compared to the proposed original design domains. In this paper, we extended the study to three-dimensional (3D) topologies, investigating the use of 3D TO to redesign novel LCPs to minimize the stress shielding phenomenon. Three initial plate designs with different screw hole numbers (four-, six-, and eight-hole plates) were redesigned considering different loading conditions (compression, bending, torsion, and a combination of these loads) imposing different volume reductions to the initial designs (25, 45, and 75%). The effect of mesh density on the TO is also investigated and discussed. Topology-optimized plate design considering bending load presented bending elastic modulus equivalent to native bone.

2. TO

TO is an automatic iterative design technique to obtain optimal structural topologies based on the user-defined loading and boundary conditions. The goal is to achieve a design with an optimal material distribution (**Ω***) from an initially given design domain (**Ω**), which is discretized into number of finite elements (N). The aim was to redesign the domain by minimizing compliance (maximizing stiffness):

$$\min_{\rho_e, u} f^T \bullet u \tag{2.1}$$

where u is the displacement vectors and f is load vectors governed by:

$$f = K(k_e) \bullet u = \sum_{e=1}^{N} \bullet K_e(k_e) \tag{2.2}$$

where K is the global stiffness matrix, K_e is the matrices of the element stiffness, and k_e is the stiffness of each element.

The density (ρ) is considered as a function to modify the design's stiffness matrix and treated as a design variable. Therefore, the density imposed on each element (ρ_e) of the design domain follows a binary variation resulting in either ρ_e=1 (i.e., keeping the element) or ρ_e=0 (i.e., removing the element) values. Solving this problem through mathematical programming algorithms require the rewriting of optimization problem (2.1) as follows:

$$\min Z(\rho_e) = f^T \cdot u \tag{2.3}$$

$$s.t. \begin{cases} V = \sum_{e=1}^{N} \rho_e v_e \le V, \\ \rho_e = 0 \, or \, 1, \quad e = 1, \ldots, N, \end{cases} \tag{2.3a}$$

where V is the initial volume and v_e is volume of each element.

The Solid Isotropic Microstructure with Penalization (SIMP), a gradient-based TO approach, was considered to solve the TO problem[13,14]. SIMP forces the design variable, to have a penalized continuous convergence as follows:

$$0 < \rho_0 \le \rho_e \le 1 \tag{2.4}$$

$$E(x,y,z) = [\rho(x,y,z)]^p \cdot E^i \tag{2.5}$$

$$K(\rho) = \sum_{e=1}^{N} \rho_e{}^p \cdot K_e \tag{2.6}$$

where ρ_0 is the non-zero minimum density, p is the penalization factor (recommended to have a value of three for a better convergence), and E^i is the initial Elastic modulus at ρ=1 of the material.

Therefore, SIMP solves equation (2.3) as follows:

$$\min_{\rho_e} Z(\rho_e) = f^T \cdot u \tag{2.7}$$

$$s.t \begin{cases} \sum_{e=1}^{N} (\rho_e) v_e \le V, \\ \sum_{e=1}^{N} (\rho_e^p) K_e u = f, \\ 0 < \rho_0 \le \rho_e \le 1, \end{cases} \tag{2.7a) (2.7b) (2.7c}$$

The iterative steps to achieve optimality through TO are shown in **Figure 1**. The solution starts with the given design domain, **Ω**, comprising the user-defined material being discretized into a set of finite elements, with each element consisting of a density value contributing to the overall design density. Then, sensitivity breakdown is defined across the displacement field according to the loading and boundary conditions, which means that the density is updated toward optimality, satisfying the objective function and constraints in each iteration.

The first step in each computational iteration corresponds to the calculation of element sensitivity based on deriving Eq. 2.7 in respect to the density:

$$\frac{\partial Z}{\partial \rho_e} = -\frac{p}{\rho_e{}^p} [u]^T [k_e][u] \tag{2.8}$$

Sensitivity filtering determines the element distribution passing through filtering formulas (e.g., mesh-

independent filtering and sensitivity filtering to prevent checkerboarding) along the design domain.

3. Simulation and optimization

3.1. Initial design domains

The DePuy Synthes narrow LCP, commonly used for the treatment of long bones such as humerus, femur, and tibia, was considered as a reference design. Three plates (four-screw holes, six-screw holes, and eight-screw holes) were designed using Solidworks (Dassault Systèmes, France) with a length of 180 mm, width of 14 mm, and thickness of 5 mm (**Table 1**). Abaqus (Dassault Systèmes, France) was used to perform the TO and finite element analysis. Plates were considered to be made with Ti-6Al-4V (120 GPa of Elastic Modulus and 0.3 of Poisson's ratio). Finite element meshes were created using eight-node linear hexahedral elements and approximately 400,000 elements were considered. Different mesh densities were also considered for the mesh dependency study.

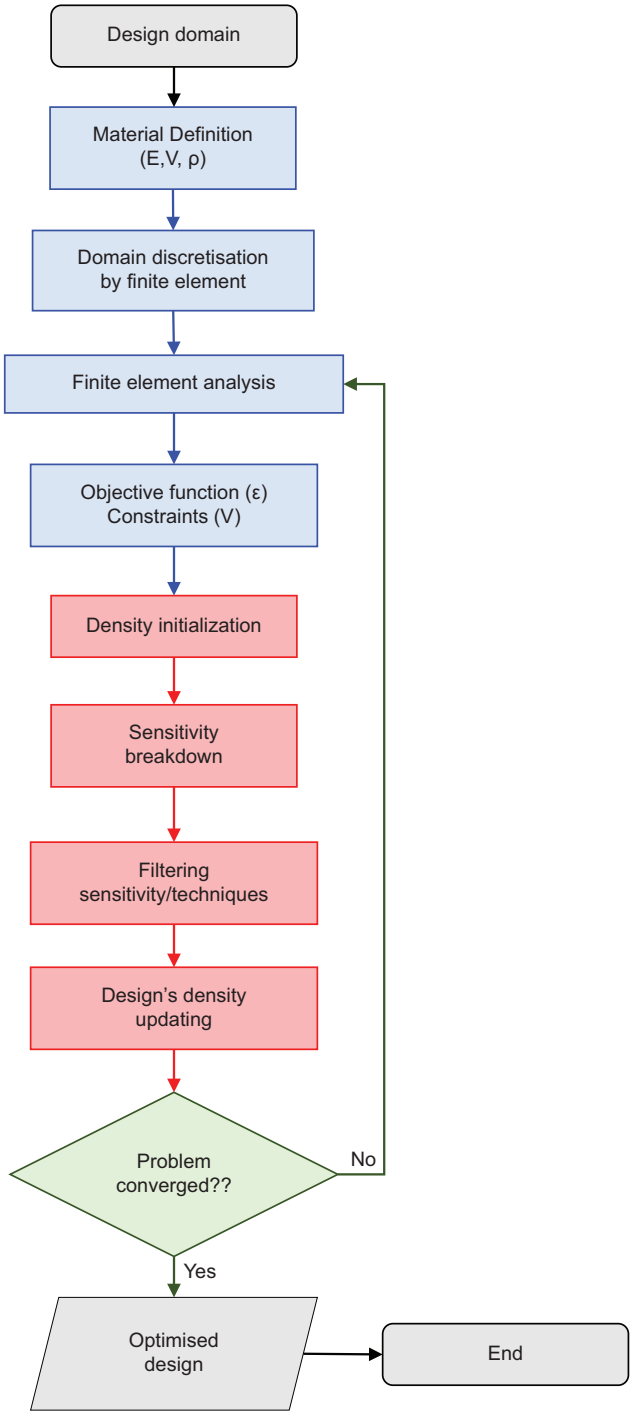


Figure 1. Workflow of SIMP optimisation.

3.2. Loading and boundary conditions

Considering possible physiological events, the plate was subjected to four types of loadings: compression, bending, torsion, and a combination of these loads that mainly occur on the screw holes and the mid-plate (**Table 2**). Compression corresponded to a static compressing force along the X-axis (the axis along the length of the plate) applied on both far-end sides of the plate and constraining the six nodes on the two opposite middle faces of the plate in all directions and rotations ($d_x=d_y=d_z=r_x=r_y=r_z=0$), symbolized by an encastre constraint. Bending corresponded to a static four-point bending test applied on the plate according to the bone fixation plate testing standards (ISO 9585:1990)[15]. The two loading points were separated with a distance of two screw holes and at least one screw hole between the load and support point. The support points constrained the bone plate from moving across the Z-axis (dx=dy=0, dz≠0) (the axis crossing the thickness of the plate), symbolized by a red-colored pin constraint. An additional two constraints were used to ensure stability in the X and Y axis (dx=dy≠0, dz=0) (the axis along the width of the plate) during loading, symbolized by an orange color pin constraint. Torsion corresponded to static moment acting along the X-axis on one end and constrained (i.e. pinned) on the other end of the plate (dx=dy=dz=0), symbolized by an orange color pin constraint. Combined load was the combination of compression, bending, and torsion, considering the constraints of the compression test. It is important to note that SIMP method was not sensitive to the load magnitude when the compliance for a given load was minimized.

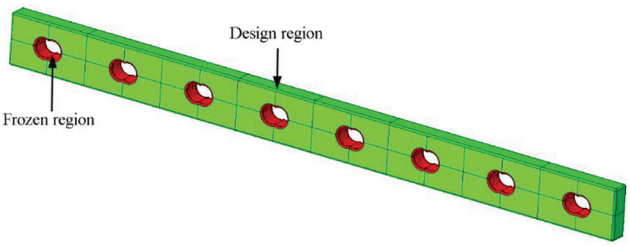
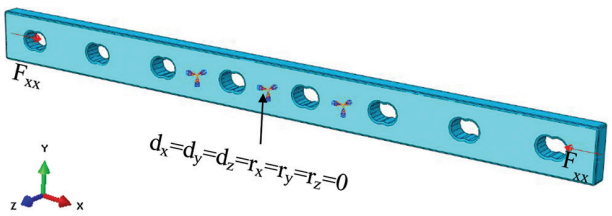
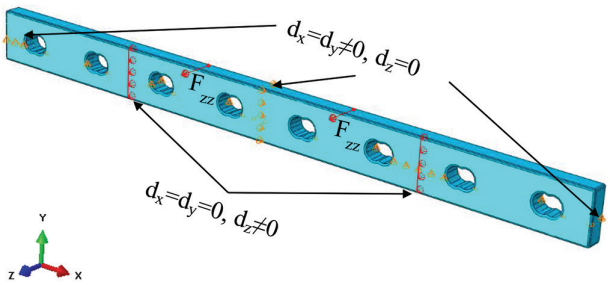
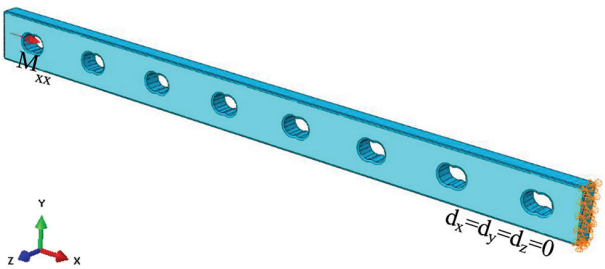
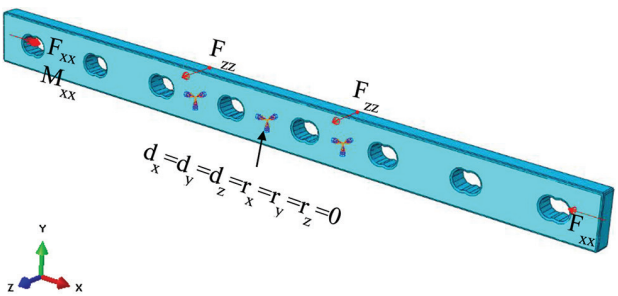


Figure 2. Design (green) and frozen (red) regions of the bone plates.

Table 1. The initial designs considered for the bone plates

Plate reference	Number of holes	
ID4	4	
ID6	6	
ID8	8	

Table 2. Loading and boundary conditions considered for topology optimization

Loading type	Description
Compression load	
Bending load	
Torsion load	
Combined load	

SIMP optimization was used to minimize the strain energy of the plate designs shown in **Table 1**, considering different volume reductions (25, 45, and 75%) of the initial design volume. To guarantee the integrity of the screw holes to preserve their shape during TO, the holes were considered frozen regions, as shown in **Figure 2**.

3.3. Mesh dependency

Similar to any numerical approximation method, TO results are dependent on the meshing quality[16]. Therefore, a preliminary study was conducted considering an eight screw holes plate under compression loading and a volume reduction of 45%, discretized with eight-node

linear hexahedral elements and meshed with different number of elements (5000 elements, 10,000 elements, 25,000 elements, 50,000 elements, 75,000 elements, 100,000 elements, 250,000 elements, 350,000 elements, and 400,000 elements).

3.4. Stress shielding analysis

The stiffness of each plate, for different loading conditions, is the main criteria to determine possible stress shielding problems. In all cases, the optimized plates were considered homogeneous and isotropic. Based on the numerical finite element analyses and their loading and boundary conditions in **Table 2**, the corresponding equivalent stiffness of each plate was determined[12]. For the compression case (similar to combined load case), the equivalent stiffness was calculated considering the longitudinal reaction uniaxial force (RF_{xx}) in kilonewton (kN) along the X-axis applied on one end of the bone plate and constraining the opposite side, as follows:

$$K_{Te} = \frac{RF_{xx}}{D_{xx}} \tag{3.1}$$

where KTe is the equivalent stiffness in kN/mm and Dxx is the resulted displacement in mm. In the bending case, the equivalent bending stiffness was calculated according to the following equation (British Standard 1991)[15]:

$$K_B = \frac{\left(4h^2 + 12h\varsigma + \varsigma^2\right)Sh}{24} \tag{3.2}$$

where K_B is the equivalent bending stiffness in $N.m^2$, h is the distance between the load and support points, is the distance between the load points, and S is the slope of the load-deflection curve.

The equivalent elastic bending modulus was measured as follows (ASTM Standard 2017)[17]:

$$E_B = 0.17L^3S / bd^3 \tag{3.3}$$

where E_B is the equivalent bending elastic modulus in GPa, L is the support span, b is the plate's width, and d is the plate's thickness.

For the torsion case, the equivalent stiffness was determined considering the reaction moment across the X-axis (T_{xx}) applied on one end of the plate, constraining the other end. The resulted angle of twist along the X-axis direction (ϕ_{xx}) was recorded and the torsional stiffness was determined as follows:

$$K_{Tr} = \frac{T_{xx}}{\varphi_{xx}} \tag{3.4}$$

where K_{Tr} is the torsional stiffness in Nmm/Rad.

4. Results and discussion

Despite utilizing mesh-dependency filtering techniques, TO in commercial software appears to be affected by the mesh density[16,18]. The effect of mesh size on the optimization process is shown in **Figure 3** and the corresponding equivalent stiffness is presented in **Figure 4**. Coarse mesh results in less material removal

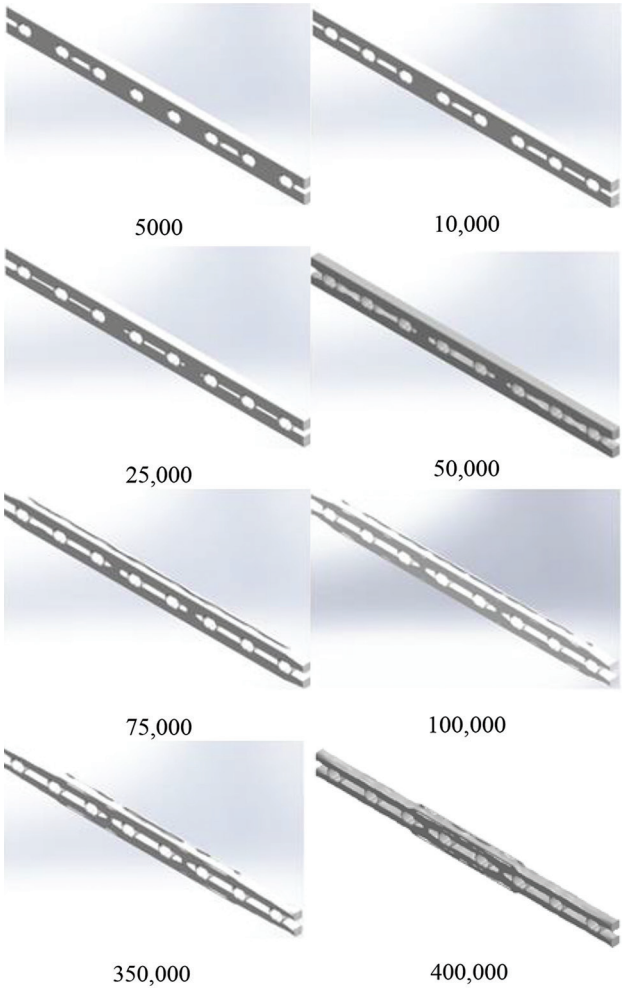


Figure 3. Mesh dependency - plate redesigns for different number of elements.

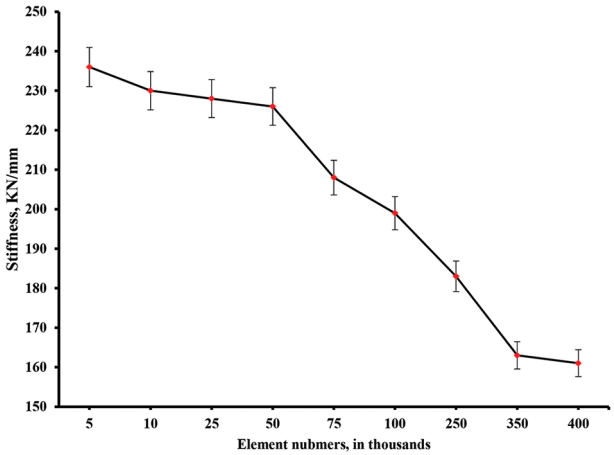


Figure 4. Equivalent stiffness values as a function of mesh size.

and lower computational time, while finer mesh increases the volume reduction and the computational time. As observed, no significant difference in equivalent stiffness values will be obtained if elements were to be increased more than 400,000 elements and the computational cost will significantly increase.

Figures 5-8 present the optimized designs for all plates (eight-, six-, and four- screw holes), different loading conditions, and volume reduction. Imposed volume reductions vary between 25% and 75% as values higher than 75% can jeopardize the design's structural integrity, while values lower than 25% have no significant effect on the stiffness reduction. The corresponding equivalent stiffness values are presented in **Tables 3-6**. In all cases, the equivalent stiffness decreases by increasing the volume reductions, confirming previously reported observations for TO of 2D plates[12]. Several authors observed similar results using TO to address stress shielding by redesigning orthopedic implants in the case of pelvic prosthetics[19], hip prosthetics,[20] and spine implants[21]. The results also indicate that the mechanical properties are directly related to the material volume as

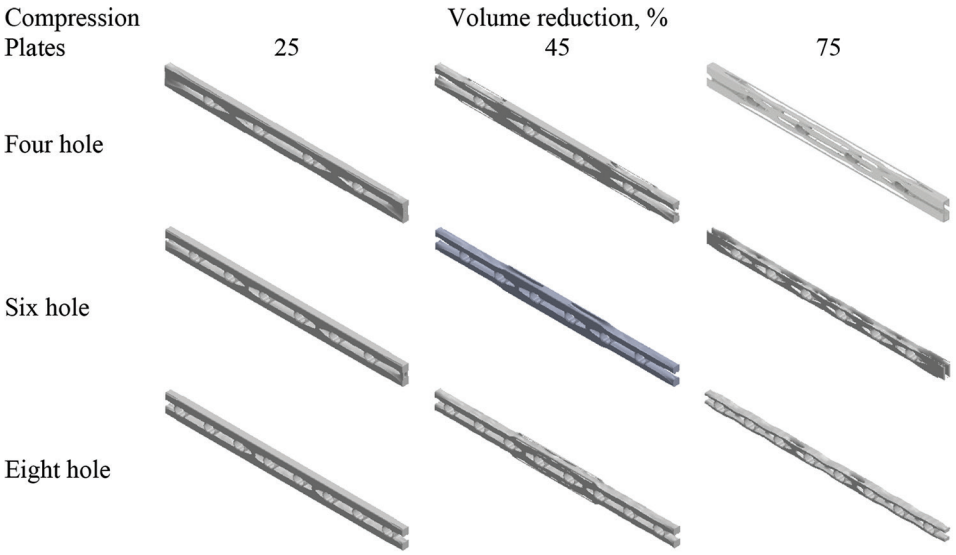


Figure 5. Topology-optimized plates under compression conditions.

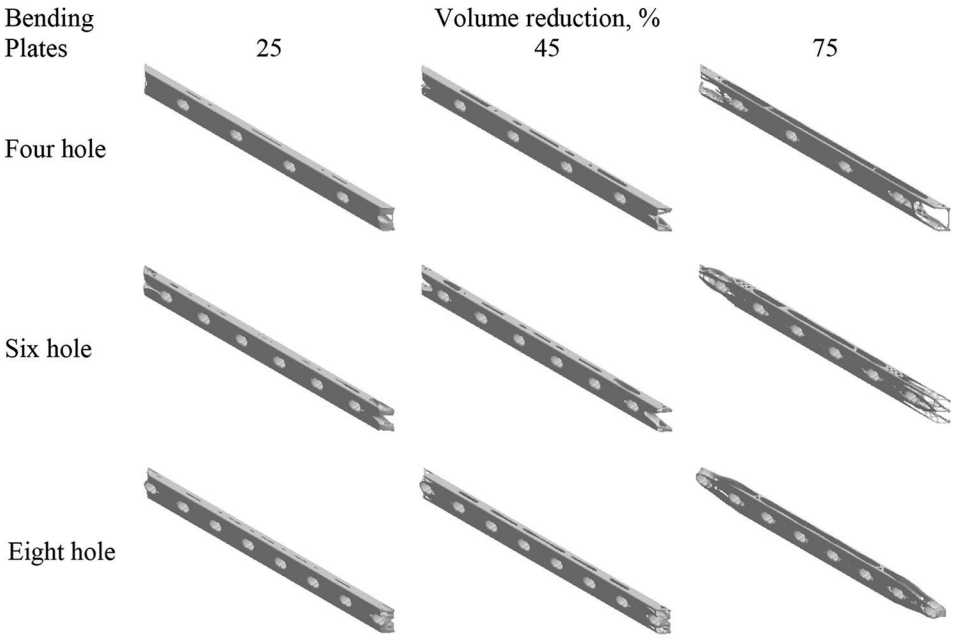


Figure 6. Topology-optimized plates under bending loading conditions.

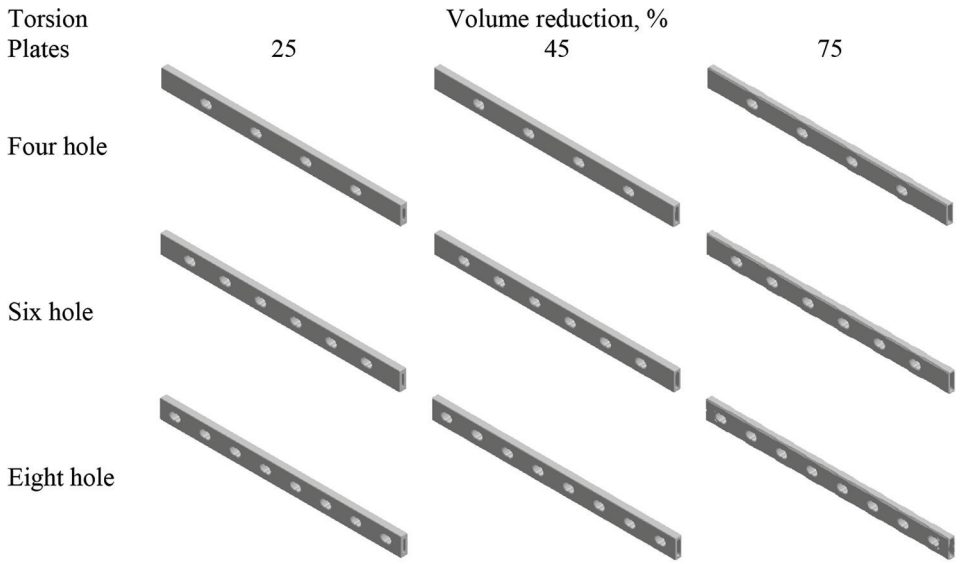


Figure 7. Topology-optimised plates under torsion loading conditions.

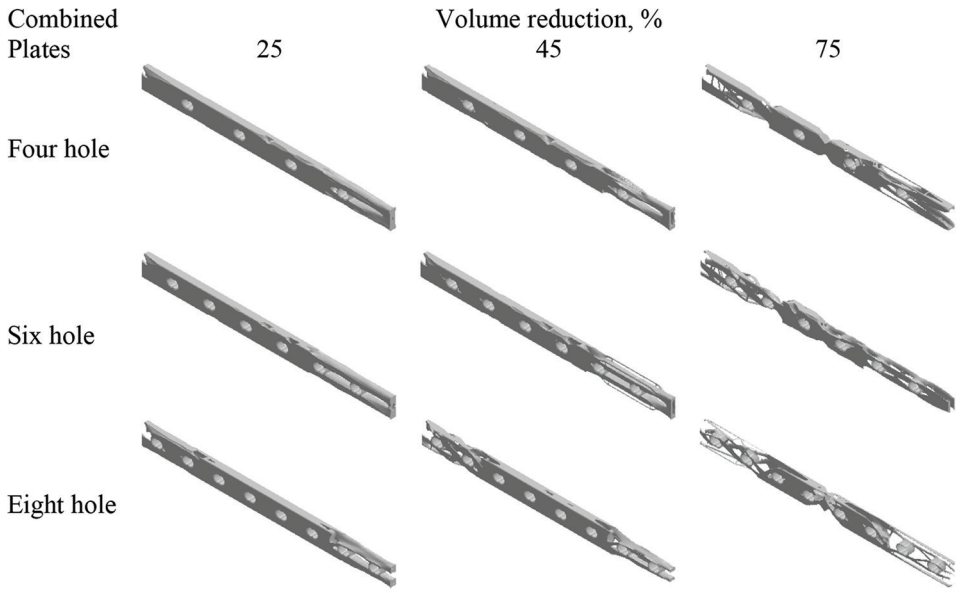


Figure 8. Topology-optimised plates under combined loading conditions.

Table 3. Equivalent stiffness of optimized plate designs considering compression loading conditions

Volume reduction %	Equivalent stiffness (kN/mm)		
	Plate with 4 holes	Plate with 6 holes	Plate with 8 holes
Initial design	306±6.46	247±12.65	237±5.38
25	252±5.32	203±10.39	196±4.45
45	167±3.52	135±6.91	161±3.65
75	23±0.48	21±1.07	28±0.63

Table 4. Equivalent stiffness of optimized plate designs considering bending loading conditions

Volume reduction %	Equivalent stiffness (N.m^2)		
	Plate with 4 holes	Plate with 6 holes	Plate with 8 holes
Initial design	19.27±0.41	18.68±0.96	16.22±0.39
25	16.32±0.34	15.41±0.79	13.38±0.3
45	13.23±0.28	11.34±0.58	4.81±0.11
75	9.26±0.19	4.14±0.21	2.34±0.05

it is clear that for all the loading cases with the same volume reduction, plates containing four holes are stiffer than plates containing six holes, which are also stiffer than plates containing eight holes. These results present

Table 5. Equivalent stiffness of optimized plate designs considering torsion loading conditions.

Volume reduction %	Equivalent stiffness (Nmm/Rad)		
	Plate with 4 holes	Plate with 6 holes	Plate with 8 holes
Initial design	28550±602	26170±1336	24792±562
25	23550±496	24574±1258	15737±357
45	15767±333	17539±898	13348±302
75	3653±77	6932±355	7304±166

Table 6. Equivalent stiffness of optimized plate designs considering combined loading conditions

Volume reduction %	Equivalent stiffness (kN/mm)		
	Plate with 4 holes	Plate with 6 holes	Plate with 8 holes
Initial design	306±6.45	247±12.65	237±5.38
25	237±5.00	214±10.96	145±3.29
45	158±3.33	101±5.17	123±2.79
75	22±0.46	20±1.02	28±0.63

significant findings of the possibility of optimizing the bone plate's stiffness considering physiological loads by reducing the design's material volume. In addition, a significant reduction of the stiffness is a major indication of reduced risk of the stress shielding (i.e., bone loss), thus promoting callus formation and bone formation[22-24]. Considering that the bone elastic bending modulus ranges between 9 to 15 GPa, the bending optimized plate with eight holes and 75% of volume reduction showed an equivalent elastic bending modulus (11 GPa) within this region[25]. This proves that using topology optimization is possible to obtain designs that are able to match the mechanical properties of native bone and thus, and eliminate the main cause to stress shielding. In addition, previous studies reported that using TO in designing generic fixation plates[26] and mandible fixation plates[27], which depends on the volume reduction and loading condition, is possible to reduce the plate's stiffness while maintaining its mechanical stability to withstand stresses.

Design symmetry is important when considering design to manufacture and to eliminate the design complexity for the surgeons during surgery. Symmetrical designs were observed in the case of compression and torsion due to the considered symmetrical loading and boundary conditions. Bending optimized designs were symmetrical in YZ plane but not in the XY plane due to the bending load which compresses one side of the plate and tensions the other. In the combined load case, the designs were freely designed regardless of the symmetry as the combination of compression, bending, and torsion loads result in asymmetric stress and strain distributions.

In addition, the optimized bone plates produced using TO present complex features which are impossible to manufacture using conventional manufacturing but possible through additive manufacturing[28]. Researchers previously reported the successful combination of TO, electron beam melting, and selective laser melting, considering different conditions (i.e. low mesh density)[29], and similar conclusions were also obtained by other researchers[19].

5. Conclusion

Stress shielding is a common problem in standard bone fixation plates, requiring new tools to redesign them and new fabrication methods to produce them. This paper, extending previously reported results considering 3D plates, shows that TO is a suitable tool to redesign bone fixation plates with different geometries, considering different loading conditions and volume reduction, allowing to obtain plates with reduced equivalent stiffness that matches the mechanical properties of native bone in case of eight-hole plate, and considering bending load and 75% volume reduction. A trend between volume reduction and equivalent stiffness was observed. A significant stiffness reduction was achieved for high volume reductions, preventing stress shielding and potentially avoiding bone resorption and eventual plate failure.

Previously reported results showed the ability of topology-optimized fixation plates, obtained by different conditions (i.e., low mesh density), to withstand stresses in a biomechanical setting. This study did not investigate the potential stress concentration regions resulting from the TO and the mechanical strength (yield stress) of the optimized plates with high mesh density. Future studies must address this limitation by computationally assessing the optimized bone plate designs with high mesh density designs from a biomechanical perspective in a fractured bone configuration.

Acknowledgments

Researchers Supporting Project number (RSP-2021/299), King Saud University, Riyadh, Saudi Arabia.

Conflicts of interest

The author declare no conflicts of interest.

References

1. Amin S, Achenback S, Atkinson E, *et al*., 2014, Trends in Fracture Incidence: A Population-based Study Over 20 Years. *J Bone Miner Res*, 29:581–9. https://doi.org/10.1002/jbmr.2072
2. Kramer D, Xu S, Kesselheim A, 2012, Regulation of Medical Devices in the United States and European Union. *N Engl J*

Med, 366:848–55.
https://doi.org/10.1056/nejmhle1113918

3. Green M, Wishart N, Young E, 2016, NJR 14th Annual Report. National Joint Registry, England.
4. Alsop H, 2013, An introduction to fractures' in porter. In: Tidy's Physiotherapy. 15th ed., Ch. 22. Churchill Livingstone, United Kingdom.
5. Uhthoff HK, Poitras P, Backman DS, 2006, Internal Plate Fixation of Fractures: Short History and Recent Developments. *J Orthop Sci*, 11:118–26.
https://doi.org/10.1007/s00776-005-0984-7
6. Szypryt P, Forward D, 2009, The Use and Abuse of Locking Plates. *Orthop Trauma*, 23:281–90.
https://doi.org/10.1016/j.mporth.2009.07.002
7. Elias CN, Lima JHC, Valiev R, *et al*., 2008, Biomedical Applications of Titanium and its Alloys. *JOM*, 60:46–9.
https://doi.org/10.1007/s11837-008-0031-1
8. McNamara L, 2011, Bone as a Material in Ducheyne. In: Comprehensive Biomaterials, Elsevier, Oxford.
9. Prasad K, Bazaka O, Chua M, *et al*., 2017, Metallic Biomaterials: Current Challenges and Opportunities. *Materials*, 10:884.
https://doi.org/10.3390/ma10080884
10. Mahmoud D, Elbestawi MA, 2017, Lattice Structures and Functionally Graded Materials Applications in Additive Manufacturing of Orthopedic Implants: A Review. *J Manufact Mater Proc*, 1:13.
https://doi.org/10.3390/jmmp1020013
11. Pałka K, Pokrowiecki R, 2018, Porous Titanium Implants: A Review. *Adv Eng Mater*, 20:1700648.
https://doi.org/10.1002/adem.201700648
12. Al-Tamimi A, Fernandes PRA, Peach C, *et al*., 2017, Metallic Bone Fixation Implants: A Novel Design Approach for Reducing the Stress Shielding Phenomenon. *Virtual Phys Prototy*, 12:141–51.
https://doi.org/10.1080/17452759.2017.1307769
13. Bendsøe MP, 1989, Optimal Shape Design as a Material Distribution Problem. *Struct Optim*, 1:193–202.
https://doi.org/10.1007/bf01650949
14. Bendsøe MP, Sigmund O, 2004, Topology Optimization by Distribution of Isotropic Material in Topology Optimization: Theory, Methods, and Applications. Springer Berlin Heidelberg, Berlin, Heidelberg.
https://doi.org/10.1007/978-3-662-05086-6_1
15. British Standard, 1991, Implants for Osteosynthesis-Part 23: Bone Plates-Section 23.1 Method for Determination of Bending Strength and Stiffness. British Standard, United Kingdom.
https://doi.org/10.3403/00189873u
16. Sigmund O, Petersson J, 1998, Numerical Instabilities in Topology Optimization: A Survey on Procedures Dealing with Checkerboards, Mesh-dependencies and Local Minima. *Struct Optim*, 16:68–75.
https://doi.org/10.1007/bf01214002
17. ASTM Standard, 2017, Standard Test Method for Flexural Properties of Unreinforced and Reinforced Plastics and Electrical Insulating Materials by Four-point Bending, ASTM Standard, United States, pD6272–17.
https://doi.org/10.1520/d6272-02r08e01
18. Buhl T, Pedersen C, Sigmund O, 2000, Stiffness Design of Geometrically Nonlinear Structures Using Topology Optimization. *Struct Multidisc Optim*, 19:93–104.
https://doi.org/10.1007/s001580050089
19. Iqbal T, Wang L, Li D, *et al*., 2019, A General Multi-objective Topology Optimization Methodology Developed for Customized Design of Pelvic Prostheses. *Med Eng Phys*, 69:8–16.
https://doi.org/10.1016/j.medengphy.2019.06.008
20. Saravana KG, George S, 2017, Optimization of Custom Cementless Stem Using Finite Element Analysis and Elastic Modulus Distribution for Reducing Stress-shielding Effect. *Proc Inst Mech Eng H*, 231:149–59.
https://doi.org/10.1177/0954411916686125
21. Chuah HG, Rahim IA, Yusof MI, 2010, Topology Optimisation of Spinal Interbody Cage for Reducing Stress Shielding Effect. *Comput Methods Biomech Biomed Eng*, 13:319–26.
https://doi.org/10.1080/10255840903208189
22. Woo S, Simon B, Akeson W, *et al*., 1977, An Interdisciplinary Approach to Evaluate the Effect of Internal Fixation Plate on Long Bone Remodeling. *J Biomech*, 10:87–95.
https://doi.org/10.1016/0021-9290(77)90072-0
23. Goodship A, Kenwright J, 1985, The Influence of Induced Micromovement Upon the Healing of Experimental Tibial Fractures. *J Bone Joint Surg Br*, 67:650–5.
https://doi.org/10.1302/0301-620x.67b4.4030869
24. Claes L, Augat P, Suger G, *et al*., 1997, Influence of Size and Stability of the Osteotomy Gap on the Success of Fracture Healing. *J Orthop Res*, 15:577–84.
https://doi.org/10.1002/jor.1100150414
25. Keller TS, Mao Z, Spengler DM, 1990, Young's Modulus, Bending Strength, and Tissue Physical Properties of Human Compact Bone. *J Orthop Res*, 8:592–603.
https://doi.org/10.1002/jor.1100080416

26. Al-Tamimi AA, Quental C, Folgado J, *et al.*, 2020, Stress Analysis in a Bone Fracture Fixed with Topology-optimised Plates. *Biomech Model Mechanobiol*, 19:693–9. https://doi.org/10.1007/s10237-019-01240-3

27. Liu Y, Fan Y, Jiang X, *et al*., 2017. A Customized Fixation Plate with Novel Structure Designed by Topological Optimization for Mandibular Angle Fracture Based on Finite Element Analysis. *BioMedical Eng Online*, 16:1–17. https://doi.org/10.1186/s12938-017-0422-z

28. Zegard T, Paulino GH, 2016, Bridging Topology Optimization and Additive Manufacturing. *Struct Multidiscip Optim*, 53:175–92. https://doi.org/10.1007/s00158-015-1274-4

29. Al-Tamimi AA, Hernandez MA, Omar A, *et al*., 2020, Mechanical, Biological and Tribological Behaviour of Fixation Plates 3D Printed by Electron Beam and Selective Laser Melting. *Int J Adv Manufact Technol*, 109: 673–88. https://doi.org/10.1007/s00170-020-05676-1

INTERNATIONAL JOURNAL OF BIOPRINTING

ISSN (print): 2424-7723

ABOUT THE JOURNAL

International Journal of Bioprinting is a biannual, double-blind peer-reviewed, open access journal. This journal focuses on the use of 3D printing technology with materials that incorporate viable living cells or biological elements to produce tissue or biotechnological products. Further discourses and technological advancements in bioprinting are the goals behind acceptance of high-quality basic and applied research: from concept creation to fabrication of the bioprinting process, associated clinical applications as well as social implications.



Whioce Publishing, official publisher for the journal welcomes researchers to submit their papers relevant to bioprinting for consideration via **http://ijb.whioce.com/** For general enquiries and order for prints and reprints, please write in to **IJB@whioce.com** for a fast response.

SUBMIT YOUR PAPERS HERE

WHIOCE
PUBLISHING PTE. LTD.

ABOUT THE PUBLISHER

Whioce Publishing in Singapore is a registered publisher of excellent quality academic journals for an international readership. We deliver exceptional editorial support for the advancement and dissemination of scientific research by linking readers and researchers with networks and industries. We have ambitions to get our journals indexed in prominent databases such as EI, SCI, SSCI and AHCI, thereby aiming to be a first-class knowledge platform for researchers worldwide.

Whioce Publishing also engages in publishing e-books, organizing academic conferences and educational trainings, and providing translational services.

International Journal of Bioprinting is an
independent open access journal published
by Whioce Publishing Pte.Ltd.



WHIOCE PUBLISHING PTE. LTD.
PROVIDING
FIRST-CLASS SCIENTIFIC INFORMATION
FOR TOP SCHOLARS

Whioce Publishing Pte.Ltd.
7030 Ang Mo Kio Avenue 5
#04-15 Northstar@AMK
Singapore 569880
Tel: +65 65702707/65702718
Fax: +65 65702803

See www.whioce.com/contact for a full list of offices and contact information.

Whioce Publishing Pte.Ltd. is a company registered in Singapore (No. 201427293E), whose registered office is at 7030 Ang Mo Kio Avenue 5 #04-15 Northstar@AMK Singapore 569880